

# **CARBON NANO-ONIONS AS PROMISING NANOMATERIAL FOR BIOMEDICAL AND ELECTROCHEMICAL APPLICATIONS**

**DOCTORAL THESIS**

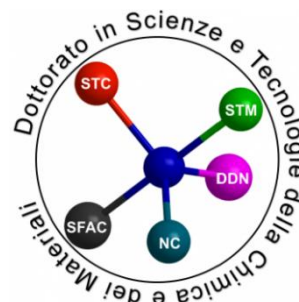


**UNIVERSITÀ DEGLI STUDI  
DI GENOVA**

**PhD student: Adalberto Camisasca**

**Supervisor: Prof. Silvia Giordani**

**14<sup>th</sup> March 2019**



# **CARBON NANO-ONIONS AS PROMISING NANOMATERIAL FOR BIOMEDICAL AND ELECTROCHEMICAL APPLICATIONS**

**A thesis submitted to the University of Genoa  
for the degree of Doctor of Philosophy**

**Department of Chemistry and Industrial Chemistry**

**Doctorate School in Sciences and Technologies  
of Chemistry and Materials**

**Curriculum: Nanochemistry**

**XXXI Cycle**

***IIT Supervisor: Prof. Silvia Giordani***

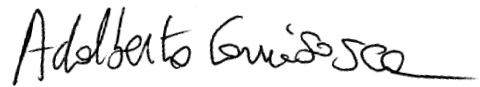
***UniGe Supervisor: Prof. Fabio Canepa***

***PhD student: Adalberto Camisasca***

**14<sup>th</sup> March 2019**

# Declaration

This thesis is being submitted for the degree of Doctor of Philosophy in the University of Genoa, Italy and has not been submitted before for any degree or examination in this or any other University. Except where acknowledgment is given, all work described is original and carried out by the author alone. Permission is granted so that the Library may lend or copy this thesis upon request. This permission covers only single copies, made for study purposes, subject to normal condition of acknowledgment.

A handwritten signature in black ink, reading "Adalberto Camisasca", positioned above a horizontal line.

Adalberto Camisasca

To my parents, my sister and my brother



“Life exists in the universe only because the carbon atom possesses certain exceptional properties.”

-Sir James Jeans

# Acknowledgements

This thesis dissertation is the culmination of a three-year long work and all this would not have been possible without the support of several people. With considerable gratitude, herein I would like to acknowledge all of them.

Foremost, I wish to express my sincere thanks to my PhD supervisor Prof. Silvia Giordani for her valuable guidance and continuous support over the last three years. Her scientific insight and motivation played a central role in pursuing my doctorate degree. Her great devotion for science has inspired me all along.

I would like to thank Prof. Robert Forster from Dublin City University (Ireland) and Prof. Toru Maekawa from Toyo University (Japan) for hosting me in their research centers. The knowledge they shared with me has been crucial for my growth as scientist.

I would like to thanks Prof. Robert Forster from Dublin City University (Ireland) and Prof. Paula Colavita from Trinity College Dublin (Ireland) for their valuable comments in evaluating my thesis.

I would also like to extend my appreciations to all the present and previous members of the NACM group. Firstly, I am profoundly thankful to Dr. Stefania Lettieri for the synthesis of the dye molecules and for her constant scientific support with valuable and constructive advices throughout my work.

I would like to thank Dr. Marta d'Amora for performing the biological studies and for her help on the understanding of bio-related results. To Francesca and Viviana for making this working experience unique. To Dr. Jurgen Bartelmess and Dr. Michele Baldrighi for sharing their experience with me. Also, I would like to thank Dr. Mirtha Lourenço for proof-reading my thesis and for her valuable suggestions.

A special thanks to Dr. Adriano Sacco for his kind collaboration and availability for fruitful conversations about electrochemistry.

Many thanks to Pascal (Pasky), Cristina (La Prof), Denis and all the people who personally helped me during my stay in Turin.

I would like to acknowledge the Istituto Italiano di Tecnologia for financial support and the University of Genoa for giving me the opportunity to purse my doctoral degree. Also, I am grateful to the NACH and NAPH departments and at IIT for access to instrumentation and their technicians for the technical support.

I am deeply thankful to my dear friends Marco and Emanuele (Immy) for their personal support during all these years. It has been a great pleasure to share this journey together. You guys have become part of my family.

A special thanks to Lea for making my stay in Genoa easier and pleasant since the moment we met.

May thanks to my lifelong friends in Rome who, even if we were apart, always supported me.

Last but not the least, I would like to thank my parents, Luigi and Serenella, and my beloved sister Gaia and brother Eugenio for their consistent patience, encouragement and support. I owe them for the person I became today.

# Table of contents

<b>Abstract of dissertation .....</b>	<b>i</b>
<b>List of figures.....</b>	<b>iii</b>
<b>List of tables.....</b>	<b>viii</b>
<b><i>Chapter 1 - Introduction .....</i></b>	<b>1</b>
<b>1.1 Carbon nanomaterials .....</b>	<b>1</b>
<b>1.2 Carbon nano-onions.....</b>	<b>3</b>
<b>1.2.1 Synthetic approaches for production of carbon nano-onions.....</b>	<b>4</b>
<b>1.2.2 Physico-chemical properties and applications of carbon nano-onions .....</b>	<b>12</b>
<b>1.3 Carbon nano-onions in nanomedicine.....</b>	<b>16</b>
<b>1.3.1 <i>In vitro</i> bio-evaluation of carbon nano-onions.....</b>	<b>16</b>
<b>1.3.2 <i>In vivo</i> bio-evaluation of carbon nano-onions .....</b>	<b>21</b>
<b>1.4 Carbon nano-onions in electrocatalysis .....</b>	<b>23</b>
<b>1.4.1 Fuel cells and oxygen reduction reaction.....</b>	<b>23</b>
<b>1.4.2 Carbon nanomaterials as ORR catalyst.....</b>	<b>26</b>
<b>1.4.3 Carbon nano-onions as ORR catalyst .....</b>	<b>32</b>
<b>1.5 References .....</b>	<b>37</b>
<b><i>Chapter 2 - Synthesis of carbon nano-onions by thermal annealing .....</i></b>	<b>47</b>
<b>2.2 Experimental .....</b>	<b>49</b>
<b>2.3 Results and discussion .....</b>	<b>49</b>
<b>2.3.1 Transmission electron microscopy .....</b>	<b>49</b>
<b>2.3.2 Electron energy loss spectroscopy .....</b>	<b>52</b>
<b>2.3.3 X-ray diffraction .....</b>	<b>53</b>
<b>2.3.4 X-ray photoelectron spectroscopy .....</b>	<b>54</b>
<b>2.3.5 Raman spectroscopy .....</b>	<b>56</b>
<b>2.3.6 Fourier-transform infrared spectroscopy.....</b>	<b>60</b>
<b>2.3.7 Thermogravimetric analysis .....</b>	<b>60</b>

2.3.8 BET nitrogen adsorption analysis .....	61
2.4 Conclusion.....	63
2.5 References .....	64
<i>Chapter 3 - Far-red fluorescent carbon nano-onions as bright biological imaging agents .....</i>	<i>67</i>
3.1 Introduction.....	67
3.2 Experimental .....	69
3.2.1 Synthesis of pristine carbon nano-onions .....	69
3.2.2 Synthesis of oxidized carbon nano-onions .....	69
3.2.3 Synthesis of fluorescently labelled carbon nano-onions .....	69
3.3 Results and discussion .....	70
3.3.1 Transmission electron microscopy .....	70
3.3.2 X-ray photoelectron spectroscopy .....	71
3.3.3 Raman spectroscopy .....	74
3.3.4. Thermogravimetric analysis .....	75
3.3.5 Dynamic light scattering and zeta potential .....	76
3.3.6 Absorption and emission spectroscopies.....	78
3.3.7 <i>In vitro</i> investigation.....	80
3.4 Conclusion.....	82
3.5 References .....	83
<i>Chapter 4 - Boron/nitrogen co-doped carbon nano-onions as efficient and durable electrocatalysts for the oxygen reduction reaction.....</i>	<i>85</i>
4.2 Experimental .....	87
4.2.1 Synthesis of pristine and boron/nitrogen co-doped carbon nano-onions .....	87
4.3 Results and discussion .....	87
4.3.1 Transmission electron microscopy .....	87
4.3.2 Electron energy loss spectroscopy .....	89
4.3.3 X-ray photoelectron spectroscopy .....	89
4.3.4 X-ray diffraction .....	93

4.3.5 Raman spectroscopy .....	94
4.3.6 Thermogravimetric analysis .....	95
4.3.7 Fourier-transform infrared spectroscopy .....	96
4.3.8 BET nitrogen adsorption analysis .....	96
4.3.9 Electrocatalytic investigation towards oxygen reduction reaction .....	97
4.4 Conclusion.....	104
4.5 References .....	105
<i>Chapter 5 - Materials and methods</i> .....	109
5.1 Materials .....	109
5.2 Methods.....	109
5.2.1 Transmission electron microscopy .....	109
5.2.2 X-ray photoelectron spectroscopy .....	110
5.2.3 X-ray diffraction .....	110
5.2.4 Raman spectroscopy .....	110
5.2.5 Thermogravimetric analysis .....	110
5.2.6 Fourier-transform infrared spectroscopy .....	111
5.2.7 Absorption and emission spectroscopy .....	111
5.2.8 BET nitrogen adsorption analysis .....	111
5.2.9 Dynamic light scattering and zeta-potential .....	111
5.2.10 Biological methods .....	112
5.2.11 Electrochemical characterization .....	112
5.3 References .....	114
<i>Chapter 6 - Conclusions and future perspectives</i> .....	115

# Abstract of dissertation

Carbon nanomaterials (CNMs) are a class of materials that aroused great interest in the last decades in several research fields. In particular, CNMs showed great potentialities in biomedical applications because their advantageous nanometric size and biocompatibility. In addition, CNMs have been also investigated as materials for electrocatalysis due to high surface and outstanding electro-mechanical properties. In particular, doping with heteroatoms have shown to be efficiently improve their electroactivity due to the formation of active sites in the inherent graphitic skeleton.

Carbon nano-onions (CNOs) are a member of the carbon family with a structure composed of concentric graphitic shells akin to that of an onion. CNOs were firstly discovered by Ugarte in 1992, but only in the last two decades aroused great interest in the scientific community due to peculiar features such as small size, large surface area and interesting physical and chemical properties. To date, CNOs have been successfully applied in several applicative area with remarkable outcomes in biological and electrochemical applications.

The aim of the present thesis is to developed novel CNO derivatives for possible applications in biomedicine and electrocatalysis in order to expand the current knowledge in these research fields.

**Chapter 1** contains an introduction on the fascinating world of carbon nanomaterials with particular emphasis given to carbon nano-onions. The structural characteristics and the reported production methods are discussed in details in the first part, while the second part illustrates the remarkable physico-chemical properties, the functionalization strategies exploited to enhance their dispersing abilities, concluding with the description of current applications involving CNOs. A detailed description has been provided in two applicative fields, which are of interest for the present thesis. In the first part, the biological investigations performed on CNOs have been described with particular attention on the *in vitro* and *in vivo* bio-evaluation, showing that CNOs are a biocompatible material. In the second part, the operative principles of fuel cells and information about oxygen reduction reaction have been discussed in detailed. Later, a literature review on the doping strategies performed on carbon nanomaterials for electrocatalysis has been provided with particular emphasis given on the use of CNOs as electrocatalysts for the oxygen reduction reaction.

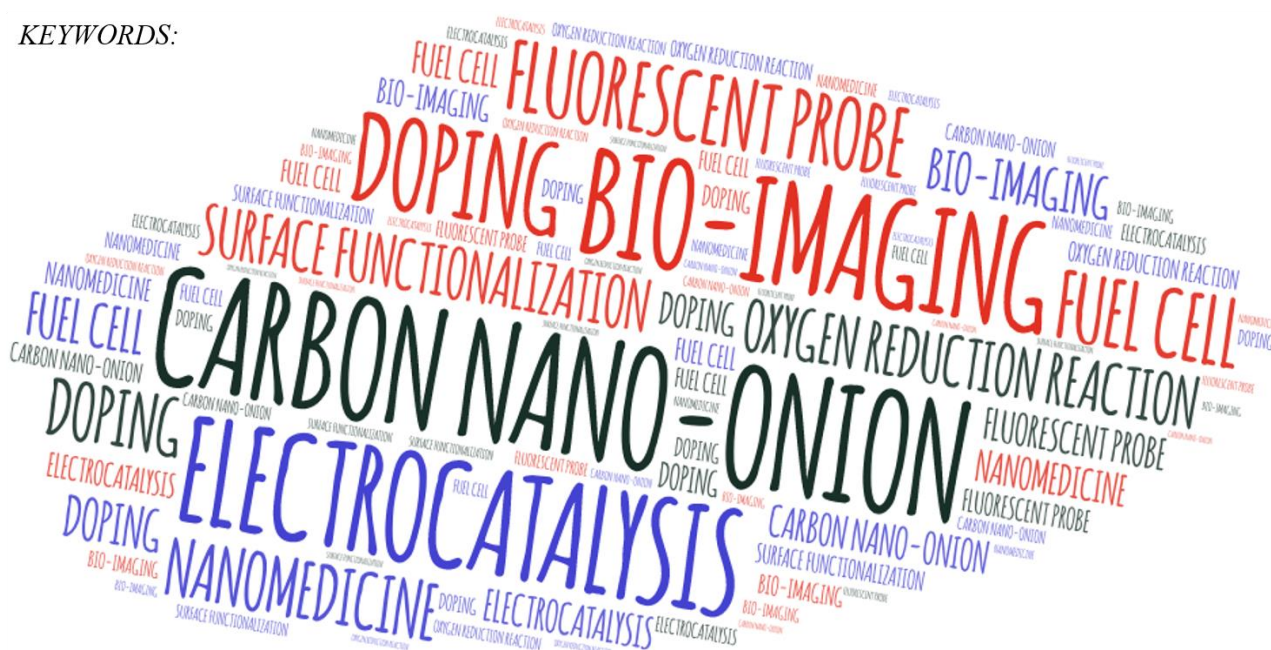
**Chapter 2** illustrates the synthesis and characterization of 5 nm-sized pristine CNOs (p-CNOs). Thermal annealing of detonation nanodiamonds was employed to fabricate CNOs and the successful formation was corroborated by several characterization techniques such as x-ray diffraction (XRD), x-ray photoelectron spectroscopy (XPS), high-resolution transmission electron microscopy (HRTEM), Raman, electron energy loss (EEL) and Fourier-transform infra-red (FTIR) spectroscopies.

**Chapter 3** reports the development of a novel CNO-based biological imaging agent. A novel far-red fluorescent BODIPY dyes, synthesized in our laboratory, was attached by esterification reaction to the CNO surface bearing carboxylic acid functionalities and tested on human breast cancer cells (MCF-7). Fluorescent CNOs exhibited bright fluorescence upon internalization and negligible effect on the cell viability at different concentrations. Low cytotoxicity, ease of internalization and remarkable emission properties confirmed the outstanding abilities of CNO derivatives in biological applications.

**Chapter 4** illustrates the development of an efficient and low cost CNO-based electrocatalyst for the oxygen reduction reaction (ORR). The introduction of boron and nitrogen into the CNO framework was accomplished by an *in-situ* co-doping strategy based on thermal annealing of a mixture of detonation nanodiamonds and boric acid. The electroactivity towards ORR of the CNO derivatives were compared with that of p-CNOs and standard carbon-supported platinum catalysts (Pt/C). The results showed that the co-doped materials exhibit enhanced ORR performance, higher long-term stability and negligible metal crossover effect as a consequence of the presence of large amount of active sites (i.e. pyridinic N and substitutional B species), thus confirming the abilities of the proposed co-doping approach to create a new material able to efficiently catalyze the ORR.

**Chapter 5** describes the materials and methods used for the experimental work of the proposed thesis. Finally, **Chapter 6** contains the conclusions as well as the future perspectives of the presented doctoral activity.

**KEYWORDS:**





# List of figures

Figure 1.1: Schematic representation of the main members of carbon nanomaterials. ....	2
Figure 1.2: HRTEM image (left) and structure (right) of CNOs, showing the concentric graphitic morphology. Reprinted with permission from [15]. ....	4
Figure 1.3: HRTEM images of CNOs produced by A) electron irradiation and B) arc discharge. Adapted with permission from [23] and [25], respectively. ....	5
Figure 1.4: Schematic representation of A) arc discharge apparatus and B) CNO formation mechanism. Adapted with permission from [26]. ....	6
Figure 1.5: HRTEM images of DNDs (a) and spherical CNOs produced by thermal annealing. Adapted with permission from [28]. ....	6
Figure 1.6: HRTEM images of the evolution of the transformation of DNDs to CNOs. (a) Initial stage, (b) intermediate stage and (c) final stage. Reprinted with permission from [30]. ....	7
Figure 1.7: Schematic representation of the DND-CNO transformation during annealing, including TEM micrographs and optical images. Reprinted with permission from [17]. ....	8
Figure 1.8: HRTEM images of CNOs synthesized by A) CVD and B) radio frequency plasma. Adapted with permission from [47] and [49], respectively. ....	10
Figure 1.9: HRTEM images of CNOs produced by A) ball milling and B) ion implantation. Adapted from [51] and [53], respectively. ....	11
Figure 1.10: HRTEM images of CNOs produced by A) laser ablation, B) thermolysis of $\text{NaN}_3\text{-C}_6\text{Cl}_6$ mixture, C) counterflow diffusion flames and D) pyrolysis of wood wool. Adapted with permission from [54],[55],[58] and [62], respectively. ....	12
Figure 1.11: Covalent functionalization pathways for CNOs. Reprinted with permission from [65]. ....	13
Figure 1.12: Cell viability measurements after treatment with CNO derivatives of A) skin fibroblast cells and comparison with MWCNTs, B) HUVECs and C) rat dermal fibroblasts. Adapted with permission from [126], [127] and [82], respectively. ....	17
Figure 1.13: Confocal images of A) C57BL/6 BMDCs, B) MCF-7 cells and C) HeLa cells incubated with different fluorescent CNO derivatives at 10 $\mu\text{g/mL}$ CNO concentration. Adapted with permission from [73], [75] and [76]. ....	18
Figure 1.14: Confocal images of HeLa cells incubated with A) CNO derivatives bearing FA and FITC ligands at 10 $\mu\text{g/mL}$ for 12 h at 37 $^\circ\text{C}$ and B) p-CNO/pyrene-BODIPY derivatives at 10 $\mu\text{g/mL}$ for 30 min at 37 $^\circ\text{C}$ . The inset shows the uptake of the same CNO derivative incubated at 4 $^\circ\text{C}$ . Adapted with permission from [129] and [83], respectively. ....	19

Figure 1.15: Confocal images of HeLa cells incubated with A) Me-CNOs and B) fluo-CNOs. Adapted with permission from [74] and [92], respectively. ....	21
Figure 1.16: Fluorescence images of A) CNO-fed <i>Drosophila melanogaster</i> , under 488 and 561 nm filters and B) CNO- <i>E. Coli</i> -fed <i>C. Elegans</i> under 385, 488 nm and 561 nm band-pass filters. Adapted with permission from [61]. ....	22
Figure 1.17: A) In vivo uptake and biodistribution in <i>Hydra</i> of CNOs decorated with 1) benzoic acid, 2) pyridine and 3) methylpyridinium. B) In vivo imaging of the superior part of a zebrafish larvae treated with BODIPY-CNOs; E:eye, YS: yolk sac. Adapted with permission from [132] and [133], respectively. ....	23
Figure 1.18: A) Operative schematization of a fuel cell and ORR process in alkaline and acidic media. Adapted with permission from [140] and [141], respectively. ....	24
Figure 1.19: Evaluation of electrocatalytic activities towards ORR. A) LSV curves of electrocatalysts in oxygen-saturated electrolyte with different rotating rates and B) Oxygen reduction curves on the disc and ring electrodes of RRDE at 5 mV s <sup>-1</sup> scan rate at 1600 rpm, respectively. Adapted with permission from [141]. ....	25
Figure 1.20: A) Common heteroatoms used for the doping of graphitic structure with heteroatoms and B) schematic representation of their effects on the structure. Adapted with permission from [140]. ....	27
Figure 1.21: A) RRDE voltammograms for oxygen reduction in air-saturated 0.1 M KOH at the Pt-C/GC (curve 1), VA-CCNT/GC (curve 2), and VA-NCNT (curve 3) electrodes. B) Calculated charge density distribution for the VA-NCNTs. Adapted with permission from [150]. ....	27
Figure 1.22: A) RDE curves of the N-SWCNTs in oxygen-saturated 0.5 M H <sub>2</sub> SO <sub>4</sub> at different speeds at a scan rate of 10 mV/s (the inset showing the Koutecky–Levich plots derived from RDE measurements). B) RRDE voltammograms for the ORR in air-saturated 0.1 M KOH at the C-graphene electrode (red line), Pt/C electrode (green line), and N-graphene electrode (blue line) at 1000 rpm and scan rate of 0.01 V/s. Adapted with permission from [152] and [153], respectively. ....	28
Figure 1.23: A) Schematic representation of N bonding configurations, including typical XPS binding energies. B) Schematic pathway for ORR on N-doped CNMS. Adapted with permission from [145] and [155], respectively. ....	29
Figure 1.24: ORR Electrocatalytic activities of B-CNTs in O <sub>2</sub> -saturated 1m NaOH electrolyte. A) CV curves at scan rate of 50 mVs <sup>-1</sup> . B) RDE voltammetry at 2500 rpm and scan rate of 10 mVs <sup>-1</sup> . For comparison, corresponding examinations for CNTs and commercial Pt/C catalysts (20 and 40 wt% Pt loading) are shown. B <sub>1</sub> CNT, B <sub>2</sub> CNT and B <sub>3</sub> CNT exhibit different B content (0.86, 1.33 and 2.24 at%, respectively). Adapted with permission from [156]. ....	30

Figure 1.25: A) LSV curves of the ND, oxi- and N-CNOs (at different oxidation time) and Pt/C. B) LSV curves of p-, oxi- and, N-CNOs in comparison with 20% Pt/C at 1600 rpm. C) RDE polarization curves derived from three different heat treated samples and commercial Pt/C catalyst. Adapted with permission from [177], [178] and [179].	33
Figure 1.26: ORR investigation of B-CNOs produced by annealing at 1500 °C with 10 wt% of boric acid (B-OLC-1-10). A) LSV curves at rotation rate from 400 to 2500 rpm and at scan rate of 5 mV/s <sup>-1</sup> . B) Durability evaluation for 10 000 s at 0.6 V and a rotation rate of 900 rpm compared to Pt/C. C) Chronoamperometric responses with 3 M methanol added into an O <sub>2</sub> -saturated KOH electrolyte at a constant potential of 0.6 V with a rotation rate of 900 rpm and compared to Pt/C. Adapted with permission from [182].	34
Figure 1.27: A) ORR activities of p-, Ph <sub>30</sub> - and TPP-CNOs in a 0.1 M KOH electrolyte at 2500 rpm and 10 mV/s <sup>-1</sup> as scan rate. B) ORR activity of all Ph <sub>x</sub> -CNOs. Adapted with permission from [185].	35
Figure 2.1: A) Tube furnace used for the annealing process and B) synthetic procedure of the production of p-CNOs by thermal annealing.	49
Figure 2.2: HRTEM images of DNDs with inset in A) and B) showing diamond (111) plane and SAED pattern, respectively.	50
Figure 2.3: HRTEM images of p-CNOs with inset in A) and B) showing graphitic (002) plane and SAED pattern, respectively.	51
Figure 2.4: Particle size distribution of p-CNOs, showing an average size of $5.94 \pm 1.2 \text{ nm}$	51
Figure 2.5: Low-loss region of EELS spectra of A) DNDs and B) p-CNOs.	52
Figure 2.6: EELS Carbon K-edge spectra of A) DNDs and B) p-CNOs.	53
Figure 2.7: XRD patterns of A) DNDs and B) p-CNOs, showing characteristic peaks of the diamond and graphite phases.	54
Figure 2.8: XPS survey spectra of A) DNDs and B) p-CNOs. The peaks denoted by * are due to the gold substrate used for the analyses.	55
Figure 2.9: High-resolution XPS spectra of the C1s region of A) DNDs and B) p-CNOs, including peak-fitting analyses. Experimental and fitting curves are reported in black and red, respectively.	56
Figure 2.10: Raman spectra of DNDs at A) $\lambda_{exc} = 633 \text{ nm}$ and B) $\lambda_{exc} = 325 \text{ nm}$ , including Lorentzian peak fitting.	57
Figure 2.11: Calculated phonon dispersion relations of two dimensional graphite. Adapted with permission from [46].	58
Figure 2.12: Raman spectrum of p-CNOs at $\lambda_{exc} = 633 \text{ nm}$ , showing a prominent D-band.	59
Figure 2.13: FTIR spectra of A) DNDs and B) p-CNOs.	60

Figure 2.14: Thermogravimetric analysis (solid lines) and the corresponding weight loss derivatives (dotted lines) of DNDs (black) and p-CNOs (blue), showing the higher thermal stability of p-CNOs.....	61
Figure 2.15: BET isotherm of A) DNDs and B) p-CNOs.....	62
Figure 2.16: Pore size distribution of A) DNDs and B) p-CNOs calculated by DFT method. ....	62
Figure 3.1: Schematization of the oxidation procedure to yield oxi-CNOs.....	69
Figure 3.2: Schematization of the coupling procedure to yield fluo-CNOs. ....	70
Figure 3.3: Representative HRTEM images of A) oxi-CNOs and B) fluo-CNOs. ....	71
Figure 3.4: XPS survey spectra of p- (black), oxi- (blue) and fluo-CNOs (red). The peaks denoted by * are due to the gold substrate used for the analyses. ....	72
Figure 3.5: High-resolution XPS spectra of the C1s region of A) oxi- and B) fluo-CNOs, including peak-fitting analysis. Experimental and fitting curves are reported in black and red lines, respectively. ....	73
Figure 3.6: High-resolution XPS spectra of the O1s region of A) p-, B) oxi- and C) fluo-CNOs, including peak-fitting analysis. Experimental and fitting curves are reported in black and red lines, respectively. ....	74
Figure 3.7: Raman spectra of p- (black), oxi- (blue) and fluo-CNOs (red) at $\lambda_{exc} = 633\text{ nm}$ . All the spectra were normalized with respect to the G-band. The intensity ratio between the D- and the G-band is reported.....	75
Figure 3.8: Thermogravimetric analysis (solid lines) and the corresponding weight loss derivatives (dotted lines) of p- (black), oxi- (blue) and fluo-CNOs (red). All experiments were performed in air. ....	76
Figure 3.9: Effective hydrodynamic diameter of A) oxi-CNOs (blue line) and B) fluo-CNOs (red) in water at three different concentrations (5, 10 and 20 $\mu\text{g/mL}$ ). ....	77
Figure 3.10: Effective hydrodynamic diameter of oxi-CNOs (blue line) and fluo-CNOs (red line) at a concentration of 5 $\mu\text{g/mL}$ in 0.01M PBS. ....	77
Figure 3.11: Absorption spectra of BODIPY (black line, 0.022 $\mu\text{M}$ ) and fluo-CNOs (red line, 20 $\mu\text{g/mL}$ ). ....	78
Figure 3.12: A) Emission spectra of fluo-CNOs at 5 $\mu\text{g/mL}$ (red dotted line), 10 $\mu\text{g/mL}$ (red dashed line) and 20 $\mu\text{g/mL}$ (red solid line) in DMSO. The emission spectrum of BODIPY dye (black line) is reported as inset in A. Excitation at 550 nm; emission at 634 nm. B) Emission spectra of fluo-CNOs at 5 $\mu\text{g/mL}$ (red dotted line), 10 $\mu\text{g/mL}$ (red dashed line) and 20 $\mu\text{g/mL}$ (red solid line) in DMEM. Excitation at 561nm; Emission at 632 nm.....	79

Figure 3.13: Cellular viability of MCF-7 and HeLa cells treated with different concentrations (0,5 1, 5, 10 and 20 $\mu\text{g/mL}$ ) of A) oxi- and B) fluo-CNOs for 12, 24, 28 and 72 h.....	80
Figure 3.14: Confocal images of MCF-7 cells incubated for 24 hours with fluo-CNOs at A) 5 and B) 20 $\mu\text{g/mL}$ . The nuclei were stained with Hoechst 33 342 (blue). Scale bars: 10 $\mu\text{m}$ . ....	81
Figure 3.15: Confocal images of MCF7 cells incubated for 24 hours with 20 $\mu\text{g/mL}$ of fluo CNOs. A) red signal from fluo-CNOs; B) green signal from Lysotracker- marked lysosomes and C) Merged images. The nuclei were stained with Hoechst 33 342 (blue). Scale bars: 10 $\mu\text{m}$ . ....	81
Figure 4.1: Schematic representation of the synthesis of p- and BN-CNOs.....	87
Figure 4.2: Representative HRTEM images of BN-CNOs, showing A) mainly polyhedral shape and B) a small fraction of spherical CNOs. The characteristic morphology is highlighted with black dotted lines. ....	88
Figure 4.3: Zero-loss bright-field TEM image (A) and corresponding EFTEM elemental mapping of BN-CNOs showing C, B, and N maps in red, green, and cyan, respectively (B-D). ....	88
Figure 4.4: EELS spectrum of BN-CNOs showing distinct B, C, and N K-edges. ....	89
Figure 4.5: XPS survey spectra of p-(black) and BN-CNOs (blue), showing the additional presence of B and N in the doped catalyst.. ....	90
Figure 4.6: High-resolution XPS C1s spectra of A) p- and B) BN-CNOs, including peak deconvolution. Experimental and fitting curves are reported in black and red lines, respectively. ..	91
Figure 4.7: High-resolution XPS A) N1s and B) B1s spectra of BN-CNOs, including peak deconvolution. Experimental and fitting curves are reported in black and red lines, respectively. ..	92
Figure 4.8: XRD patterns of p- (black line) and BN-CNOs (blue line). ....	93
Figure 4.9: Raman spectra of p- (black line) and BN-CNOs (blue line). Fitting curves are reported in red lines. ....	94
Figure 4.10: TGA (solid lines) and the corresponding weight loss derivatives (dotted lines) of p- (black line) and BN-CNOs (blue line). ....	95
Figure 4.11: FTIR spectra of p-(black line) and BN-CNOs (blue line). ....	96
Figure 4.12: Adsorption/desorption isotherms and BJH pore size distributions (inset) of p- (upper panel) and BN-CNOs (bottom panel). ....	97
Figure 4.13: Schematic representation of functional groups incorporated on the CNO surface. N1–N5 correspond to different N types (i.e., pyridinic, pyrrolic, graphitic, and oxide, respectively) and B-bonded N atoms; B1–B3 correspond to B-bonded C and N atoms and B oxide, respectively; C1–C3 correspond to hydroxyl, carbonyl, and carboxylic functional groups, respectively. ....	98
Figure 4.14: CV curves of p- and BN-CNOs in O <sub>2</sub> - and N <sub>2</sub> -saturated aqueous solutions (0.1 M KOH) at 10 mV/s as scan rate. ....	99

Figure 4.15: RDE polarization curves of A) p- and B) BN-CNOs at different rotation speeds. C) Onset and half-wave potentials of p-CNOs, BN-CNOs, and reference Pt/C catalysts at 1600 rpm. D) Koutecky–Levich plots of p-CNOs, BN-CNOs, and reference Pt/C catalysts at +0.38 V (n represents the electron-transfer numbers). .....	100
Figure 4.16: A) Ring and B) disk current densities obtained from RRDE analyses of CNO samples and reference Pt/C catalysts at 2500 rpm and a potential of the ring electrode of 1.18 V. C) Comparison of the electron-transfer number (left axis) and the peroxide percentage (right axis) estimated from RRDE analyses at 2500 rpm and different potentials for all of the catalysts. ....	101
Figure 4.17: Nyquist plots of p- (black line) and BN-CNOs (blue line) measured at +0.68 V and 2500 rpm. Points correspond to the experimental data and continuous lines to the calculated curves. ....	102
Figure 4.18: Chronoamperometric curves of BN-CNOs and Pt/C catalysts measured at +0.68 V and 2500 rpm in a 0.1 M KOH solution. Both curves have been normalized to the initial current values. The inset shows the CA curves of BN-CNOs acquired with and without the addition of 3 M CH <sub>3</sub> OH (the arrow indicates the moment of methanol addition). ....	103

## List of tables

Table 2.1: Fit parameters from the HRTEM particles size distribution.....	51
Table 2.2: Elemental composition of DNDs and p-CNOs from XPS analyses. ....	55
Table 2.3: Chemical state, position, area (%) and FWHM of the different peaks from the fitting of the C 1s peak of DNDs. ....	56
Table 2.4: Chemical state, position, area (%) and FWHM of the different peaks from the fitting of the C 1s peak of p-CNOs. ....	56
Table 2.5: decomposition temperature for DNDs and p-CNOs.....	61
Table 2.6: Specific surface areas (SSAs) of DNDs and p-CNOs. ....	62
Table 3.1: Elemental composition of p-, oxi- and fluo-CNOs from XPS analyses. ....	71
Table 3.2: Chemical state, position, area (%) and FWHM of the different peaks from the fitting of the C1s peak of p-, oxi- and fluo-CNOs. ....	73
Table 3.3: Chemical state, position and area (%) of the different peaks from the fitting of the O1s peak of p-, oxi- and fluo-CNOs. ....	74
Table 3.4: Decomposition temperature of p-CNOs, oxi-CNOs and fluo-CNOs .....	76
Table 3.5: Effective hydrodynamic diameter of oxi- and fluo-CNOs in water obtained from DLS analyses at different concentrations. ....	77

Table 3.6: Effective hydrodynamic diameter from DLS analyses and zeta potential of oxi- and fluo-CNOs at 5 $\mu\text{g/mL}$ .....	78
Table 3.7: Photophysical data for BODIPY dye and fluo-CNOs. $\lambda_{abs}$ is the absorption maximum, $\lambda_{em}$ the emission maximum and $\phi F$ the fluorescence quantum yield. Excitation at 550 nm. ....	79
Table 4.1: Elemental composition of p- and BN-CNOs from XPS analyses. ....	90
Table 4.2: Chemical state, positions, relative area percentages and FWHM of the deconvoluted C1s peaks of p- and BN-CNOs obtained from XPS analyses.....	91
Table 4.3: Chemical state, positions, relative area percentages and FWHM of the deconvoluted N1s and B1s peaks of BN-CNOs obtained from XPS analysis.....	92
Table 4.4: D- and G-band positions and $I_D/I_G$ values of p- and BN-CNOs from Raman analyses. ..	94
Table 4.5: Decomposition temperatures and residues of p- and BN-CNOs from TGA analyses.....	95
Table 4.6: BET surface areas, BJH pore volumes and pore sizes of p- and BN-CNOs from BET analyses. ....	97
Table 4.7: Onset and half-wave of p- and BN-CNOs from RDE analyses.....	101
Table 4.8: Charge-transport and charge-transfer resistances of p- and BN-CNOs from EIS analyses. ....	102

# ***Chapter 1 - Introduction***

## **1.1 Carbon nanomaterials**

Carbon is one of the most abundant elements on earth and plays a key role in nature, as it is the principal constituent of all organic materials. Due to the small energy gap between the 2s and 2p electron shells in its ground-state orbital configuration (i.e.  $1s^2 2s^2 2p^2$ ), one of the electrons from a 2s orbital can be excited to a 2p orbital. This allows carbon to show different hybridization states, namely  $sp$ ,  $sp^2$  and  $sp^3$  and, therefore, to exist in several allotrope forms, each showing unique structure and physico-chemical properties. Diamond and graphite, the traditional bulk carbon forms present in nature, show different arrangement and bonding of C atoms in their structure. Diamond is composed of a three-dimensional cubic lattice of strongly covalently bonded  $sp^3$  C atoms, which gives rise to its remarkable physical properties (i.e. high hardness and thermal conductivity). Graphite, by contrast, consists of a three-dimensional layered structure with each sheet composed of  $sp^2$  bonded C atoms arranged in a hexagonal honeycomb lattice; these layers, held together by weak van der Waals forces, are able to slide over each other, making graphite a good lubricant.

In 1985, another allotropic form of carbon,  $C_{60}$  fullerene [1], was discovered and marked the beginning of a new era in the carbon research. In the last thirty years, the carbon family has expanded after the discovery of several new carbon nanomaterials (CNMs) [2], attracting great interest from both scientific and industrial point of view. The unique and outstanding properties exhibited by these nanomaterials enabled their investigation for a wide range of applications. The main members of the nanocarbon family are schematically reported in Figure 1.1.

Fullerenes are a family of enclosed cage-like carbon structures composed of twelve pentagon and a variable number of hexagon, following the Euler's theorem for polyhedral. In particular,  $C_{60}$ , the most famous and investigated component of the family, consists of 20 hexagonal and 12 pentagonal faces to form a spherical closed structure of 0.7 nm in size similar to a soccer ball, with carbon atoms (i.e. 60) located at the vertices of a regular truncated icosahedron. Furthermore, larger molecular weight



fullerenes have been also reported [3]. The  $C_{60}$  molecule, historically known as Buckminsterfullerene in honor of the geodesic domes built by the architect R. Buckminster Fuller, was firstly synthesized via laser ablation of graphite targets in helium (He) gas and detected by mass spectroscopy by Kroto, Smalley and Curl [1]. The great impact that this discovery had on the scientific community was confirmed in 1996, when they were awarded with the Nobel Prize for chemistry.

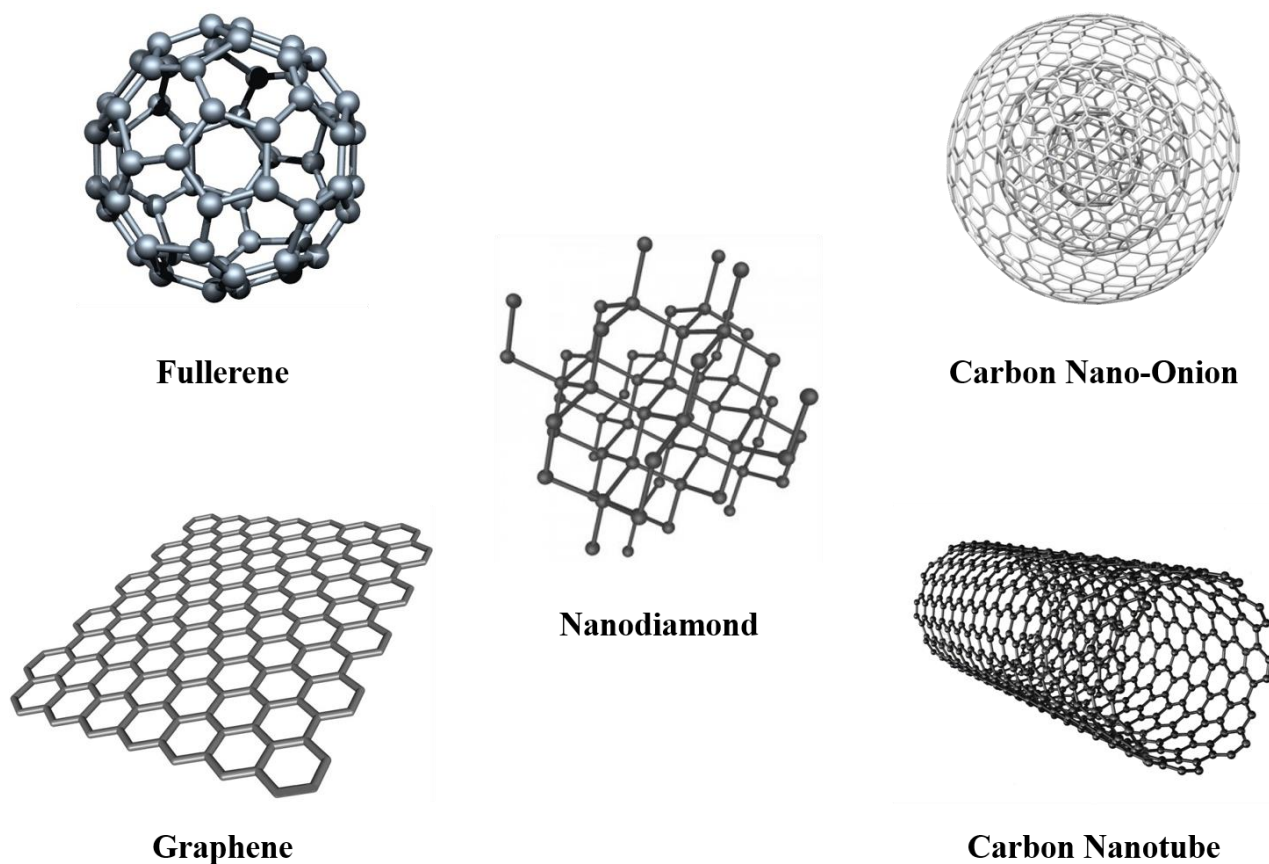


Figure 1.1: Schematic representation of the main members of carbon nanomaterials.

In addition, the development by Kratschmer *et al.* [4] of a gram-scale synthesis method, consisting of an alternating current (AC) arc discharge between high purity graphite rods in He gas, paved the way for the intensive investigation of fullerene and, progressively, of CNMs.

In 1991, Iijima observed by electron microscopy the formation of cylindrical structures, consisting of coaxial tubes of graphitic sheets, on the cathode of the standard arc discharge apparatus used for the synthesis of fullerenes [5]. This material, consisting of a diameter ranging from 5 to 40 nm and a length of several  $\mu\text{m}$ , is nowadays known as multi-walled carbon nanotubes (MWCNTs). Two years later, Iijima [6] and Bethune [7] independently observed the formation of tubes composed of a single graphitic sheet, namely single-walled carbon nanotubes (SWCNTs), by doping one of the electrodes with elements such as cobalt. This kind of CNMs display a diameter of 1–3 nm and a variable length up to tens of micrometers. Depending on the structure, CNTs display very interesting properties, such

as high aspect ratio and high thermal and electrical conductivity. Interestingly, the electronic properties of SWCNTs are strongly affected by the way that the graphitic sheet rolls up to form the tube; depending on this orientation with respect to the tube axis (namely, the chirality), they show metallic, semi-metallic or semiconducting behavior [8].

Only one year after the observation of MWCNTs, in 1992, Ugarte described the formation of multi-shell fullerenes, also known as carbon nano-onions (CNOs), by irradiating amorphous carbon with the high energy beam of an high resolution electron microscope [9].

Graphene has been for the first time isolated by mechanical exfoliation in 2004 by Geim and Novoselov [10], who were awarded the 2010 Nobel Prize in Physics for the discovery of this fascinating material. Its structure, consisting of single layers of  $sp^2$ -hybridized carbon atoms in a two-dimensional hexagonal lattice, can be considered the building block of all graphitic materials. Due to the excellent mechanical, electrical and thermal properties, which approach very closely the theoretical ones, graphene is nowadays the most attractive CNM [11].

Nanodiamonds, the nanoscale counterpart of bulk diamond, were firstly synthesized by detonation process in the 1960s [12]. They exhibit mainly rounded shape with an average size of 4-5 nm and the  $sp^3$  diamond core is typically stabilized by different functional groups or reconstructed into  $sp^2$  carbon shells. Nowadays, due to the remarkable physico-chemical properties and controllable surface chemistry, have a wide range of potential applications [13].

Carbon-based nanostructures have been extensively investigated in the last decades as promising materials for a large number of applications, becoming a hot topic in the scientific community. In the next section, the structure, the synthesis and the applications of a fascinating member of the carbon family, namely carbon nano-onions, will be discussed in details.

## 1.2 Carbon nano-onions

Despite carbon nano-onions were discovered at the same time as carbon nanotubes, they remained in the shadow of its carbon counterpart for many years before arousing interest in the scientific community.

CNOs, also reported as onion-like carbon (OLCs), are quasi-spherical carbon nanoparticles composed of concentric graphitic shells to form a peculiar cage-in-cage structure that resembles the one of an onion [14, 15] (Figure 1.2). The multi-layered morphology typically consists of a  $C_{60}$  fullerene molecule as innermost shell, but hollow and metallic cores have been also reported [16, 17]). The outer graphitic layers are approximately 3.4 Å apart and the size ranges from few to tens of nanometers [18]. Ideally, they exhibit a spherical structure with the number of carbon atoms following the formula  $60 \cdot n^2$ , where  $n$  is the number of graphitic layers; however, the high defectiveness in the

structure gives rise to quasi-spherical or polyhedral arrangements [19, 20]. The morphological features of CNOs (i.e. shape, size and number of graphitic shells), and thus the physico-chemical properties, strictly depends upon the synthesis method, as reported by Echegoyen *et al.* [21].

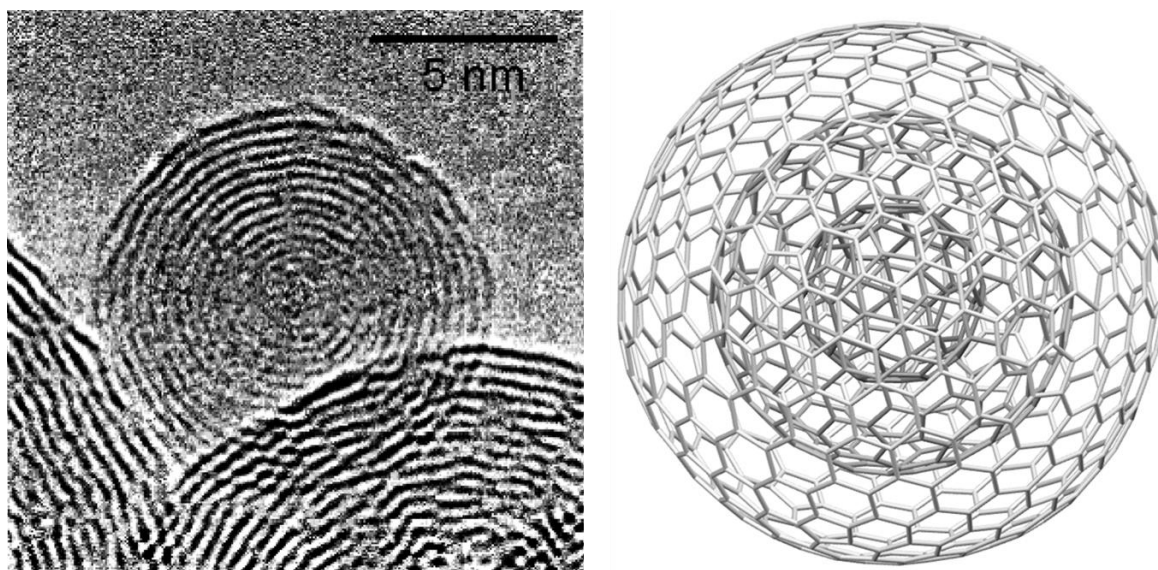


Figure 1.2: HRTEM image (left) and structure (right) of CNOs, showing the concentric graphitic morphology. Reprinted with permission from [15].

Historically, it is due to S. Iijima the first reported evidence of CNOs. In 1980 he observed, by high-resolution transmission electron microscope (HRTEM), the presence of small nearly spherical particles in amorphous carbon films prepared by vacuum deposition [22].

However, only a decade later, D. Ugarte reported the first *in-situ* formation of onion-like structures with average size around 45 nm and about 70 graphitic shells. The highly energetic irradiation process, driven by an intense electron beam, induced the graphitization and the following curling of amorphous carbon, leading to the formation of multi-layered particles [9]. However, this method was not suitable to produce large quantities. The need for a bulk synthesis of CNOs to fully understand the properties of these novel CNMs led to the development of several fabrication strategies. Nowadays, a large number of production methods are available with thermal annealing of detonation nanodiamonds (DNDs) playing a key role as it is the only method with potentialities for industrial scalability [15]. The detailed discussion of the different methods is reported in the following paragraph.

### 1.2.1 Synthetic approaches for production of carbon nano-onions

Conventionally reported as the first method to show a reproducible way to generate CNOs [9], electron beam irradiation of carbon soot have been object of further investigation in the following years. Xu *et al.* reported the formation of giant onion-like structures, consisting of 10 to 54 graphitic shells and diameter ranging from 4 to 38 nm, by irradiating amorphous carbon film in the presence

of Al nanoparticles (Figure 1.3A). The CNO formation is promoted by the metal catalyst acting as nucleation sites and the mechanism involves three distinctive and consecutive steps. In the first stage, the presence of Al nanoparticles catalyze the formation of a nucleus and the first graphitic shell. The second step involves the gradual growth of irregular layers surrounding an inner hollow core as the catalyst NPs are moved out by the electron irradiation. Finally, the hollow interior is eliminated, forming a quasi-spherical structure [23].

Arc discharge is a traditional production method for the synthesis of CNMs, as reported for fullerenes [24]. In 2001, Sano *et al.* employed this method as a viable way to produce CNOs with average size of 25-30 nm and consisting of 15-30 carbon shells (Figure 1.3B); the main technological advantage consists in the possibility to produce high amount of materials without the need of a vacuum equipment.

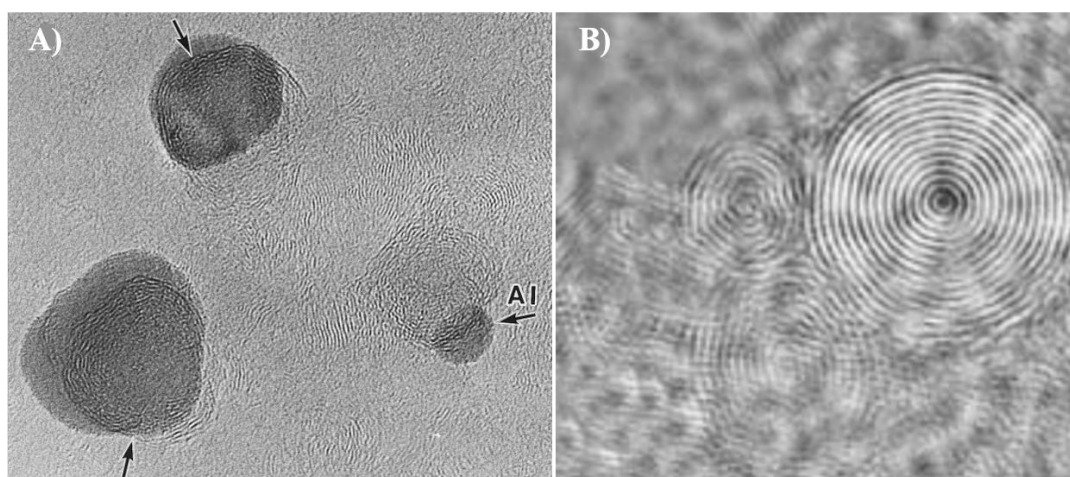


Figure 1.3: HRTEM images of CNOs produced by A) electron irradiation and B) arc discharge. Adapted with permission from [23] and [25], respectively.

CNOs were synthesized by applying a discharge voltage (16-17 V) in the presence of a constant current (30 A) between two graphite electrodes submerged in deionized water and collected as floating powder on the liquid surface due to its hydrophobic nature that causes the formation of large clusters induced by van der Waals interactions [25], as shown in Figure 1.4A.

The formation mechanism has been proposed by the same group and schematically showed in Figure 1.4B. The process involves the formation of a hot plasma zone, with temperatures reaching around 4000 K, between the two electrodes. This entails the generation of vaporized carbon from the surrounding liquid and its following rapid solidification to yield CNOs when in contact with the surrounding cold aqueous environment. However, this method leads to the inevitable formation of other carbon nanostructures, such as CNTs, as results of the different quenching zones in the plasma [26].

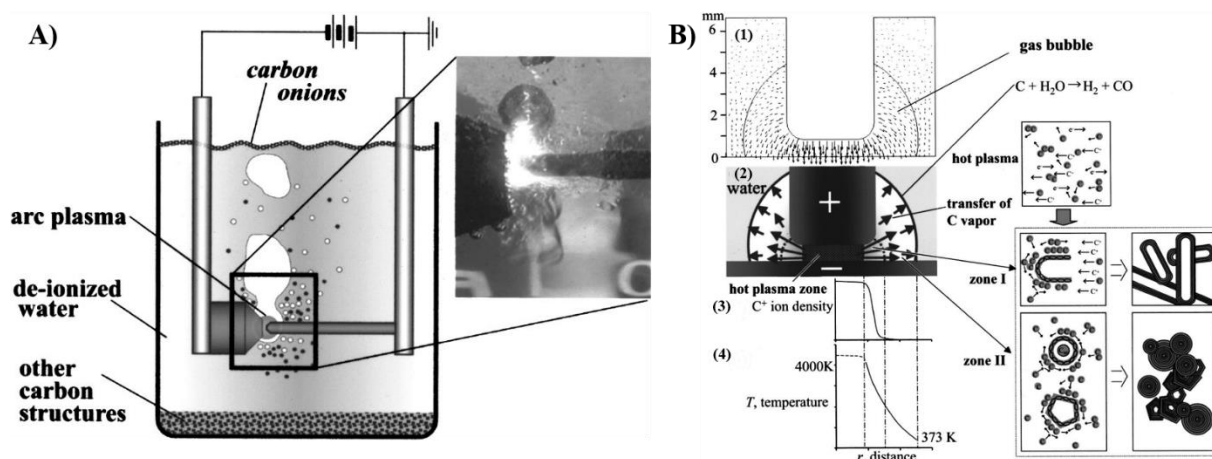


Figure 1.4: Schematic representation of A) arc discharge apparatus and B) CNO formation mechanism. Adapted with permission from [26].

To overcome this problem, Borgohain and co-workers have reported an optimization of the arc discharge method proposed by Sano; by controlling the synthetic conditions through different processing parameters, homogeneous CNOs (20-25 nm in size) with minimal carbon-based impurities were produced. In addition, they proposed an efficient purification pathway, exploiting the preferential adsorption of phosphotungstic acid onto CNOs compared to the other impurities [27]. Thermal annealing of detonation nano-diamonds (DNDs) is nowadays the only method that showed potentialities for the industrial scalability, as it ensures low cost and high yield (close to 100%) along with the high purity and narrow size distribution of the products. Typically, DNDs with size around 5 nm (Figure 1.5A) are employed as precursor material to yield small CNOs with an average diameter of 5-8 nm and composed of 5-10 graphitic layers (Figure 1.5B) [28].

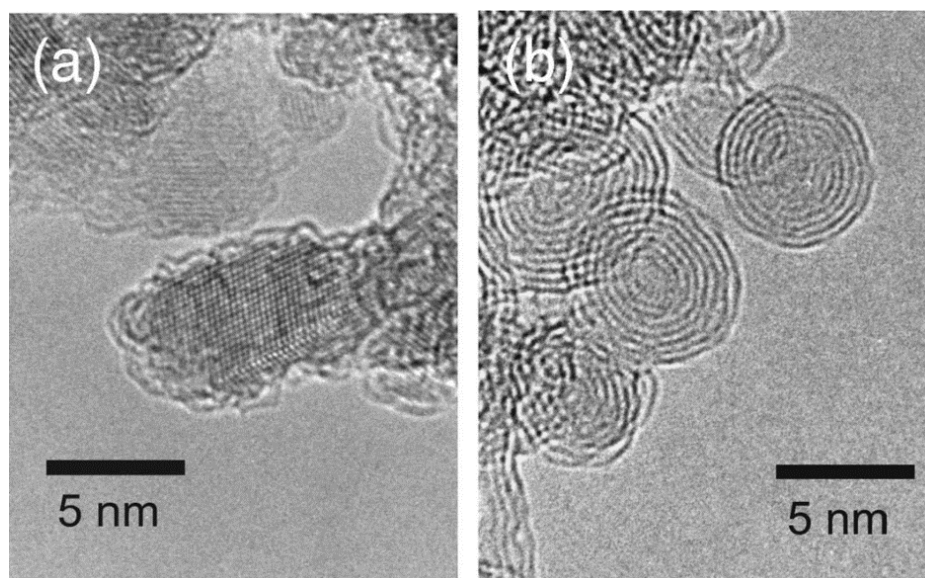


Figure 1.5: HRTEM images of DNDs (a) and spherical CNOs produced by thermal annealing. Adapted with permission from [28].



The synthesis of CNOs by vacuum annealing was proposed for the first time by Kuznetsov and co-workers in 1994 [29]; five years later, based on semi-empirical calculations, they demonstrated that the transformation of DNDs into spherical onions occurs through the preferential exfoliation of (111) planes. Therefore, they proposed a zipper-like scheme as formation mechanism for which three (111) diamond planes reconstruct into two (002) graphite planes as the interface migrates towards the diamond core [30].

The graphitization of the (111) facets begins at the diamond surface with the formation of graphitic fragments and proceeding towards the inside, as shown in Figure 1.6A where the formation of the first carbon layers is observed. During the intermediate stages, due to energetic reasons, the graphitic sheets tend gradually to connect and curve, surrounding the diamond core (Figure 1.6B). Finally, the graphitization process ends with the formation of closed graphitic shells around a hollow core (Figure 1.6C) and CNOs exhibit a size that is similar to the starting diamond particles [31].

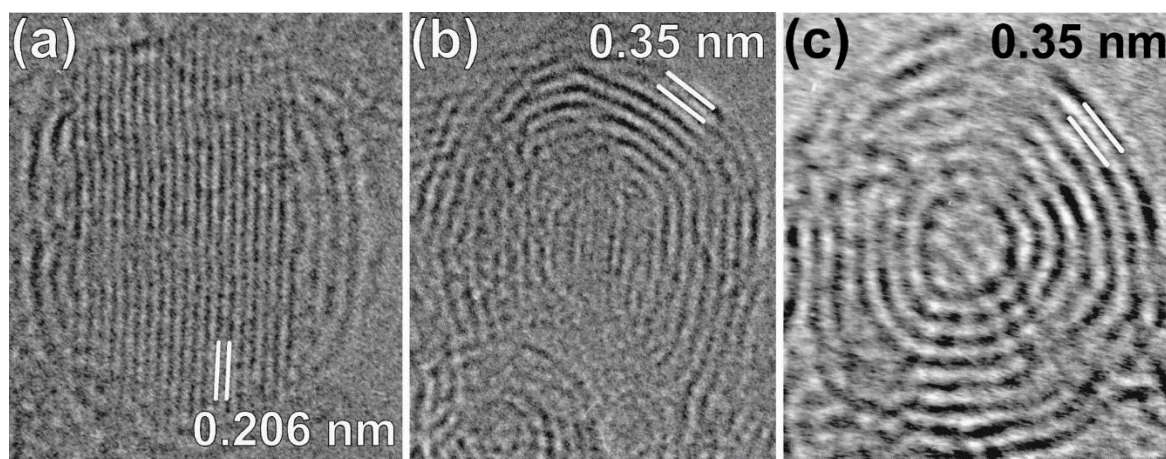


Figure 1.6: HRTEM images of the evolution of the transformation of DNDs to CNOs. (a) Initial stage, (b) intermediate stage and (c) final stage. Reprinted with permission from [30].

From the thermodynamics point of view, as graphite is the most stable carbon form, the formation of flat graphitic sheets should be preferentially promoted over a curved structure. However, at the nanoscale the surface energy of the particles is extremely high. For this reason, the graphitic sheets are forced to curl in order to reduce this contribution by elimination of the dangling bonds at the carbon atoms boundary [32].

Kinetically, as enough energy has to be provided to break the C-C bonds in the diamond structure (namely, 348 kJ/mol), the graphitization process should take place at least at 1100-1200 °C. Actually, the defectiveness of the structure along with the higher energy content of the surface than the interior allows to reduce the energy barrier required for the graphitization to start, resulting in the formation of the first graphitic fragments even at 900 °C [31].

The conversion of DNDs to CNOs is a multistage process, as shown in Figure 1.7. Below 900 °C, no graphitization occurs and NDs undergo to a thermo-desorption process of the non-carbon contaminants [17]. This step includes the desorption of water and oxygen-containing groups at around 200 °C, while the further increase of temperature allows for the detachment of acidic moieties such as carboxyl, lactone and anhydride groups to yield CO and CO<sub>2</sub> gases; at around 850 °C, the last non-carbon impurity, hydrogen, desorbs from the ND surface [17, 33, 34]. The formation of dangling bonds, as result of the detachment of the surface functional groups, indicates the beginning of the graphitization, with the creation of sp<sup>2</sup> carbon shells on the ND surface and proceeding towards the inner part. Between 1100 and 1300 °C, the external carbon shells acquire a higher degree of graphitization and the continuous sp<sup>3</sup>-sp<sup>2</sup> phase transformation with the increase of temperature lead to the formation of spherical onions at temperature higher than 1500 °C. Finally, at temperature above 1800 °C, a progressive polygonization of CNOs is observed [17, 31].

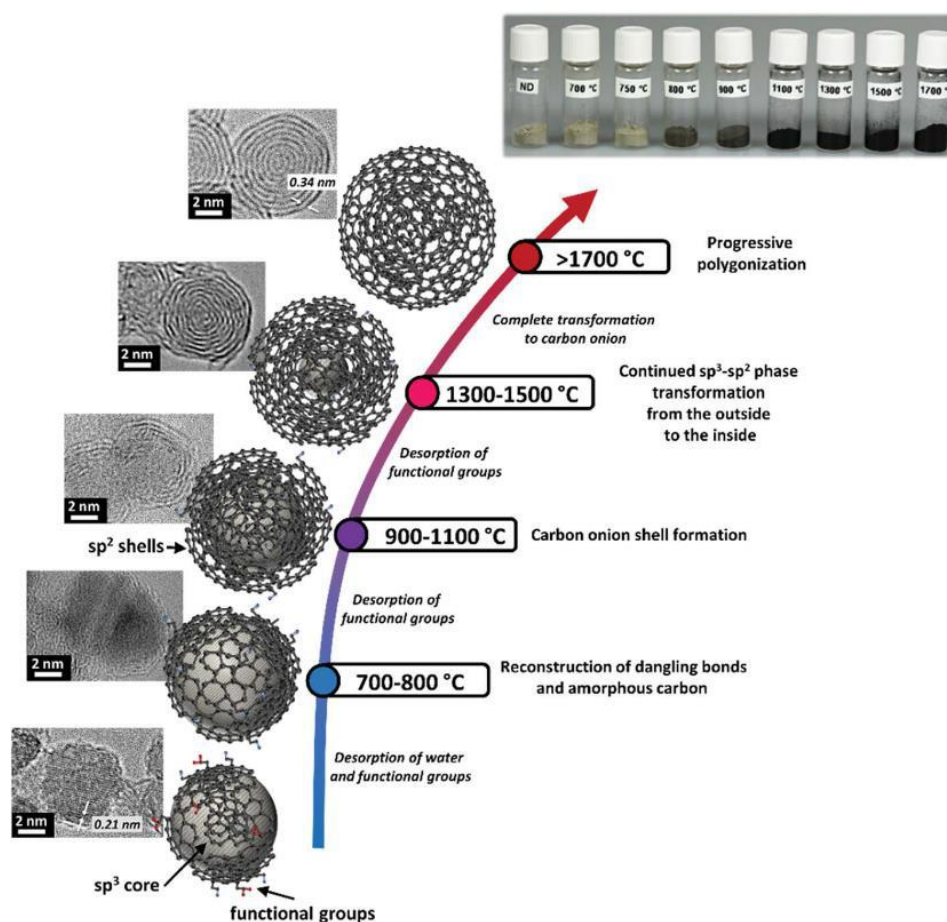


Figure 1.7: Schematic representation of the DND-CNO transformation during annealing, including TEM micrographs and optical images. Reprinted with permission from [17].

Similarly to vacuum annealing, performing the process in inert atmosphere have shown to be an efficient way to synthesize CNOs. So far, successful transformation have been reported in several inert gases, such as argon [35], nitrogen [36], hydrogen [37] as well as in helium [21, 38].

Several parameters have to be taken into account when thermal annealing is chosen as production method. First, the annealing atmosphere is an important parameter in the CNO synthesis. In vacuum, spherical CNOs can be produced at around 1700 °C, where NDs are completely transformed, and increasing the temperature leads to a polygonal-shaped nanoparticles [28, 39]. In the presence of an inert atmosphere, lower temperatures are required to form spherical-shaped CNOs with higher ordering occurring at increased annealing holding time [40]. In addition, the annealing atmosphere has a direct impact on the CNO purity. While in vacuum CNOs are the main product, annealing NDs in an inert gas may lead to the formation of graphene nanoribbons as by-product. The generation of carbon-containing gases as a result of the desorption of functional groups from the ND surface induces a partial pressure inside the furnace, resulting in a local etching process that form unwanted graphitic structures [41]. Finally, ND size and annealing time are two other important factors. In the first case, the graphitization process may take place at lower temperatures for smaller NDs particles as they exhibit a higher contribute of surface energy. In addition, an enhanced degree of graphitization may occur at lower temperatures with the prolongation of the heating holding time [42].

Chemical vapor deposition (CVD) is another effective way to produce CNOs due to the direct control on the synthetic parameters. Typically, hydrocarbons such as methane are employed as carbon sources in the presence of a catalyst to yield CNOs bearing hollow or metallic core [43, 44]. CNOs consisting of a Fe<sub>3</sub>C core (15-50 nm in size) were synthesized by Yang and co-workers through the decomposition of C<sub>2</sub>H<sub>2</sub> at 420 °C catalyzed by a NaCl-supported iron catalyst [45].

He *et al.* achieved the synthesis of CNOs by low temperature CVD via catalytic decomposition of CH<sub>4</sub> in the presence of Al-supported Ni catalysts [46]. The formation is promoted by the presence of the Ni-based catalyst, which act as nucleation site. The mechanism involves, during the gas phase, the adsorption of carbon vapor onto the surface of the metal and the following formation and bending of several graphitic layers to yield CNOs with size ranging from 5 to 50 nm (Figure 1.8A) [46]. Therefore, the shape (quasi-spherical or polyhedral) and the core structure (hollow or metallic) strictly depend on the nickel particles morphology and size [47].

Chen *et al.* reported the formation of spherical CNOs (from few to several tens of nm in size) via radio-frequency plasma CVD by using a mixture of CH<sub>4</sub>-H<sub>2</sub> in the presence of a Co catalyst [48]. This method ensured high yield and, more importantly, high purity because the graphitic shells do not encapsulate the catalyst. The growth mechanism involves the formation of carbon rings, due to the decomposition of CH<sub>4</sub>, on the surface of the catalysts and their stabilization in the presence of atomic hydrogen. The resulting formation of a fullerene dome and its following growth leads to the emergence of the first cage, which acts as substrate for the further formation of spherical cages to form an encapsulated structure [48].



Radio-frequency plasma was employed by Du *et al.* by using coal and a mixture with graphite as precursors to synthesize hollow CNOs with quasi-spherical and polyhedral morphology. The presence of graphite, acting as additional aromatic fragment source, ensures higher degree of graphitization and more regular morphology with an average diameter ranging from 10 to 35 nm (Figure 1.8B) [49].

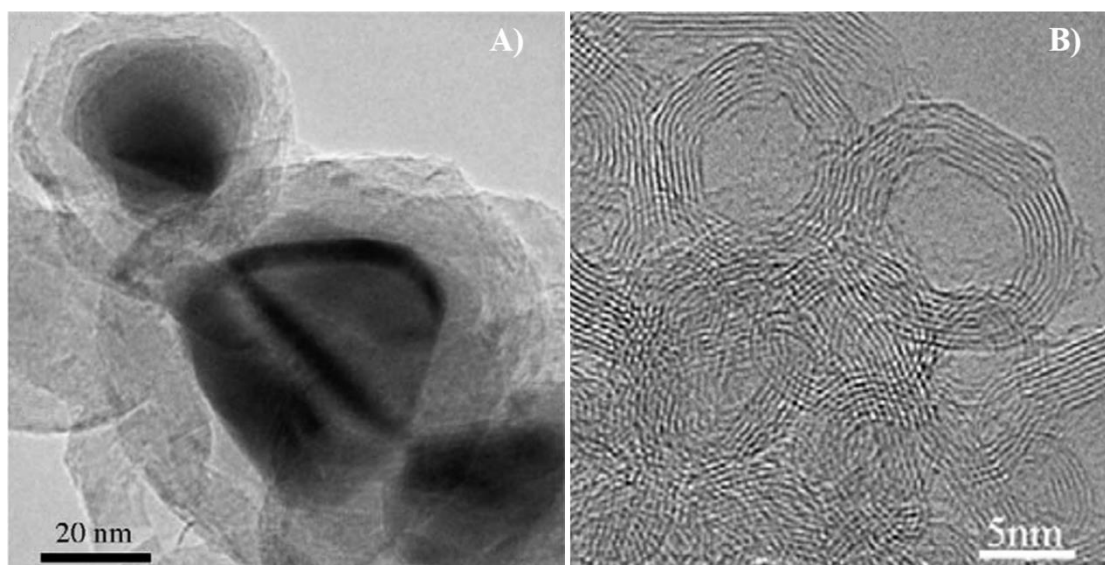


Figure 1.8: HRTEM images of CNOs synthesized by A) CVD and B) radio frequency plasma. Adapted with permission from [47] and [49], respectively.

High-energy ball milling of graphite is another efficient method to fabricate CNOs, reported by Huang *et al.* in 1999 [50]. The formation mechanism involves two subsequent steps. In the first, the heavy mechanical deformation introduces strain and lattice defects in the structure, leading to the bending and curvature of the graphitic sheets. Then, when the energy provided by the ball milling is high enough to induce the graphitization of the curved defective fragments, the formation of closed structures occurs (Figure 1.9A). The main drawback is the low purity of the method, as different carbon structures, such as nanoparticles consisting of an inner metal core, are typically produced [51]. Ion implantation was proposed for the first time in 1995 by Cabioc'h *et al.* as viable method to produce CNOs onto copper substrates (Figure 1.9B) [52]. Further investigations performed by the same groups confirmed the efficiency of this technique to produce CNOs with variable size (from 3 to 30 nm) and controllable microstructure by varying synthesis parameters such as ion flux and temperature. The formation of CNOs, occurring inside the substrate, is due to the immiscibility of carbon in the metal matrix; however, the main drawback was the low purity of the product due the presence of hetero-atoms in the CNO structure [53].

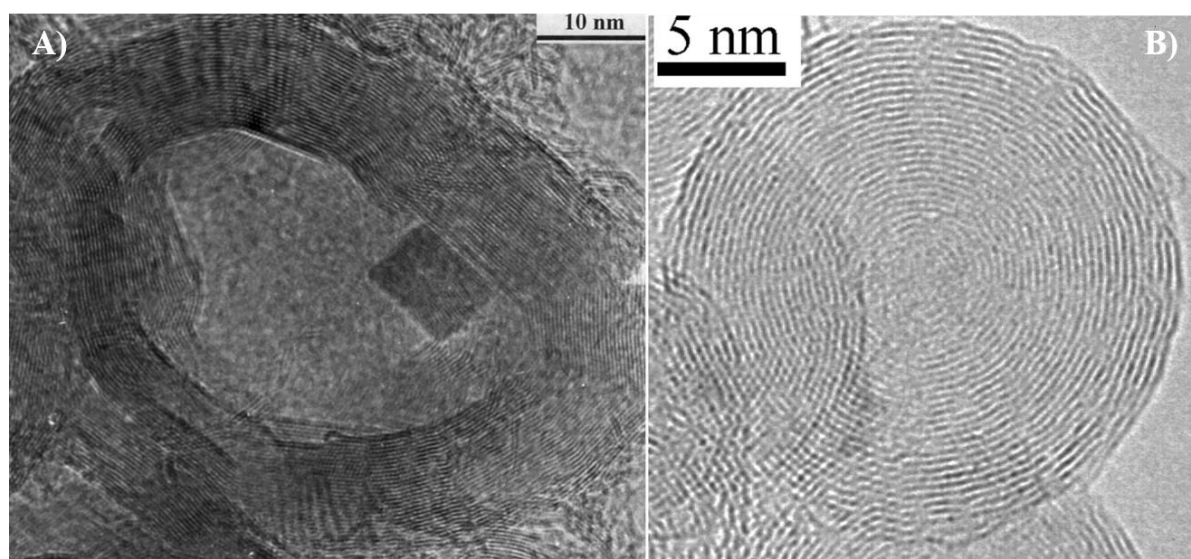


Figure 1.9: HRTEM images of CNOs produced by A) ball milling and B) ion implantation. Adapted from [51] and [53], respectively.

Several other synthetic pathways have been reported so far. Laser ablation of commercial pure graphite targets allowed for the production of highly pure spherical CNOs with size ranging from 10 to 25 nm and consisting of a hollow core surrounded by 10-20 carbon shells (Figure 1.10A) [54].

Carbon nano-onions with average size between 30 and 100 nm were synthesized by the catalyst-free thermolysis of a sodium azide ( $\text{NaN}_3$ ) and hexachlorobenzene ( $\text{C}_6\text{Cl}_6$ ) mixture (Figure 1.10B), while a purification step efficiently removed byproducts such as amorphous carbon nanoparticles and  $\text{NaCl}$ . The formation is due to the coalescence of phenyl radicals as a result of the rapid increase of pressure during the process [55].

Flash pyrolysis of naphthalene vapor onto a glass or ceramic substrate [56] and thermal reduction of a mixture of glycerin and magnesium at 650 °C in a stainless steel autoclave [57] were also reported. In the first case, large quantities of high purity CNOs (50 nm in size and composed of around 50 shells) are achieved, while, in the second case, larger CNOs (size ranging from 60 to 90 nm) are obtained.

Counterflow diffusion flame synthesis onto a catalytic Ni substrate was reported by Hou and co-workers in 2009 by using a mixture of  $\text{C}_2\text{H}_4/\text{CH}_4/\text{N}_2$  as fuel stream and  $\text{O}_2/\text{N}_2$  as oxidizer stream. In particular, they investigated the influence of ethylene, methane and oxygen concentrations on the selective formation of CNOs (Figure 1.10C). Furthermore, they showed the possibility to control the CNO size (from 5 to 60 nm) by varying the methane concentration (from 15 to 45%) [58].

Yan *et al.* exploited a low temperature solution-phase synthesis method by using commercial mesophase pitches (MPs) as a carbon precursor to obtain different graphitic structures, including CNOs with size between 30 and 80 nm, small carbon nanoparticles and carbon nanopores [59].

Nanoparticles consisting of several to 20 graphitic layers and 10-30 nm in average size were synthesized under strong shock compression of SiC [60], while smaller CNOs have been produced by pyrolysis of wood wool (Figure 1.10D) [61-63] and combustion of common carbonaceous sources such as camphor and polystyrene foam [64].

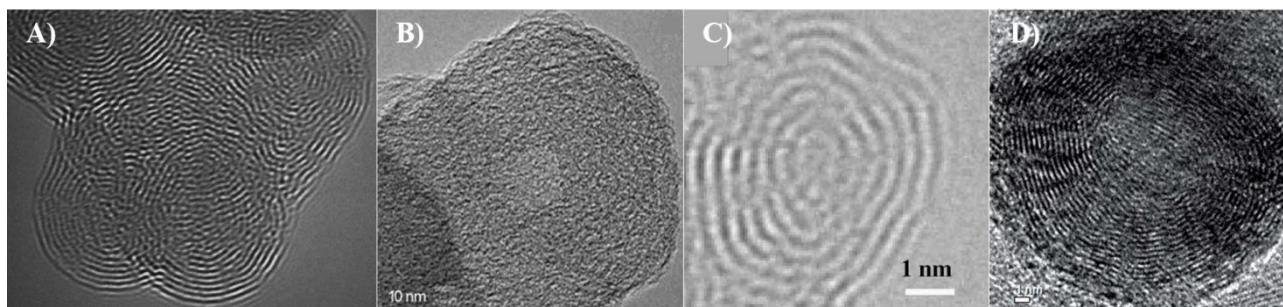


Figure 1.10: HRTEM images of CNOs produced by A) laser ablation, B) thermolysis of  $\text{NaN}_3\text{-C}_6\text{Cl}_6$  mixture, C) counterflow diffusion flames and D) pyrolysis of wood wool. Adapted with permission from [54],[55],[58] and [62], respectively.

### 1.2.2 Physico-chemical properties and applications of carbon nano-onions

The choice of the synthetic procedure to produce carbon nano-onions is an essential factor in relation to the selected applicative use. In general, CNOs exhibit common properties such as a low density and a high surface area to volume ratio. However, depending on the synthetic approach used for the production, CNOs exhibit different morphological features (i.e, size, number of graphitic layers and shape) and this determines their physico-chemical properties. In 2007, Echegoyen and co-workers investigated the effects of the synthetic approach on the properties and reactivity of CNOs. Thermal annealing and arc discharge methods were employed to produce CNOs with an average size of 5 nm and 15-25 nm, respectively. They showed through different characterization techniques that ND-derived CNOs displayed a more defective structure, higher thermal stability as well as an higher reactivity as a consequence of the higher curvature and larger surface area [21].

Carbon nano-onions, as the other  $\text{sp}^2$  carbon materials, exhibit a poor solubility in most of the common organic solvents as well in water, thus limiting to some extent their possible applicative use; their intrinsic hydrophobic nature is due to pronounced tendency to form aggregate induced by strong intermolecular interactions promoted by van der Waals forces. The chemical functionalization of CNO is an efficient route to enhance the solubility of the material by introducing different functional groups onto the graphitic surface. Inspired by the extensive literature regarding CNTs, covalent and non-covalent approaches have been investigated and successfully applied in the last decade [65].

Generally, covalent functionalization methods impart hydrophilicity to the inert graphitic surface via introduction of new functional groups, as depicted in Figure 1.11, and allows for further modifications with a wide range of organic moieties (i.e. dyes molecules).

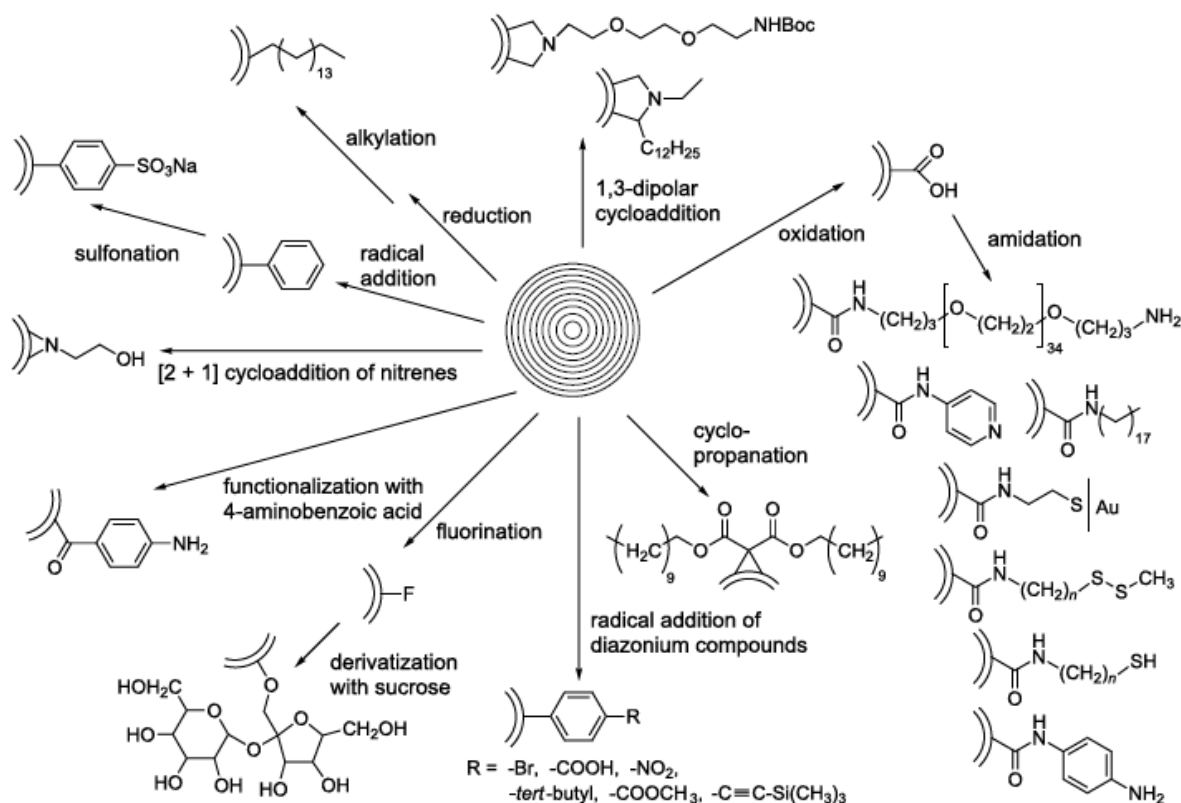


Figure 1.11: Covalent functionalization pathways for CNOs. Reprinted with permission from [65].

Several covalent pathways have been investigated so far. The first covalent modification of CNOs has been reported by Prato *et al.* in 2003, where CNOs were functionalized through an azomethine ylide addition reaction, which imparted good dispersability in common organic solvents [66]. A modification of the 1,3-dipolar cycloaddition reaction reported by Prato was proposed by Echegoyen and co-workers two years later; in the same work, the authors showed two novel and efficient covalent approaches for CNOs (i.e. pegylation and amidation reactions) [67]. In another work, the same group reported a successful CNO functionalization via cyclopropanation and radical addition reaction [21]. Improved solubility in organic solvents such as ethanol and DMF was accomplished by direct fluorination of CNOs at different temperatures [68], while good dispersion in water was obtained with the following modification with sucrose [69]. The first supramolecular CNO conjugate has been reported by Echegoyen *et al.* in 2008, where a pyridyl functionalized CNOs were complexed with a Zn/porphyrin derivatives, showing very good solubility in water [70]. The modification of the CNO surface with several functional groups such as benzoic acid via Tour reaction has been reported by Flavin *et al.* [71].

Interestingly, the addition of a similar Zn/porphyrin derivatives to the one reported by Ecehegoyen was obtained through a new synthetic approach supported by XPS and ToF-SIMS [72]. Furthermore, the presence of benzoic acid functionalities onto the CNO surface was exploited for the following incorporation of dyes molecules via amidation/esterification reactions to yield fluorescent CNOs, which have been successfully used as biological imaging agents [73-75].

Chemical oxidation is one of the most common covalent approach as it leads to an improvement of solubility by introducing oxygen-containing functionalities such as carboxylic groups onto the CNO surface; furthermore, it is often used as initial step for further CNO modification. Strong acids such as nitric acid [21, 67, 76] or concentrated acid solutions such as mixture of nitric and sulfuric acid [70] are typically employed for this purpose. Oxidation by ozonation have shown to impart hydrophilicity to CNOs and in addition, compared to traditional oxidation methods, is considered a green approach as the use of hazardous substances is not required [77]. Other covalent approaches have been reported, such as alkylation [78], [2+1] cycloaddition [79, 80], radical polymerization [81] as well as functionalization with biomolecules [82].

Covalent functionalization, as discussed above, have the potentialities to enhance the solubility and stability of CNOs. On the other hand, the structure of the material as well as its native properties may be seriously altered by the reaction conditions. The introduction of defectiveness induced by these chemical modifications may lead to the disruption of the graphitic structure and to the loss of its  $\pi$  conjugation character.

For this reason, non-covalent functionalization is a convenient route to modify the hydrophobic characteristic of the CNO surface, while preserving their intrinsic properties. Non-covalent approaches are based on the adsorption of aromatic compounds or macromolecules such as surfactants and polymers onto the surface of the CNO via  $\pi$ - $\pi$  or hydrophobic interactions to achieve a stable suspension. One relevant example of non-covalent functionalization of CNOs has been reported by Giordani et al, where a fluorescent pyrene-BODIPY dyes derivative was immobilized onto the CNO surface exploiting the  $\pi$ - $\pi$  supramolecular interactions established between the pyrene moieties and the extended CNO  $\pi$ -systems [83].

The current availability of several functionalization methods for the chemical modification of CNOs have opened up a wide range of possible applications in different areas. In the last decade, electrochemical [16, 17] and biomedical [15] applications of CNOs are probably the most studied topics and several investigation have been performed in these field. The possibility to decorate the surface with selected functional groups and the further conjugation with molecular entities such as fluorophores conferred to CNO derivatives an enhanced water solubility and biocompatibility. Furthermore, promising features such as low cytotoxicity, weak inflammatory and enhanced cell

penetration capability have been proved both *in vitro* and *in vivo*, confirming that CNOs is a safe material to be employed in biological applications. The detailed discussion of the bio-related applications of CNOs will be proposed in the following paragraph.

Similarly to the other CNMs [84], CNOs have shown promising outcomes in the field of sensing. CNO-based sensors exhibited enhanced sensitivity and selectivity for the detection of several molecules of interest, such as biotin/avidin [82], DNA [85], glucose [86-88] and other enzymes [89], dopamine [90], ascorbic acid [91] as well as pH sensors [74, 92, 93].

In electronics, CNOs have been employed for different purposes. One of the most interesting applications is as electrode material in supercapacitors and several works have been published after that Portet and co-workers proved its efficacy in this application [94]. Bushueva *et al.* showed how the electrochemical performances in terms of capacity and conductivity were correlated to the annealing temperature used for the CNO production [95], while Pech *et al.* reported the first CNO-based micro-supercapacitor, which showed higher capacity than the conventional ones [96]. In 2012, Borgohain *et al.* reported the development of a RuO<sub>2</sub>-CNO composite material with higher specific capacitance and increased cyclic stability [97]. In the same year, McDonough and co-workers investigated the influence of different parameters such as structure, physical and electrical properties of carbon nano-onions and nature of electrolytes on the supercapacitor performance, correlating the results with simulation data obtained by molecular dynamics (MD) modeling [98]. The results showed higher capacitive performance of carbon nano-onions at high charge/discharge rates compared to other carbon materials; furthermore, carbon nano-onions annealed at 1800 °C exhibited the highest conductivity the best capacitive performance at high rates, despite a lower specific surface area than the ones annealed at 1500 °C [98]. In 2013, Gao *et al.* investigated the electrochemical performance of CNO-based supercapacitor electrodes after the controlled introduction of porosity on the outer shells of CNOs by chemical KOH activation. The results showed five times larger capacitance along with a higher power density and energy density than the pristine ones [99]. Other reported electronic applications involving the use of CNOs are as material for hydrogen storage [100] and Li-ion batteries [101-103], in optical limiting [104] and electromagnetic shielding [105-107].

In catalysis, remarkable performance towards the oxidative dehydrogenation of ethylbenzene to styrene have been reported by using CNOs, who allowed for a high conversion yield [108, 109]; in addition, CNO as support for Pt nanoparticles showed enhanced electroactivity towards methanol oxidation compared to the benchmark Pt/Vulcan XC-72 catalyst [110, 111].

Finally, interesting applications in environmental remediation of heavy metal ions [112, 113] and tribology as lubricants [114-116] have been also reported.

## 1.3 Carbon nano-onions in nanomedicine

The development of new nano-carriers bearing both imaging and therapeutic units is the object of an intense scientific research in nanomedicine for its possible use for the treatment of several diseases, in particular cancer. Compared to the standard treatment such as chemotherapy, the possibility to use nanoplateforms allows for the targeted delivery of drugs to malignant tissues and with enhanced therapeutic efficacy [117].

In the last decades, CNMs such as carbon nanotubes [118, 119], fullerene [120, 121], graphene and its derivatives [122] as well as carbon dots [123, 124] have shown promising features in relevant bio-related applications. Their unique intrinsic physico-chemical properties together with the development of established chemical modification approaches made possible the creation of new functionalized nanoplateforms for bio-imaging and drug delivery purposes. In addition, their favorable nanometer size is comparable to that of relevant biomolecules such DNA and proteins, making them attractive for biological applications [125].

In the perspective of biological applications, a careful evaluation regarding the biocompatibility and the safety of a material is required and, in this context, *in vitro* and *in vivo* investigations are essential for a practicable use in living entities.

Low cytotoxicity, efficient cellular uptake and weak inflammatory potential revealed that CNOs are a biocompatible material suitable for different bio-applications such biological imaging and drug delivery. In the two following paragraphs, the current state of the art in the use of CNOs for these purposes will be presented, discussing both *in vitro* and *in vivo* investigations with particular attention to the production method employed for the CNO synthesis.

### 1.3.1 *In vitro* bio-evaluation of carbon nano-onions

The first *in vitro* evaluation of CNOs has been reported by Ding *et al.* in 2005. Large CNOs (around 30 nm in size) were produced by arch discharge method and the effects towards human skin fibroblast cells were evaluated and compared to MWCNTs. The results showed toxic responses for both nanomaterials, inducing a variation in the mRNA levels and affecting the cellular activity in terms of growth and differentiation (Figure 1.12A). However, compared to MWCNTs, CNOs induced less stress and no response from the cell immune system [126].

Xu *et al.* tested the same CNOs on human umbilical vein endothelial cells (HUVECs) and a dose-dependent effect on cell growth was observed with significant toxicity at high concentration (from 25 to 200  $\mu\text{g/mL}$ ) (Figure 1.12B). In addition, DNA damage and apoptosis was found to be induced by the presence of CNOs [127].

The cytotoxic effect of pristine and functionalized (i.e. oxidized and pegylated) CNOs on the viability of rat dermal fibroblasts has been investigated by Luszczyński *et al.* in 2010 and any toxic effect was observed for all the CNO materials (Figure 1.12C). More interestingly, this was the first evidence of the biocompatibility of NDs-derived CNOs [82].

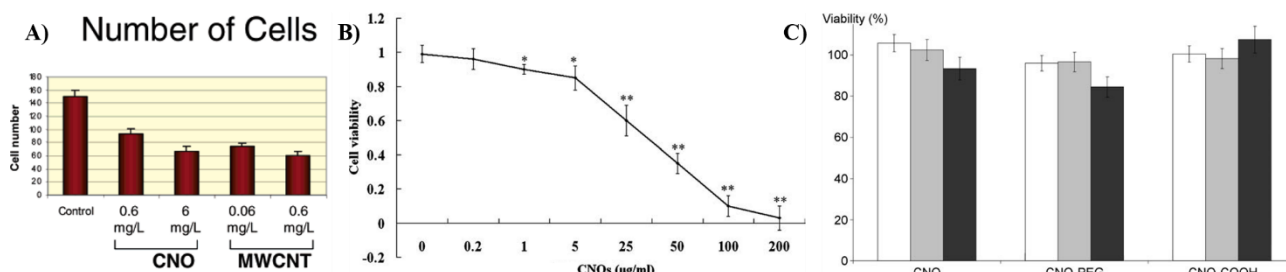


Figure 1.12: Cell viability measurements after treatment with CNO derivatives of A) skin fibroblast cells and comparison with MWCNTs, B) HUVECs and C) rat dermal fibroblasts. Adapted with permission from [126], [127] and [82], respectively.

Kang and co-workers reported the comparison between the cellular cytotoxicity induced by spherical CNOs, synthesized by laser irradiation, and CVD-derived MWCNTs on a normal human bronchial epithelial cell line. The results showed a better biocompatibility of CNOs and a lower generation of intracellular reactive oxygen species (ROS), ascribed to their spherical morphology. In addition, the same trend was observed in the presence of an anti-oxidant with a remarkable decrease of the ROS level induced by MWCNTs [128].

In 2006, a report on the use of onion-like nanoparticles as imaging agent was published by Tripathi *et al.* In this work, the intrinsic and tunable fluorescence of the particles, synthesized by pyrolysis and arisen from the surface passivation induced by oxidation, was employed to image *Escherichia coli* and *Pseudomonas putida* cells. In addition, the fluorescent system was employed as biosensor for the detection of glucose exploiting an on/off fluorescence mechanism [87].

The small size and the ease of functionalization of CNOs produced by thermal annealing have been exploited by Giordani's group to develop novel nanosystems suitable for both imaging and targeting. In 2013, they conducted an *in vitro* and *in vivo* investigation on the inflammatory potential induced by CNO derivatives were tested on immortalized bone-marrow derived mouse macrophages (iBMM) and mouse bone-marrow-derived dendritic cells (BMDCs). For this purpose, ND-derived pristine CNOs were firstly decorated by benzoic acid via Tour reaction [71] and then coupled with a fluoresceinamine dye by amidation reaction to enable their cellular visualization, as suggested by the green emission in Figure 1.13A. The release of the inflammatory cytokines IL-1  $\beta$  by BMDCs in the presence of toll-like receptor (TLR) was promoted by the CNOs, which in addition induced the activation of the NLRP3 inflammasome. Furthermore, benzoic acid-decorated CNOs were found to produce low *in vitro* inflammation and to reduce the *in vivo* recruitment of neutrophils and monocytes.



Finally, CNOs were efficiently uptaken by antigen-presenting cells and targeted to draining lymph nodes [73].

In 2014, Giordani *et al.* developed a novel CNO-based imaging platform, which was tested in human breast cancer cells (MCF-7). CNOs bearing benzoic acid functionalities were coupled with a green emitting boron dipyrromethene dyes (BODIPY-CNOs) by esterification reaction, as confirmed by several characterization techniques; its *in vitro* toxicity was investigated by studying the metabolic activity of the cells at different CNO concentrations and no toxic effects were observed up to 72 h. In addition, the fluorescent nanoparticles were efficiently internalized by the cells and localized in the lysosomes, as depicted by the yellow co-localization signal in the confocal image in Figure 1.13B [75].

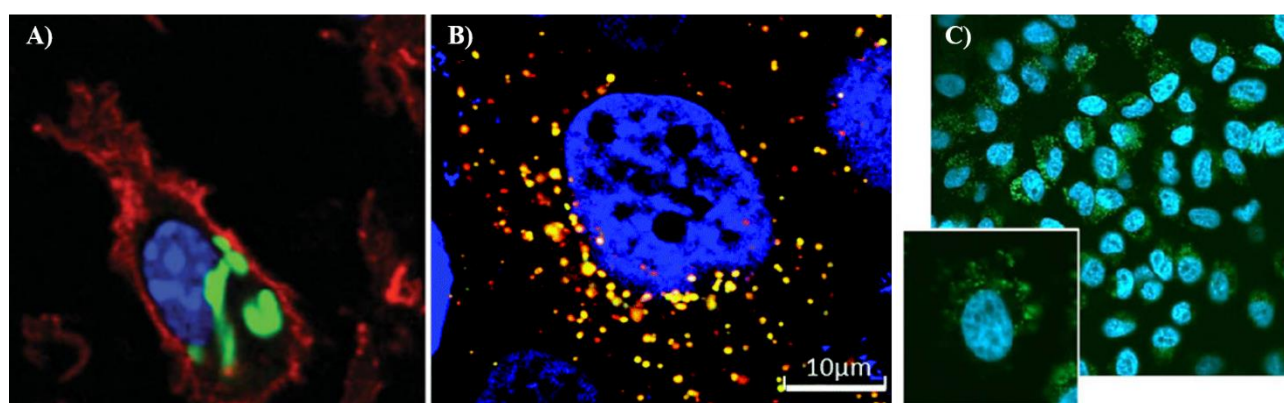


Figure 1.13: Confocal images of A) C57BL/6 BMDCs, B) MCF-7 cells and C) HeLa cells incubated with different fluorescent CNO derivatives at 10 µg/mL CNO concentration. Adapted with permission from [73], [75] and [76].

A novel oxidation procedure allowed Giordani and co-workers to develop a CNO-based imaging agent with enhanced solubility in biological fluids. The oxidation was carried out in 3 M nitric acid for 48 h to yield oxidized CNOs (oxi-CNOs) with much higher surface coverage of carboxylic acid functionalities (around 210 per CNO) than the one obtained via Tour reaction [71], as confirmed by TGA; the following attachment with a fluoresceinamine dye was accomplished by ester bond as discussed above to create a fluorescent nanoprobe (fluo-CNOs) with enhanced dispersing ability and stability in water, as confirmed by dynamic light scattering and zeta potential. The successful CNO modification was confirmed by different spectroscopic techniques. The biocompatibility of all the functionalized CNOs was tested in HeLa cells by using a PrestoBlue cell viability assay and the results showed that CNO derivatives didn't affect the cell viability at any of the concentrations tested. Furthermore, fluo-CNOs were efficiently internalized by the cells, as confirmed by confocal imaging (Figure 1.13C), by an endocytosis pathway [76].

The same group reported a multiple covalent modification approach with the aim to create a novel CNO platform capable of both imaging and targeting. For this purpose, a FITC dye and folic acid

(FA) were attached to the surface of benzoic acid CNOs and the CNO modification was confirmed by FTIR, Raman, XPS and ToF-SIMS spectroscopies. CNOs bearing both ligands (CNO-4) or only the dye molecules (CNO-5) were tested in HeLa and KB cells by assessing their metabolic activity at different incubation times and no significant cytotoxicity was observed in both cell lines for all the CNO derivatives.

Confocal imaging and correlative imaging analysis (CLEM) confirmed the internalization of fluorescent CNOs by HeLa cells with localization in the lysosomal vesicles. In addition, as KB cells exhibit an overexpression of folate receptors, CNO-4 were internalized to a greater extent than CNO-5 by the cells (Figure 1.14A) through a folate-mediated endocytosis pathway; further confirm was given by the minimal internalization in the presence of free FA in solution, which would compete for the folate receptors [129].

The first CNO fluorescent probe exploiting non-covalent interactions was published in 2015, where a pyrene-BODIPY dye molecule was coupled with p-CNOs through  $\pi$ - $\pi$  stacking interactions between the extended aromatic CNO graphitic network and the pyrene unit of the dyes, as confirmed by absorption, fluorescence and FTIR spectroscopies. HeLa wild type (wt) cervical cancer cells were incubated with different concentrations of CNOs and no significant cytotoxicity was observed even at prolonged time of incubation. The widely spread green emission of CNO derivatives in the perinuclear region (Figure 1.14B) confirms the efficient uptake by HeLa cells. In addition, after that the cells were incubated at 4 °C, the CNO hybrids were internalized to a very low extent (inset in Figure 1.14B), suggesting an endocytosis mechanism for their uptake instead of a passive diffusion pathway [83].

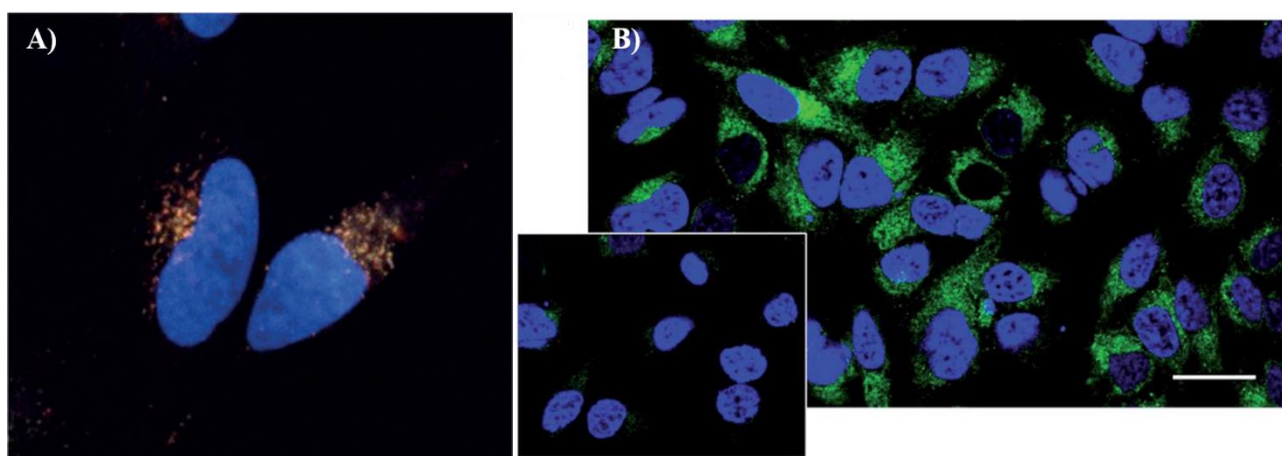


*Figure 1.14: Confocal images of HeLa cells incubated with A) CNO derivatives bearing FA and FITC ligands at 10  $\mu$ g/mL for 12 h at 37 °C and B) p-CNO/pyrene-BODIPY derivatives at 10  $\mu$ g/mL for 30 min at 37 °C. The inset shows the uptake of the same CNO derivative incubated at 4 °C. Adapted with permission from [129] and [83], respectively.*

As in the visible region of the electromagnetic spectrum photons are largely absorbed and scattered by biological tissues and water, for bio-imaging purposes the use of dye emitting in this range may

be limited due to the attenuation of the fluorescence signal. An efficient approach to overcome this limitation is to use dye with emission in the near-infrared (NIR) region and many efforts have been involved in the development of NIR emitting fluorescent probes. In this particular imaging window, tissues show unsubstantial absorbance allowing for an extended penetration of the light, thus improving the ability of bio-imaging agents [125]. With this in mind, Giordani and co-workers moved from green emitting dyes (as the ones discussed above) to novel dyes with emission at longer wavelength (far-red and NIR region). In 2014, the same authors reported a new fluorescent CNO derivatives with emission in the NIR region and they investigated its potentiality as imaging agent in HeLa cells [74]. CNOs bearing benzoic acid groups were coupled with two boron difluoride azadipyrromethene BODIPY dyads showing a methoxy- and hydroxy-substitution to yield Me- and OH-CNOs, respectively. Spectroscopy techniques as well as microscopy confirmed the CNO surface modification. The metabolic activity was assessed by a PrestoBlue assay and both CNO derivatives exhibited a negligible cytotoxicity after internalization in HeLa cells, even at the highest concentration tested (i.e. 100  $\mu\text{g/mL}$ ). Laser scanning confocal microscopy (LSCM) confirmed the excellent internalization of Me-CNOs, as depicted by the strong NIR emission in the perinuclear area (Figure 1.15A). Interestingly, the OH-CNO derivatives displayed a fluorescence on/off switching phenomenon as a function of the pH. This switching ability was proved to be retained and reversible both in solution and *in vitro*. In particular, a strong NIR emission was observed from the cell only at acidic pH, while a weak signal was detected at pH 8.5. This peculiar characteristic is very attractive in the perspective of cancer cell imaging [74].

A novel highly fluorescent bromo-terminated BODIPY alkyl ether dyes was employed to create a new interesting bio-imaging fluorescent probe with emission in the far-red/NIR region. The successful formation of the CNO derivative was proved by several spectroscopy techniques (Raman, absorption and emission) as well as thermogravimetric analysis. Furthermore, the remarkable emission properties of the fluorescent CNO nanoprobe were confirmed by laser confocal microscopy, after the dispersion of the sample in a polystyrene slide, with the 3D z-stacking images displaying an intense red fluorescent emission arising from the whole sample [130].

Recently, another interesting example of CNO-based pH probe was published by the same group [92]. In this work, oxidized CNOs were covalently functionalized with a  $\pi$ -extended distyryl-substituted boron dipyrromethene (BODIPY) dye and the as-produced fluo-CNOs were tested in HeLa cells, showing remarkable cytocompatibility. The emission on/off switching properties, promoted by the protonation of the dimethylamino unit present in the BODIPY dye, were retained in solution as well as *in vitro*. In particular, no emission was detected by confocal imaging at

physiological pH; the emission properties were, instead, activated in response to an acidic pH, as confirmed by the strong red emission signal (Figure 1.15B) [92].

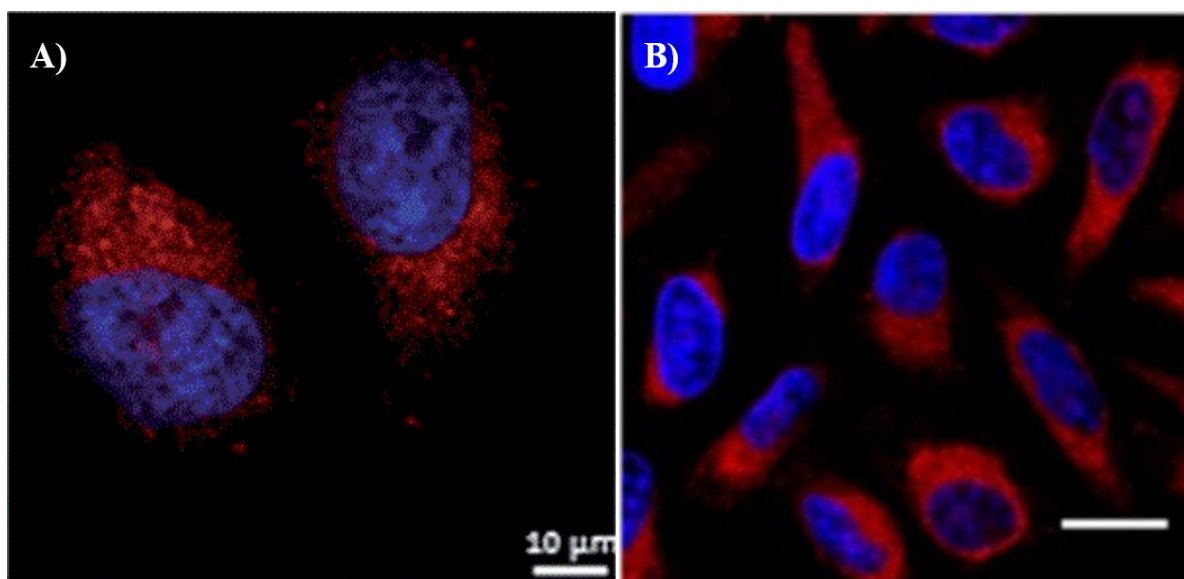


Figure 1.15: Confocal images of HeLa cells incubated with A) Me-CNOs and B) fluo-CNOs. Adapted with permission from [74] and [92], respectively.

### 1.3.2 *In vivo* bio-evaluation of carbon nano-onions

The *in vitro* studies performed so far on CNO derivatives have demonstrated the biocompatibility of this carbon nanomaterial; in particular, minimal systemic toxicity and high capability to be uptaken by the tested cell lines have been reported. In addition to the *in vitro* investigation, systematic *in vivo* analyses on cytotoxicity and bio-distribution on complex living systems are required and, to date, few evaluations have been published. Sarkar and co-workers reported two *in vivo* investigation of onion-like nanoparticles synthesized by conventional pyrolysis method of wood wool. The further oxidation process led to a high surface coverage of carboxylic acid functionalities onto the CNO surface, which increased the dispersing ability of these nanoparticles in water, and to a surface passivation effect, which induced tunable emission properties from visible to NIR region. In the first investigation, *Drosophila Melanogaster* was fed with the fluorescent CNOs and the life cycle from pupal to adult stages was monitored by optical fluorescence spectroscopy (Figure 1.16A).

The results showed no effects on the normal activity of the *D. Melanogaster* induced by CNOs; in addition, the fluorescent nanoparticles were normally excreted [61]. The same nanoparticles were used as biological imaging agents in the prokaryotic *Escherichia Coli* and in a more complex eukaryotic organism like multicellular *Caenorhabditis Elegans*. The presence of CNOs, which allowed for the imaging of *E. Coli*, showed no negative effect on the bacterial growth of this organism. In addition, *C. Elegans* was later fed with CNO-treated *E. Coli* and no detrimental effect was induced on the complex organism, suggesting the lack of toxicity of CNOs even when used in a food chain

(Figure 1.16B) [63]. In another work, the same group showed that a fragmentation procedure with repetitive nitric acid treatment led to a lower CNO size, allowing them to cross through the blood brain barrier of the treated mice with good excretion efficiency [131].

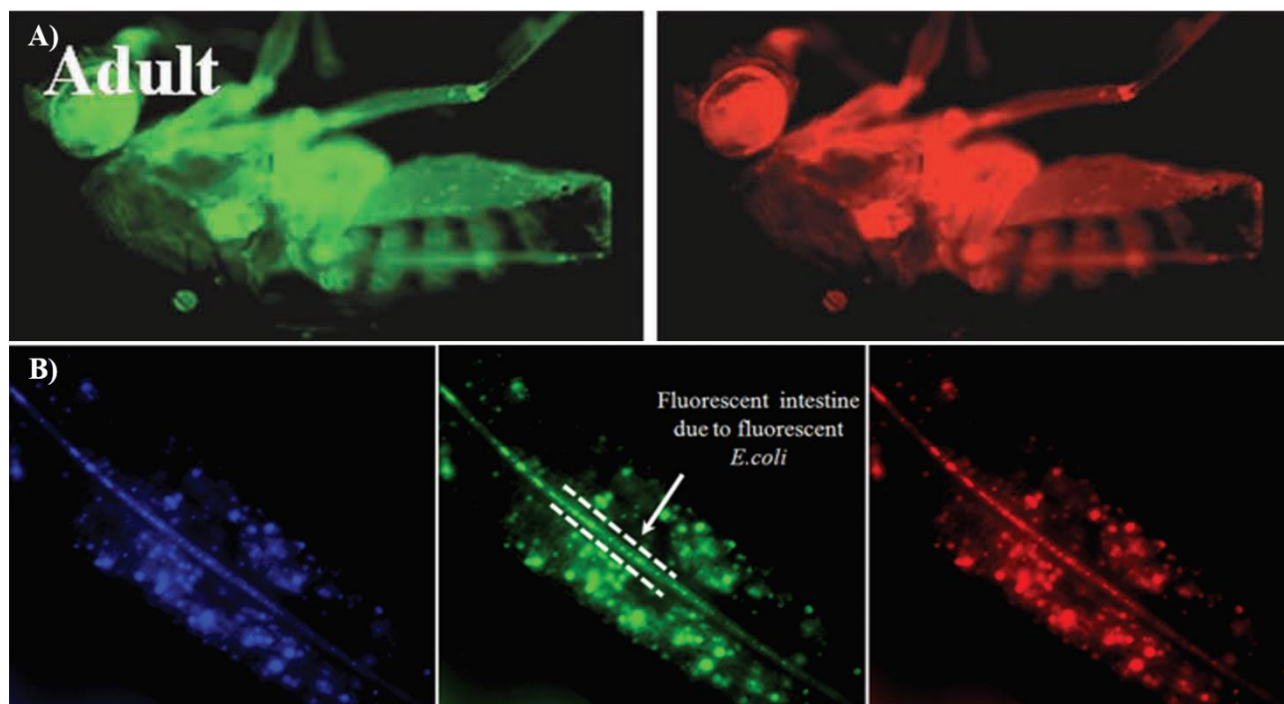


Figure 1.16: Fluorescence images of A) CNO-fed *Drosophila melanogaster*, under 488 and 561 nm filters and B) CNO-*E. coli*-fed *C. elegans* under 385, 488 nm and 561 nm band-pass filters. Adapted with permission from [61].

The eco-toxicological consequences of CNOs freshwater polyp *Hydra vulgaris* were evaluated by Giordani *et al.* in 2015, investigating different parameters such as morphology, reproductive and regenerative capabilities. Pristine CNOs as well as CNO derivatives bearing benzoic acid, pyridine and methylpyridinium were used to assess *in vivo* analyses on uptake and bio-distribution. The results showed efficient internalization for all the CNO derivatives, as shown by the presence of black spots inside the animal (Figure 1.17A), following a micropinocytosis mechanism. No alterations on behavior and morphology were observed along with no effects on the long-term reproductive and regenerative capabilities, confirming the lack of toxicity of CNOs over a long time scale [132].

The first evaluation of CNO impact on zebrafish (*Danio Rerio*) during the development as vertebrate model was published in 2016. The possible systemic effect of CNOs functionalized with benzoic acid and BODIPY dyes were evaluated exposing zebrafish embryos and *larvae* to different CNO concentrations. Firstly, the presence of CNOs showed no adverse effect on survival and hatching rates as well as on the heart beat rate and frequency of movements; the same results was observed regarding the animal organogenesis. By using inverted selective plane illumination microscopy (iSPIM), fluorescent CNOs were found to be distributed inside the zebrafish *larvae* in a homogenous way, as shown in Figure 1.17B [133]. These outcomes confirmed the outstanding *in vivo* biocompatibilities of



CNOs in this vertebrate model, in contrast to what reported for other CNMs such as fullerenes [134], graphene quantum dots [135] and graphene oxide [136].

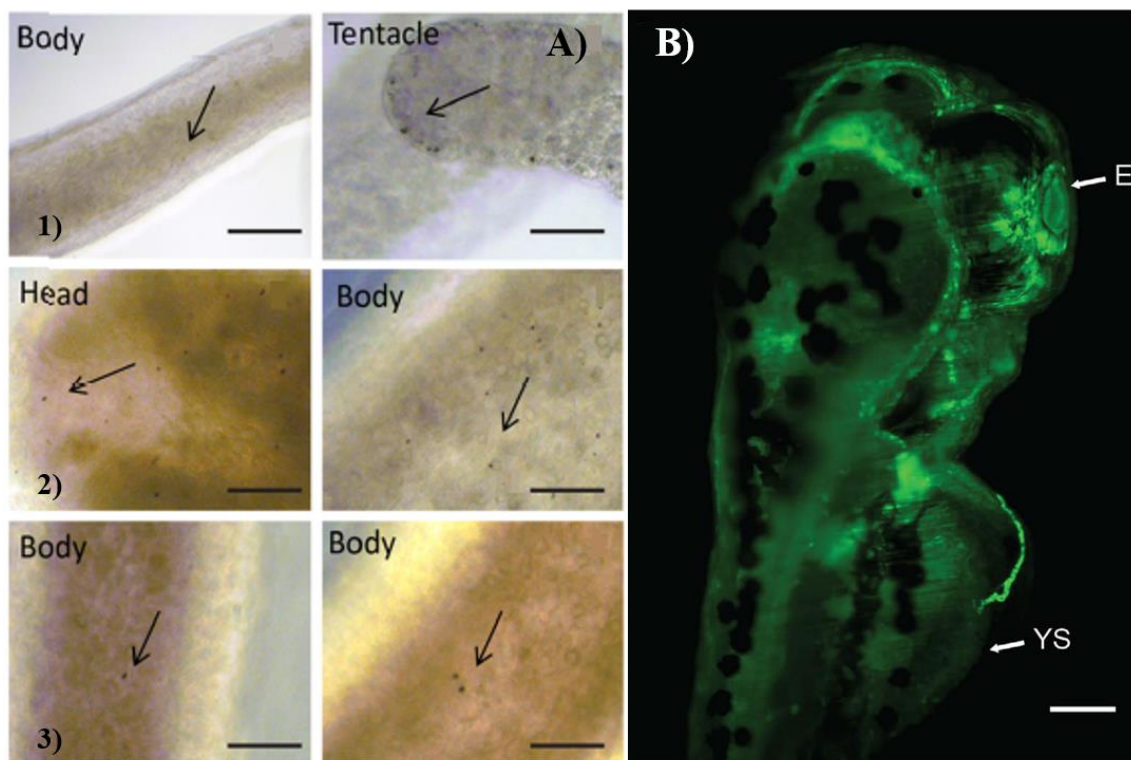


Figure 1.17: A) In vivo uptake and biodistribution in *Hydra* of CNOs decorated with 1) benzoic acid, 2) pyridine and 3) methylpyridinium. B) In vivo imaging of the superior part of a zebrafish larvae treated with BODIPY-CNOs; E:eye, YS: yolk sac. Adapted with permission from [132] and [133], respectively.

## 1.4 Carbon nano-onions in electrocatalysis

### 1.4.1 Fuel cells and oxygen reduction reaction

Nowadays, the growing energy demand and the drop of natural fossil fuels along with the increasing environmental concerns related to their use makes of outmost importance the development of new and renewable cheap energy sources with high efficiency [137, 138]. Fuel cell is currently the most promising technological strategy proposed to solve the energetic issues [139]. The schematization of the operating principle of a fuel cell is reported in Figure 1.18A. In this energy device, electricity can be generated by the electrochemical oxidation of a fuel (typically, hydrogen) and the reduction of oxygen to produce water. Briefly, the hydrogen is pumped at the anodic side of the cell where is split in protons and electrons, which follow two different pathways. The electrons leave the anode, providing electricity, and reduce the oxygen at the cathode side. The protons, instead, crossing through the cell, react with the oxygen species at the cathode to produce water [140].

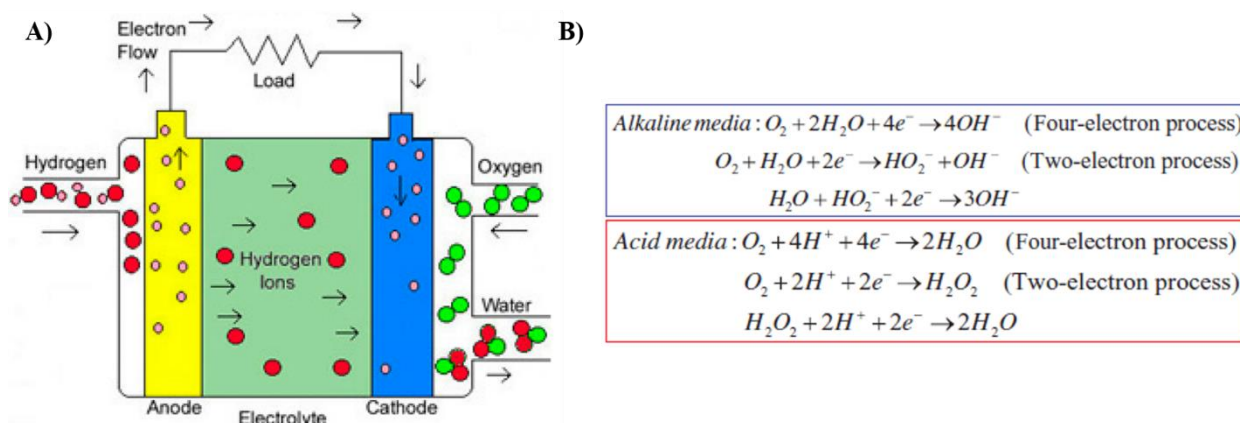


Figure 1.18: A) Operative schematization of a fuel cell and ORR process in alkaline and acidic media. Adapted with permission from [140] and [141], respectively.

Typically, ORR can occur in both alkaline and acidic media following two different routes: the first is through a two-step two-electron pathway with the intermediate formation of  $H_2O_2$  (in acidic environment) or  $HO_2^-$  (in alkaline environment). The second route, which is the preferred one, is the direct reduction of oxygen into  $H_2O$  in acidic medium or the intermediate formation of  $OH^-$  in alkaline medium to form water by combination with protons through a four-electron pathway (Figure 1.18B) [140, 141].

Commonly, the evaluation of the ORR electrocatalytic performance of a catalyst is achieved by using techniques such as rotating disc electrode (RDE), rotating ring-disc electrode (RRDE) and linear sweep voltammetry (LSV). An example of LSV curves at different rotating speeds ( $\omega$ ) obtained by RDE is reported in Figure 1.19A. In general, the current density increases by increasing  $\omega$  as an enhanced oxygen convection and its following reduction occurs at the electrode surface; in addition, the plateau obtained at high overpotentials is due to the extremely fast oxygen reduction process. Onset potential ( $E_{onset}$ ) and half-wave potential ( $E_{1/2}$ ) are the two parameters usually employed to establish the activity of a catalyst. They can be determined from the polarization curves and, typically, higher values correspond to better catalytic activities.

The overall measured ORR current ( $J$ ) depends on the kinetic current ( $J_k$ ) and the diffusion-limiting current ( $J_d$ ), as shown in equation (1). At high enough overpotentials, the concentration of oxygen at the electrode surface is almost zero because every atom or ion reacts instantaneously when reaching the electrode, resulting in a diffusion-limiting plateau.  $J_d$  is therefore dependent on the diffusion rate and thus to  $\omega$ . Equation (1), known as Koutecky-Levich (K-L) equation, is expressed as:

$$\frac{1}{J} = \frac{1}{J_k} + \frac{1}{J_d} = \frac{1}{J_k} + \frac{1}{B\omega^{0.5}} \quad (1)$$

$B$  is determined from the slope of the K-L plot through the Levich equation:

$$B = KnF(D_{O_2})^{2/3}v^{-1/6}C_{O_2} \quad (2)$$

where  $K$  is a constant dependent on  $\omega$  (0.2 or 0.62 if expressed in rpm or rad/s),  $n$  the transferred electron number,  $F$  the Faraday constant (96485 C/mol),  $D$  the oxygen diffusion coefficient in the electrolyte ( $1.9 \cdot 10^{-5} \text{ cm}^2/\text{s}$  in 0.1 M KOH),  $v$  the electrolyte kinetic viscosity ( $0.01 \text{ cm}^2/\text{s}$  in 0.1 M KOH) and  $C$  the oxygen bulk concentration ( $1.2 \cdot 10^{-6} \text{ mol}/\text{cm}^3$  in 0.1 M KOH) [141, 142].

Another essential technique to give insight on kinetics and ORR mechanism is the RRDE, where the disc ( $I_D$ ) and ring currents ( $I_R$ ) are recorded as the disc electrode potential is varied (Figure 1.19B). The molar  $H_2O_2/HO_2^-$  ratio of produced species on the ring can be evaluated through RRDE.  $I_D$  is composed of two contributes, as depicted in the following equation:

$$I_D = I_{H_2O} + I_{H_2O_2} = I_{H_2O} + \frac{I_R}{N} \quad (3)$$

where  $I_{H_2O}$  and  $I_{H_2O_2}$  are the oxygen reduction and intermediate currents, respectively, and  $N$  the collection efficiency of the ring, defined as  $N = -I_R/I_D$  and corresponds to the fraction of product produced at the disk that is detected at the ring.

The  $H_2O_2$  yield ( $\%H_2O_2$ ) and  $n$  can be determined as follows [141]:

$$n = 4 \frac{I_D}{I_D + I_R/N} \quad (4)$$

$$\%H_2O_2 = 200 \frac{I_R/N}{I_D + I_R/N} \quad (5)$$

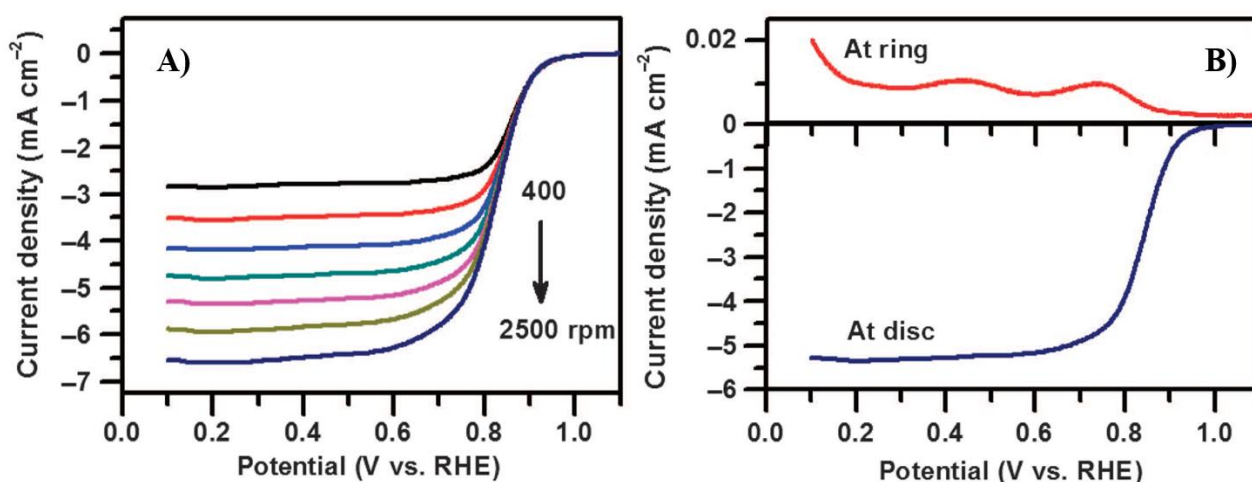


Figure 1.19: Evaluation of electrocatalytic activities towards ORR. A) LSV curves of electrocatalysts in oxygen-saturated electrolyte with different rotating rates and B) Oxygen reduction curves on the disc and ring electrodes of RRDE at 5 mV s⁻¹ scan rate at 1600 rpm, respectively. Adapted with permission from [141].



The main limiting factor of fuel cell performance, which hindered their commercialization, is related to the kinetically slow oxygen reduction reaction (ORR) occurring at the cathode side [143], which is reported to be about six orders of magnitude slower than the hydrogen oxidation reaction [141]. Ideally, the fuel cell voltage should be 1.23 V, which is called reversible cell voltage; however, due to a series of irreversibilities arising during the cell operation, this value is not approached even at zero current (i.e. open circuit). For a single electrode, the difference between the cell voltage at a specific value of the current density and the reversible cell voltage is known as overpotential [144]. In order to enhance the electrochemical reduction of the oxygen (i.e. reduce the overpotential and the activation energy of the reaction), the use of a catalyst is strictly required. Currently, carbon-supported platinum (Pt/C) is the most performing electrocatalyst for the ORR, as it exhibits low overpotential and outstanding current density. However, the high cost and the scarcity of natural reserves of Pt limits its use; in addition, it exhibits several drawbacks such as including poor operation durability, fuel crossover and CO poisoning effect [145]. For this reason, extensive efforts have been devoted to find a competitive, low cost and durable alternative to Pt. Several materials have been proposed for this purpose, including Pt-free noble metals [145], non-precious metals [146, 147] and metal-free catalysts [140]. Among the metal-free materials proposed so far, CNMs showed to be a relevant alternative to the expensive Pt-based catalysts. The discussion about their use for ORR is reported in the following section.

## 1.4.2 Carbon nanomaterials as ORR catalyst

Carbon nanomaterials are currently the most investigated metal-free catalysts due the large surface specific area with tunable porosity, outstanding mechanical and electrical properties, high durability and reasonable cost [148]. In their native form, CNMs display low catalytic performance due to the absence of active sites, thus requiring the modification of the surface charge distributions. An effective way to improve their catalytic activity is through the introduction of heteroatoms such nitrogen (N), boron (B), sulfur (S) or phosphorus (P) in the inherent graphitic structure (Figure 1.20A). The enhanced ORR catalytic activity is related to the breaking of the electro-neutrality of the  $sp^2$  carbon network as a result of the charge redistribution induced by the dopants, which allows for the creation of active charged site suitable for the oxygen adsorption [145].

Due to the different size and electronegativity ( $\chi$ ) of the heteroatoms, an electron modulation is induced in the structure, which change the electronic properties of the pristine materials. In addition, the presence of foreign atoms causes lattice distortion and defects in the structure, which potentially change the chemical activity of the material (Figure 1.20B) [140, 149].

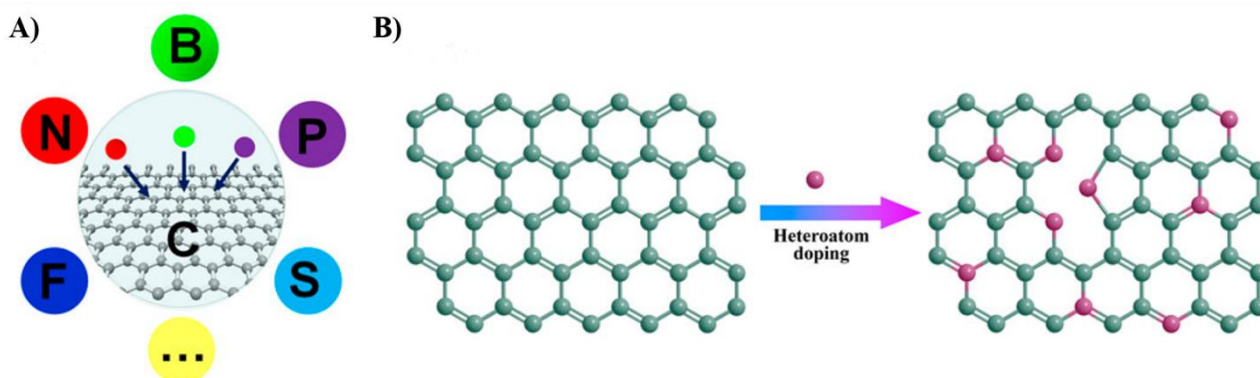


Figure 1.20: A) Common heteroatoms used for the doping of graphitic structure with heteroatoms and B) schematic representation of their effects on the structure. Adapted with permission from [140].

In 2009, Gong and co-workers reported the first evidence of the superior performance of a doped carbon structure compared to Pt. Nitrogen-doped vertically aligned CNTs (VA-NCNTs) were synthesized via pyrolysis of iron (II) phthalocyanine and electrochemically purified to remove the iron catalyst traces. The electrocatalytic activity towards ORR was investigated in alkaline medium and the results showed unexpectedly much higher performance than Pt with lower overpotential and higher diffusion current (Figure 1.21A) along with longer durability. The quantum mechanics calculation they performed to explain this behavior showed that the strong N electron affinity induces an increased positive charge density on the N-adjacent carbon atoms and the corresponding charge delocalization produces new catalytic sites able to weaken the O-O bonding and thus facilitating the ORR process (Figure 1.21B) [150].

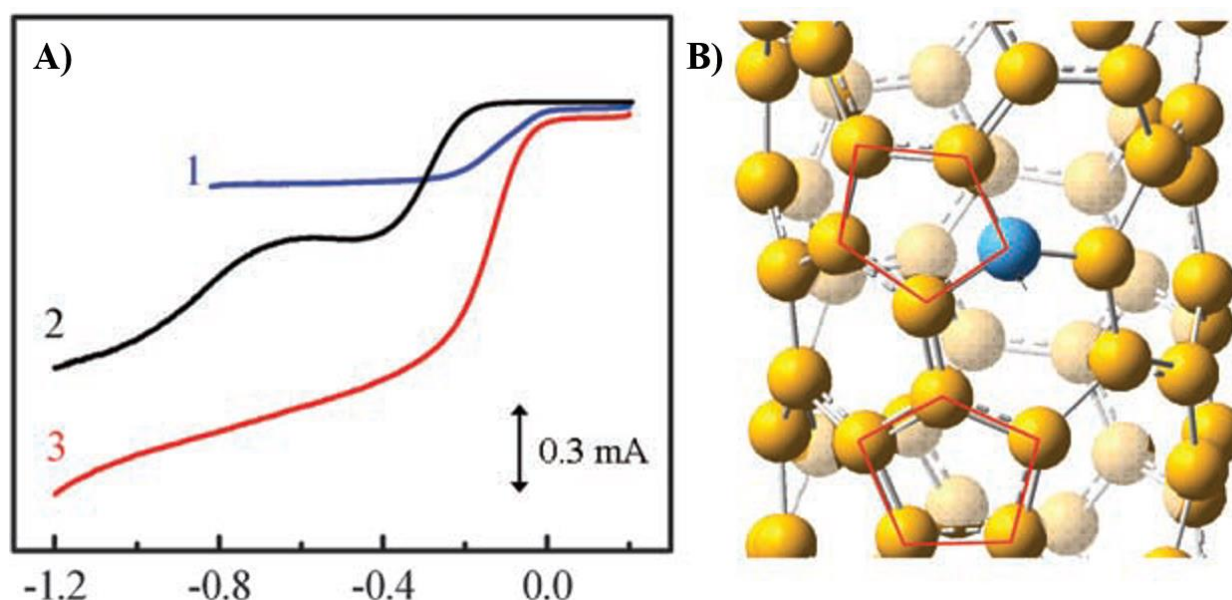


Figure 1.21: A) RRDE voltammograms for oxygen reduction in air-saturated 0.1 M KOH at the Pt-C/GC (curve 1), VA-CCNT/GC (curve 2), and VA-NCNT (curve 3) electrodes. B) Calculated charge density distribution for the VA-NCNTs. Adapted with permission from [150].

From that moment, a large number of approaches have been developed to dope CNMs, opening a novel research area in the field of electrocatalysis. Two different strategies are commonly employed to doped CNMs; the first approach is based on the *in situ*-doping during the material synthesis, which enables an homogeneous distribution of the dopant atoms in the carbon framework, while the second approach relies on a post-doping treatment with heteroatom precursors, which leads to a surface modification of the material.

The most common doping strategies include chemical vapor deposition (CVD), pyrolysis of heteroatom precursors, heat treatment in the presence of precursor gases and ball milling [149].

Nitrogen doping is the most popular approach and, as previously discussed, causes a modification of the structural charge density due to the difference in  $\chi$  between C (2.55) and N (3.07). This charge redistribution is the responsible for the easier oxygen chemisorption and improved electron transfer [149, 150]. VA-NCNTs, synthesized by CVD in the presence of a catalyst in a similar way as reported by Gong [150], showed higher ORR performance to that of Pt/C even in acidic environment with higher current density and better electron transfer process [151]. An efficient metal-free catalyst approach was proposed by Yu *et al.* in 2010, where nitrogen-doped SWCNTs (N-SWCNTs) were synthesized by CVD exploiting SiO<sub>2</sub> nanoparticles as catalytic substrate. The as-synthesized N-SWCNTs, exhibiting a N content of 3.6 at%, showed improved ORR activity via a four-electron pathway and longer durability in acidic medium compared to the pristine sample (Figure 1.22A) [152].

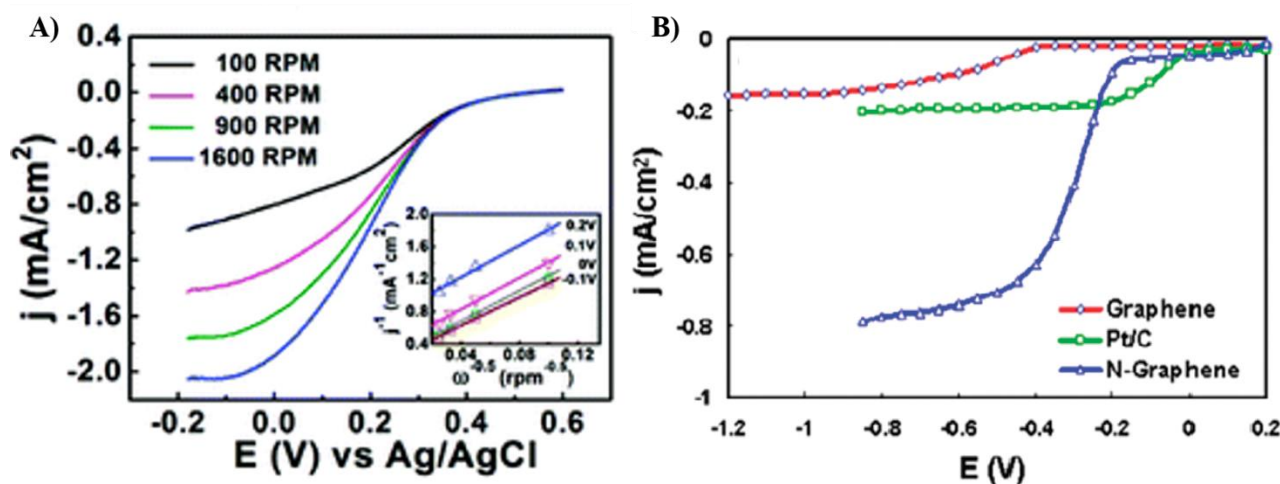


Figure 1.22: A) RDE curves of the N-SWCNTs in oxygen-saturated 0.5 M H<sub>2</sub>SO<sub>4</sub> at different speeds at a scan rate of 10 mV/s (the inset showing the Koutecky–Levich plots derived from RDE measurements). B) RRDE voltammograms for the ORR in air-saturated 0.1 M KOH at the C-graphene electrode (red line), Pt/C electrode (green line), and N-graphene electrode (blue line) at 1000 rpm and scan rate of 0.01 V/s. Adapted with permission from [152] and [153], respectively.

Besides CNTs, N-doped graphene also showed its effectiveness as ORR catalyst. Qu and co-workers achieved the first N-doping of graphene through CVD method using a gas mixture of CH<sub>4</sub> and NH<sub>3</sub> over a Ni-coated Si substrate and investigated the electrochemical performance in comparison to

pristine graphene and Pt/C catalysts. The results (Figure 1.22B) showed a quasi-ideal four-electron pathway for the oxygen reduction, while the pristine samples showed a two-step two-electron reduction route. In addition, higher current density (i.e. 3 times) and stability and remarkable tolerance to methanol crossover and CO poisoning compared to Pt-based catalysts was observed, suggesting the importance of the N-doping [153].

The configuration of the dopants inside the graphitic structure plays a key role in enhancing the catalytic activity of the doped material as it determines the electronic structure of the doped system and thus the catalytic behavior. As a proof of concept, the different nitrogen bonding configurations in the carbon structure are schematically shown in Figure 1.23A. Pyridinic and pyrrolic N atoms are present at the edges or incorporated at defective positions (i.e. into a five member ring). In both cases, each N atom is bonded to two C atoms, sharing one or two p electrons to the aromatic system, respectively. On the other hand, graphitic N atoms replace carbon atoms in the graphitic network [145, 154].

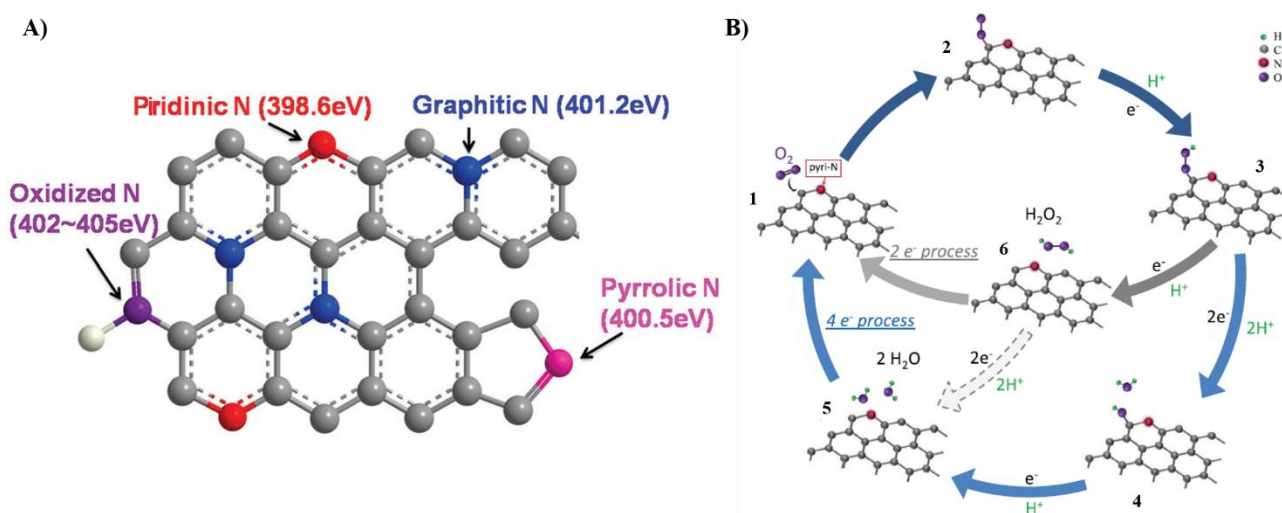


Figure 1.23: A) Schematic representation of N bonding configurations, including typical XPS binding energies. B) Schematic pathway for ORR on N-doped CNMs. Adapted with permission from [145] and [155], respectively.

In general, pyridinic (pyr-) and graphitic (grap-) N atoms are reported to be responsible of the improved ORR performance of N-doped CNMs, influencing onset potential and current density, respectively [149]. Recently, Guo *et al.* performed an extensive investigation with the aim to determinate the N ORR active site. They synthesized pyridinic (pyr-) and graphitic (grap-) highly oriented pyrolytic graphite (HOPG) samples and tested the different samples in acidic medium. The results showed that the pyr-HOPG with the lowest N amount exhibited better ORR activity to that of the grap-HOPG with the highest concentration, thus demonstrating that the presence of pyr-N plays the key role in enhancing the ORR performance of N-doped catalysts. In addition, they proposed a mechanism for the ORR induced by pyr-N atoms (Figure 1.23B). As the presence of these N atoms

creates Lewis base sites, oxygen molecules are adsorbed onto the N-adjacent carbon atoms (step 2 in Figure 1.23B) and then protonated (step 3). At this point, two routes can be followed. A four-electron pathway, where two other protons bind the two oxygen atoms, causing the breakage of the O-OH species and the formation of OH species (step 4). Then, the formation of H<sub>2</sub>O occurs when the OH species react with an additional proton (step 5). Otherwise, if a two-step two-electron reaction pathway is followed, at step 3, the O-OH species react with a proton to form H<sub>2</sub>O<sub>2</sub> (step 6), followed by its readsorption and reduction by two protons to finally form H<sub>2</sub>O [155].

Besides N-doped CNMs, B doping have shown to be an effective approach for the synthesis of ORR electrocatalysts. The first boron-based carbon catalysts were proposed by Yang and co-workers in 2011. Boron-doped CNTs (B-CNTs) were synthesized by CVD of benzene with triphenylborane (TPB) as B precursor and ferrocene as catalyst; different concentrations of TPB were used to yield a tunable B content between 0 and around 2%. The results showed enhanced ORR performance compared to the pristine CNTs through a two-electron reduction pathway; in addition, the ORR activity was found to increase with the increase of the boron content. Contrary to the electron-rich N atoms, the presence of electron-deficient B atoms in the graphitic network induces a different mechanism for the enhanced electroactivity. Exploiting DFT calculations, they proposed a mechanism for the electrocatalytic activity induced by B-doping. In this case, in contrast with N-type doping, the B itself is positively polarized, acting as active site for the adsorption of oxygen; furthermore, B accumulates  $\pi$  electrons from the carbon atoms and transfer them to the oxygen, acting as a bridge [156].

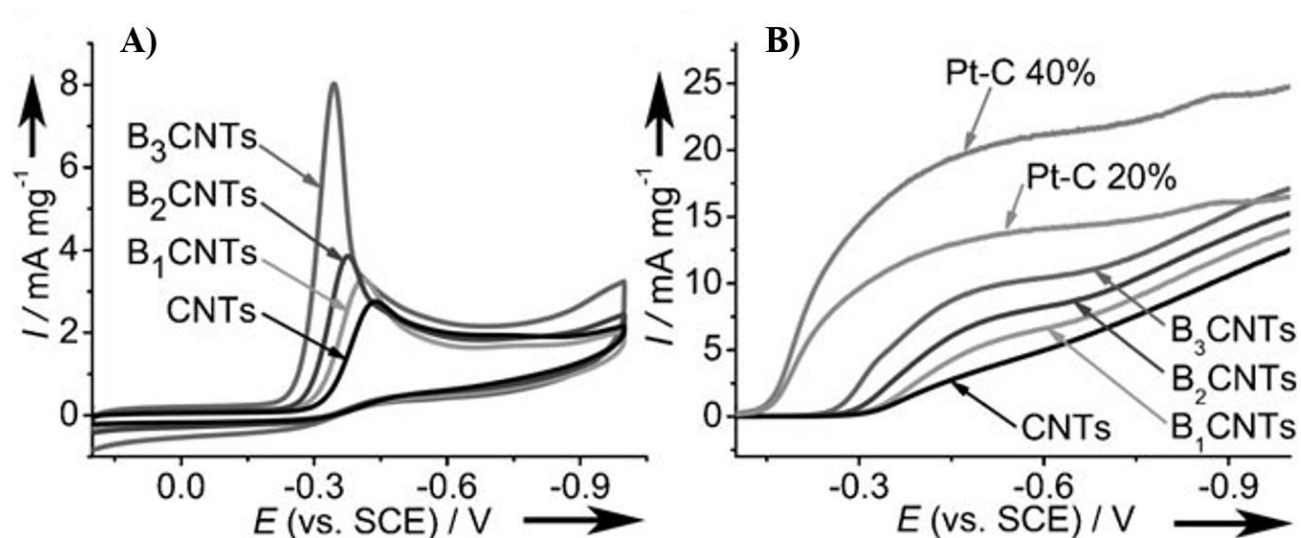


Figure 1.24: ORR Electrocatalytic activities of B-CNTs in O<sub>2</sub>-saturated 1M NaOH electrolyte. A) CV curves at scan rate of 50 mVs<sup>-1</sup>. B) RDE voltammetry at 2500 rpm and scan rate of 10 mVs<sup>-1</sup>. For comparison, corresponding examinations for CNTs and commercial Pt/C catalysts (20 and 40 wt% Pt loading) are shown. B<sub>1</sub>CNT, B<sub>2</sub>CNT and B<sub>3</sub>CNT exhibit different B content (0.86, 1.33 and 2.24 at%, respectively). Adapted with permission from [156].

Remarkable results have been reported also for the B-doping of graphene. In particular, Sheng *et al.* introduced B dopants into the graphitic structure through thermal annealing at 1200 °C under inert atmosphere (i.e. Ar) of graphene oxide (GO) by using boric acid as precursor. The ORR activity of the B-doped GO, showing a B content of 3.2%, was investigated in alkaline condition and compared to pristine graphene and Pt/C catalysts. The doped catalysts showed enhanced catalytic performance to that of graphene via a four-electron reduction pathway, similarly to Pt/C. In addition, no poisoning effects from methanol nor CO were observed for the doped samples along with an higher operational stability [157].

Several other heteroatoms such as S [158, 159], P [160] and halogens (I, Cl and Br) [161, 162] have been introduced in CNMs with outstanding results in enhancing the ORR performance. Different explanations have been reported for the increased ORR features. Due to the larger size and lower  $\chi$ , the presence of P promotes the creation of active ORR sites; the same charge delocalization induces the enhanced catalytic performance of CNMs doped with halogens [149]. On the contrary, in the case of S, being  $\chi$  comparable with that of C (2.58 vs 2.55), the intramolecular charge transfer induced by S is negligible and the improvement is related to an electron spin redistribution [159].

Furthermore, codoping strategies have shown to be an efficient way to improve the ORR activity of CNMs with even better results from those obtained by single atom doping.

In 2011, Wang *et al.* reported the first codoping approach of CNMs with boron and nitrogen atoms. The synthesis of codoped VA-CNTs was achieved by pyrolysis of melamine diborate and the activity towards ORR was investigated in comparison with N- and B-VA-CNTs. The improved catalytic performance (i.e. more positive onset and larger current density) in alkaline medium was correlated to the synergistic effect of the dopants in the structure as a consequence of charge redistribution induced by the electronegativity difference between B, N and C [163]. The following year, the same group achieved the same codoping on graphene via thermal annealing of a mixture of graphene oxide and boric acid under ammonia atmosphere, showing better ORR activity compared to Pt/C. The improved performance were attributed through DFT calculations to the lowering of the energy bandgap and to the higher charge and spin densities [164].

Several combinations of binary [165-168] and even ternary [169, 170] doped carbon structure have been reported in the last years, confirming that the doping of CNMs is a relevant and effective strategy to enhance the poor intrinsic activity of carbon nanomaterials towards ORR.

In contrast to other CNMs, heteroatom-doping approaches of carbon nano-onions have been only recently proposed; furthermore, very few investigations reporting the doping for possible applications as ORR catalysts have been reported.



CNOs are an attractive material for electrochemical applications due to their small size and large surface area, which results to a high number of catalytic active sites. In addition, the high curvature confers high reactivity to the structure, opening the way for simple chemical modification. Furthermore, from the cost point of view, CNOs can be synthesized in large scale with low cost and high purity, making them an inexpensive alternative to the Pt-based electrodes.

In the following section, the-state-of-the-art regarding doped CNOs and their electrocatalytic activity towards ORR will be discussed.

### 1.4.3 Carbon nano-onions as ORR catalyst

Heteroatom-doping, as discussed in the previous paragraph, is an efficient way to modify the physico-chemical properties of CNMs and thus opening the way to possible new applicative uses. CNO doping has been only recently proposed as strategy to improve their electrochemical performance.

After that Xu *et al.* showed that CNOs exhibited remarkable properties as support for Pt nanoparticles (NPs) for the electro-oxidation of methanol [110], a number of investigations regarding the use of CNOs in electrocatalysis have been performed. In 2010, Wu and co-workers reported the use of N-doped magnetic CNOs as supporting material for Pt NPs. The catalysts, synthesized through the pyrolysis of a hexamethylene diamine-metal complex and the following immobilization of Pt (2 wt%), showed enhanced catalytic performance towards ORR compared to the standard Pt/C catalyst. This was ascribed to synergistic effect of both nitrogen and metallic (i.e. Co or Fe) species, acting as new active sites, and to the better dispersion of Pt onto the support [171]. Further investigations on N-doped CNO/transition metals composites showed their potentialities as non-precious catalysts for ORR [172] and dye-sensitized solar cells [173].

The first report on a metal-free N-doped CNO-based catalyst was published in 2014 by Lin and co-workers. The doping was achieved via thermal annealing of oxidized CNOs, obtained through nitric acid treatment of ND-derived CNOs, under ammonia atmosphere. Interestingly, a tunable N content (from 2.06 to 3.95 at. %) was achieved by changing the annealing temperature. The doped materials showed remarkable catalytic properties towards the epoxidation of styrene to styrene oxide, even higher than that of common catalysts, with excellent conversion and selectivity [174]. The same material was applied for the oxygen electrode reaction in Li-O<sub>2</sub> battery, showing superior performance in terms of capacity, stability and high round-trip efficiency [175].

Mykhailiv *et al.* reported an interesting *in-situ* doping approach of CNO, where thermal annealing of aminated-NDs was exploited to synthesize N-doped CNOs. The CNO catalyst was tested for the enzymatic-free detection of hydrogen peroxide by cyclic voltammetry in phosphate buffer solution. The results showed higher electroactivity of the doped material compared to the pristine CNOs with

a lower reduction overpotential; in addition, a linear response between the reduction current and the hydrogen peroxide concentration was observed [176].

Nitrogen-doped CNOs were only recently investigated for ORR. In 2017, Choi *et al.* synthesized p-CNOs via thermal annealing of DNDs followed by oxidation by Hummers method to yield oxi-CNOs; the doping was finally achieved via pyrolysis method in the presence of urea, producing N-CNOs. The doping content was controlled by changing the oxidation time and thus the oxygen content of oxidized CNOs with the highest content obtained after 6h of oxidation (N = 3.09%). The N-CNOs were tested in alkaline medium, showing improved ORR catalytic activity (i.e. higher onset potential and current density) than p- and oxi-CNOs (Figure 1.25A); compared to the Pt/C catalysts, the ORR activity was lower but with a longer stability and better resistance to methanol crossover [177].

The same synthetic procedure was used by Zhang and co-workers to produce doped-CNOs with the only exception of the oxidation procedure (in this case, a nitric acid treatment was performed). The catalytic performance was investigated in comparison to p-, oxi-CNOs and Pt/C in 0.1 KOH. Polarization curves showed more positive onset potential and large current density for N-CNOs than the other CNO derivatives (Figure 1.25B) via a quasi-ideal four-electron transfer pathway ( $n = 3.8$ ) with low production of peroxide species (around 10%). In addition, N-CNOs showed enhanced long-term durability and good tolerance to methanol. The enhanced ORR performance was attributed to the large amount of pyridinic and graphitic N atoms in the sample [178].

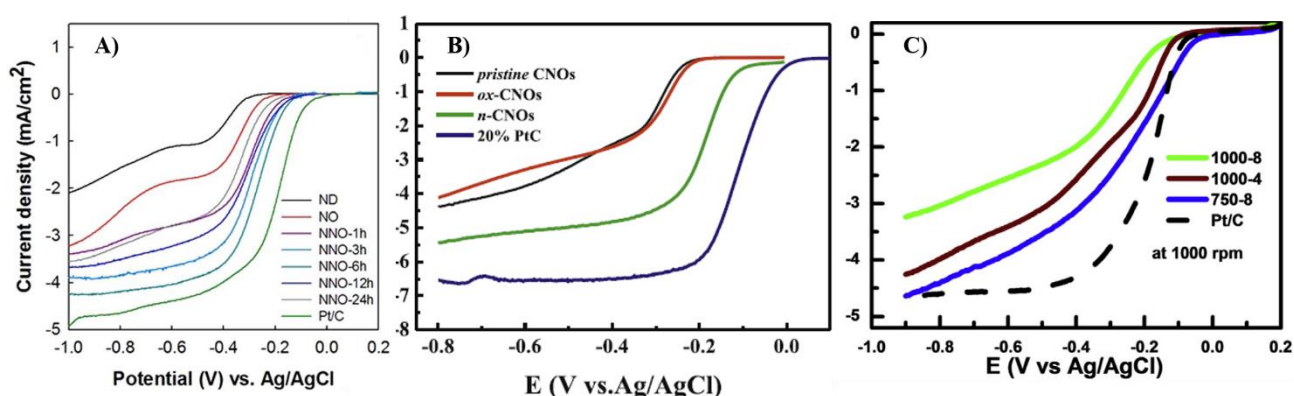


Figure 1.25: A) LSV curves of the ND, oxi- and N-CNOs (at different oxidation time) and Pt/C. B) LSV curves of p-, oxi- and, N-CNOs in comparison with 20% Pt/C at 1600 rpm. C) RDE polarization curves derived from three different heat treated samples and commercial Pt/C catalyst. Adapted with permission from [177], [178] and [179].

An interesting and direct N-doping of CNOs was achieved by Chatterjee *et al.* by pyrolysis of collagen waste source as N precursor at different temperature (750 °C for 4 h and 1000 °C for 4 and 8 h). The particles showed an onion-like structure with a tunable N content from 7.5 to 3.1%. The ORR activity was investigated in alkaline medium, showing superior activity for the sample annealed at 750 °C in terms of onset potential and current density compared to the other CNO conjugates (Figure 1.25C). RRDE analyses showed an electron transfer number ranging from 3.5 to 3.7 and a



hydrogen peroxide production between 20-30%, suggesting a predominant four-electron pathway. Enhanced ORR performance was observed compared to Pt/C catalyst, showing more positive onset potential, higher stability and excellent methanol crossover tolerance; the remarkable catalytic activity was attributed to the extensive presence of pyridinic N species and the large surface areas of N-CNOs [179].

Other heteroatoms such as B and P have been successfully introduced in the CNO structure; however, their use as electrocatalysts for ORR has been investigated to a very small extent.

The first B-doping of CNOs was proposed by Lin *et al.* in 2015 via thermal annealing of DNDs in the presence of boric acid and the as-produced material was tested as catalyst for the nitroarene hydrogenation. The results showed excellent catalytic activity compared to the pristine catalyst with a conversion of nitrobenzene over 80% and remarkable reduction selectivity to aniline of 97% [180]. The same group performed a systematic investigation in order to correlate the tunable B content and the annealing temperature with the corresponding ORR activity. For this purpose, a mixture of DNDs and 5 wt% boric acid was annealed at different T (1500, 1800, 2100 and 2400 °C). XPS analyses showed a decrease in the B content (from 1 to 0.63 at%) while increasing the annealing temperature; furthermore, the sample annealed at 1500 °C exhibited the highest amount of substitutional B species ( $\text{BC}_3$ ), which is reported to be the highest ORR active sites [165, 181]. For this reason, this temperature was chosen as optimum. In second instance, the percentage of boric acid was increased to 10 and 20 wt% and the mixture annealed at 1500 °C, leading to an increase of the B content (from 1 to 4.57%). The doped-CNOs were tested for ORR in alkaline environment and showed good ORR activity via a four-electron pathway for the oxygen reduction (similar to Pt/C), in contrast to the two-electron route for the pristine samples. Interestingly, the sample with 10 wt% of boric acid showed the most positive onset potential and highest current density among the different B-CNOs with a  $n$  value equal to 3.95 (close to the Pt/C value of 3.97) (Figure 1.26A).

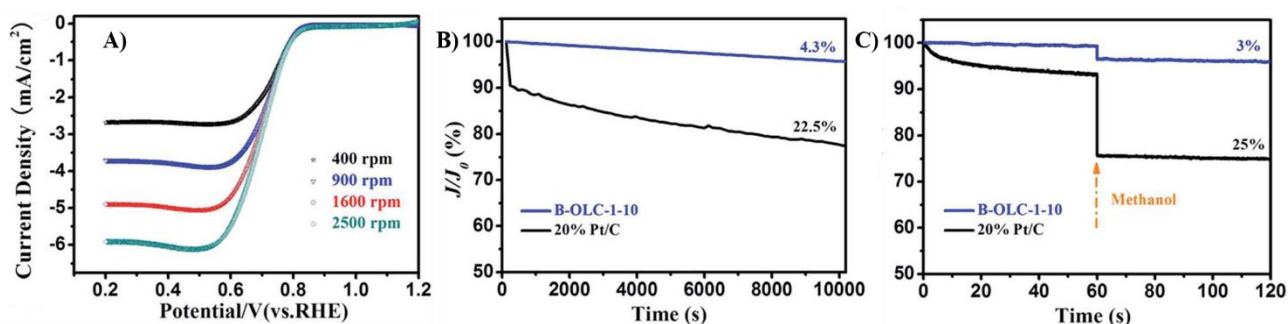


Figure 1.26: ORR investigation of B-CNOs produced by annealing at 1500 °C with 10 wt% of boric acid (B-OLC-1-10). A) LSV curves at rotation rate from 400 to 2500 rpm and at scan rate of  $5 \text{ mV}/\text{s}^{-1}$ . B) Durability evaluation for 10 000 s at 0.6 V and a rotation rate of 900 rpm compared to Pt/C. C) Chronoamperometric responses with 3 M methanol added into an  $\text{O}_2$ -saturated KOH electrolyte at a constant potential of 0.6 V with a rotation rate of 900 rpm and compared to Pt/C. Adapted with permission from [182].

In addition, higher stability and tolerance to methanol to that of Pt/C was observed (Figure 1.26B-C), even if with an more negative onset potential [182]. The potentialities of thermal annealing as efficient way to introduce B dopants in the CNO structure have been demonstrated in other works, with interesting results of the doped material for electrochemical energy storage [183] and as bi-functional catalysts in sodium–oxygen batteries [184].

Besides B and N, the influence of P doping to the ORR activity of CNOs have been investigated by Sun *et al.*, who synthesized P-doped CNOs (P-CNOs) through a post-synthesis treatment of ND-derived CNOs. Firstly, p-CNOs were oxidized in concentrated nitric acid and then doped following two different approaches. In the first, oxi-CNOs were impregnated with different amounts of phosphate and calcinated at 700 °C ( $\text{Ph}_x\text{-CNOs}$ ,  $x = 5, 10, 20$  and 30 wt%). The second approach involves a CVD process at 700 °C with triphenylphosphine (TPP) as P source (TPP-CNOs). XPS analyses showed the presence of C-O-P bonds in the first catalyst (their amount increases with the increase of the phosphate loading) and the additional presence of C-P bonds in the second one. The ORR investigation of the different P-CNOs was performed in alkaline solution. TPP-CNOs showed very poor ORR activity, suggesting that the C-P bonding state is not an ORR active site; this is furthermore confirmed by the  $\text{Ph}_{30}\text{-CNO}$  samples, which shows good performance even if exhibits the same amount of C-P bonds, suggesting thus the ORR activity of C-O-P bonds (Figure 1.27A).

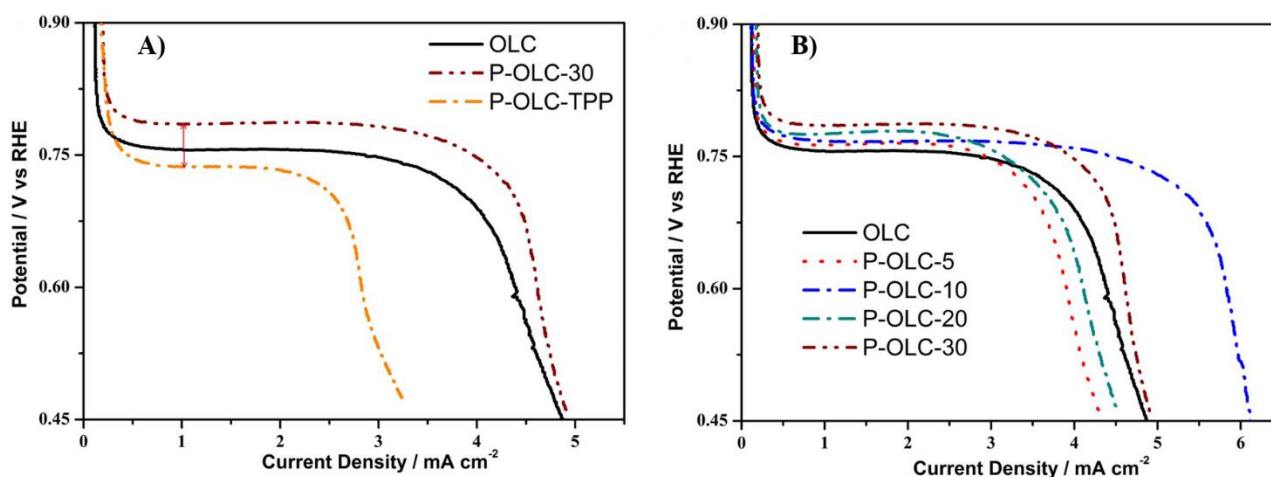


Figure 1.27: A) ORR activities of p-,  $\text{Ph}_{30}$ - and TPP-CNOs in a 0.1 M KOH electrolyte at 2500 rpm and 10  $\text{mV/s}^{-1}$  as scan rate. B) ORR activity of all  $\text{Ph}_x\text{-CNOs}$ . Adapted with permission from [185].

Regarding the  $\text{Ph}_x\text{-CNO}$  samples, the ORR activity increases as the P content increases, with the higher current density for  $\text{Ph}_{10}\text{-CNOs}$  (Figure 1.27B); in addition, all the P-CNOs showed good long-term stability. Finally, ultraviolet photoelectron spectroscopy (UPS) showed that the work function linearly increases by increasing the C-O-P bonding states with the lowest value for TPP-CNOs. This further confirms that C-O-P bonds may be beneficial for ORR, stabilizing the OOH species in the reduction process [185].

As discussed below, CNOs have been only recently investigated for ORR. Doping strategies to introduce heteroatoms such as N, B or P have shown to be an efficient way to improve the electrocatalytic performance in alkaline electrolytes. In addition, multi-atom doping has shown to further increase the activity of CNMs. However, this kind of approaches have not been yet reported for CNOs.

## 1.5 References

- [1] Kroto, H.W.; Heath, J.R.; O'Brien, S.C.; Curl, R.F.; Smalley, R.E., C60: Buckminsterfullerene. *Nature*, **1985**, *318*, 162-163.
- [2] Delgado, J.L.; Herranz, M.; Martín, N., The nano-forms of carbon. *J. Mater. Chem.*, **2008**, *18*, (13), 1417.
- [3] Dresselhaus, M.S.; Dresselhaus, G.; Eklund, P.C., Fullerenes. *J. Mater. Res.*, **2011**, *8*, (08), 2054-2097.
- [4] W. Krätschmer, L.D.L., K. Fostiropoulos & Donald R. Huffman, Solid C60: a new form of carbon. *Nature*, **1990**, *347*, 354-358.
- [5] Iijima, S., Helical microtubules of graphitic carbon. *Nature*, **1991**, *354*, 56-58.
- [6] Iijima, S.; Ichihashi, T., Single-shell carbon nanotubes of 1-nm diameter. *Nature*, **1993**, *363*, 603 - 605.
- [7] D. S. Bethune, C.H.K., M. S. de Vries, G. Gorman, R. Savoy, J. Vazquez & R. Beyers, Cobalt-catalysed growth of carbon nanotubes with single-atomic-layer walls. *Nature*, **1993**, *363*, 605-607.
- [8] Ajayan, P.M., Nanotubes from Carbon. *Chem. Rev.*, **1999**, *99*, (7), 1787-1800.
- [9] Ugarte, D., Curling and closure of graphitic networks under electron-beam irradiation. *Nature*, **1992**, *359*, 707-709.
- [10] Novoselov, K.S.; Geim, A.K.; Morozov, S.V.; Jiang, D.; Zhang, Y.; Dubonos, S.V.; Grigorieva, I.V.; Firsov, A.A., Electric field effect in atomically thin carbon films. *Science*, **2004**, *306*, (5696), 666-669.
- [11] Geim, A.K.; Novoselov, K.S., The rise of graphene. *Nat. Mater.*, **2007**, *6*, 183 - 191.
- [12] Danilenko, V.V., On the History of the Discovery of Nanodiamond Synthesis. *Phys. Solid State*, **2004**, *46*, (4), 595-599.
- [13] Mochalin, V.N.; Shenderova, O.; Ho, D.; Gogotsi, Y., The properties and applications of nanodiamonds. *Nat. Nanotechnol.*, **2011**, *7*, (1), 11-23.
- [14] Ugarte, D., Onion-Like graphitic particles. *Carbon*, **1995**, *33*, 989-993.
- [15] Camisasca, A.; Giordani, S., Carbon nano-onions in biomedical applications: Promising theranostic agents. *Inorg. Chim. Acta*, **2017**, *468*, 67-76.
- [16] Mykhailiv, O.; Zubyk, H.; Plonska-Brzezinska, M.E., Carbon nano-onions: Unique carbon nanostructures with fascinating properties and their potential applications. *Inorganica Chimica Acta*, **2017**, *468*, 49-66.
- [17] Zeiger, M.; Jäckel, N.; Mochalin, V.N.; Presser, V., Review: carbon onions for electrochemical energy storage. *J. Mater. Chem. A*, **2016**, *4*, (9), 3172-3196.
- [18] Tomita, S.; Burian, A.; Dore, J.C.; LeBolloch, D.; Fujii, M.; Shinji, H., Diamond nanoparticles to carbon onions transformation: X-ray diffraction studies. *Carbon*, **2002**, *40*, 1469-1474.
- [19] Terrones, H.; Terrones, M., The Transformation of Polyhedral Particles into Graphitic Onions. *J. Phys. Chem. Solids*, **1997**, *58*, (11), 1789-1796.
- [20] Kevin R. Bates; Scuseria, G.E., Why are buckyonions round? *Theor. Chem. Acc.*, **1998**, *99*, 29-33.
- [21] Palkar, A.; Melin, F.; Cardona, C.M.; Elliott, B.; Naskar, A.K.; Edie, D.D.; Kumbhar, A.; Echegoyen, L., Reactivity differences between carbon nano onions (CNOs) prepared by different methods. *Chem. Asian J.*, **2007**, *2*, (5), 625-633.
- [22] Iijima, S., Direct observation of the tetrahedral bonding in graphitized carbon black by high resolution electron microscopy. *J. Cryst. Growth*, **1980**, *50*, 675-683.
- [23] Xu, B.S.; Tanaka, S.-I., Formation of giant onion-like fullerenes under Al nanoparticles by electron irradiation. *Acta Mater.*, **1998**, *46*, (15), 5249-5257.
- [24] Alekseyev, N.I.; Dyuzhev, G.A., Fullerene formation in an arc discharge. *Carbon*, **2003**, *41*, (7), 1343-1348.
- [25] Sano, N.; Wang, H.; Chhowalla, M.; Alexandrou, I.; Amaratunga, G.A.J., Synthesis of carbon 'onions' in water. *Nature*, **2001**, *414*, 506-507.

- [26] Sano, N.; Wang, H.; Alexandrou, I.; Chhowalla, M.; Teo, K.B.K.; Amaratunga, G.A.J.; Iimura, K., Properties of carbon onions produced by an arc discharge in water. *J. Appl. Phys.*, **2002**, 92, (5), 2783-2788.
- [27] Borgohain, R.; Yang, J.; Selegue, J.P.; Kim, D.Y., Controlled synthesis, efficient purification, and electrochemical characterization of arc-discharge carbon nano-onions. *Carbon*, **2014**, 66, 272-284.
- [28] Tomita, S.; Sakurai, T.; Ohta, H.; Fujii, M.; Hayashi, S., Structure and electronic properties of carbon onions. *J. Chem. Phys.*, **2001**, 114, (17), 7477-7482.
- [29] Kuznetsov, V.L.; Chuvilin, A.L.; Butenko, Y.V.; Mal'kov, I.Y.; Titov, V.M., Onion-like carbon from ultra-disperse diamond. *Chem. Phys. Lett.*, **1994**, 222, 343-348.
- [30] Kuznetsov, V.L.; Zilberberg, I.L.; Butenko, Y.V.; Chuvilin, A.L.; Segall, B., Theoretical study of the formation of closed curved graphite-like structures during annealing of diamond surface. *J. Appl. Phys.*, **1999**, 86, (2), 863-870.
- [31] Zou, Q.; Wang, M.; Li, Y.; Zhao, Y.; Zou, L., Fabrication of onion-like carbon from nanodiamond by annealing. *Sci. China Ser. E-Tech. Sci.*, **2009**, 52, (12), 3683-3689.
- [32] Butenko, Y.V.; Šiller, L.; Hunt, M.R.C. *Carbon Onions*, **2013**.
- [33] Butenko, Y.V.; Kuznetsov, V.L.; Paukshtis, E.A.; Stadnichenko, A.I.; Mazov, I.N.; Moseenkov, S.I.; Boronin, A.I.; Kosheev, S.V., The Thermal Stability of Nanodiamond Surface Groups and Onset of Nanodiamond Graphitization. *Fuller. Nanotub. Car. N.*, **2006**, 14, (2-3), 557-564.
- [34] Obratsova, E.D.; Fujii, M.; Hayashi, S.; Kuznetsov, V.L.; Butenko, Y.V.; Chuvilin', A.L., Raman identification of onion-like carbon. *Carbon*, **1998**, 36, (5-6), 821-826.
- [35] Chen, J.; Deng, S.Z.; Chen, J.; Yu, Z.X.; Xu, N.S., Graphitization of nanodiamond powder annealed in argon ambient. *Appl. Phys. Lett.*, **1999**, 74, (24), 3651-3653.
- [36] Xie, F.Y.; Xie, W.G.; Gong, L.; Zhang, W.H.; Chen, S.H.; Zhang, Q.Z.; Chen, J., Surface characterization on graphitization of nanodiamond powder annealed in nitrogen ambient. *Surf. Interface Anal.*, **2010**, 42, (9), 1514-1518.
- [37] Aleksenski, A.E.; Baĭdakova, M.V.; Vul', A.Y.; Dideĭkin, A.T.; Siklitskiĭ, V.I.; Vul', S.P., Effect of Hydrogen on the Structure of Ultradisperse Diamond. *Phys. Solid State*, **2000**, 42, (8), 1575-1578.
- [38] Mykhailiv, O.; Lapinski, A.; Molina-Ontoria, A.; Regulaska, E.; Echegoyen, L.; Dubis, A.T.; Plonska-Brzezinska, M.E., Influence of the Synthetic Conditions on the Structural and Electrochemical Properties of Carbon Nano-Onions. *Chem. Phys. Chem.*, **2015**, 16, (10), 2182-2191.
- [39] Tomita, S.; Fujii, M.; Hayashi, S.; Yamamoto, K., Electron energy-loss spectroscopy of carbon onions. *Chem. Phys. Lett.*, **1999**, 305, 225-229.
- [40] Bogdanov, K.; Fedorov, A.; Osipov, V.; Enoki, T.; Takai, K.; Hayashi, T.; Ermakov, V.; Moshkalev, S.; Baranov, A., Annealing-induced structural changes of carbon onions: High-resolution transmission electron microscopy and Raman studies. *Carbon*, **2014**, 73, 78-86.
- [41] Zeiger, M.; Jäckel, N.; Weingarth, D.; Presser, V., Vacuum or flowing argon: What is the best synthesis atmosphere for nanodiamond-derived carbon onions for supercapacitor electrodes? *Carbon*, **2015**, 94, 507-517.
- [42] Zheng, Y.; Zhu, P., Carbon nano-onions: large-scale preparation, functionalization and their application as anode material for rechargeable lithium ion batteries. *RSC Adv.*, **2016**, 6, (95), 92285-92298.
- [43] Zhao, N.; Cui, Q.; He, C.; Shi, C.; Li, J.; Li, H.; Du, X., Synthesis of carbon nanostructures with different morphologies by CVD of methane. *Mater. Sci. Eng. A*, **2007**, 460-461, 255-260.
- [44] He, C.N.; Tian, F.; Liu, S.J.; Du, Z.J.; Liu, C.J.; Li, F.; Chen, S.Q., Characterization and magnetic property of carbon coated metal nanoparticles and hollow carbon onions fabricated by CVD of methane. *Mater. Lett.*, **2008**, 62, (21-22), 3697-3699.

- [45] Yang, Y.; Liu, X.; Guo, X.; Wen, H.; Xu, B., Synthesis of nano onion-like fullerenes by chemical vapor deposition using an iron catalyst supported on sodium chloride. *J. Nanopart. Res.*, **2010**, *13*, (5), 1979-1986.
- [46] He, C.N.; Zhao, N.; Du, X.; Shi, C.; Ding, J.; Li, J.; Li, Y., Low-temperature synthesis of carbon onions by chemical vapor deposition using a nickel catalyst supported on aluminum. *Scripta Mater.*, **2006**, *54*, (4), 689-693.
- [47] He, C.N.; Zhao, N.; Shi, C.; Du, X.; Li, J., Carbon nanotubes and onions from methane decomposition using Ni/Al catalysts. *Mater. Chem. Phys.*, **2006**, *97*, (1), 109-115.
- [48] Chen, X.H.; Deng, F.M.; Wang, J.X.; Yang, H.S.; Wu, G.T.; Zhang, X.B.; Peng, J.C.; Li, W.Z., New method of carbon onion growth by radio-frequency plasma-enhanced chemical vapor deposition. *Chem. Phys. Lett.*, **2001**, *336*, 201-204.
- [49] Du, A.B.; Liu, X.G.; Fu, D.J.; Han, P.D.; Xu, B.S., Onion-like fullerenes synthesis from coal. *Fuel*, **2007**, *86*, (1-2), 294-298.
- [50] Huang, J.Y.; Yasuda, H.; Mori, H., Highly curved carbon nanostructures produced by ball-milling. *Chem. Phys. Lett.*, **1999**, *303*, (1), 130-134.
- [51] Chen, X.H.; Yang, H.S.; Wu, G.T.; Wang, M.; Deng, F.M.; Zhang, X.B.; Peng, J.C.; Li, W.Z., Generation of curved or closed-shell carbon nanostructures by ball-milling of graphite. *J. Cryst. Growth*, **2000**, *218*, (1), 57-61.
- [52] Cabioc'h, T.; Riviere, J.P.; Delafond, J., A new technique for fullerene onion formation. *J. Mater. Sci.*, **1995**, *30*, (19), 4787-4792.
- [53] Cabioc'h, T.; Jaouen, M.; Thune, E.; Gu'erin, P.; Fayoux, C.; Denanot, M.F., Carbon onions formation by high-dose carbon ion implantation into copper and silver. *Surf. Coat. Technol.*, **2000**, *128*, 43-50.
- [54] Dorobantu, D.; Bota, P.M.; Boerasu, I.; Bojin, D.; Enachescu, M., Pulse laser ablation system for carbon nano-onions fabrication. *Surface Engineering and Applied Electrochemistry*, **2014**, *50*, (5), 390-394.
- [55] Bystrzejewski, M.; Rummeli, M.H.; Gemming, T.; Lange, H.; Huczko, A., Catalyst-free synthesis of onion-like carbon nanoparticles. *New Carbon Materials*, **2010**, *25*, (1), 1-8.
- [56] Choucair, M.; Stride, J.A., The gram-scale synthesis of carbon onions. *Carbon*, **2012**, *50*, (3), 1109-1115.
- [57] Du, J.; Liu, Z.; Li, Z.; Han, B.; Sun, Z.; Huang, Y., Carbon onions synthesized via thermal reduction of glycerin with magnesium. *Mater. Chem. Phys.*, **2005**, *93*, (1), 178-180.
- [58] Hou, S.-S.; Chung, D.-H.; Lin, T.-H., High-yield synthesis of carbon nano-onions in counterflow diffusion flames. *Carbon*, **2009**, *47*, (4), 938-947.
- [59] Yan, Y.; Yang, H.; Zhang, F.; Tu, B.; Zhao, D., Low-temperature solution synthesis of carbon nanoparticles, onions and nanoropes by the assembly of aromatic molecules. *Carbon*, **2007**, *45*, (11), 2209-2216.
- [60] Kobayashi, T.; Sekine, T.; He, H., Formation of Carbon Onion from Heavily Shocked SiC. *Chem. Mater.*, **2003**, *15*, 2681-2683.
- [61] Ghosh, M.; Sonkar, S.K.; Saxena, M.; Sarkar, S., Carbon nano-onions for imaging the life cycle of *Drosophila melanogaster*. *Small*, **2011**, *7*, (22), 3170-3177.
- [62] Sonkar, S.K.; Roy, M.; Babar, D.G.; Sarkar, S., Water soluble carbon nano-onions from wood wool as growth promoters for gram plants. *Nanoscale*, **2012**, *4*, (24), 7670-7675.
- [63] Sonkar, S.K.; Ghosh, M.; Roy, M.; Begum, A.; Sarkar, S., Carbon Nano-Onions as Nontoxic and High-Fluorescence Bioimaging Agent in Food Chain—An In Vivo Study from Unicellular *E. coli* to Multicellular *C. elegans*. *Mater. Express*, **2012**, *2*, (2), 105-114.
- [64] Dubey, P.; Tripathi, K.M.; Sonkar, S.K., Gram scale synthesis of green fluorescent water-soluble onion-like carbon nanoparticles from camphor and polystyrene foam. *RSC Adv.*, **2014**, *4*, (12), 5838.
- [65] Bartelmeß, J.; Giordani, S., Carbon nano-onions (multi-layer fullerenes): chemistry and applications. *Beilstein J. Nanotechnol.*, **2014**, *5*, 1980-1998.

- [66] Georgakilas, V.; Guldi, D.M.; Signorini, R.; Bozio, R.; Prato, M., Organic Functionalization and Optical Properties of Carbon Onions. *J. Am. Chem. Soc.*, **2003**, *125* (47), 14268-14269.
- [67] Rettenbacher, A.S.; Elliott, B.; Hudson, J.S.; Amirkhanian, A.; Echegoyen, L., Preparation and functionalization of multilayer fullerenes (carbon nano-onions). *Chem. Eur. J.*, **2005**, *12*, (2), 376-387.
- [68] Liu, Y.; Vander Wal, R.L.; Khabashesku, V.N., Functionalization of Carbon Nano-onions by Direct Fluorination. *Chem. Mater.*, **2007**, *19*, 778-786.
- [69] Kuznetsov, O.V.; Pulikkathara, M.X.; Lobo, R.F.M.; Khabasheskua, V.N., Solubilization of carbon nanoparticles, nanotubes, nano-onions, and nanodiamonds through covalent functionalization with sucrose. *Russian Chemical Bulletin*, **2010**, *59*, (8), 1495-1505.
- [70] Palkar, A.; Kumbhar, A.; Athans, A.J.; Echegoyen, L., Pyridyl-Functionalized and Water-Soluble Carbon Nano Onions: First Supramolecular Complexes of Carbon Nano Onions. *Chemistry of Materials*, **2008**, *20*, (5), 1685-1687.
- [71] Flavin, K.; Chaur, M.N.; Echegoyen, L.; Giordani, S., Functionalization of Multilayer Fullerenes (Carbon Nano-Onions) using Diazonium Compounds and "Click" Chemistry. *Org. Lett.*, **2009**, *12*, (4), 840-843.
- [72] Spampinato, V.; Ceccone, G.; Giordani, S., Surface analysis of zinc-porphyrin functionalized carbon nano-onions. *Biointerphases*, **2015**, *10*, (1), 019006.
- [73] Yang, M.; Flavin, K.; Kopf, I.; Radics, G.; Hearnden, C.H.; McManus, G.J.; Moran, B.; Villalta-Cerdas, A.; Echegoyen, L.A.; Giordani, S.; Lavelle, E.C., Functionalization of carbon nanoparticles modulates inflammatory cell recruitment and NLRP3 inflammasome activation. *Small*, **2013**, *9*, (24), 4194-4206.
- [74] Giordani, S.; Bartelmess, J.; Frasconi, M.; Biondi, I.; Cheung, S.; Grossi, M.; Wu, D.; Echegoyen, L.; O'Shea, D.F., NIR fluorescence labelled carbon nano-onions: synthesis, analysis and cellular imaging. *J. Mater. Chem. B*, **2014**, *2*, (42), 7459-7463.
- [75] Bartelmess, J.; De Luca, E.; Signorelli, A.; Baldrighi, M.; Becce, M.; Brescia, R.; Nardone, V.; Parisini, E.; Echegoyen, L.; Pompa, P.P.; Giordani, S., Boron dipyrromethene (BODIPY) functionalized carbon nano-onions for high resolution cellular imaging. *Nanoscale*, **2014**, *6*, (22), 13761-13769.
- [76] Frasconi, M.; Maffei, V.; Bartelmess, J.; Echegoyen, L.; Giordani, S., Highly surface functionalized carbon nano-onions for bright light bioimaging. *Methods Appl. Fluoresc.*, **2015**, *3*, (4), 044005.
- [77] Plonska-Brzezinska, M.E.; Lapinski, A.; Wilczewska, A.Z.; Dubis, A.T.; Villalta-Cerdas, A.; Winkler, K.; Echegoyen, L., The synthesis and characterization of carbon nano-onions produced by solution ozonolysis. *Carbon*, **2011**, *49*, (15), 5079-5089.
- [78] Molina-Ontoria, A.; Chaur, M.N.; Plonska-Brzezinska, M.E.; Echegoyen, L., Preparation and characterization of soluble carbon nano-onions by covalent functionalization, employing a Na-K alloy. *Chem. Commun.*, **2013**, *49*, (24), 2406-2408.
- [79] Cioffi, C.T.; Palkar, A.; Melin, F.; Kumbhar, A.; Echegoyen, L.; Melle-Franco, M.; Zerbetto, F.; Rahman, G.M.A.; Ehli, C.; Sgobba, V.; Guldi, D.M.; Prato, M., A Carbon Nano-Onion–Ferrocene Donor–Acceptor System: Synthesis, Characterization and Properties. *Chemistry – A European Journal*, **2009**, *15*, (17), 4419-4427.
- [80] Zhou, L.; Gao, C.; Zhu, D.; Xu, W.; Chen, F.F.; Palkar, A.; Echegoyen, L.; Kong, E.S.-W., Facile Functionalization of Multilayer Fullerenes (Carbon Nano-Onions) by Nitrene Chemistry and "Grafting from" Strategy. *Chemistry – A European Journal*, **2009**, *15*, (6), 1389-1396.
- [81] Rettenbacher, A.S.; Perpall, M.W.; Echegoyen, L.; Hudson, J.; Smith, D.W., Radical Addition of a Conjugated Polymer to Multilayer Fullerenes (Carbon Nano-onions). *Chemistry of Materials*, **2007**, *19*, (6), 1411-1417.
- [82] Luszczyn, J.; Plonska-Brzezinska, M.E.; Palkar, A.; Dubis, A.T.; Simionescu, A.; Simionescu, D.T.; Kalska-Szostko, B.; Winkler, K.; Echegoyen, L., Small noncytotoxic carbon nano-onions: first covalent functionalization with biomolecules. *Chem. Eur. J.*, **2010**, *16*, (16), 4870-4880.

- [83] Bartelmeß, J.; Frascioni, M.; Balakrishnan, P.B.; Signorelli, A.; Echegoyen, L.; Pellegrino, T.; Giordani, S., Non-covalent functionalization of carbon nano-onions with pyrene–BODIPY dyads for biological imaging. *RSC Adv.*, **2015**, 5, (62), 50253–50258.
- [84] Baptista, F.R.; Belhout, S.A.; Giordani, S.; Quinn, S.J., Recent developments in carbon nanomaterial sensors. *Chem. Soc. Rev.*, **2015**, 44, (13), 4433–4453.
- [85] Bartolome, J.P.; Echegoyen, L.; Fragoso, A., Reactive Carbon Nano-Onion Modified Glassy Carbon Surfaces as DNA Sensors for Human Papillomavirus Oncogene Detection with Enhanced Sensitivity. *Anal. Chem.*, **2015**, 87, (13), 6744–6751.
- [86] Mohapatra, J.; Ananthoju, B.; Nair, V.; Mitra, A.; Bahadur, D.; Medhekar, N.V.; Aslam, M., Enzymatic and non-enzymatic electrochemical glucose sensor based on carbon nano-onions. *Applied Surface Science*, **2018**, 442, 332–341.
- [87] Tripathi, K.M.; Bhati, A.; Singh, A.; Gupta, N.R.; Verma, S.; Sarkar, S.; Sonkar, S.K., From the traditional way of pyrolysis to tunable photoluminescent water soluble carbon nano-onions for cell imaging and selective sensing of glucose. *RSC Adv.*, **2016**, 6, (44), 37319–37329.
- [88] Singh, V., Natural source derived carbon nano-onions as electrode material for sensing applications. *Diamond and Related Materials*, **2018**, 87, 202–207.
- [89] Sok, V.; Fragoso, A., Preparation and characterization of alkaline phosphatase, horseradish peroxidase, and glucose oxidase conjugates with carboxylated carbon nano-onions. *Prep Biochem Biotechnol*, **2018**, 48, (2), 136–143.
- [90] Breczko, J.; Plonska-Brzezinska, M.E.; Echegoyen, L., Electrochemical oxidation and determination of dopamine in the presence of uric and ascorbic acids using a carbon nano-onion and poly(diallyldimethylammonium chloride) composite. *Electrochim. Acta*, **2012**, 72, 61–67.
- [91] Bartolome, J.P.; Fragoso, A., Electrochemical detection of nitrite and ascorbic acid at glassy carbon electrodes modified with carbon nano-onions bearing electroactive moieties. *Inorganica Chimica Acta*, **2017**, 468, 223–231.
- [92] Lettieri, S.; d’Amora, M.; Camisasca, A.; Diaspro, A.; Giordani, S., Carbon nano-onions as fluorescent on/off modulated nanoprobes for diagnostics. *Beilstein J. Nanotechnol.*, **2017**, 8, 1878–1888.
- [93] Zuaznabar-Gardona, J.C.; Fragoso, A., A wide-range solid state potentiometric pH sensor based on poly-dopamine coated carbon nano-onion electrodes. *Sensors and Actuators B: Chemical*, **2018**, 273, 664–671.
- [94] Portet, C.; Yushin, G.; Gogotsi, Y., Electrochemical performance of carbon onions, nanodiamonds, carbon black and multiwalled nanotubes in electrical double layer capacitors. *Carbon*, **2007**, 45, (13), 2511–2518.
- [95] Bushueva, E.G.; Galkin, P.S.; Okotrub, A.V.; Bulusheva, L.G.; Gavrilov, N.N.; Kuznetsov, V.L.; Moiseev, S.I., Double layer supercapacitor properties of onion-like carbon materials. *physica status solidi (b)*, **2008**, 245, (10), 2296–2299.
- [96] Pech, D.; Brunet, M.; Durou, H.; Huang, P.; Mochalin, V.; Gogotsi, Y.; Taberna, P.L.; Simon, P., Ultrahigh-power micrometre-sized supercapacitors based on onion-like carbon. *Nat. Nanotechnol.*, **2010**, 5, (9), 651–654.
- [97] Borgohain, R.; Li, J.; Selegue, J.P.; Cheng, Y.T., Electrochemical Study of Functionalized Carbon Nano-Onions for High-Performance Supercapacitor Electrodes. *J. Phys. Chem. C*, **2012**, 116, (28), 15068–15075.
- [98] McDonough, J.K.; Frolov, A.I.; Presser, V.; Niu, J.; Miller, C.H.; Ubieta, T.; Fedorov, M.V.; Gogotsi, Y., Influence of the structure of carbon onions on their electrochemical performance in supercapacitor electrodes. *Carbon*, **2012**, 50, (9), 3298–3309.
- [99] Gao, Y.; Zhou, Y.S.; Qian, M.; He, X.N.; Redepenning, J.; Goodman, P.; Li, H.M.; Jiang, L.; Lu, Y.F., Chemical activation of carbon nano-onions for high-rate supercapacitor electrodes. *Carbon*, **2013**, 51, 52–58.



- [100] Zhang, C.; Li, J.; Liu, E.; He, C.; Shi, C.; Du, X.; Hauge, R.H.; Zhao, N., Synthesis of hollow carbon nano-onions and their use for electrochemical hydrogen storage. *Carbon*, **2012**, *50*, (10), 3513-3521.
- [101] Han, F.-D.; Yao, B.; Bai, Y.-J., Preparation of Carbon Nano-Onions and Their Application as Anode Materials for Rechargeable Lithium-Ion Batteries. *The Journal of Physical Chemistry C*, **2011**, *115*, (18), 8923-8927.
- [102] Wang, Y.; Yan, F.; Liu, S.W.; Tan, A.Y.S.; Song, H.; Sun, X.W.; Yang, H.Y., Onion-like carbon matrix supported Co<sub>3</sub>O<sub>4</sub> nanocomposites: a highly reversible anode material for lithium ion batteries with excellent cycling stability. *Journal of Materials Chemistry A*, **2013**, *1*, (17), 5212-5216.
- [103] Wang, Y.; Han, Z.J.; Yu, S.F.; Song, R.R.; Song, H.H.; Ostrikov, K.; Yang, H.Y., Core-leaf onion-like carbon/MnO<sub>2</sub> hybrid nano-urchins for rechargeable lithium-ion batteries. *Carbon*, **2013**, *64*, 230-236.
- [104] Koudoumas, E.; Kokkinaki, O.; Konstantaki, M.; Couris, S.; Korovin, S.; Detkov, P.; Kuznetsov, V.; Pimenov, S.; Pustovoi, V., Onion-like carbon and diamond nanoparticles for optical limiting. *Chemical Physics Letters*, **2002**, *357*, (5), 336-340.
- [105] Macutkevicius, J.; Adomavicius, R.; Krotkus, A.; Seliuta, D.; Valusis, G.; Maksimenko, S.; Kuzhir, P.; Batrakov, K.; Kuznetsov, V.; Moseenkov, S.; Shenderova, O.; Okotrub, A.V.; Langlet, R.; Lambin, P., Terahertz probing of onion-like carbon-PMMA composite films. *Diamond and Related Materials*, **2008**, *17*, (7), 1608-1612.
- [106] Shenderova, O.; Tyler, T.; Cunningham, G.; Ray, M.; Walsh, J.; Casulli, M.; Hens, S.; McGuire, G.; Kuznetsov, V.; Lipa, S., Nanodiamond and onion-like carbon polymer nanocomposites. *Diamond and Related Materials*, **2007**, *16*, (4), 1213-1217.
- [107] Shenderova, O.; Grishko, V.; Cunningham, G.; Moseenkov, S.; McGuire, G.; Kuznetsov, V., Onion-like carbon for terahertz electromagnetic shielding. *Diamond and Related Materials*, **2008**, *17*, (4), 462-466.
- [108] Keller, K.; Maksimova, N.I.; Roddatis, V.V.; Schur, M.; Mestl, G.; Butenko, Y.V.; Kuznetsov, V.L.; Schlögl, R., The Catalytic Use of Onion-Like Carbon Materials for Styrene Synthesis by Oxidative Dehydrogenation of Ethylbenzene. *Angew. Chem. Int. Ed.*, **2002**, *41*, (11), 1885-1888.
- [109] Su, D.; Maksimova, N.I.; Mestl, G.; Kuznetsov, V.L.; Keller, V.; Schlögl, R.; Keller, N., Oxidative dehydrogenation of ethylbenzene to styrene over ultra-dispersed diamond and onion-like carbon. *Carbon*, **2007**, *45*, (11), 2145-2151.
- [110] Xu, B.; Yang, X.; Wang, X.; Guo, J.; Liu, X., A novel catalyst support for DMFC: Onion-like fullerenes. *Journal of Power Sources*, **2006**, *162*, (1), 160-164.
- [111] Santiago, D.; Rodríguez-Calero, G.G.; Palkar, A.; Barraza-Jimenez, D.; Galvan, D.H.; Casillas, G.; Mayoral, A.; Jose-Yacamán, M.; Echegoyen, L.; Cabrera, C.R., Platinum Electrodeposition on Unsupported Carbon Nano-Onions. *Langmuir*, **2012**, *28*, (49), 17202-17210.
- [112] Seymour, M.B.; Su, C.; Gao, Y.; Lu, Y.; Li, Y., Characterization of carbon nano-onions for heavy metal ion remediation. *Journal of Nanoparticle Research*, **2012**, *14*, (9), 1087.
- [113] Sakulthaew, C.; Chokejaroenrat, C.; Poapolathep, A.; Satapanajaru, T.; Poapolathep, S., Hexavalent chromium adsorption from aqueous solution using carbon nano-onions (CNOs). *Chemosphere*, **2017**, *184*, 1168-1174.
- [114] Cabioc'h, T.; Thune, E.; Rivière, J.P.; Camelio, S.; Girard, J.C.; Guérin, P.; Jaouen, M.; Henrard, L.; Lambin, P., Structure and properties of carbon onion layers deposited onto various substrates. *J. Appl. Phys.*, **2002**, *91*, (3), 1560-1567.
- [115] Hirata, A.; Igarashi, M.; Kaito, T., Study on solid lubricant properties of carbon onions produced by heat treatment of diamond clusters or particles. *Tribology International*, **2004**, *37*, (11), 899-905.
- [116] Joly-Pottuz, L.; Vacher, B.; Ohmae, N.; Martin, J.M.; Epicier, T., Anti-wear and Friction Reducing Mechanisms of Carbon Nano-onions as Lubricant Additives. *Tribol. Lett.*, **2008**, *30*, (1), 69-80.

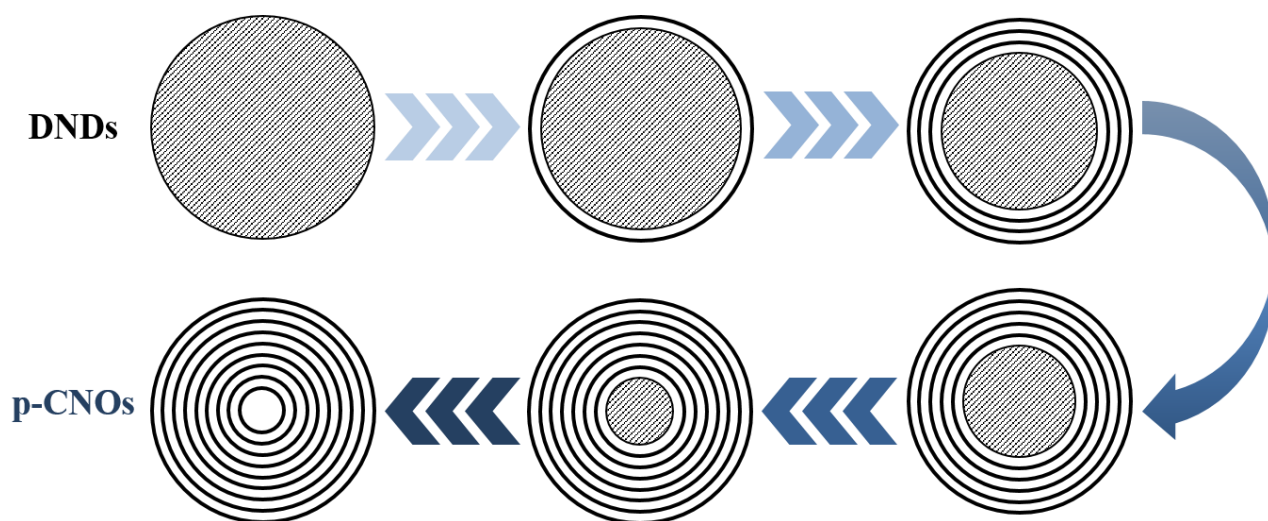
- [117] Hong, G.; Diao, S.; Antaris, A.L.; Dai, H., Carbon Nanomaterials for Biological Imaging and Nanomedicinal Therapy. *Chem. Rev.*, **2015**, *115*, (19), 10816-10906.
- [118] Yang, W.; Thordarson, P.; Gooding, J.J.; Ringer, S.P.; Braet, F., Carbon nanotubes for biological and biomedical applications. *Nanotechnology*, **2007**, *18*, (41), 412001.
- [119] Liu, Z.; Tabakman, S.; Welsher, K.; Dai, H., Carbon Nanotubes in Biology and Medicine: in vitro and in vivo Detection, Imaging and Drug Delivery. *Nano Res.*, **2009**, *2*, (2), 85-120.
- [120] Sayes, C.M.; Fortner, J.D.; Guo, W.; Lyon, D.; Boyd, A.M.; Ausman, K.D.; Tao, Y.D.; Sitharaman, B.; Wilson, L.J.; Hughes, J.B.; West, J.L.; Colvin, V.L., The Differential Cytotoxicity of Water-Soluble Fullerenes. *Nano Lett.*, **2004**, *4*, (10), 1881-1887.
- [121] Bosi, S.; Da Ros, T.; Spalluto, G.; Prato, M., Fullerene derivatives: an attractive tool for biological applications. *Chem. Commun.*, **2003**, *38*, (11-12), 913-923.
- [122] Chung, C.; Kim, Y.-K.; Shin, D.; Ryoo, S.-R.; Hong, B.H.; Min, D.-H., Biomedical Applications of Graphene and Graphene Oxide. *Acc. Chem. Res.*, **2013**, *46*, (10), 2211-2224.
- [123] Cao, L.; Wang, X.; Mezzani, M.J.; Lu, F.; Wang, H.; Luo, P.G.; Lin, Y.; Harruff, B.A.; Veca, L.M.; Murray, D.; Xie, S.-Y.; Sun, Y.-P., Carbon Dots for Multiphoton Bioimaging. *J. Am. Chem. Soc.*, **2007**, *129*, 11318-11319.
- [124] Zheng, X.T.; Ananthanarayanan, A.; Luo, K.Q.; Chen, P., Glowing graphene quantum dots and carbon dots: properties, syntheses, and biological applications. *Small*, **2015**, *11*, (14), 1620-1636.
- [125] Bartelmeß, J.; Quinn, S.J.; Giordani, S., Carbon nanomaterials: multi-functional agents for biomedical fluorescence and Raman imaging. *Chem. Soc. Rev.*, **2015**, *44*, (14), 4672-4698.
- [126] Ding, L.; Stilwell, J.; Zhang, T.; Elboudwarej, O.; Jiang, H.; Selegue, J.P.; Cooke, P.A.; Gray, J.W.; Chen, F.F., Molecular Characterization of the Cytotoxic Mechanism of Multiwall Carbon Nanotubes and Nano-Onions on Human Skin Fibroblast. *Nano Lett.*, **2005**, *5*, (12), 2448-2464.
- [127] Xu, Y.; Wang, S.Y.; Yang, J.; Gu, X.; Zhang, J.; Zheng, Y.F.; Yang, J.; Xu, L.; Zhu, X.Q., Multiwall carbon nano-onions induce DNA damage and apoptosis in human umbilical vein endothelial cells. *Environ. Toxicol.*, **2013**, *28*, (8), 442-450.
- [128] Kang, S.; Kim, J.-E.; Kim, D.; Woo, C.G.; Pikhitsa, P.V.; Cho, M.-H.; Choi, M., Comparison of cellular toxicity between multi-walled carbon nanotubes and onion-like shell-shaped carbon nanoparticles. *J. Nanopart. Res.*, **2015**, *17*, 9.
- [129] Frasconi, M.; Marotta, R.; Markey, L.; Flavin, K.; Spampinato, V.; Ceccone, G.; Echegoyen, L.; Scanlan, E.M.; Giordani, S., Multi-Functionalized Carbon Nano-onions as Imaging Probes for Cancer Cells. *Chem. Eur. J.*, **2015**, *21*, (52), 19071-19080.
- [130] Bartelmeß, J.; Baldrighi, M.; Nardone, V.; Parisini, E.; Buck, D.; Echegoyen, L.; Giordani, S., Synthesis and Characterization of Far-Red/NIR-Fluorescent BODIPY Dyes, Solid-State Fluorescence, and Application as Fluorescent Tags Attached to Carbon Nano-onions. *Chem. Eur. J.*, **2015**, *21*, (27), 9727-9732.
- [131] Pakhira, B.; Ghosh, M.; Allam, A.; Sarkar, S., Carbon nano onions cross the blood brain barrier. *RSC Adv.*, **2016**, *6*, (35), 29779-29782.
- [132] Marchesano, V.; Ambrosone, A.; Bartelmeß, J.; Strisciante, F.; Tino, A.; Echegoyen, L.; Tortiglione, C.; Giordani, S., Impact of Carbon Nano-Onions on *Hydra vulgaris* as a Model Organism for Nanoecotoxicology. *Nanomaterials*, **2015**, *5*, (3), 1331-1350.
- [133] d'Amora, M.; Rodio, M.; Bartelmeß, J.; Sancataldo, G.; Brescia, R.; Cella Zanacchi, F.; Diaspro, A.; Giordani, S., Biocompatibility and biodistribution of functionalized carbon nano-onions (f-CNOs) in a vertebrate model. *Sci. Rep.*, **2016**, *6*, 33923.
- [134] Usenko, C.Y.; Harper, S.L.; Tanguay, R.L., Fullerene C60 exposure elicits an oxidative stress response in embryonic zebrafish. *Toxicol. Appl. Pharmacol.*, **2008**, *229*, (1), 44-55.
- [135] Wang, Z.G.; Zhou, R.; Jiang, D.; Song, J.E.; Xu, Q.; Si, J.; Chen, Y.P.; Zhou, X.; Gan, L.; Li, J.Z.; Zhang, H.; Liu, B., Toxicity of Graphene Quantum Dots in Zebrafish Embryo. *Biomed. Environ. Sci.*, **2015**, *28*, (5), 341-351.
- [136] d'Amora, M.; Camisasca, A.; Lettieri, S.; Giordani, S., Toxicity Assessment of Carbon Nanomaterials in Zebrafish during Development. *Nanomaterials*, **2017**, *7*, (12), 414.

- [137] Whitesides, G.M.; Crabtree, G.W., Don't Forget Long-Term Fundamental Research in Energy. *Science*, **2007**, *315*, (5813), 796-798.
- [138] Lewis, N.S.; Nocera, D.G., Powering the planet: chemical challenges in solar energy utilization. *Proc. Natl. Acad. Sci. USA*, **2006**, *103*, (43), 15729-15735.
- [139] Steele, B.C.H.; Heinzel, A., Materials for fuel-cell technologies *Nature*, **2001**, *414*, 345-352.
- [140] Dai, L.; Xue, Y.; Qu, L.; Choi, H.J.; Baek, J.B., Metal-free catalysts for oxygen reduction reaction. *Chem. Rev.*, **2015**, *115*, (11), 4823-4892.
- [141] Zhang, J.; Xia, Z.; Dai, L., Carbon-based electrocatalysts for advanced energy conversion and storage. *Science Advances*, **2015**, *1*, (7).
- [142] Xia, W.; Mahmood, A.; Liang, Z.; Zou, R.; Guo, S., Earth-Abundant Nanomaterials for Oxygen Reduction. *Angew. Chem. Int. Ed.*, **2016**, *55*, (8), 2650-2676.
- [143] Gewirth, A.A.; Thorum, M.S., Electroreduction of dioxygen for fuel-cell applications: materials and challenges. *Inorg. Chem.*, **2010**, *49*, (8), 3557-3566.
- [144] Ramani, V.K.; Cooper, K.; Fenton, J.M.; Kunz, H.R. In *Springer Handbook of Electrochemical Energy*. Breitkopf, C.; Swider-Lyons, K., Eds.; Springer Berlin Heidelberg: Berlin, Heidelberg, **2017**, pp 649-711.
- [145] Nie, Y.; Li, L.; Wei, Z., Recent advancements in Pt and Pt-free catalysts for oxygen reduction reaction. *Chem. Soc. Rev.*, **2015**, *44*, (8), 2168-2201.
- [146] Jaouen, F.; Proietti, E.; Lefèvre, M.; Chenitz, R.; Dodelet, J.-P.; Wu, G.; Chung, H.T.; Johnston, C.M.; Zelenay, P., Recent advances in non-precious metal catalysis for oxygen-reduction reaction in polymer electrolyte fuel cells. *Energy & Environmental Science*, **2011**, *4*, (1), 114-130.
- [147] Shao, M.; Chang, Q.; Dodelet, J.P.; Chenitz, R., Recent Advances in Electrocatalysts for Oxygen Reduction Reaction. *Chem. Rev.*, **2016**, *116*, (6), 3594-3657.
- [148] Sawant, S.Y.; Han, T.H.; Cho, M.H., Metal-Free Carbon-Based Materials: Promising Electrocatalysts for Oxygen Reduction Reaction in Microbial Fuel Cells. *Int. J. Mol. Sci.*, **2016**, *18*, (1), 25.
- [149] Liu, X.; Dai, L., Carbon-based metal-free catalysts. *Nature Reviews Materials*, **2016**, *1*, 16064.
- [150] Gong, K.; Du, F.; Xia, Z.; Durstock, M.; Dai, L., Nitrogen-Doped Carbon Nanotube Arrays with High Electrocatalytic Activity for Oxygen Reduction. *Science*, **2009**, *323*, ( 5915), 760-764.
- [151] Xiong, W.; Du, F.; Liu, Y.; Perez, A.J.; Supp, M.; Ramakrishnan, T.S.; Dai, L.; Jiang, L., 3-D Carbon Nanotube Structures Used as High Performance Catalyst for Oxygen Reduction Reaction. *J. Am. Chem. Soc.*, **2010**, *132*, 15839-15841.
- [152] Yu, D.; Zhang, Q.; Dai, L., Highly Efficient Metal-Free Growth of Nitrogen-Doped Single-Walled Carbon Nanotubes on Plasma-Etched Substrates for Oxygen Reduction. *Journal of the American Chemical Society*, **2010**, *132*, (43), 15127-15129.
- [153] Qu, L.; Liu, Y.; Baek, J.-B.; Dai, L., Nitrogen-Doped Graphene as Efficient Metal-Free Electrocatalyst for Oxygen Reduction in Fuel Cells. *ACS Nano*, **2010**, *4*, (3), 1321-1326.
- [154] Yang, Z.; Nie, H.; Chen, X.a.; Chen, X.; Huang, S., Recent progress in doped carbon nanomaterials as effective cathode catalysts for fuel cell oxygen reduction reaction. *J. Power Sources*, **2013**, *236*, 238-249.
- [155] Guo, D.; Shibuya, R.; Akiba, C.; Saji, S.; Kondo, T.; Nakamura, J., Active sites of nitrogen-doped carbon materials for oxygen reduction reaction clarified using model catalysts. *Science*, **2016**, *351*, (6271), 361-365.
- [156] Yang, L.; Jiang, S.; Zhao, Y.; Zhu, L.; Chen, S.; Wang, X.; Wu, Q.; Ma, J.; Ma, Y.; Hu, Z., Boron-doped carbon nanotubes as metal-free electrocatalysts for the oxygen reduction reaction. *Angew. Chem. Int. Ed.*, **2011**, *50*, (31), 7132-7135.
- [157] Sheng, Z.-H.; Gao, H.-L.; Bao, W.-J.; Wang, F.-B.; Xia, X.-H., Synthesis of boron doped graphene for oxygen reduction reaction in fuel cells. *J. Mater. Chem.*, **2012**, *22*, (2), 390-395.

- [158] Yang, Z.; Yao, Z.; Li, G.; Fang, G.; Nie, H.; Liu, Z.; Zhou, X.; Chen, X.a.; Huang, S., Sulfur-Doped Graphene as an Efficient Metal-free Cathode Catalyst for Oxygen Reduction. *ACS Nano*, **2012**, 6, (1), 205-211.
- [159] Jeon, I.-Y.; Zhang, S.; Zhang, L.; Choi, H.-J.; Seo, J.-M.; Xia, Z.; Dai, L.; Baek, J.-B., Edge-Selectively Sulfurized Graphene Nanoplatelets as Efficient Metal-Free Electrocatalysts for Oxygen Reduction Reaction: The Electron Spin Effect. *Advanced Materials*, **2013**, 25, (42), 6138-6145.
- [160] Liu, Z.-W.; Peng, F.; Wang, H.-J.; Yu, H.; Zheng, W.-X.; Yang, J., Phosphorus-Doped Graphite Layers with High Electrocatalytic Activity for the O<sub>2</sub> Reduction in an Alkaline Medium. *Angewandte Chemie International Edition*, **2011**, 50, (14), 3257-3261.
- [161] Jeon, I.-Y.; Choi, H.-J.; Choi, M.; Seo, J.-M.; Jung, S.-M.; Kim, M.-J.; Zhang, S.; Zhang, L.; Xia, Z.; Dai, L.; Park, N.; Baek, J.-B., Facile, scalable synthesis of edge-halogenated graphene nanoplatelets as efficient metal-free eletrocatalysts for oxygen reduction reaction. *Scientific reports*, **2013**, 3, 1810-1810.
- [162] Yao, Z.; Nie, H.; Yang, Z.; Zhou, X.; Liu, Z.; Huang, S., Catalyst-free synthesis of iodine-doped graphene via a facile thermal annealing process and its use for electrocatalytic oxygen reduction in an alkaline medium. *Chemical Communications*, **2012**, 48, (7), 1027-1029.
- [163] Wang, S.; Iyyamperumal, E.; Roy, A.; Xue, Y.; Yu, D.; Dai, L., Vertically Aligned BCN Nanotubes as Efficient Metal-Free Electrocatalysts for the Oxygen Reduction Reaction: A Synergetic Effect by Co-Doping with Boron and Nitrogen. *Angewandte Chemie International Edition*, **2011**, 50, (49), 11756-11760.
- [164] Wang, S.; Zhang, L.; Xia, Z.; Roy, A.; Chang, D.W.; Baek, J.B.; Dai, L., BCN graphene as efficient metal-free electrocatalyst for the oxygen reduction reaction. *Angew. Chem. Int. Ed.*, **2012**, 51, (17), 4209-4212.
- [165] Zheng, Y.; Jiao, Y.; Ge, L.; Jaroniec, M.; Qiao, S.Z., Two-step boron and nitrogen doping in graphene for enhanced synergistic catalysis. *Angew. Chem. Int. Ed.*, **2013**, 52, (11), 3110-3116.
- [166] Zehtab Yazdi, A.; Fei, H.; Ye, R.; Wang, G.; Tour, J.; Sundararaj, U., Boron/nitrogen co-doped helically unzipped multiwalled carbon nanotubes as efficient electrocatalyst for oxygen reduction. *ACS Appl. Mater. Interfaces*, **2015**, 7, (14), 7786-7794.
- [167] Shi, Q.; Peng, F.; Liao, S.; Wang, H.; Yu, H.; Liu, Z.; Zhang, B.; Su, D., Sulfur and nitrogen co-doped carbon nanotubes for enhancing electrochemical oxygen reduction activity in acidic and alkaline media. *Journal of Materials Chemistry A*, **2013**, 1, (47), 14853-14857.
- [168] Yu, D.; Xue, Y.; Dai, L., Vertically Aligned Carbon Nanotube Arrays Co-doped with Phosphorus and Nitrogen as Efficient Metal-Free Electrocatalysts for Oxygen Reduction. *The Journal of Physical Chemistry Letters*, **2012**, 3, (19), 2863-2870.
- [169] Zhao, S.; Liu, J.; Li, C.; Ji, W.; Yang, M.; Huang, H.; Liu, Y.; Kang, Z., Tunable ternary (N, P, B)-doped porous nanocarbons and their catalytic properties for oxygen reduction reaction. *ACS Appl. Mater. Interfaces*, **2014**, 6, (24), 22297-22304.
- [170] Cao, C.; Wei, L.; Wang, G.; Shen, J., Superiority of boron, nitrogen and iron ternary doped carbonized graphene oxide-based catalysts for oxygen reduction in microbial fuel cells. *Nanoscale*, **2017**, 9, (10), 3537-3546.
- [171] Wu, G.; Dai, C.; Wang, D.; Li, D.; Li, N., Nitrogen-doped magnetic onion-like carbon as support for Pt particles in a hybrid cathode catalyst for fuel cells. *J. Mater. Chem.*, **2010**, 20, 3059-3068.
- [172] Wu, G.; Nelson, M.; Ma, S.; Meng, H.; Cui, G.; Shen, P.K., Synthesis of nitrogen-doped onion-like carbon and its use in carbon-based CoFe binary non-precious-metal catalysts for oxygen-reduction. *Carbon*, **2011**, 49, 3972 - 3982.
- [173] Zhu, C.; Xu, F.; Chen, J.; Min, H.; Dong, H.; Tong, L.; Qasim, K.; Li, S.; Sun, L., Nitrogen-doped carbon onions encapsulating metal alloys as efficient and stable catalysts for dye-sensitized solar cells. *Journal of Power Sources*, **2016**, 303, 159-167.
- [174] Lin, Y.; Pan, X.; Qi, W.; Zhang, B.; Su, D.S., Nitrogen-doped onion-like carbon: a novel and efficient metal-free catalyst for epoxidation reaction. *J. Mater. Chem. A*, **2014**, 2, (31), 12475-12483.

- [175] Shu, C.; Lin, Y.; Su, D., N-doped onion-like carbon as an efficient oxygen electrode for long-life Li–O<sub>2</sub> battery. *J. Mater. Chem. A*, **2016**, *4*, 2128-2136.
- [176] Mykhailiv, O.; Zubyk, H.; Brzezinski, K.; Gras, M.; Lota, G.; Gniadek, M.; Romero, E.; Echegoyen, L.; Plonska-Brzezinska, M.E., Improvement of the Structural and Chemical Properties of Carbon Nano-onions for Electrocatalysis. *ChemNanoMat* **2017**, *3*, 583 - 590.
- [177] Choi, E.Y.; Kim, C.K., Fabrication of nitrogen-doped nano-onions and their electrocatalytic activity toward the oxygen reduction reaction. *Sci. Rep.*, **2017**, *7*, (1), 4178.
- [178] Zhang, Y.; Reed, A.; Kim, D.Y., Nitrogen doped carbon nano-onions as efficient and robust electrocatalysts for oxygen reduction reactions. *Curr. Appl. Phys.*, **2018**, *18*, 417-423.
- [179] Chatterjee, K.; Ashokkumar, M.; Gullapalli, H.; Gong, Y.; Vajtai, R.; Thanikaivelan, P.; Ajayan, P.M., Nitrogen-rich carbon nano-onions for oxygen reduction reaction. *Carbon* **2018**, *130*, 645-651.
- [180] Lin, Y.; Wu, S.; Shi, W.; Zhang, B.; Wang, J.; Kim, Y.A.; Endo, M.; Su, D.S., Efficient and highly selective boron-doped carbon materials-catalyzed reduction of nitroarenes. *Chem. Commun.*, **2015**, *51*, (66), 13086-13089.
- [181] Wu, X.; Radovic, L.R., Ab Initio Molecular Orbital Study on the Electronic Structures and Reactivity of Boron-Substituted Carbon. *J. Phys. Chem. A*, **2004**, *108*, (42), 9180-9187.
- [182] Lin, Y.; Zhu, Y.; Zhang, B.; Kim, Y.A.; Endo, M.; Su, D.S., Boron-doped onion-like carbon with enriched substitutional boron: the relationship between electronic properties and catalytic performance. *J. Mater. Chem. A*, **2015**, *3*, 21805-21841.
- [183] Mykhailiv, O.; Brzezinski, K.; Sulikowski, B.; Olejniczak, Z.; Gras, M.; Lota, G.; Molina-Ontoria, A.; Jakubczyk, M.; Echegoyen, L.; Plonska-Brzezinska, M.E., Boron-Doped Polygonal Carbon Nano-Onions: Synthesis and Applications in Electrochemical Energy Storage. *Chem. Eur. J.*, **2017**, *23*, (29), 7132-7141.
- [184] Shu, C.; Lin, Y.; Zhang, B.; Hamid, S.B.A.; Su, D., Mesoporous boron-doped onion-like carbon as long-life oxygen electrode for sodium–oxygen batteries. *J. Mater. Chem. A*, **2016**, *4*, 6610-6619.
- [185] Sun, X.; Xu, J.; Ding, Y.; Zhang, B.; Feng, Z.; Su, D.S., The Effect of Different Phosphorus Chemical States on an Onion-like Carbon Surface for the Oxygen Reduction Reaction. *ChemSusChem*, **2015**, *8*, (17), 2872-2876.

## *Chapter 2 - Synthesis of carbon nano-onions by thermal annealing*



### **2.1 Introduction**

Since Ugarte reported, for the first time, the formation of spherical multi-layered structures by irradiating amorphous carbon [1, 2], many efforts have been devoted to the development of synthetic approaches for a large-scale production of CNOs. In the last two decades, a large number of strategies have been employed for this purpose, including arc discharge [3, 4], chemical vapor deposition [5, 6], ball milling [7, 8] and ion implantation [9, 10].

In 1994, Kuznetsov proposed a viable way to produce small CNOs (with size below 10 nm) in high quantity through the thermal annealing of detonation nanodiamonds (DNDs) in vacuum [11]. Due to the high temperatures reached during the synthesis, an overall transformation occurs in the carbon structure, which involves the conversion of the  $sp^3$  carbon atoms into a  $sp^2$  network. The graphitization process occurs from the ND surface and proceeds towards the interior, inducing the curling and the final closure of the graphitic fragments to form the typical multi-shell structure of CNOs [12].

Thermal annealing is currently the common method to produce small CNOs with a size between 5 and 10 nm and consisting of 6-12 graphitic shells. The main advantages of this method are related to the narrow size distribution and purity of the products. Furthermore, due to the high yield (close to 100%), low cost and excellent reproducibility, this method has the potential for an industrial scale-up. In addition, the possibility to perform the process under inert atmosphere (i.e. argon [13, 14] and helium [15]) avoids the use of an expensive high-vacuum equipment.

As discussed in the first chapter, the production method has to be carefully selected in relation to the applicative use, for instance in biological and electrochemical applications. Different synthetic approaches lead to CNOs showing distinct features and physico-chemical properties.

An important factor is the size, which ranges from few (5-8 nm for thermal annealing for instance) to tens of nanometers (20-50 nm for arc discharge and CVD methods). Smaller nanoparticles can more easily cross the cell membrane, thus improving their potentialities in bio-related applications; in addition, higher surface area to volume ratio can allow for an increased loading of a biomolecule of interest (i.e. drugs for drug delivery purposes) or for a better dispersion of catalysts in electrochemical applications. The purity has direct impact on the cell viability, thus affecting the biocompatibility of a material; furthermore, the presence of impurity can modify to some extent the electroactivity of a catalyst. Methods such as CVD and ball milling can lead to metal-encapsulated CNOs or leave catalyst impurities in the product; this may have toxic effects on the biological entities and affect the catalytic performance [16]. The size plays also a key role in determining the physico-chemical properties. In 2007, Palkar and co-workers investigated the effects of the production method on the properties and reactivity of CNOs; for this purpose, they compared CNOs produced by two different methods, exhibiting different size [15]. Thermal annealing of DNDs led to the formation of small CNOs (5 nm as average size and consisting of 6-8 graphitic shells), while bigger CNOs (15-25 nm in size and 20-30 layers) were produced by arc discharge. In general, a smaller radius imparts higher curvature to a structure, leading thus to a higher reactivity of the particles. In addition, ND-derived CNOs showed a more defective nature of the outer shells, as suggested by Raman spectroscopy. According to this, differences are expected in terms of reactivity between the two types of CNOs. The authors carried out three different functionalization approaches (i.e. [2+1] cycloaddition, free-radical addition and oxidation) on both CNOs and showed that only the smaller CNOs were successfully functionalized, while, in the same condition, no surface modification occurred on the bigger CNOs. They experimentally proved the higher reactivity of ND-derived CNOs as a consequence of the small size, high structural curvature and high degree of defectiveness [15].

In this chapter, I will describe the synthesis and characterization of carbon nano-onions produced by thermal annealing of commercially available detonation nanodiamonds. This synthetic method

enables the production of high amount of homogeneous CNOs. The proposed heat treatment is able to transform the  $sp^3$ -hybridized NDs into a quasi-spherical graphitic structure and the successful conversion has been confirmed by several characterization techniques by studying the surface and structural properties of these nanomaterials.

## 2.2 Experimental

### 2.2.1 Synthesis of pristine carbon nano-onions

The synthesis of pristine carbon nano-onions (p-CNOs) has been achieved by traditional thermal annealing process [11, 15]. Commercially available detonation nano-diamonds with a particle size of 4-6 nm were used as precursor. The annealing process was carried out in a tube furnace (model: GSL-1700X-KS, MTI corporation, Figure 2.1A) under helium atmosphere. In a typical procedure (Figure 2.1B), the right amount of DNDs were loaded in a graphitic crucible and transferred into the tube furnace. Prior to the process, the furnace was thoroughly purged with helium to remove any traces of air. The sample was thermally treated at 1650 °C at a heating rate of 3.5 °K min<sup>-1</sup> and kept at that temperature for 1 h. Finally, the samples were slowly cooled down to room temperature and recovered. To remove any traces of amorphous carbon, the sample was further treated at 450 °C for 4 h to yield high-purity CNOs.

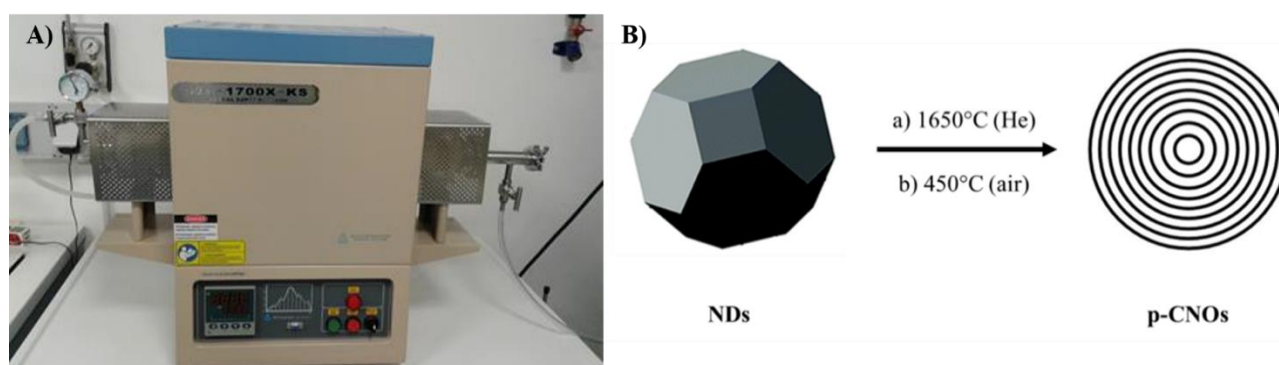


Figure 2.1: A) Tube furnace used for the annealing process and B) synthetic procedure of the production of p-CNOs by thermal annealing.

## 2.3 Results and discussion

### 2.3.1 Transmission electron microscopy

The morphological characteristics of DNDs and p-CNOs were investigated by high-resolution transmission electron microscopy (HRTEM) investigations, proving the formation of quasi-spherical CNOs. Figure 2.2 shows the HRTEM images of DNDs. The particles display mainly a rounded shape with uniform size between 4 and 6 nm and consist of a crystalline diamond core. The irregular and



non-crystalline shells around the diamond core suggest the presence of amorphous carbon surrounding DNDs, as reported for NDs [17].

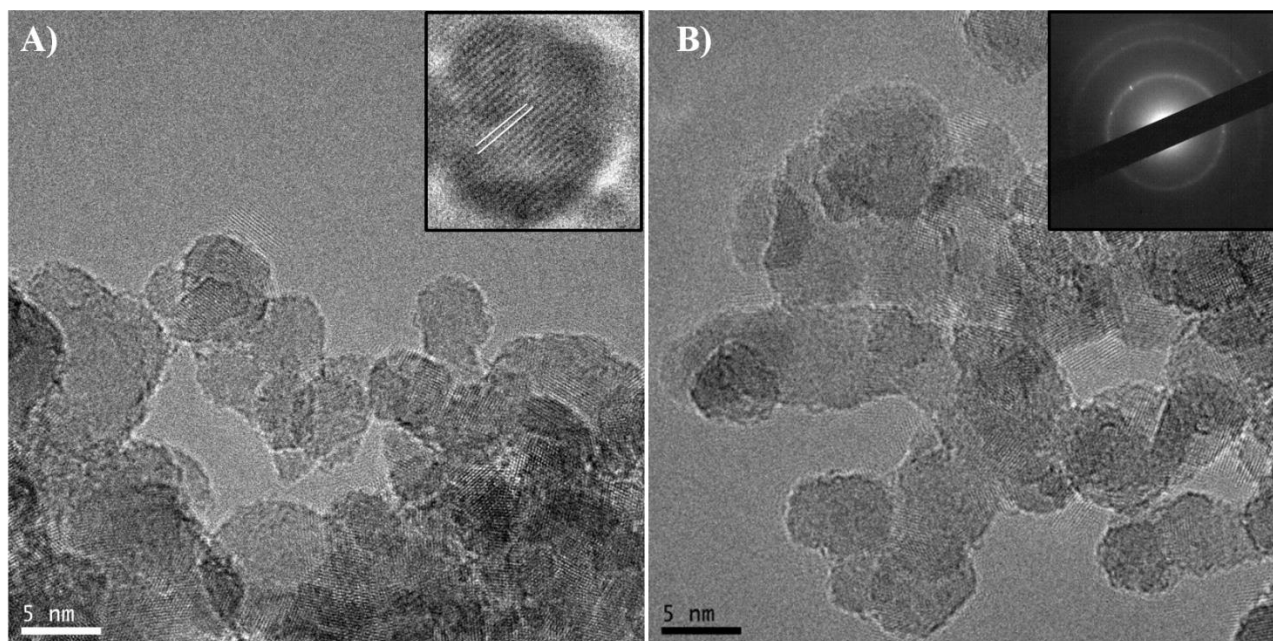


Figure 2.2: HRTEM images of DNDs with inset in A) and B) showing diamond (111) plane and SAED pattern, respectively.

The inset of Figure 2.2A shows the presence of the typical crystal lattice composed by parallel (111) planes separated by 2.06 Å. The selected area electron diffraction (SAED) pattern of DNDs is shown as inset of Figure 2.2B. The inner ring is assigned to the (111) plane, while the middle and the outer ring in the electron diffraction pattern to the (220) and (113) diamond planes [18]. The lattice fringes and the SAED pattern indicate the crystallinity of the diamond cores.

Representative HRTEM images of p-CNOs are shown in Figure 2.3, confirming the presence of the typical layered graphitic structure.

p-CNOs exhibit a closed quasi-spherical shape with an average size of 5 nm and highly defective outermost shells. In particular, p-CNOs consist of several (up to 8-10) graphitic shells enclosing a hollow core, while no traces of a remaining diamond core are observed. The averaged inter-layer distance between the carbon shells is around 3.4 Å (inset in Figure 2.3A), slightly different from that of graphite. The SAED pattern (inset in Figure 2.3B) shows four different diffraction rings corresponding to graphite (002), (100), (004), and (110) layer planes, respectively [19].

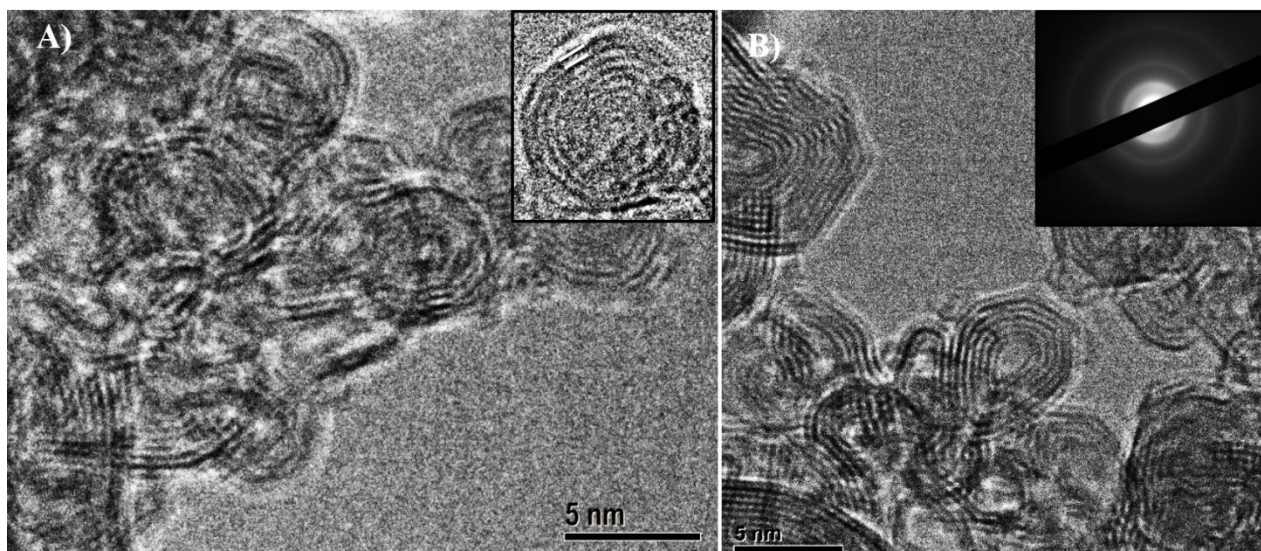


Figure 2.3: HRTEM images of p-CNOs with inset in A) and B) showing graphitic (002) plane and SAED pattern, respectively.

A size distribution analysis has been performed to have information about the size of the CNOs (Figure 2.4). The diameter of 331 different nanoparticles were calculated by using ImageJ and as result an average size equal to  $5.94 \pm 1.2$  nm was obtained. The parameters obtained from the fit are reported in Table 2.1.

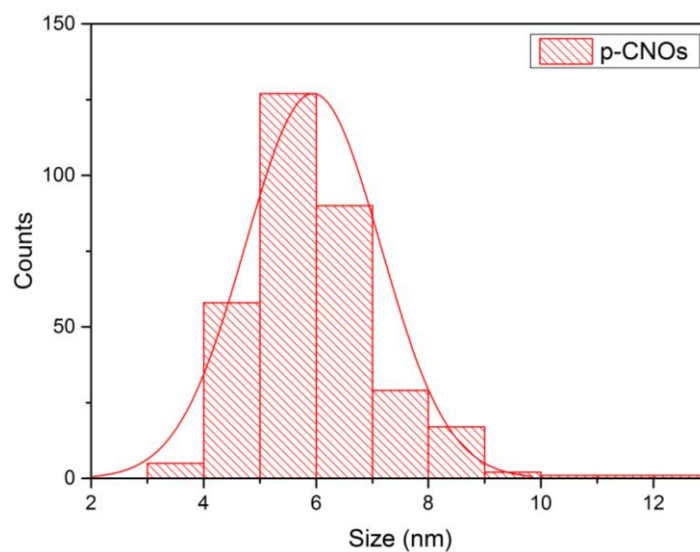


Figure 2.4: Particle size distribution of p-CNOs, showing an average size of  $5.94 \pm 1.2$  nm .

Table 2.1: Fit parameters from the HRTEM particles size distribution.

N total	Mean (nm)	Geometric mean (nm)	Mode (nm)	Minimum (nm)	Maximum (nm)	Median (nm)
331	$5.94 \pm 1.20$	$5.83 \pm 1.20$	5.50	3.60	12.73	5.79

### 2.3.2 Electron energy loss spectroscopy

Electron energy loss spectroscopy (EELS) is a powerful tool for the analysis of electronic states in carbon-based nanostructures. Figure 2.5A shows the low-loss region of the EELS spectrum for NDs, exhibiting a broad peak at around 28 eV, which can be attributed to the superposition of two different plasmonic peaks. The first is due to the collective excitation of  $\sigma$  electrons in the valence band of the ND core ( $\sigma$ -plasmon peak), while the second originates from the amorphous carbon layer onto the DND surface, generated by the collective excitation of the  $\pi+\sigma$  valence electrons ( $\pi+\sigma$  plasmon peak) [20, 21]. Figure 2.5B shows the low-loss region of the EELS spectrum for p-CNOs. Compared to the spectrum of DNDs, the  $\pi+\sigma$  plasmon peak is shifted towards lower energies (located at 24 eV); this can be explained by the increase of this contribution and the simultaneous disappearance of the diamond peak as a consequence of the transformation, confirming the successful conversion from  $sp^3$  to  $sp^2$  carbon atoms. Further confirm is given by the appearance of a weak peak at around 5 eV, assigned to the collective excitation of  $\pi$  electrons ( $\pi$  plasmon peak) [21, 22].

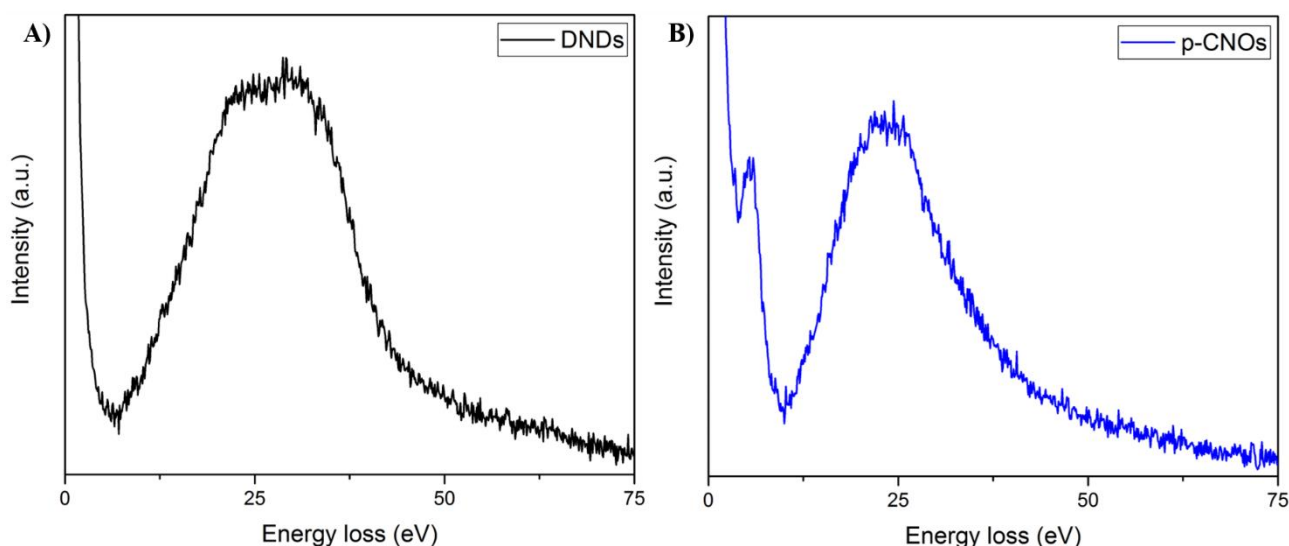


Figure 2.5: Low-loss region of EELS spectra of A) DNDs and B) p-CNOs.

Figure 2.6A shows the Carbon K-edge region of the EELS spectrum of DNDs. The spectrum contains a sharp edge at 288 eV with three characteristic peaks at 292, 297.4 and 305.4 eV corresponding to  $sp^3$  bonding state ( $1s \rightarrow \sigma^*$  transition), as observed for diamond. The weak peak at 285 eV is attributed to the  $1s \rightarrow \pi^*$  transition and reveals the presence of amorphous carbon on the particle surface, in agreement with what observed in the HRTEM images of DNDs.

The relative intensity of the  $1s \rightarrow \pi^*/1s \rightarrow \sigma^*$  increases as results of the conversion of the carbon atoms. The EELS C K-edge spectrum of p-CNOs (Figure 2.6B) exhibits a narrow peak due to the transition from the  $1s$  core level to the corresponding unoccupied  $\pi^*$  band ( $1s \rightarrow \pi^*$  transition) at

285.2 eV, indicating predominantly  $sp^2$ -bonded carbon atoms and a weaker peak at about 292.5 eV, corresponding to a  $1s \rightarrow \sigma^*$  transition [20, 21, 23].

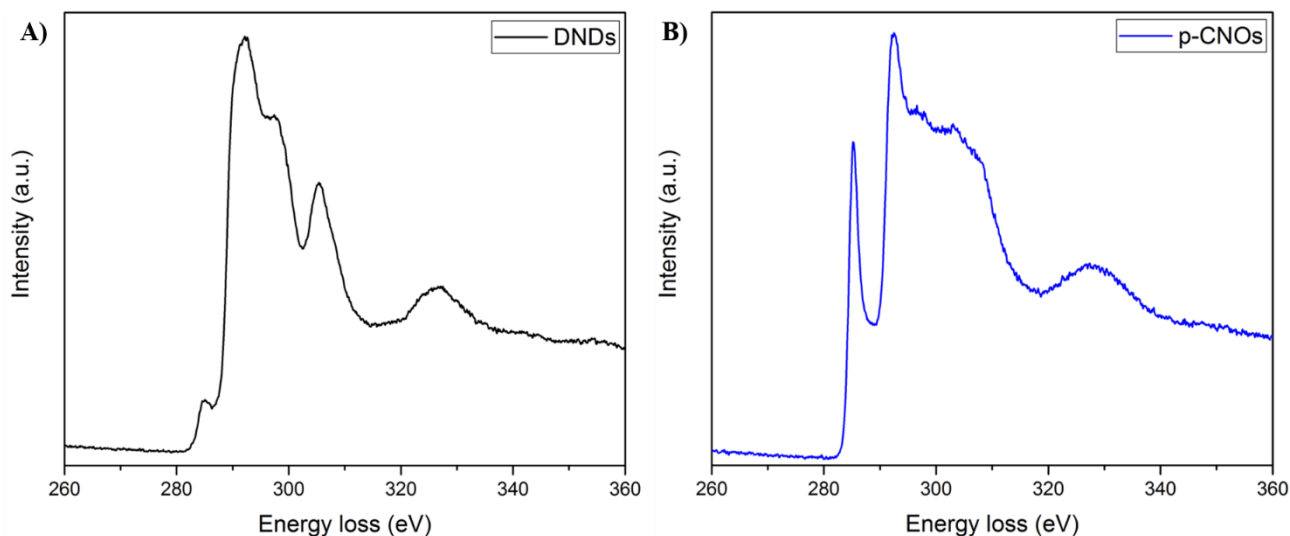


Figure 2.6: EELS Carbon K-edge spectra of A) DNDs and B) p-CNOs.

### 2.3.3 X-ray diffraction

XRD analyses were performed in order to analyze the crystal structure of the different samples and to confirm the transformation of nanodiamonds, composed of  $sp^3$  carbon atoms, into graphitic carbon onions. XRD spectrum of DNDs (Figure 2.7A) displays the presence of two peaks related to the diamond phase: the peak at  $43.88^\circ$  corresponds to the (111) plane, whereas the peak at  $75.33^\circ$  to the (220) plane [20, 24].

The XRD spectrum of p-CNOs (Figure 2.7B) shows significant differences from that of DNDs. After the annealing process, the two intense peaks of diamond disappear, confirming the absence of a residual diamond phase in the sample in agreement with HRTEM analysis.

The most obvious change in the pattern is the growth of four peaks related to the graphitic phase. The broad peak at  $25.91^\circ$  is assigned to the (002) crystal planes, while the low intensity peaks at  $43.42^\circ$ ,  $53.83^\circ$  and  $78.58^\circ$  are attributed to the (100+101), (004) and (110) graphitic planes, respectively [20, 25]. The inter-planar distance ( $d$ -spacing) can be evaluated by using the Bragg law ( $2d \sin \theta = \lambda$ ), where  $\lambda = 1.5418 \text{ \AA}$  (Cu  $k\alpha$  radiation source). For DNDs, from the position of the first peak at  $43.88^\circ$ , a value equal to  $2.06 \text{ \AA}$  can be measured, which corresponds to the typical diamond (111) inter-planar distance [11, 26]. For p-CNOs, from the position of the first peak at  $25.91^\circ$ , a value equal to  $3.43 \text{ \AA}$  is calculated, which is slightly greater from the perfect graphite (002) inter-planar distance ( $3.35 \text{ \AA}$ ) [25].

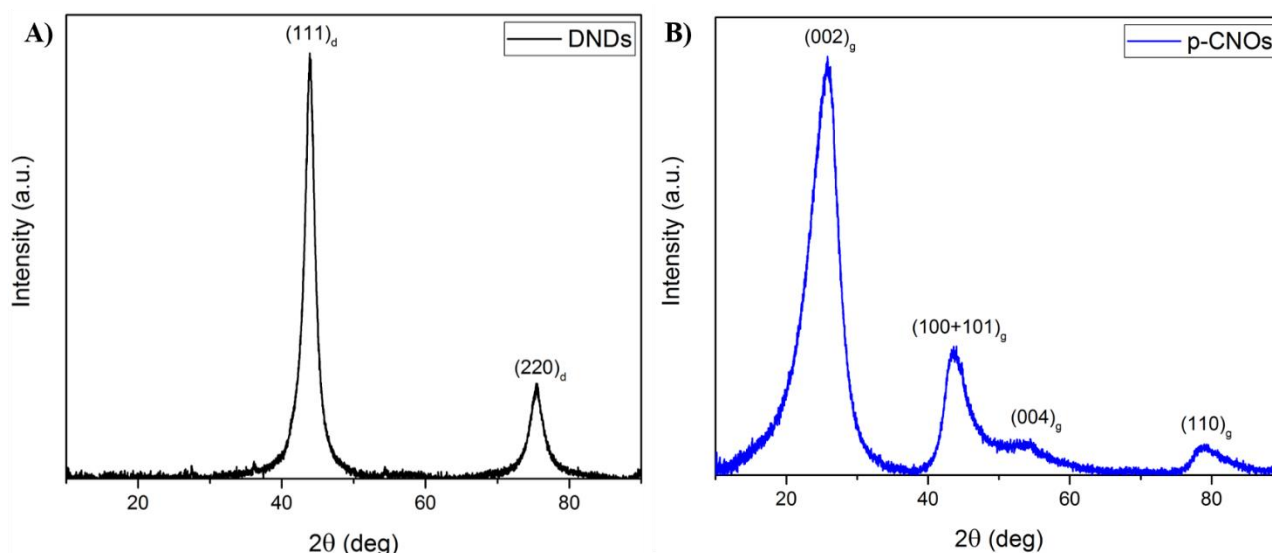


Figure 2.7: XRD patterns of A) DNDs and B) p-CNOs, showing characteristic peaks of the diamond and graphite phases.

The Scherrer equation is often employed for the determination of the powder particles size as it relates the size to the broadening of a peak in a diffraction pattern [27]. The Scherrer equation can be written as  $d = (0.9 \cdot \lambda) / (\beta \cdot \cos \theta)$ , where  $\lambda$  is the x-ray wavelength ( $\lambda = 1.5418 \text{ \AA}$ ),  $\beta$  is the full width at half the maximum (FWHM) in radians and  $\theta$  is the Bragg angle in degree. By using this formula, a value equal to 5.26 nm was obtained for the diamond (111) plane, which is in good agreement with HRTEM investigation. However, the value calculated for p-CNOs (1.71 nm) differs from the HRTEM observations; this is due to the broadening of the (002) peak originated mostly from the structural microstrains, as also observed in multiwall carbon nanotubes [20].

XRD analyses confirmed the conversion from  $sp^3$ - to  $sp^2$ -hybridized carbon atoms, thus proving the formation of graphitic CNOs.

### 2.3.4 X-ray photoelectron spectroscopy

XPS analyses were performed in order to obtain information about the elemental composition and the chemical bonding states of each element to further confirm the formation of a graphitic structure.

The XPS survey spectrum of DNDs, reported in Figure 2.8A, exhibits an intense peak attributed to the presence of carbon (93.3%) and two low intensity peaks assigned to nitrogen and oxygen (5.2% and 1.5%, respectively). The presence of nitrogen in DNDs is commonly reported and attributed to the nitrogen-containing explosives used for the detonation process employed for the synthesis [28, 29]. On the other side, the presence of oxygen is due to the purification treatments, which DNDs undergo after the production [30].

After the annealing process, the most evident difference is the complete disappearing of the nitrogen peak. p-CNOs are mainly composed of carbon (99%), as depicted by the intense related in the spectrum in Figure 2.8B, while the oxygen peak exhibits a very low intensity, suggesting its small



content (i.e. 1.0%). The peaks present in both spectra (listed as \*) are due to the gold substrate used for the analyses. The elemental composition for both samples is shown in Table 2.2.

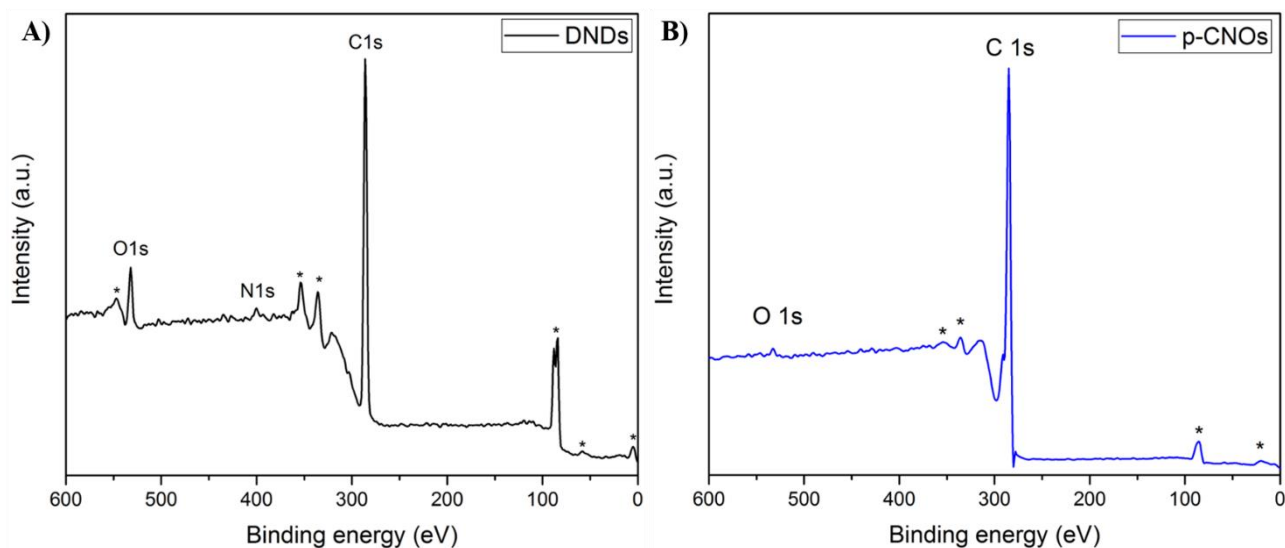


Figure 2.8: XPS survey spectra of A) DNDs and B) p-CNOs. The peaks denoted by \* are due to the gold substrate used for the analyses.

Table 2.2: Elemental composition of DNDs and p-CNOs from XPS analyses.

Sample	C content (at %)	O content (at %)	N content (at %)
NDs	93.3	5.2	1.5
p-CNOs	99.0	1.0	-

The different chemical states of carbon were investigated by acquiring the high-resolution C1s core level XPS spectra for both samples; the different contributes were assigned through a fitting procedure.

The C1s spectrum of DNDs, reported in Figure 2.9A, evidences the presence of predominant  $sp^3$ -hybridized carbon species, as depicted by the intense peak centered at 285.4 eV. In line with the elemental composition, the peak at higher binding energy (about 287.0 eV) is attributed to carbon bound to oxygen/nitrogen-containing groups [31].

The C1s core level XPS spectrum of p-CNOs, reported in Figure 2.9B, exhibits the characteristic asymmetrically broadened peak profile of conductive materials such as graphite, which is induced by the creation of electron-hole pairs during the process [32].

The spectrum was deconvoluted into five individual peaks, corresponding to the carbon atoms in different bonding states. The most intense peak at 284.48 eV and the lower intensity peak at 285.4 eV are attributed to carbon atoms with  $sp^2$  and  $sp^3$  hybridization, respectively [32]. The shifting of the  $sp^2$  carbon peak with respect to the value reported for graphite (i.e. 284 eV) is associated to the weakening of C–C bonding resulting from the curvature of the graphitic sheets [33, 34]. The higher binding energy peaks located at 286.5 eV and 287.9 eV are assigned to oxygen-bonded carbon atoms

in the form of hydroxyl and epoxy/ether groups (C–O) and carbonyl/quinone groups (C=O), while the presence of carboxylic acid groups (COOH) (peak at around 289.5 eV) is negligible (< 0.2%) [34–36]. Finally, the satellite peak at 290.7 eV corresponds to the  $\pi$ - $\pi^*$  transition in the aromatic systems, characteristic of graphitic structures [32, 34, 37].

The chemical state, the position and the area (%) for every peaks are reported in Table 2.3 and Table 2.4 for DNDs and p-CNOs, respectively.

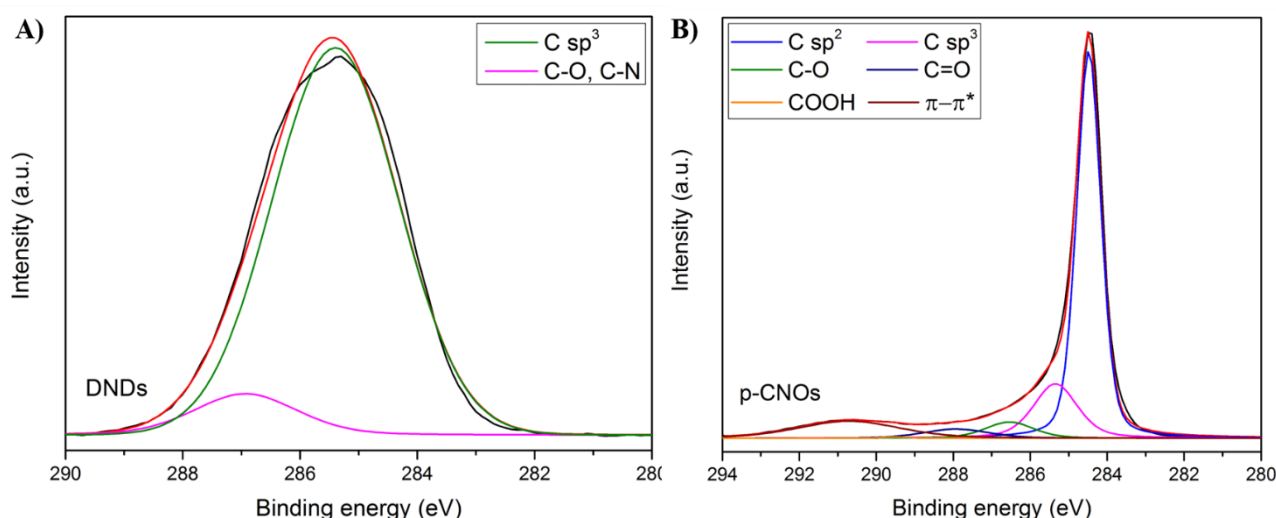


Figure 2.9: High-resolution XPS spectra of the C1s region of A) DNDs and B) p-CNOs, including peak-fitting analyses. Experimental and fitting curves are reported in black and red, respectively.

Table 2.3: Chemical state, position, area (%) and FWHM of the different peaks from the fitting of the C 1s peak of DNDs.

Sample	C-C sp <sup>3</sup> (eV)	C-O/C-N (eV)
DNDs	285.40 (91.30 %, 2.50)	286.93 (8.70 %, 2.00)

Table 2.4: Chemical state, position, area (%) and FWHM of the different peaks from the fitting of the C 1s peak of p-CNOs.

Sample	C-C sp <sup>2</sup> (eV)	C-C sp <sup>3</sup> (eV)	C-O (eV)	C=O (eV)	COOH (eV)	$\pi$ - $\pi^*$ (eV)
p-CNOs	284.48 (62.66 %, 0.75)	285.35 (16.47 %, 1.34)	286.54 (5.17 %, 1.47)	287.92 (3.99 %, 2.00)	289.50 (0.18 %, 0.69)	290.71 (11.53 %, 3.11)

### 2.3.5 Raman spectroscopy

Raman spectroscopy is a common and non-destructive technique for the structural characterization of carbon materials as it provides unique information about the structure, crystal size and  $\text{sp}^3/\text{sp}^2$  ratio [38–40]. A crucial factor in the Raman analysis of DNDs is the excitation wavelength as a strong fluorescence background is produced by exciting with visible light [41]. Therefore, as shown in

Figure 2.10A, where a 633 nm laser was employed to excite DNDs, it is impossible to determine diamond peak shape, position, and width.

While visible light-Raman scattering is more sensitive to  $\pi$  bonding, which exists in graphitic structures (C=C double bonds), UV-Raman scattering is more susceptible to the  $\sigma$  bonding states common to all carbon structures [20]. Due to the small Raman scattering cross-section of DNDs and the shielding effect of graphitic or amorphous carbon onto the ND surface, ultraviolet (UV) lasers are commonly employed for Raman investigation of DNDs to create near-resonance conditions. As the UV photon energy almost matches the energy band gap between electronic states of the ND  $\sigma$  bonds (i.e. 5.47 eV), its use allows for the amplification of the ND Raman signal and the suppression of the D band of graphitic carbon that may overlap with a weak diamond peak [29].

Figure 2.10B shows the Raman spectrum of DNDs excited with a 325 nm laser, showing two predominant broad peaks located at around  $1325\text{ cm}^{-1}$  and at  $1640\text{ cm}^{-1}$ . The typical Raman spectrum of single-crystal diamond exhibits a single peak corresponding to the vibrations of the two interpenetrating cubic sub-lattices at  $1333\text{ cm}^{-1}$  with a typical full-width at half-maximum (FWHM) equal to  $1\text{--}2\text{ cm}^{-1}$  [42]. Compared to natural diamond, the long-range order  $sp^3$  bonding ( $F_{2g}$  mode) results downshifted ( $\sim 8\text{ cm}^{-1}$ , located at  $1325\text{ cm}^{-1}$ ) and broadened (FWHM  $\sim 35\text{ cm}^{-1}$ ). In addition, a left-sided asymmetric narrow shoulder at  $\sim 1250\text{ cm}^{-1}$  is observed in the diamond peak, which originates from smaller NDs particles or smaller coherent scattering domains separated by defects in larger ND particles [29].

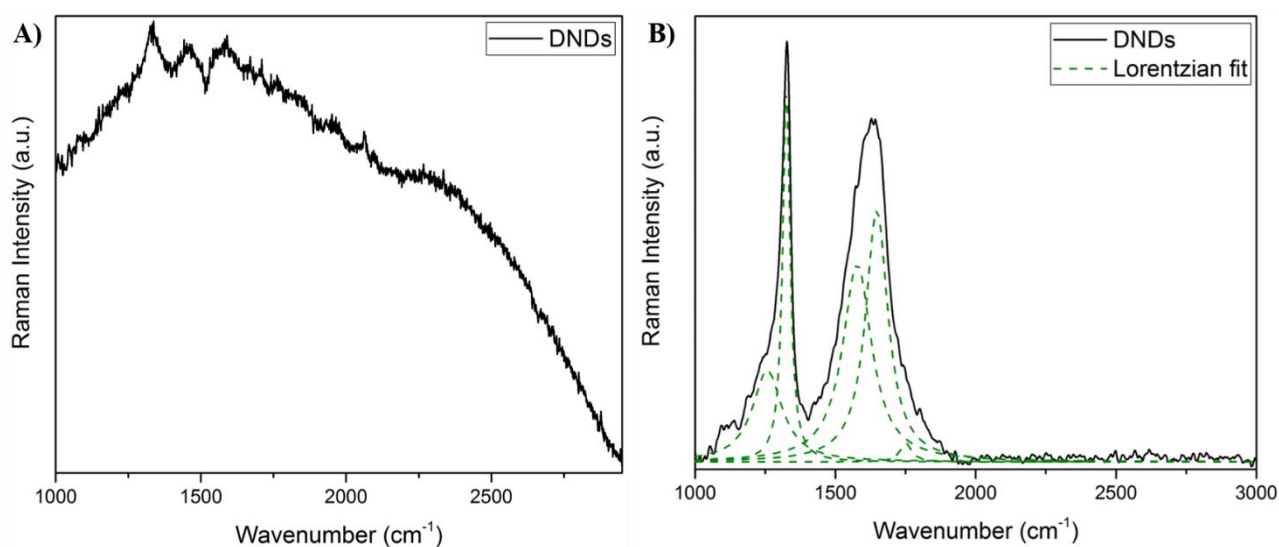


Figure 2.10: Raman spectra of DNDs at A)  $\lambda_{exc} = 633\text{ nm}$  and B)  $\lambda_{exc} = 325\text{ nm}$ , including Lorentzian peak fitting.

This behavior is usually observed for Raman spectra of DNDs and is due to the phonon confinement effect in nanostructures, which results in asymmetrically down-shifted and broadened Raman lines [41]. In an infinite crystal, because of momentum conservation between phonons and incident light,



only the phonons near the center of the Brillouin zone ( $q \sim 0$ ) are Raman active. However, in a finite crystal, the presence of crystal boundaries or defects can induce phonon confinement and this lead to the breakdown of selection rules in terms of quasi-momentum conservation, allowing phonons with  $q \neq 0$  to contribute to the Raman spectrum [43, 44].

The second broad peak observed in Figure 2.10B is attributed to the superposition of three different contributions. In particular, the peak located at  $1577 \text{ cm}^{-1}$  is assigned to the graphitic carbon band (G band), the O–H bending peak, coming from adsorbed or covalently linked species on the ND surface is located at  $1647 \text{ cm}^{-1}$ , while the shoulder at  $1751 \text{ cm}^{-1}$  is attributed to the C=O stretching vibration coming from surface functional groups [45].

To interpret the Raman spectra of graphitic structures, it is essential to analyze the phonon dispersion of graphite (Figure 2.11). The lattice of graphite exhibit two carbon atoms per unit cell and thus there are six phonon modes, three acoustic (A) and three optic (O); in addition, for all the phonon modes, two are in-plane modes (one longitudinal (L) and one transverse (iTO)) and one is an out-of-plane (oT) mode. For graphite, the LO and iTO phonon modes ( $E_{2g}$  symmetry) are degenerate at the  $\Gamma$  point (center of Brillouin zone) and are Raman active, while the oTO phonon mode is infrared active [46].

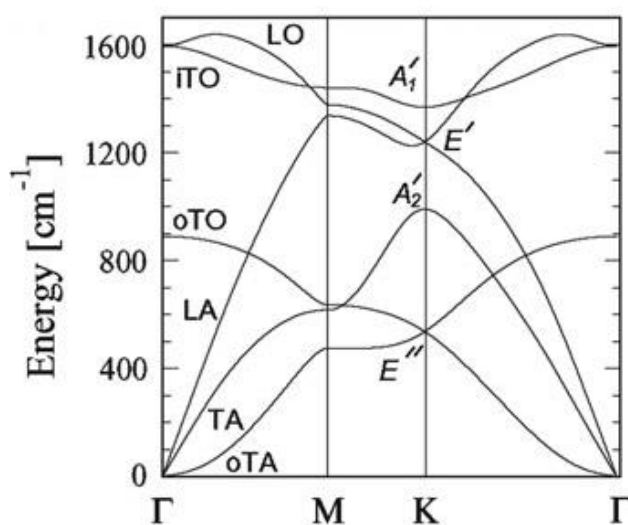


Figure 2.11: Calculated phonon dispersion relations of two dimensional graphite. Adapted with permission from [46].

Raman spectra of graphitic materials commonly exhibit different characteristic features. The G-band (appearing at  $1582 \text{ cm}^{-1}$  in graphite) is common to all graphitic materials and originates from the stretching of the C–C bond in  $sp^2$  carbon systems. This line is a doubly degenerate (iTO and LO) phonon mode ( $E_{2g}$  symmetry) at the Brillouin zone center and it is the Raman-active optic in plane stretching mode for  $sp^2$  carbon networks [46].

The D- (at around  $1350 \text{ cm}^{-1}$ ) and the D'- (at about  $1620 \text{ cm}^{-1}$ ) bands are defect-induced Raman features (thus these bands cannot be seen for a highly crystalline graphite) that become active due to the breakdown of the k-selection rule resulting from finite crystal size effects. The D peak is a

breathing mode of  $A_{1g}$  symmetry involving phonons near the K zone boundary which is forbidden in perfect graphite and it only becomes active in the presence of disorder.

The D' band, the higher-frequency component of the doublet observed at about  $1580\text{ cm}^{-1}$ , is due to a splitting of the doubly degenerate  $E_{2g}$  first-order line. The second-order G'-band (often called 2D) is a Raman-allowed feature appearing in the second-order Raman spectra of crystalline graphite in the range  $2500\text{--}2800\text{ cm}^{-1}$  activated by double resonance processes and corresponds to the overtone of the D band; interestingly, this peak has been observed even in single-crystal graphite, where the disorder-induced D band is typically absent. Finally, another disorder-induced Raman feature is observed at about  $2950\text{ cm}^{-1}$  and it is associated to combinational scattering (the D + G combination mode) [40, 47].

Figure 2.12 shows the Raman spectrum of p-CNOs excited with a 633 nm laser, which exhibits the typical features reported for CNOs [48, 49]. In particular, two prominent peaks assigned to the D-band at  $1321.9\text{ cm}^{-1}$  and the G-band at  $1580.8\text{ cm}^{-1}$  are observed along with the additional presence of the D'-band at about  $1614.4\text{ cm}^{-1}$  and the 2D-band at  $2644.4\text{ cm}^{-1}$ . The G peak center is slightly downshifted compared to that of graphite; this is due to the tensile strain in the graphitic planes induced by the introduction of pentagons during the formation of CNOs [50]. The D-band is very intense, confirming the high defectiveness of CNOs synthesized by thermal annealing [15].

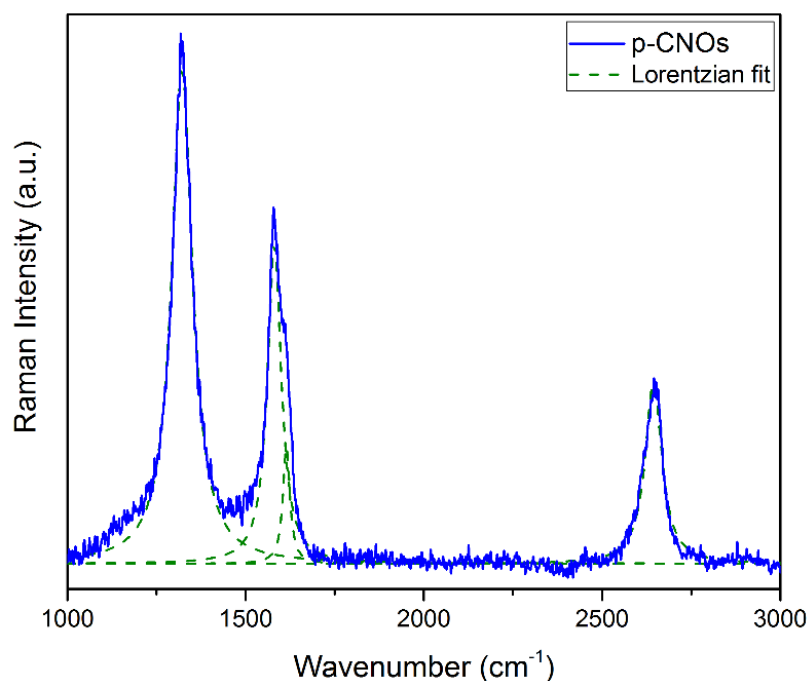


Figure 2.12: Raman spectrum of p-CNOs at  $\lambda_{exc} = 633\text{ nm}$ , showing a prominent D-band.

### 2.3.6 Fourier-transform infrared spectroscopy

Attenuated total reflectance Fourier-transform infrared spectroscopy (ATR-FTIR) analyses have been performed to have information on the functional groups preset on the material surface based on their characteristic stretching vibrations.

The FTIR spectrum of DNDs (Figure 2.13A) shows the presence of various functional groups on their surface. The broad band between 3000 and 3500  $\text{cm}^{-1}$  may be attributed to the overlapping of N-H stretching bands and the O-H bands from water molecules, while the low-intensity peaks in the 2800–3000  $\text{cm}^{-1}$  region are characteristic peaks of DNDs attributed to the stretching vibration of C-H bonds.

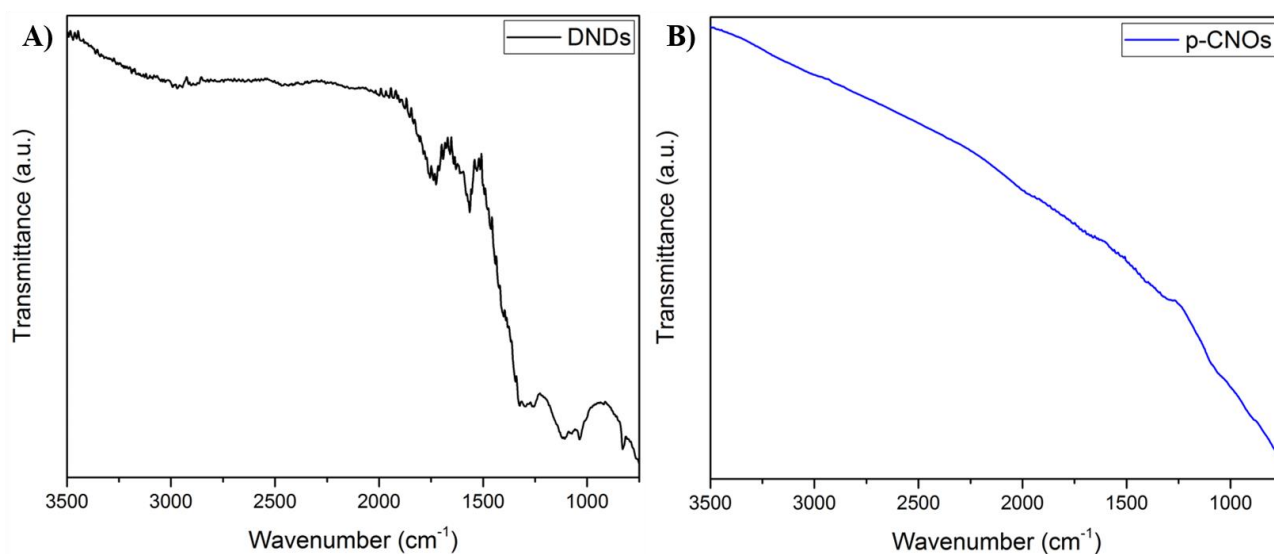


Figure 2.13: FTIR spectra of A) DNDs and B) p-CNOs.

The peaks at 1568 and 825  $\text{cm}^{-1}$  corresponds to the in-plane and out of plane bending of N-H, whereas the peak at around 1730  $\text{cm}^{-1}$  is assigned to the stretching vibrations of the carbonyl groups (C=O). The peaks around 1100–1400  $\text{cm}^{-1}$  are probably caused by C–N and N–H bonds due to nitrogen impurity distributed in diamond structure as well as to the –C–O–C– absorption. In the specific, the peaks at 1114, 1076 and 1035  $\text{cm}^{-1}$  may be assigned to the C–O vibrations in alcohol groups, while the peaks at around 1290  $\text{cm}^{-1}$  to the stretching of C–N and C–O–C groups [51, 52].

On the contrary, the FTIR spectrum of p-CNOs (Figure 2.13B) shows no significant IR bands, in agreement with what reported [23].

### 2.3.7 Thermogravimetric analysis

The thermal behavior of DNDs and p-CNOs was investigated by thermogravimetric analysis (TGA) in air. Figure 2.14 plots the TGA (solid lines) and the corresponding weight loss derivatives (dotted lines) curves of DNDs (black) and p-CNOs (blue). Both samples exhibit a single weight loss transition, suggesting their homogeneous single phase as further confirmed by the absence of any

residue. DNDs show a decomposition temperature of 575 °C, while p-CNOs decompose at 699 °C, thus showing a higher thermal stability compared to DNDs (Table 2.5).

No significant mass change in the whole temperature range is observed for both samples. DNDs exhibit a negligible mass loss in the range 200–300 °C due to the decomposition of oxygen-containing functional groups. Furthermore, an oxidation-induced weight gain of about 0.5% at around 447 °C is observed for both samples. The observed weight gain is due to the thermally oxidation of  $sp^2$  carbons into various oxygen-containing groups. In particular, in the case of NDs, this produces a reduced burning-off temperature through co-burning the diamonds with the  $sp^2$  carbons [53].

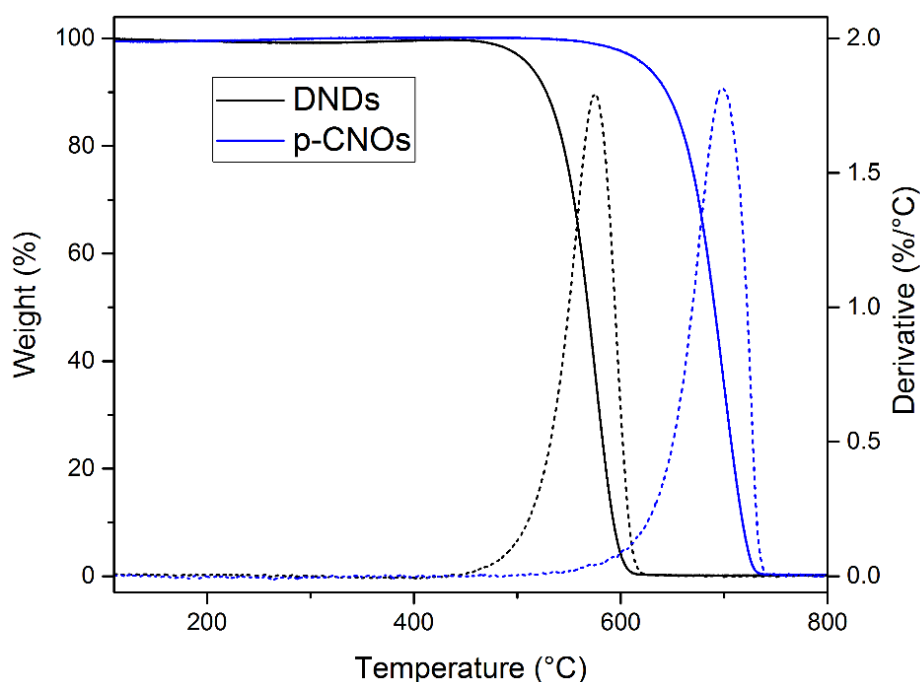


Figure 2.14: Thermogravimetric analysis (solid lines) and the corresponding weight loss derivatives (dotted lines) of DNDs (black) and p-CNOs (blue), showing the higher thermal stability of p-CNOs..

Table 2.5: decomposition temperature for DNDs and p-CNOs.

Sample	$T_{dec}$
DNDs	575 °C
p-CNOs	699 °C

### 2.3.8 BET nitrogen adsorption analysis

Brunauer, Emmett and Teller (BET) nitrogen adsorption analyses were performed in order to have information on the textural properties of the different samples. The BET isotherm graphs of DNDs and p-CNOs are reported in Figure 2.15A-B and show in both cases a type IV isotherm with a distinct hysteresis loop observed in the range of 0.8–1.0  $P/P_0$ , indicating that the main pore volume is contributed by mesopores as a consequence of the capillary condensation effect.

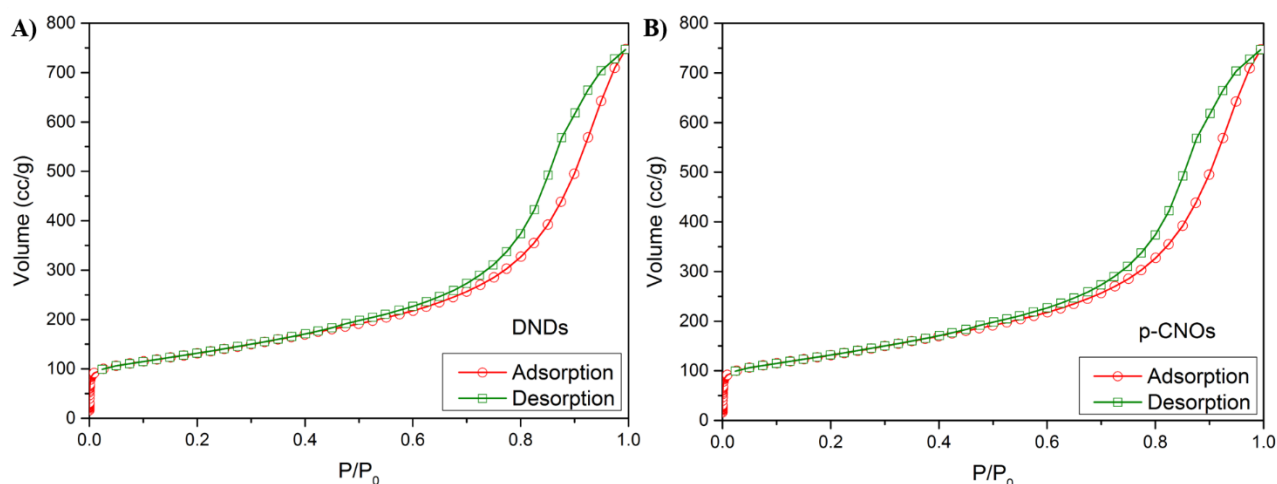


Figure 2.15: BET isotherm of A) DNDs and B) p-CNOs.

Treating the data according to the Brunauer, Emmett and Teller (BET) adsorption isotherm equation, the specific surface area (SSA) is found to be equal to 230.263 m<sup>2</sup>/g and 462.366 m<sup>2</sup>/g for DNDs and p-CNOs, respectively (Table 2.6).

Table 2.6: Specific surface areas (SSAs) of DNDs and p-CNOs.

Sample	SSA (m <sup>2</sup> /g)
DNDs	230.26
p-CNOs	462.37

The volume and pore size distribution were evaluated by density functional theory (DFT) method. Both samples have mainly a mesoporous structure with pores in the 2–50 nm diameter range. In particular, DNDs exhibit a pore size distribution centered at around 11.761 nm (Figure 2.16B), while p-CNO pore size is mainly distributed at around 10.775 nm (Figure 2.16B); in addition, a small fraction of micropores (<2 nm) was observed in both samples.

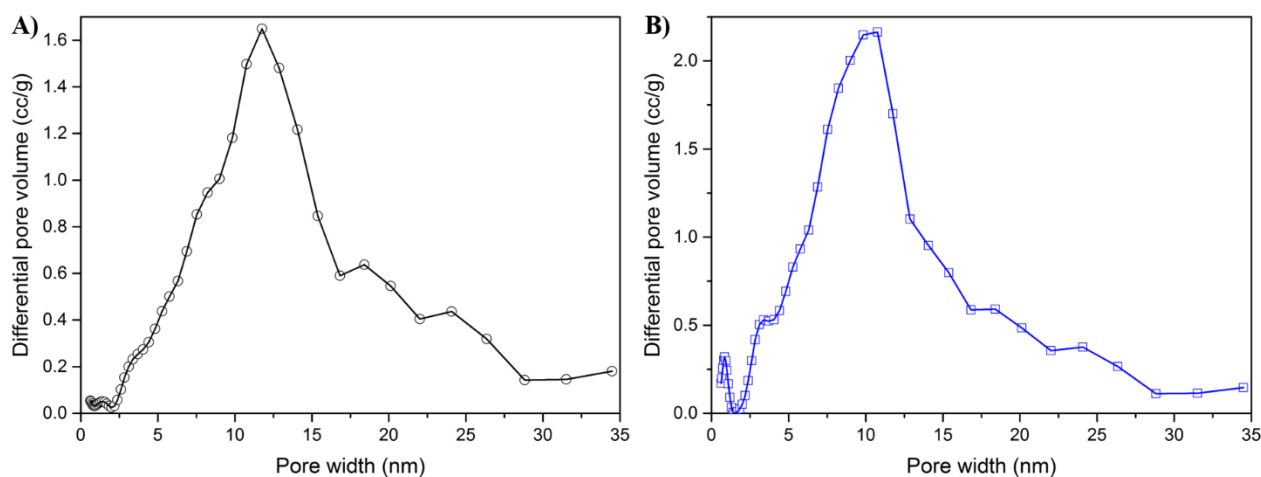


Figure 2.16: Pore size distribution of A) DNDs and B) p-CNOs calculated by DFT method.

Assuming that the particles have solid, spherical shape with smooth surface, and same size, the surface area can be related to the average equivalent particle size by the equation:

$$D_{BET} = \frac{6000}{\rho \cdot S_{BET}}$$

where  $D_{BET}$  is the average diameter of a spherical particle (in nm),  $S_{BET}$  represents the measured surface area of the powder in  $\text{m}^2/\text{g}$ , and  $\rho$  is the theoretical density in  $\text{g}/\text{cm}^3$  ( $3.51 \text{ g}/\text{cm}^3$  for DNDs and  $2.2 \text{ g}/\text{cm}^3$  for p-CNOs) [54]. The corresponding value was found to be 7.42 nm and 5.89 nm, respectively. p-CNOs exhibit in general a higher surface area and slightly lower pore sizes compared to DNDs. In addition, the diameter obtained from p-CNOs is in perfect agreement with the value obtained from HRTEM investigations.

## 2.4 Conclusion

The synthesis of small spherical CNOs have been successfully achieved by thermal annealing at  $1650^\circ\text{C}$  by using DNDs as precursor, as confirmed by several characterization techniques. HRTEM investigations have proved the formation of quasi-spherical multi-layered CNOs with an average diameter of 6 nm, as depicted from the size distribution analysis. The nanoparticles consist of 7-10 graphitic shells with an interlayer distance close to that reported for graphite surrounding a hollow core, confirming the absence of a remaining diamond phase. The graphitic nature of the synthesized CNOs was further confirmed by EELS, XRD and Raman spectroscopy, which showed characteristic features of  $\text{sp}^2$ -hybridized carbon atoms and in agreement with the reported literature for CNOs. In addition, XPS analysis showed that CNOs are mainly composed by graphitic carbon with a sufficient percentage of  $\text{sp}^3$  carbon atoms, suggesting the defectiveness of the structure; further evidence of this feature has been provided by the prominent D-band showed in the Raman spectrum and from HRTEM images, which showed defective outermost shells. This aspect, together with the high thermal stability and remarkable specific surface area, makes CNOs a very attractive material for different applications.

## 2.5 References

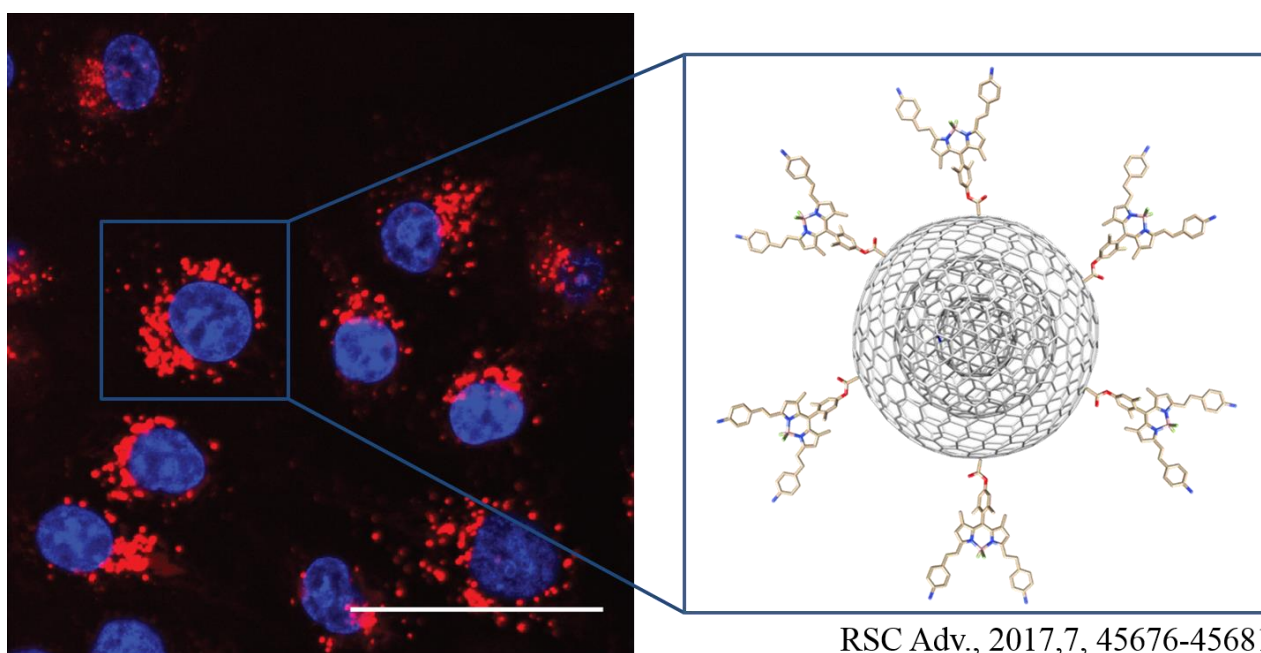
- [1] Ugarte, D., Curling and closure of graphitic networks under electron-beam irradiation. *Nature*, **1992**, 359, 707-709.
- [2] Ugarte, D., Onion-Like graphitic particles. *Carbon*, **1995**, 33, 989-993.
- [3] Sano, N.; Wang, H.; Chhowalla, M.; Alexandrou, I.; Amaratunga, G.A.J., Synthesis of carbon 'onions' in water. *Nature*, **2001**, 414, 506-507.
- [4] Sano, N.; Wang, H.; Alexandrou, I.; Chhowalla, M.; Teo, K.B.K.; Amaratunga, G.A.J.; Iimura, K., Properties of carbon onions produced by an arc discharge in water. *J. Appl. Phys.*, **2002**, 92, (5), 2783-2788.
- [5] He, C.N.; Zhao, N.; Du, X.; Shi, C.; Ding, J.; Li, J.; Li, Y., Low-temperature synthesis of carbon onions by chemical vapor deposition using a nickel catalyst supported on aluminum. *Scripta Mater.*, **2006**, 54, (4), 689-693.
- [6] Chen, X.H.; Deng, F.M.; Wang, J.X.; Yang, H.S.; Wu, G.T.; Zhang, X.B.; Peng, J.C.; Li, W.Z., New method of carbon onion growth by radio-frequency plasma-enhanced chemical vapor deposition. *Chem. Phys. Lett.*, **2001**, 336, 201-204.
- [7] Huang, J.Y.; Yasuda, H.; Mori, H., Highly curved carbon nanostructures produced by ball-milling. *Chem. Phys. Lett.*, **1999**, 303, (1), 130-134.
- [8] Chen, X.H.; Yang, H.S.; Wu, G.T.; Wang, M.; Deng, F.M.; Zhang, X.B.; Peng, J.C.; Li, W.Z., Generation of curved or closed-shell carbon nanostructures by ball-milling of graphite. *J. Cryst. Growth*, **2000**, 218, (1), 57-61.
- [9] Cabioc'h, T.; Jaouen, M.; Thune, E.; Gu'erin, P.; Fayoux, C.; Denanot, M.F., Carbon onions formation by high-dose carbon ion implantation into copper and silver. *Surf. Coat. Technol.*, **2000**, 128, 43-50.
- [10] Thune, E.; Cabioc'h, T.; Gue'rin, P.; Denanot, M.-F.; Jaouen, M., Nucleation and growth of carbon onions synthesized by ion-implantation: a transmission electron microscopy study. *Mater. Lett.*, **2002**, 54, (2), 222-228.
- [11] Kuznetsov, V.L.; Chuvilin, A.L.; Butenko, Y.V.; Mal'kov, I.Y.; Titov, V.M., Onion-like carbon from ultra-disperse diamond. *Chem. Phys. Lett.*, **1994**, 222, 343-348.
- [12] Kuznetsov, V.L.; Zilberberg, I.L.; Butenko, Y.V.; Chuvilin, A.L.; Segall, B., Theoretical study of the formation of closed curved graphite-like structures during annealing of diamond surface. *J. Appl. Phys.*, **1999**, 86, (2), 863-870.
- [13] Chen, J.; Deng, S.Z.; Chen, J.; Yu, Z.X.; Xu, N.S., Graphitization of nanodiamond powder annealed in argon ambient. *Appl. Phys. Lett.*, **1999**, 74, (24), 3651-3653.
- [14] Zeiger, M.; Jäckel, N.; Weingarth, D.; Presser, V., Vacuum or flowing argon: What is the best synthesis atmosphere for nanodiamond-derived carbon onions for supercapacitor electrodes? *Carbon*, **2015**, 94, 507-517.
- [15] Palkar, A.; Melin, F.; Cardona, C.M.; Elliott, B.; Naskar, A.K.; Edie, D.D.; Kumbhar, A.; Echegoyen, L., Reactivity differences between carbon nano onions (CNOs) prepared by different methods. *Chem. Asian J.*, **2007**, 2, (5), 625-633.
- [16] Camisasca, A.; Giordani, S., Carbon nano-onions in biomedical applications: Promising theranostic agents. *Inorg. Chim. Acta*, **2017**, 468, 67-76.
- [17] Tomita, S.; Sakurai, T.; Ohta, H.; Fujii, M.; Hayashi, S., Structure and electronic properties of carbon onions. *J. Chem. Phys.*, **2001**, 114, (17), 7477-7482.
- [18] Pichot, V.; Risse, B.; Schnell, F.; Mory, J.; Spitzer, D., Understanding ultrafine nanodiamond formation using nanostructured explosives. *Scientific Reports*, **2013**, 3, 2159.
- [19] Joly-Pottuz, L.; Vacher, B.; Ohmae, N.; Martin, J.M.; Epicier, T., Anti-wear and Friction Reducing Mechanisms of Carbon Nano-onions as Lubricant Additives. *Tribol. Lett.*, **2008**, 30, (1), 69-80.
- [20] Mykhaylyk, O.O.; Solonin, Y.M.; Batchelder, D.N.; Brydson, R., Transformation of nanodiamond into carbon onions: A comparative study by high-resolution transmission electron

- microscopy, electron energy-loss spectroscopy, x-ray diffraction, small-angle x-ray scattering, and ultraviolet Raman spectroscopy. *J. Appl. Phys.*, **2005**, 97, (7), 074302.
- [21] Tomita, S.; Fujii, M.; Hayashi, S.; Yamamoto, K., Electron energy-loss spectroscopy of carbon onions. *Chem. Phys. Lett.*, **1999**, 305, 225-229.
- [22] Chhowalla, M.; Wang, H.; Sano, N.; Teo, K.B.K.; Lee, S.B.; Amaratunga, G.A.J., Carbon Onions: Carriers of the 217.5 nm Interstellar Absorption Feature. *Physical Review Letters*, **2003**, 90, (15), 155504.
- [23] Bartelmess, J.; De Luca, E.; Signorelli, A.; Baldrighi, M.; Becce, M.; Brescia, R.; Nardone, V.; Parisini, E.; Echegoyen, L.; Pompa, P.P.; Giordani, S., Boron dipyrromethene (BODIPY) functionalized carbon nano-onions for high resolution cellular imaging. *Nanoscale*, **2014**, 6, (22), 13761-13769.
- [24] Ozerin, A.N.; Kurkin, T.S.; Ozerina, L.A.; Dolmatov, V.Y., X-ray diffraction study of the structure of detonation nanodiamonds. *Crystallogr. Rep.*, **2008**, 53, (1), 60-67.
- [25] Tomita, S.; Burian, A.; Dore, J.C.; LeBolloch, D.; Fujii, M.; Shinji, H., Diamond nanoparticles to carbon onions transformation: X-ray diffraction studies. *Carbon*, **2002**, 40, 1469-1474.
- [26] Kuznetsov, V.L.; Chuvilin, A.L.; Moroz, E.M.; Kolomiichuk, V.N.; Shaikhutdinov, S.K.; Butenko, Y.V.; Mal'kov, I.Y., Effect of explosion conditions on the structure of detonation soots: ultradisperse diamond and onion carbon. *Carbon*, **1994**, 32, (5), 873-882.
- [27] Holzwarth, U.; Gibson, N., The Scherrer equation versus the Debye-Scherrer equation. *Nature Nanotechnology*, **2011**, 6, 534.
- [28] Pichot, V.; Stephan, O.; Comet, M.; Fousson, E.; Mory, J.; March, K.; Spitzer, D., High Nitrogen Doping of Detonation Nanodiamonds. *J. Phys. Chem. C* **2010**, 114, 10082-10087.
- [29] Mochalin, V.N.; Shenderova, O.; Ho, D.; Gogotsi, Y., The properties and applications of nanodiamonds. *Nat. Nanotechnol.*, **2011**, 7, (1), 11-23.
- [30] Pichot, V.; Comet, M.; Fousson, E.; Baras, C.; Senger, A.; Le Normand, F.; Spitzer, D., An efficient purification method for detonation nanodiamonds. *Diamond and Related Materials*, **2008**, 17, (1), 13-22.
- [31] Petit, T.; Arnault, J.-C.; Girard, H.A.; Sennour, M.; Bergonzo, P., Early stages of surface graphitization on nanodiamond probed by x-ray photoelectron spectroscopy. *Physical Review B*, **2011**, 84, (23), 233407.
- [32] Estrade-Szwarczkopf, H., XPS photoemission in carbonaceous materials: A “defect” peak beside the graphitic asymmetric peak. *Carbon*, **2004**, 42, (8), 1713-1721.
- [33] Kalita, G.; Adhikari, S.; Aryal, H.R.; Umeno, M.; Afre, R.; Soga, T.; Sharon, M., Fullerene (C<sub>60</sub>) decoration in oxygen plasma treated multiwalled carbon nanotubes for photovoltaic application. *Applied Physics Letters*, **2008**, 92, (6), 063508.
- [34] Butenko, Y.V.; Krishnamurthy, S.; Chakraborty, A.K.; Kuznetsov, V.L.; Dhanak, V.R.; Hunt, M.R.C.; Šiller, L., Photoemission study of onionlike carbons produced by annealing nanodiamonds. *Physical Review B*, **2005**, 71, (7), 075420.
- [35] Plonska-Brzezinska, M.E.; Lewandowski, M.; Błaszyk, M.; Molina-Ontoria, A.; Luciński, T.; Echegoyen, L., Preparation and Characterization of Carbon Nano-Onion/PEDOT:PSS Composites. *ChemPhysChem*, **2012**, 13, (18), 4134-4141.
- [36] Haubner, K.; Murawski, J.; Olk, P.; Eng, L.M.; Ziegler, C.; Adolphi, B.; Jaehne, E., The Route to Functional Graphene Oxide. *ChemPhysChem*, **2010**, 11, (10), 2131-2139.
- [37] Leiro, J.A.; Heinonen, M.H.; Laiho, T.; Batirev, I.G., Core-level XPS spectra of fullerene, highly oriented pyrolytic graphite, and glassy carbon. *Journal of Electron Spectroscopy and Related Phenomena*, **2003**, 128, (2), 205-213.
- [38] Dresselhaus, M.S.; Jorio, A.; Hofmann, M.; Dresselhaus, G.; Saito, R., Perspectives on Carbon Nanotubes and Graphene Raman Spectroscopy. *Nano Letters*, **2010**, 10, (3), 751-758.
- [39] Ferrari, A.C., Determination of bonding in diamond-like carbon by Raman spectroscopy. *Diamond and Related Materials*, **2002**, 11, (3), 1053-1061.



- [40] Ferrari, A.C.; Robertson, J., Interpretation of Raman spectra of disordered and amorphous carbon. *Phys. Rev. B*, **2000**, *61*, 14095.
- [41] Osswald, S.; Mochalin, V.N.; Havel, M.; Yushin, G.; Gogotsi, Y., Phonon confinement effects in the Raman spectrum of nanodiamond. *Physical Review B*, **2009**, *80*, (7), 075419.
- [42] Praver, S.; Nemanich, R.J., Raman spectroscopy of diamond and doped diamond. *Philosophical Transactions of the Royal Society of London. Series A: Mathematical, Physical and Engineering Sciences*, **2004**, *362*, (1824), 2537.
- [43] Yoshikawa, M.; Mori, Y.; Obata, H.; Maegawa, M.; Katagiri, G.; Ishida, H.; Ishitani, A., Raman scattering from nanometer-sized diamond. *Applied Physics Letters*, **1995**, *67*, (5), 694-696.
- [44] Aleksenskii, A.E.; Baidakova, M.V.; Vul', A.Y.; Davydov, V.Y.; Pevtsova, Y.A., Diamond-graphite phase transition in ultradisperse-diamond clusters. *Physics of the Solid State*, **1997**, *39*, (6), 1007-1015.
- [45] Mochalin, V.; Osswald, S.; Gogotsi, Y., Contribution of Functional Groups to the Raman Spectrum of Nanodiamond Powders. *Chem. Mater.*, **2009**, *21*, (2), 273-279.
- [46] Pimenta, M.A.; Dresselhaus, G.; Dresselhaus, M.S.; Cancado, L.G.; Jorio, A.; Saito, R., Studying disorder in graphite-based systems by Raman spectroscopy. *Phys. Chem. Chem. Phys.*, **2007**, *9*, (11), 1276-1291.
- [47] Matthews, M.J.; Pimenta, M.A.; Dresselhaus, G.; Dresselhaus, M.S.; Endo, M., Origin of dispersive effects of the Raman D band in carbon materials. *Physical Review B*, **1999**, *59*, (10), R6585-R6588.
- [48] Obraztsova, E.D.; Fujii, M.; Hayashi, S.; Kuznetsov, V.L.; Butenko, Y.V.; Chuvilin', A.L., Raman identification of onion-like carbon. *Carbon*, **1998**, *36*, (5-6), 821-826.
- [49] Bacsá, W.S.; de Heer, W.A.; Ugarte, D.; Châtelain, A., Raman spectroscopy of closed-shell carbon particles. *Chemical Physics Letters*, **1993**, *211*, (4), 346-352.
- [50] Roy, D.; Chhowalla, M.; Wang, H.; Sano, N.; Alexandrou, I.; Clyne, T.W.; Amaratunga, G.A.J., Characterisation of carbon nano-onions using Raman spectroscopy. *Chemical Physics Letters*, **2003**, *373*, (1), 52-56.
- [51] Amanee, D.S.; Patrick, T.J.H.; Aliza, P.; Hadiyah, N.G.; Ho-wook, J.; Derrick, D., Nanodiamonds enhance therapeutic efficacy of doxorubicin in treating metastatic hormone-refractory prostate cancer. *Nanotechnology*, **2014**, *25*, (42), 425103.
- [52] Petit, T.; Puskar, L., FTIR spectroscopy of nanodiamonds: Methods and interpretation. *Diamond and Related Materials*, **2018**, *89*, 52-66.
- [53] Huang, H.; Dai, L.; Wang, D.H.; Tan, L.-S.; Osawa, E., Large-scale self-assembly of dispersed nanodiamonds. *Journal of Materials Chemistry*, **2008**, *18*, (12), 1347-1352.
- [54] Zeiger, M.; Jäckel, N.; Aslan, M.; Weingarth, D.; Presser, V., Understanding structure and porosity of nanodiamond-derived carbon onions. *Carbon*, **2015**, *84*, 584-598.

## *Chapter 3 - Far-red fluorescent carbon nano-onions as bright biological imaging agents*



### **3.1 Introduction**

Biomedical imaging is currently an important research area, which have taken advantage of the remarkable technologic development in the field of medicine. Nowadays, well-established imaging techniques such as computed tomography (CT), positron emission tomography (PET) and magnetic resonance imaging (MRI) are commonly used in the medical field, playing a central role due to their remarkable penetration depth. However, the restricted spatial resolution and the long acquisition time, which prevents a real-time monitoring, have hindered their progression. High sensitivity and resolution as well as fast response are the main factors that have made fluorescent-based biomedical imaging an interesting alternative to the standard tomographic techniques. On the other hand, the main disadvantage relies on their limited tissue penetration [1].

In the visible region, biological tissues and water induce the scattering and the absorption of the photons, resulting in the attenuation of the signal. An efficient way to overcome this problem is to employ imaging agents with emission in the biologically important near-infrared (NIR) region (650-900 nm). The lower absorption and scattering of tissues in this region allow for a deeper light penetration and thus an enhanced bio-imaging efficiency [1, 2].

The rapid development of nanomaterials, showing properties non-attainable in common bulk materials, has stimulated an intense research in different research fields, including biomedicine.

In this context, the use of nanoprobles with remarkable properties such as high surface area and the ease of functionalization leads to promising outcomes as imaging agents. In addition, the possibility to combine in the same platform imaging and drug delivery features allows for the development of novel approaches for both diagnosis and therapy [2].

In recent years, carbon nanomaterials (CNMs) such as CNTs [3, 4], fullerenes [5, 6], graphene and its derivative [7, 8] and carbon quantum dots [9, 10] have been explored for biomedical applications due to their small size, unique optical properties and large surface area. In particular, their size is comparable to that of biologically relevant entities such as DNA and proteins, making them ideal biocompatible platforms for biomedical purposes [11].

Among the different CNMs, carbon nano-onions (CNOs) have shown to be a biocompatible material both *in vitro* [12, 13] and *in vivo* [14, 15]. The low cytotoxicity, the efficient cellular uptake and the weak inflammatory potential play a central role for the use of CNOs in biomedical applications [16]. In this chapter, I will present the development of a novel CNO-based bio-imaging platform with high and bright fluorescence and enhanced dispersing ability in biological fluids.

For this purpose, in order to improve the solubility in water, a chemical oxidation procedure was performed to introduce carboxylic acid functional groups onto the CNO surface. A novel far-red emitting boron dipyrromethene (BODIPY) dye derivative, containing water-soluble groups, was developed in the Giordani lab. The coupling of the dye to the surface of the oxidized CNO was obtained by esterification reaction and the successful functionalization was monitored by means of several characterization analyses.

The bright luminescence in the far-red region due to the high dye quantum yield of the fluo-CNOs allowed for the *in vitro* investigations in human breast cancer cells (MCF-7). The results showed an efficient cellular uptake and negligible toxic effects, even at very low concentration, confirming the excellent features of this novel biocompatible platform for high-resolution cellular bio-imaging.

## 3.2 Experimental

### 3.2.1 Synthesis of pristine carbon nano-onions

The synthesis of 5 nm-sized pristine carbon nano-onions (p-CNOs) has been achieved by thermal annealing process as discussed in the previous chapter (paragraph 2.2.1).

### 3.2.2 Synthesis of oxidized carbon nano-onions

The oxidation of p-CNOs to introduce carboxylic acid functionalities on the CNO surface has been carried out by following a modified procedure previously reported [17]. A schematization of the oxidation procedure is reported in Figure 3.1.

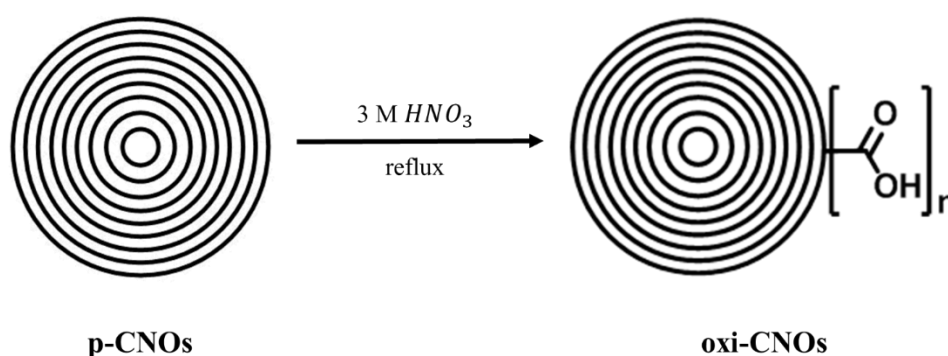


Figure 3.1: Schematization of the oxidation procedure to yield oxi-CNOs.

Briefly, 50 mg of p-CNOs were dispersed by ultrasonication (20 minutes at 37 kHz) in 30 mL of a 3 M solution of nitric acid ( $\text{HNO}_3$ ). The solution was stirred under reflux conditions for 48 hours at 110 °C. After cooling down to room temperature, oxidized CNOs (oxi-CNOs) were separated from the acidic solution by centrifugation (15 minutes at 1800 rpm) to remove the excess of  $\text{HNO}_3$  and redispersed in deionized water ( $\text{dH}_2\text{O}$ ). The dispersion was then filtered off on a 0.2  $\mu\text{m}$  pore sized-nylon filter membrane and thoroughly washed three times with  $\text{dH}_2\text{O}$ , dimethylformamide (DMF), methanol ( $\text{CH}_3\text{OH}$ ) and acetone ( $\text{C}_3\text{H}_6\text{O}$ ). 51.2 mg of oxi-CNOs were recovered as a black powder after drying overnight at room temperature.

### 3.2.3 Synthesis of fluorescently labelled carbon nano-onions

The attachment of a  $\pi$ -extended distyryl-substituted boron dipyrromethene (BODIPY) dye derivative, synthesized by Dr. Stefania Lettieri, postdoc in the NACM group at IIT, was accomplished by esterification reaction between the carboxylic acid groups onto the surface of oxi-CNOs and the hydroxyl group of the BODIPY dye through EDC coupling protocol. A schematization of the coupling procedure is reported in Figure 3.2.

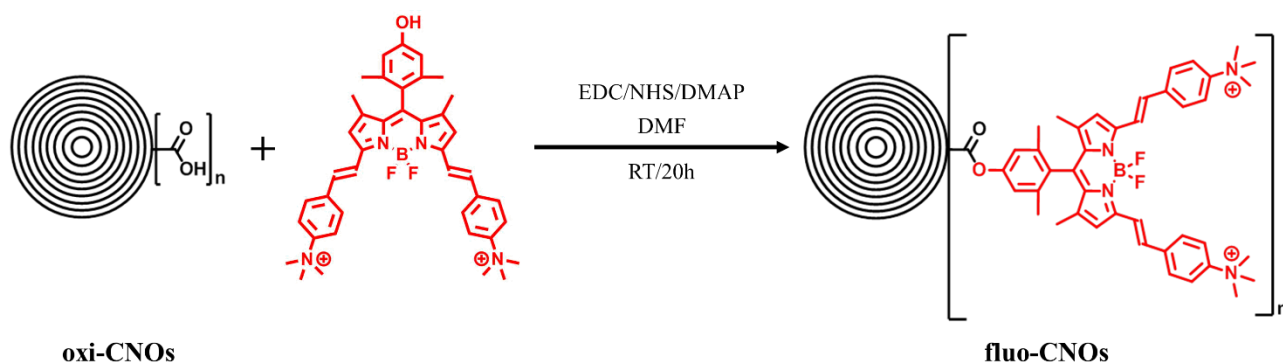


Figure 3.2: Schematization of the coupling procedure to yield fluo-CNOs.

10 mg of oxi-CNOs were dispersed by ultrasonication (30 minutes at 37 kHz) in 10 mL of anhydrous DMF. Then, 9.2 mg (0.08 mmol) of N-hydroxysuccinimide (NHS), 12 mg (0.01 mmol) of 4-dimethylaminopyridine (DMAP) and 14  $\mu\text{L}$  of 1-ethyl-3-(3-dimethylaminopropyl) carbodiimide (EDC) were added to the reaction mixture. After a brief sonication and the addition of 4 mg of BODIPY dye (0.0044 mmol), the solution was stirred at room temperature for 20 hours under nitrogen atmosphere. The fluorescent CNOs (fluo-CNOs) were filtered off on a 0.2  $\mu\text{m}$  pore sized-nylon filter membrane and thoroughly washed three times with DMF, tetrahydrofuran (THF) and  $\text{CH}_3\text{OH}$  to remove any unreacted dye and reagents. 12 mg of fluo-CNOs were recovered as a black powder after drying overnight at room temperature.

## 3.3 Results and discussion

### 3.3.1 Transmission electron microscopy

HRTEM analyses were performed to investigate the influence of the surface functionalization on the morphological features of CNOs. HRTEM images of oxi-CNOs and fluo-CNOs are shown in Figure 3.3. As clearly suggested by the analyses of the high-resolution electron micrographs, both CNO derivatives exhibit the typical concentric graphitic multi-layered structure [18]. No changes were thus observed on the CNO architecture as a consequence of the surface functionalization procedures compared to that of p-CNOs (Figure 2.3).

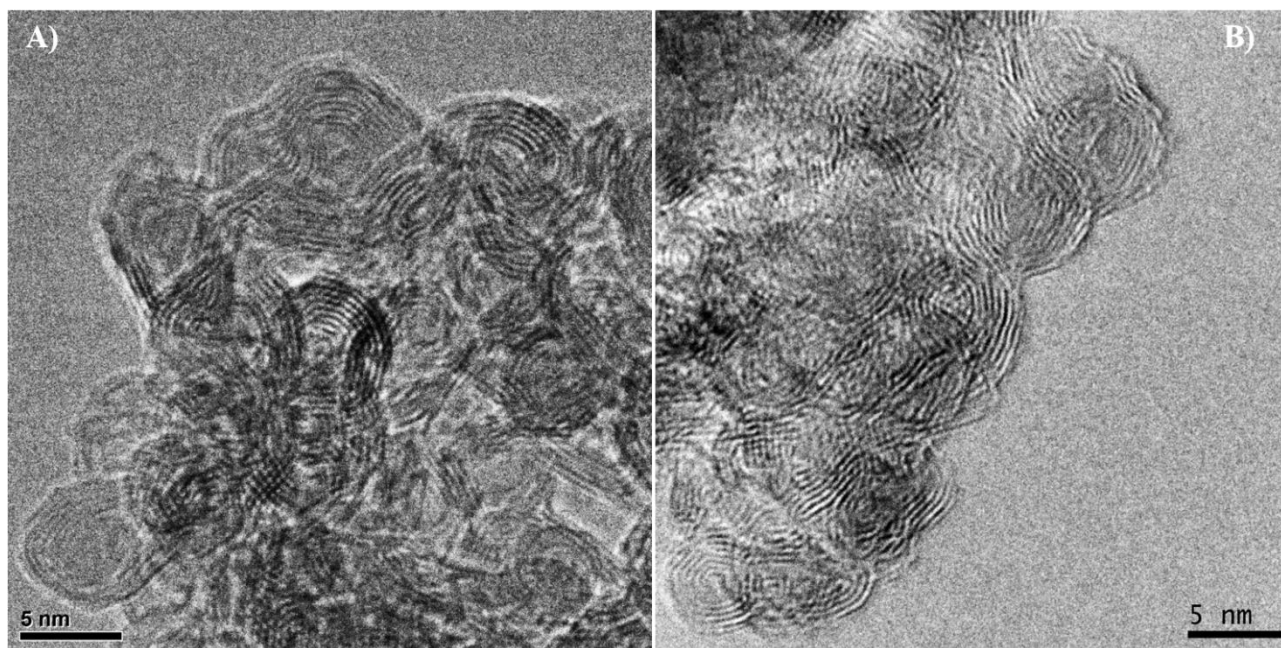


Figure 3.3: Representative HRTEM images of A) oxi-CNOs and B) fluo-CNOs.

### 3.3.2 X-ray photoelectron spectroscopy

XPS analyses were performed to investigate the elemental composition of the samples and thus confirm the successful introduction of carboxylic acid groups onto the surface of p-CNOs and the further attachment of the BODIPY dyes on oxi-CNOs. The elemental composition of all the samples is shown in Table 3.1.

Table 3.1: Elemental composition of p-, oxi- and fluo-CNOs from XPS analyses.

Sample	C content (%)	O content (%)	N content (%)	F content (%)
p-CNOs	99.0	1.0	-	-
oxi-CNOs	92.5	7.5	-	-
fluo-CNOs	90.1	7.1	1.9	0.9

The XPS survey spectra of all the CNO derivatives are reported in Figure 3.4. As discussed in the previous chapter (paragraph 2.3.4), p-CNOs consist of mainly carbon atoms (99%) with a small content of oxygen (1%). The clearest difference in the XPS spectrum of oxi-CNOs to that of p-CNOs is the marked increase in the oxygen amount upon oxidation (7.5%), which can be assigned to the successful introduction of carboxylic acid functionalities onto the CNO surface. Regarding the fluo-CNOs, the additional presence of nitrogen and fluorine in atomic percentage of 1.9% and 0.9%, respectively, confirmed the attachment of the BODIPY dyes to the oxidized surface of CNOs. Their content is in a ratio (2:1) in agreement with that of BODIPY (four nitrogen and two fluorine atoms per dye molecule), thus providing evidence of its presence and that it was not degraded.

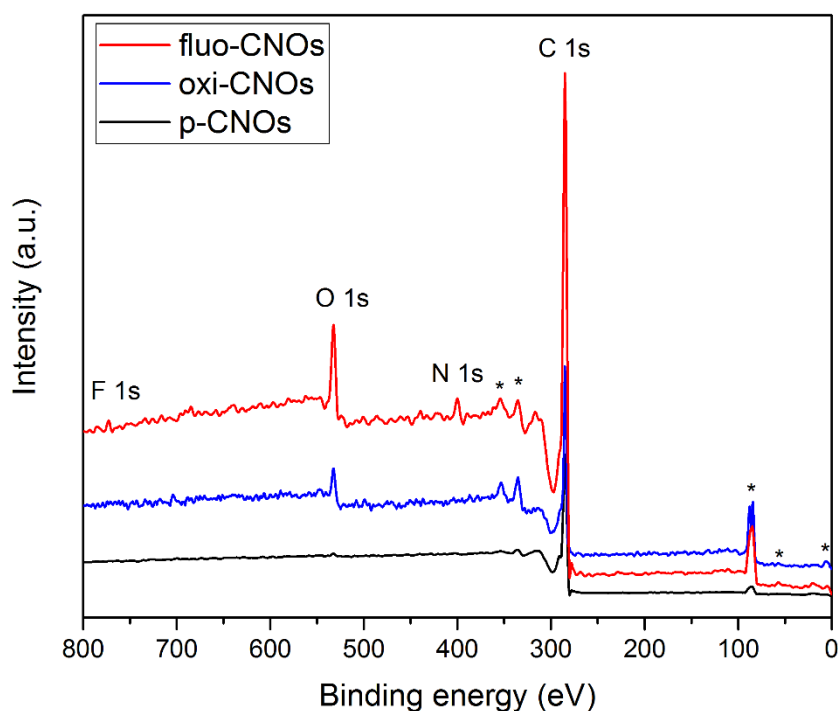


Figure 3.4: XPS survey spectra of *p*- (black), *oxi*- (blue) and *fluo*-CNOs (red). The peaks denoted by \* are due to the gold substrate used for the analyses.

In order to investigate the chemical bonding state of each element, thus confirming the introduction of carboxylic acid groups, high-resolution C1s XPS spectra of all the CNO conjugates were acquired and the different contributes assigned after peak deconvolution (Table 3.2).

As shown in Figure 2.9B, the C1s spectrum of *p*-CNOs exhibits five different contributes, where the most prominent is that assigned to  $sp^2$  carbon atoms. The lower intensity higher binding energy peaks are instead attributed to  $sp^3$ -hybridized and oxygen-bonded (C-O and C=O) carbon atoms as well as  $\pi$ - $\pi^*$  interactions [19].

The C1s XPS spectrum of *oxi*-CNOs is reported in Figure 3.5A. Besides the same peaks reported for *p*-CNOs, an additional contribute is observed at 289 eV; this is assigned to carboxylic acid functionalities [20], thus supporting their concrete introduction on the CNO surface.

In addition, a further evidence of the successful incorporation is provided by the enhancement of the C-C contribute and the lowering of the C=C and  $\pi$ - $\pi^*$  peaks, as the oxidation procedure acts directly on the graphitic carbon atoms on the CNO surface, leading to the creation of  $sp^3$  carbon atoms. This suggest that the oxidation occurs by dissociation of the  $\pi$  bonds in the graphitic carbon atoms [21].

No changes were observed in the C1s spectrum of CNOs upon attachment of the BODIPY dye, suggesting that the additional contribution of the carbon atoms coming the dye molecules cannot be resolved.



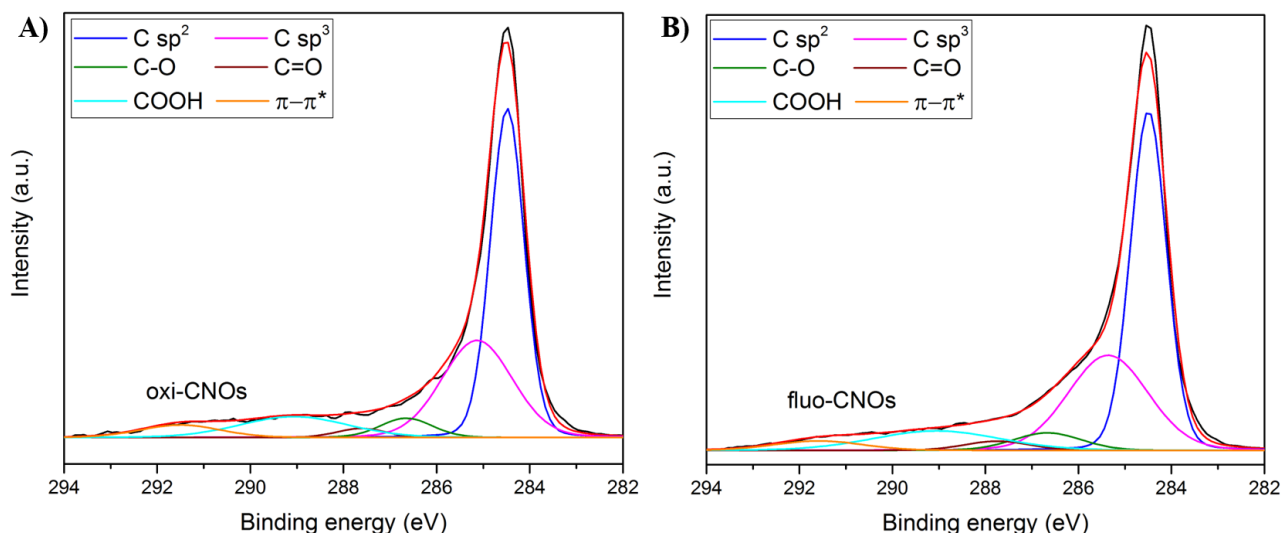


Figure 3.5: High-resolution XPS spectra of the C1s region of A) oxi- and B) fluo-CNOs, including peak-fitting analysis. Experimental and fitting curves are reported in black and red lines, respectively.

Table 3.2: Chemical state, position, area (%) and FWHM of the different peaks from the fitting of the C1s peak of p-, oxi- and fluo-CNOs.

Sample	C-C sp <sup>2</sup> (eV)	C-C sp <sup>3</sup> (eV)	C-O (eV)	C=O (eV)	COOH (eV)	π-π* (eV)
p-CNOs	284.48 (62.66%, 0.75)	285.35 (16.47%, 1.34)	286.54 (5.17%, 1.47)	287.92 (3.99%, 2.02)	289.50 (0.18%, 0.69)	290.71 (11.54%, 3.11)
oxi-CNOs	284.48 (49.09%, 0.85)	285.13 (30.25%, 1.79)	286.65 (4.43%, 1.32)	287.62 (1.95%, 1.24)	289.06 (9.93%, 2.73)	291.50 (4.40%, 2.02)
fluo-CNOs	284.49 (49.03%, 0.91)	285.36 (30.47%, 2.03)	286.66 (4.79%, 1.72)	287.74 (2.43%, 1.66)	289.05 (9.93%, 3.23)	291.59 (3.36%, 2.23)

To further elucidate the oxygen bonding states, the high-resolution O1s XPS spectra of all the CNO conjugates were acquired (Figure 3.6). All the spectra can be deconvoluted into two different contributes assigned to oxygen double (C=O/COOH at around 531 eV) and single (C-O at around 533 eV) bonds [21-23]. As depicted from Table 3.3, the two peaks contribute to the 55.5 and 45.5% of the O1s peak of p-CNOs, which is in agreement with what obtained from the analysis of the C1s (55.35 and 44.65%, respectively). The introduction of carboxylic acid functionalities onto the CNO surface is confirmed by the increase of the oxygen double bonding state, which constitutes the 73% of the total amount with perfect matching with that of C1s. Finally, as discussed for the C1s, no changes in the O1s peak of fluo-CNOs were observed.



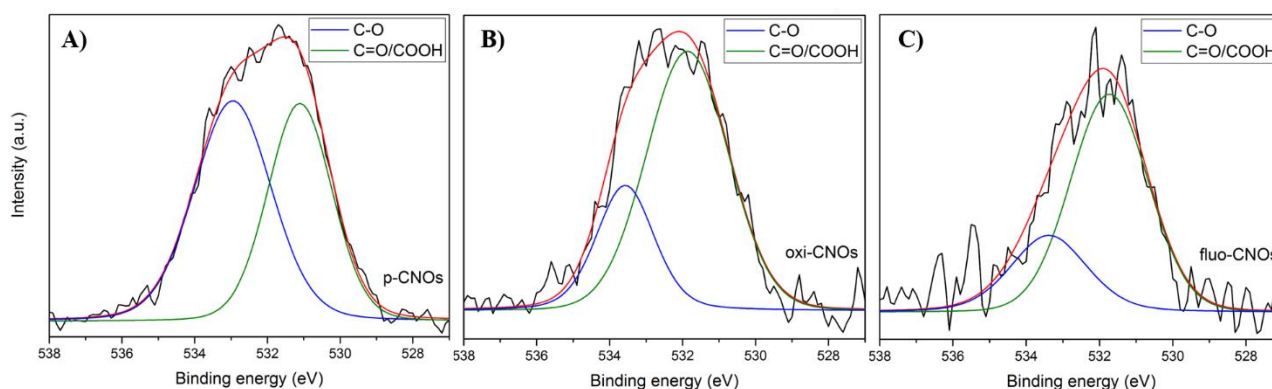


Figure 3.6: High-resolution XPS spectra of the O1s region of A) p-, B) oxi- and C) fluo-CNOs, including peak-fitting analysis. Experimental and fitting curves are reported in black and red lines, respectively.

Table 3.3: Chemical state, position and area (%) of the different peaks from the fitting of the O1s peak of p-, oxi- and fluo-CNOs.

Sample	C-O (eV)	C=O/COOH (eV)
p-CNOs	532.95 (55.5 %)	531.1 (44.5 %)
oxi-CNOs	533.37 (26.98 %)	531.8 (73.02 %)
fluo-CNOs	533.38 (27.42 %)	531.73 (72.58 %)

### 3.3.3 Raman spectroscopy

Raman spectra of p-, oxi- and fluo-CNOs are shown in Figure 3.7. Both CNO derivatives display two prominent Raman features, typical of CNOs [12]. The G-band (located at around  $1580\text{ cm}^{-1}$ ), originating from the in-plane vibration of graphitic carbon atoms ( $E_{2g}$  mode), and the D-band (arising at around  $1320\text{ cm}^{-1}$ ), originating from the photon breathing mode of  $A_{1g}$  symmetry [24]. In addition, the lower intensity 2D-band, arising from two-phonon resonant scattering process, is observed at around  $2650\text{ cm}^{-1}$  [25]. The intensity ratio of the D-band compared to G-band ( $I_D/I_G$  ratio) is commonly employed to give information about the disorder present in graphitic materials [26].

Upon oxidation, the D-band of oxi-CNOs becomes more prominent compared to the pristine materials, resulting in the increase of  $I_D/I_G$  ratio. This is correlated with the structural changes due to the introduction of defects (i.e. carboxylic acid groups) and it is in agreement with what observed from the analysis of the C1s spectrum (Figure 3.5A). No significant change in the ratio was observed

for fluo-CNOs as the coupling reaction does not involve the modification of the graphitic CNO surface.

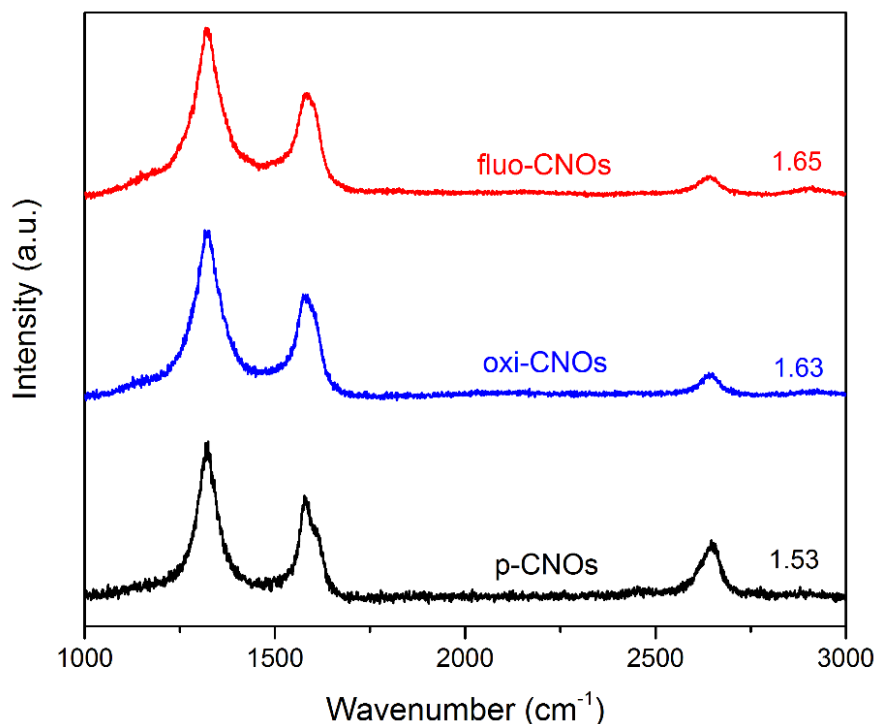


Figure 3.7: Raman spectra of p- (black), oxi- (blue) and fluo-CNOs (red) at  $\lambda_{exc} = 633$  nm. All the spectra were normalized with respect to the G-band. The intensity ratio between the D- and the G-band is reported.

### 3.3.4. Thermogravimetric analysis

The thermal behaviour of the CNO derivatives was evaluated by TGA to further confirm the surface functionalization. p-CNOs (black curve in Figure 3.8) shows high thermal stability up to 550 °C with a single net main loss at 686 °C due to the decomposition of the carbon network. Upon functionalization, both oxi- and fluo-CNOs exhibit a decrease in the decomposition temperature (667 °C and 630 °C, respectively) due to the introduction of defects in the CNO structure [27], as depicted from Table 3.4. Furthermore, from the analysis of the TGA plot, a two-step weight loss process is observed for oxi- and fluo-CNOs due to the initial thermal decomposition of the oxygen-containing functionalities (i.e. carboxylic acid groups) followed by the pyrolysis of the CNO core. The CNO surface coverage of COOH groups and dye molecules were calculated from the TGA weight loss at 450 °C [17]. Compared to the pristine sample, oxi-CNOs showed a mass loss of 7.7%, which corresponds to around 122 carboxylic functionalities per CNO. The further attachment of the BODIPY dye gives rise to an additional mass loss of 5.3% compared to the oxi-CNOs and around 5 fluorescent molecules were estimated per CNO.

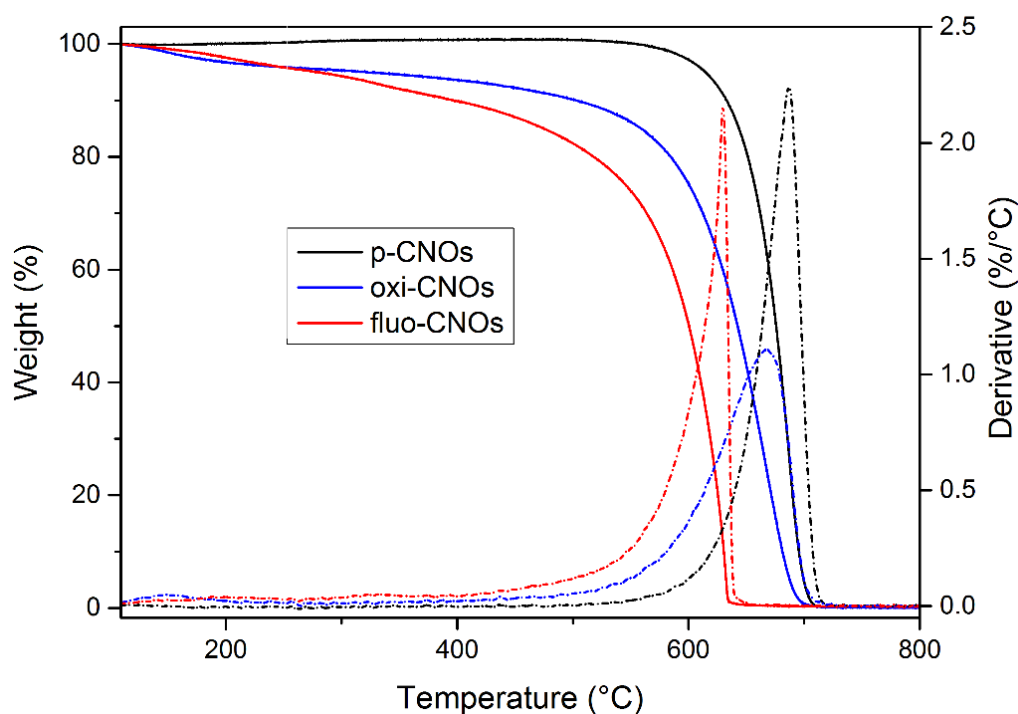


Figure 3.8: Thermogravimetric analysis (solid lines) and the corresponding weight loss derivatives (dotted lines) of p- (black), oxi- (blue) and fluo-CNOs (red). All experiments were performed in air.

Table 3.4: Decomposition temperature of p-CNOs, oxi-CNOs and fluo-CNOs

Sample	$T_{dec}$
p-CNOs	687 °C
oxi-CNOs	667 °C
fluo-CNOs	630 °C

### 3.3.5 Dynamic light scattering and zeta potential

The dispersing abilities of oxi- and fluo-CNOs were investigated by dynamic light scattering (DLS) (Table 3.6). DLS analyses were performed in water for both samples at three concentrations (5, 10 and 20  $\mu\text{g/mL}$ ) and the results are reported in Figure 3.9. Both samples showed good water dispersibility with the formation of aggregates below 250 nm. oxi-CNOs revealed hydrodynamic radii ranging from 121 to 239 nm, while increasing the concentration. The same behavior was observed for fluo-CNOs (diameter from 155 to 205 nm), suggesting a concentration-dependent aggregation process.

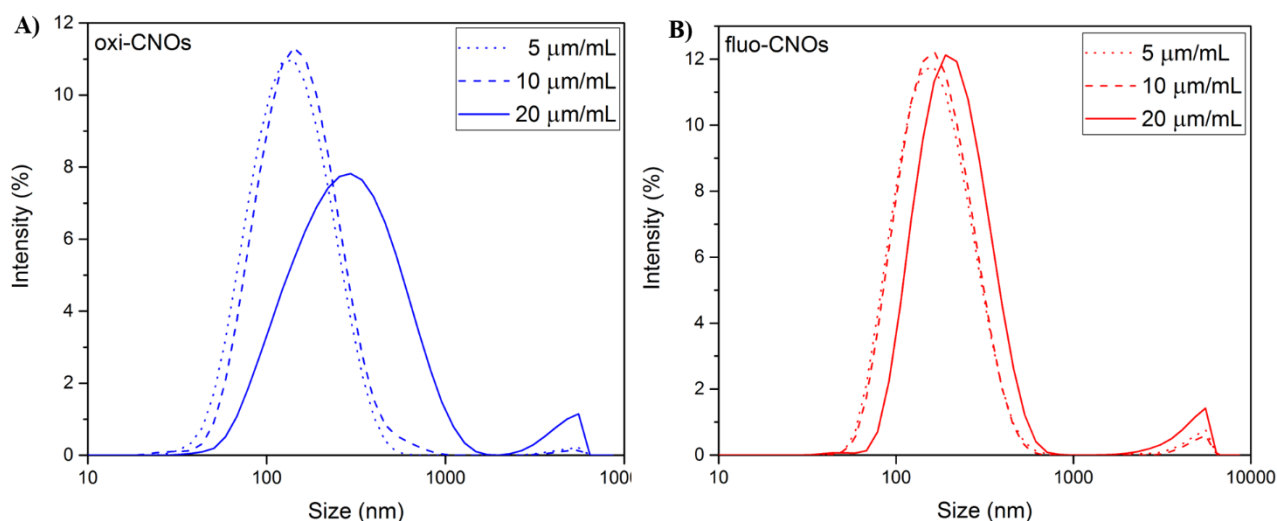


Figure 3.9: Effective hydrodynamic diameter of A) oxi-CNOs (blue line) and B) fluo-CNOs (red) in water at three different concentrations (5, 10 and 20  $\mu\text{g/mL}$ ).

Table 3.5: Effective hydrodynamic diameter of oxi- and fluo-CNOs in water obtained from DLS analyses at different concentrations.

Sample	Effective Hydrodynamic diameter (nm)		
	5 ( $\mu\text{g/mL}$ )	10 ( $\mu\text{g/mL}$ )	20 ( $\mu\text{g/mL}$ )
oxi-CNOs	121 $\pm$ 1.4	126 $\pm$ 0.8	239 $\pm$ 2.5
fluo-CNOs	155 $\pm$ 1.3	155 $\pm$ 2.0	205 $\pm$ 6.7

DLS analyses were also performed in 0.01M PBS for both oxi- and fluo-CNOs to mimic the cellular environment, showing a similar trend as the one observed in water (Figure 3.10). In detail, both CNO derivatives showed aggregates with an average size lower than 300 nm (Table 3.6).

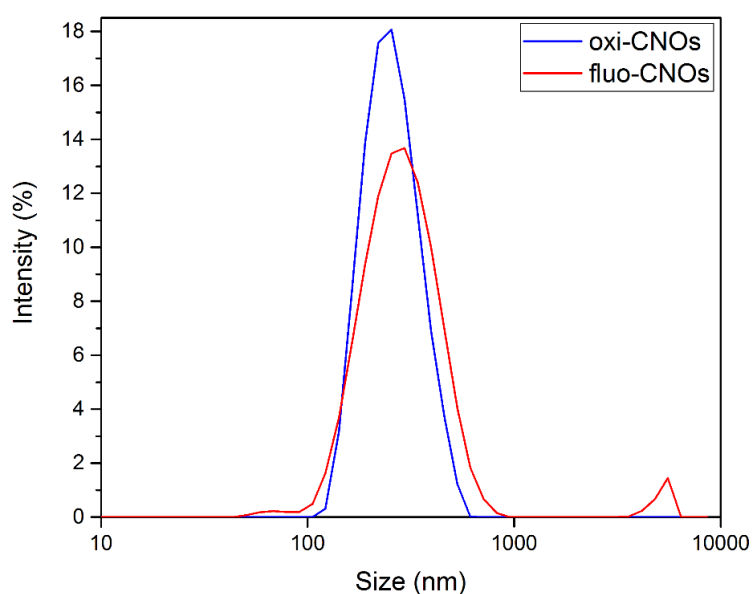


Figure 3.10: Effective hydrodynamic diameter of oxi-CNOs (blue line) and fluo-CNOs (red line) at a concentration of 5  $\mu\text{g/mL}$  in 0.01M PBS.

The stability of the CNO conjugates in solution was investigated by zeta potential in phosphate buffer at 5  $\mu\text{g/mL}$  CNO concentration (Table 3.7). fluo-CNOs exhibited a less negative value ( $-34\text{ mV}$ ) than that of oxi-CNOs ( $-45\text{ mV}$ ), which may be due to the positively charged ammonium quaternary salt present in the BODIPY dye molecules.

Overall, the conjugation of the dye to the CNO surface did not affect the dispersing and stability properties of the structure due to the water solubility of the BODIPY moieties.

Table 3.6: Effective hydrodynamic diameter from DLS analyses and zeta potential of oxi- and fluo-CNOs at 5  $\mu\text{g/mL}$ .

Sample	Effective Hydrodynamic diameter	Zeta potential
	(nm)	(mV)
	0.01M PBS	Phosphate buffer
oxi-CNOs	$274 \pm 16$	$-45 \pm 5$
fluo-CNOs	$295 \pm 17$	$-34 \pm 4$

### 3.3.6 Absorption and emission spectroscopies

Absorption and emission spectroscopies were employed to confirm the attachment of the BODIPY dye onto the surface of oxi-CNOs. The absorption spectra of the fluorophore and fluo-CNOs (at a concentration of 0.022  $\mu\text{M}$  and 20  $\mu\text{g/mL}$ , respectively) in DMSO are reported in Figure 3.11.

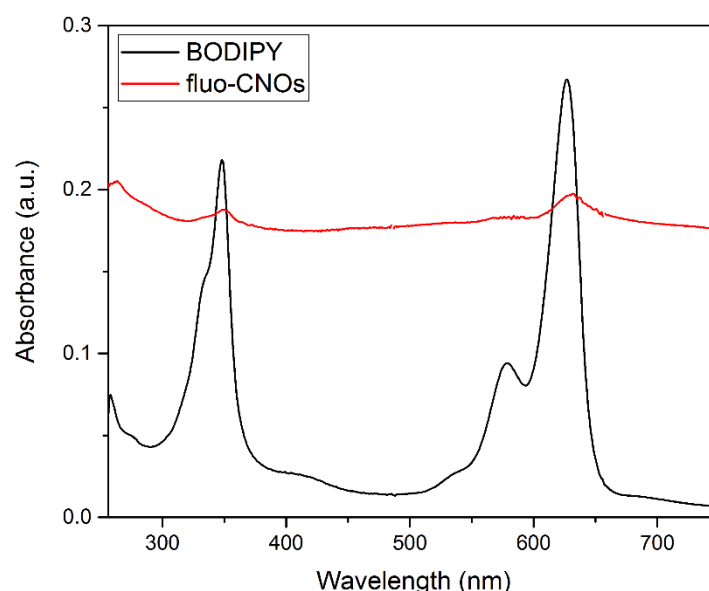


Figure 3.11: Absorption spectra of BODIPY (black line, 0.022  $\mu\text{M}$ ) and fluo-CNOs (red line, 20  $\mu\text{g/mL}$ ).

The two peaks at 350 nm and 629 nm in the absorption spectrum of fluo-CNOs confirm the presence of the BODIPY dyes onto the CNO surface, as depicted by the comparison with the absorption spectrum of the fluorescent molecule (black line in Figure 3.11). Moreover, both peaks are shifted by

2 nm as a consequence of the covalent functionalization onto CNOs. Further evidence of the successful modification is provided by the analysis of the emission spectra of fluo-CNOs (Figure 3.12). Upon photoexcitation at 550 nm in dimethyl sulfoxide (DMSO), a sharp emission band in the far-red region of the spectrum (centered at 634 nm) is observed for fluo-CNOs at all the tested concentrations in agreement with that exhibited by the dye molecule (inset in Figure 3.12). In particular, the remarkable emission properties exhibited by the fluorescent CNO derivatives are attributed to the quite high quantum yield (i.e. 0.4 compared to 0.8 of the dye alone) displayed (Table 3.7). Interestingly, the attachment of the dye molecules onto the CNO surface don't lead to a dramatic quenching of the fluorescence, in contrast to what reported for CNMs [28], where quantum yields less than a third are typically observed.

Furthermore, to prove the suitability of fluo-CNOs for biological applications, the emission properties were investigated in cell medium (DMEM). The BODIPY labelled CNOs displayed a bright fluorescence in DMEM (Figure 3.12B) with emission maximum at 632 nm, confirming their potentialities as biological imaging agent.

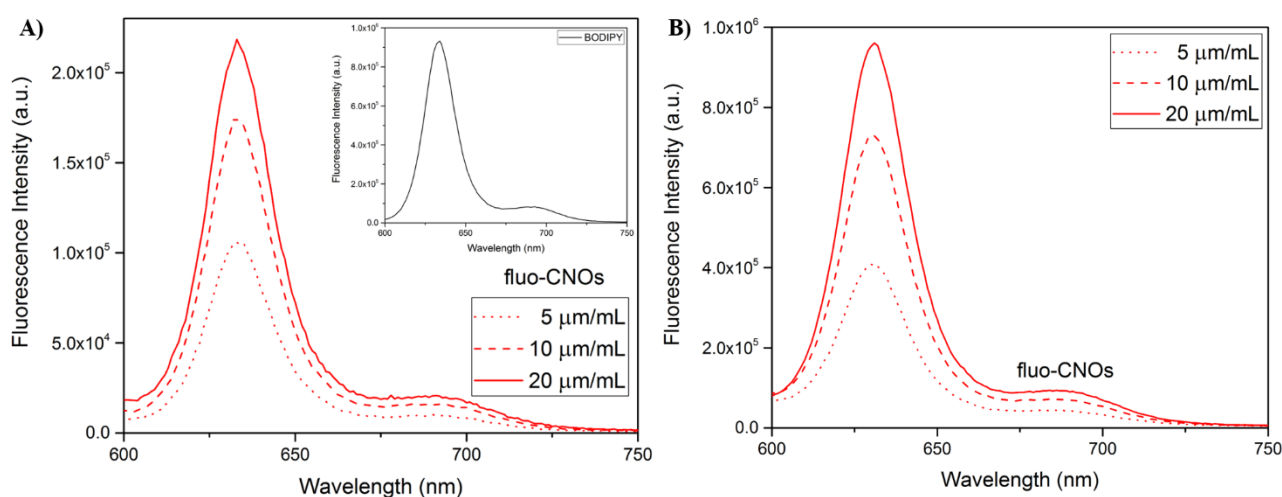


Figure 3.12: A) Emission spectra of fluo-CNOs at 5 µg/mL (red dotted line), 10 µg/mL (red dashed line) and 20 µg/mL (red solid line) in DMSO. The emission spectrum of BODIPY dye (black line) is reported as inset in A. Excitation at 550 nm; emission at 634 nm. B) Emission spectra of fluo-CNOs at 5 µg/mL (red dotted line), 10 µg/mL (red dashed line) and 20 µg/mL (red solid line) in DMEM. Excitation at 561nm; Emission at 632 nm.

Table 3.7: Photophysical data for BODIPY dye and fluo-CNOs.  $\lambda_{abs}$  is the absorption maximum,  $\lambda_{em}$  the emission maximum and  $\phi_F$  the fluorescence quantum yield. Excitation at 550 nm.

Sample	Solvent	$\lambda_{abs}(nm)$	$\lambda_{em}(nm)$	$\phi_F$
BODIPY	DMSO	626	634	0.80
fluo-CNOs	DMSO	626	634	0.40

### 3.3.7 *In vitro* investigation

The remarkable emission properties along with the good dispersing abilities in biological fluids of fluo-CNOs allowed studying their potentialities as biological imaging agents. Dr. Marta d'Amora, postdoc in the NACM group at IIT, investigated the cytotoxicity of both oxi- and fluo-CNOs at different concentrations (from 0.5 up to 20  $\mu\text{g/mL}$ ) in two different cell lines (HeLa and MCF-7 cells). The cell viability (%) was evaluated at different exposure time (12, 24, 48 and 72 h) by means of colorimetric assay (WST1) and the results compared to a non-treated control. As shown in Figure 3.13A, oxi-CNOs did not exert any significant cytotoxic effect on both test lines, which is in agreement with what reported in literature [17, 19]. Similarly, the cell viability of the cells treated with fluo-CNOs (Figure 3.13B) was higher than 80% even at higher concentration (20  $\mu\text{g/mL}$ ) up to 72 h, confirming the biocompatibility of the CNO nanoprobe [29].

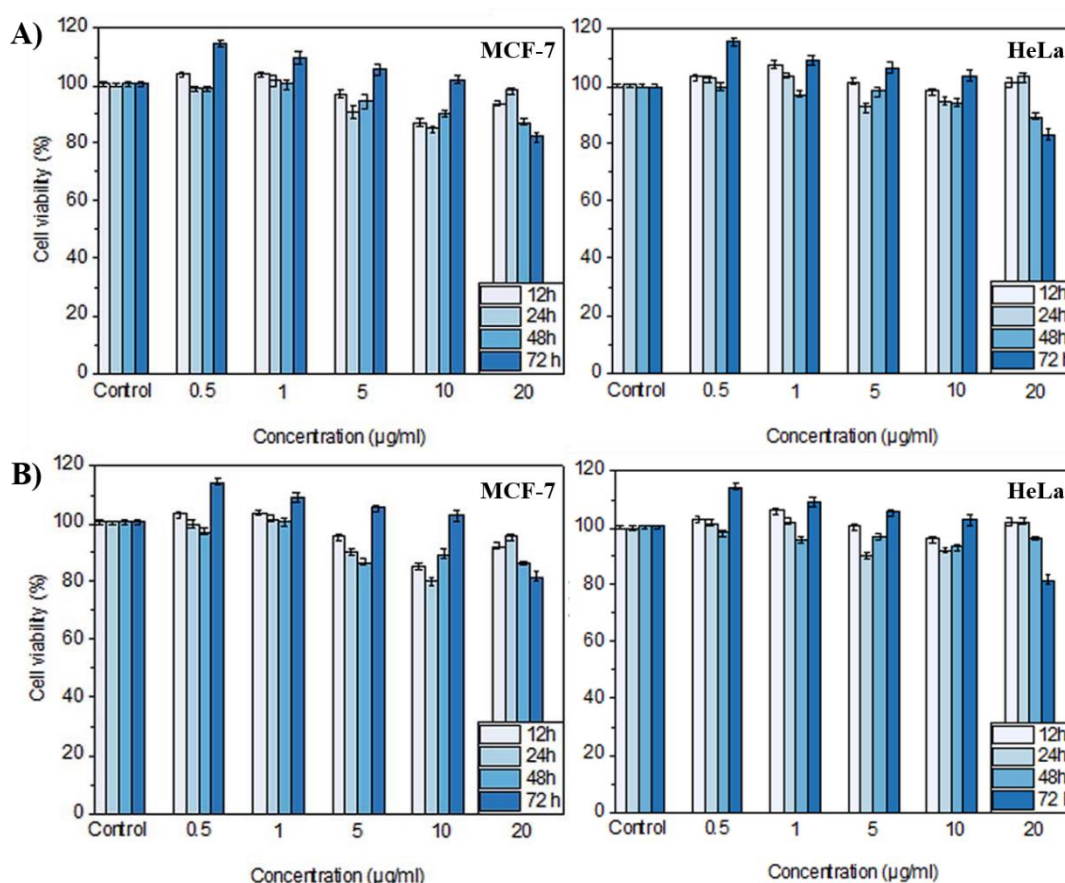


Figure 3.13: Cellular viability of MCF-7 and HeLa cells treated with different concentrations (0.5, 1, 5, 10 and 20  $\mu\text{g/mL}$ ) of A) oxi- and B) fluo-CNOs for 12, 24, 48 and 72 h.

Confocal imaging was carried out to confirm the internalization and the preservation of the fluorescent properties of fluo-CNOs in MCF-7 cells. Confocal images of MCF-7 cells incubated with two different concentrations (5 and 20  $\mu\text{g/mL}$ ) of fluo-CNOs for 24 h are reported in Figure 3.14. The results show that fluo-CNOs were efficiently uptaken by cancer cells, as depicted by the intense



and widespread red emission signal, and accumulated in the perinuclear area. More important, the emission properties of fluo-CNOs were maintained upon internalization and showed bright fluorescence even at low concentration (5  $\mu\text{g/mL}$ ).

With the aim to give further elucidation on the localization of fluo-CNOs into the cells, the lysosomes were tracked with a specific dye molecule, the LysoTracker green. As shown in Figure 3.15C, the merged confocal image show a partial yellow co-localization signal (arising from the overlapping of the red and green emission), confirming that the fluorescent CNO probes deposited in the lysosomal vesicles [29].

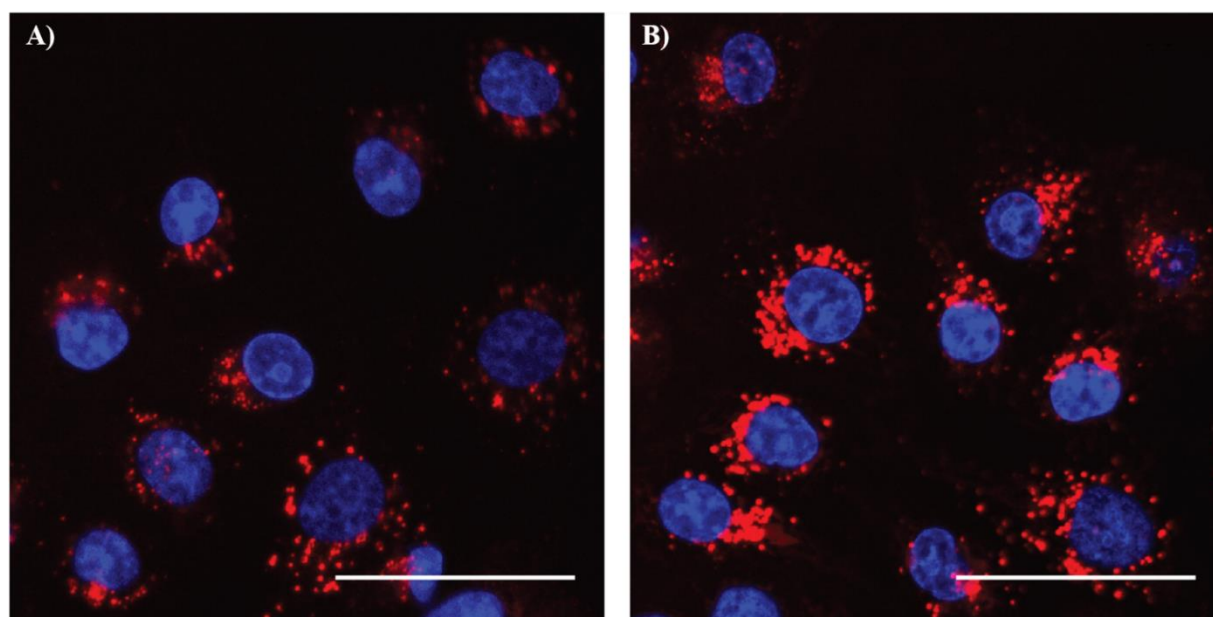


Figure 3.14: Confocal images of MCF-7 cells incubated for 24 hours with fluo-CNOs at A) 5 and B) 20  $\mu\text{g/mL}$ . The nuclei were stained with Hoechst 33 342 (blue). Scale bars: 10  $\mu\text{m}$ .

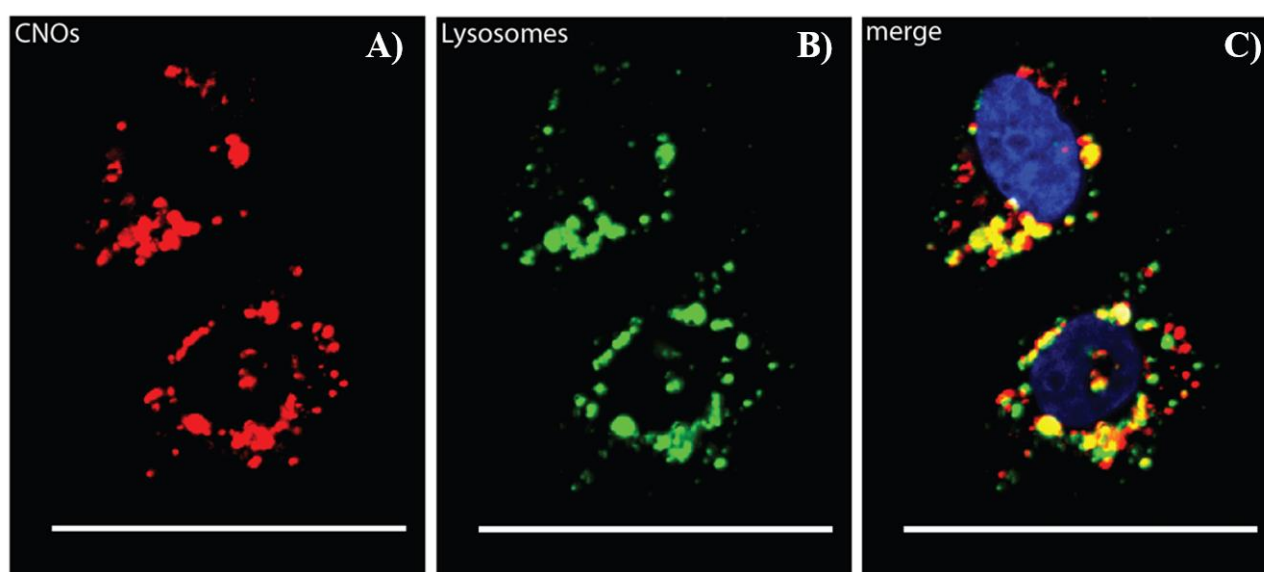


Figure 3.15: Confocal images of MCF7 cells incubated for 24 hours with 20  $\mu\text{g/mL}$  of fluo CNOs. A) red signal from fluo-CNOs; B) green signal from LysoTracker- marked lysosomes and C) Merged images. The nuclei were stained with Hoechst 33 342 (blue). Scale bars: 10  $\mu\text{m}$ .



### 3.4 Conclusion

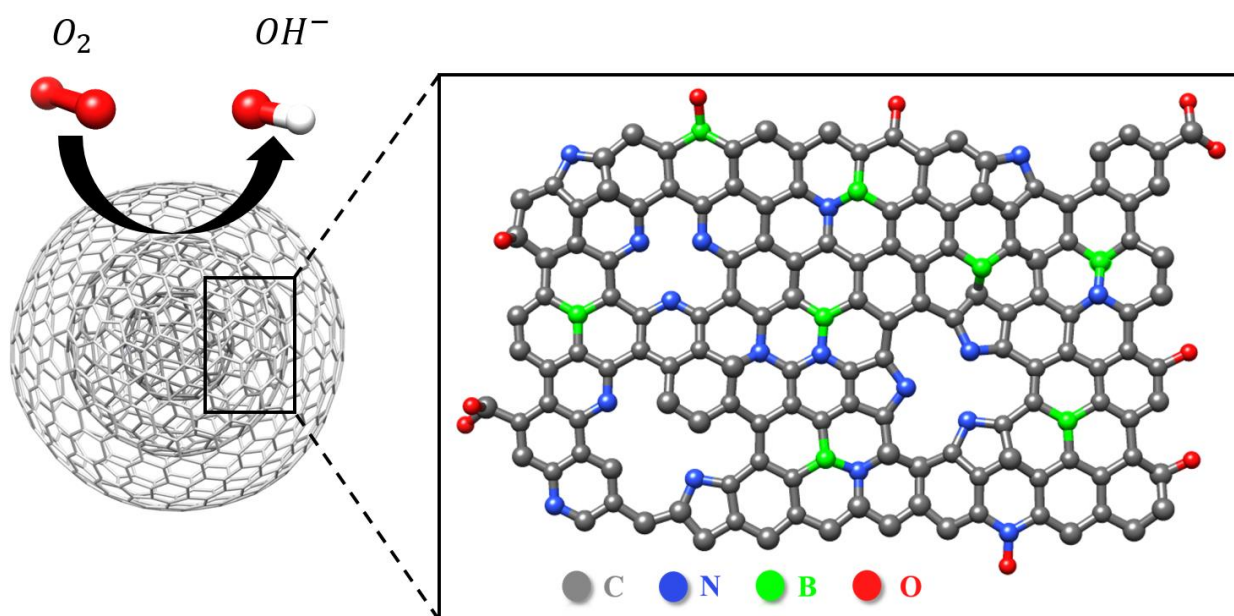
In this chapter, the development of a novel CNO-based bio-imaging agent have been demonstrated. The low dispersing abilities of p-CNOSs were firstly enhanced through oxidation procedure to introduce carboxylic acid functionalities onto the CNO surface and then coupled to the soluble BODIPY derivative, resulting in water-soluble nanoparticles. The further attachment of a novel far-red emitting BODIPY dye was accomplished by esterification reaction exploiting the hydroxyl group present in the fluorescent molecules. The successful surface functionalization of CNOs was confirmed by several characterization techniques. The as-synthesized fluorescent nanoprobe showed high emission properties, due to the high quantum yield, and excellent stability and dispersability in biological media, allowing for the *in vitro* investigation. fluo-CNOs were tested in two different cell lines (MCF-7 and HeLa cells), showing negligible toxic effects even after prolonged incubation time (72 h), thus confirming the biocompatibility of the CNO derivatives. The efficient internalization of fluo-CNOs in MCF-7 cancer cells was confirmed by confocal imaging, showing a strong red fluorescence signal even at very low concentration, with a partial localization in the lysosomes. These findings corroborated the remarkable potentialities of CNOs as platform for high-resolution biological imaging agent, thus opening the way to the development of CNO-based drug delivery systems.

### 3.5 References

- [1] Wang, R.; Zhang, F., NIR luminescent nanomaterials for biomedical imaging. *J. Mater. Chem. B*, **2014**, 2, (17), 2422.
- [2] Bartelmeß, J.; Quinn, S.J.; Giordani, S., Carbon nanomaterials: multi-functional agents for biomedical fluorescence and Raman imaging. *Chem. Soc. Rev.*, **2015**, 44, (14), 4672-4698.
- [3] Gong, H.; Peng, R.; Liu, Z., Carbon nanotubes for biomedical imaging: The recent advances. *Advanced Drug Delivery Reviews*, **2013**, 65, (15), 1951-1963.
- [4] Liu, Z.; Yang, K.; Lee, S.-T., Single-walled carbon nanotubes in biomedical imaging. *Journal of Materials Chemistry*, **2011**, 21, (3), 586-598.
- [5] Jeong, J.; Jung, J.; Choi, M.; Kim, J.W.; Chung, S.J.; Lim, S.; Lee, H.; Chung, B.H., Color-Tunable Photoluminescent Fullerene Nanoparticles. *Advanced Materials*, **2012**, 24, (15), 1999-2003.
- [6] Levi, N.; Hantgan, R.R.; Lively, M.O.; Carroll, D.L.; Prasad, G.L., C60-Fullerenes: detection of intracellular photoluminescence and lack of cytotoxic effects. *Journal of Nanobiotechnology*, **2006**, 4, (1), 14.
- [7] Feng, L.; Liu, Z., Graphene in biomedicine: opportunities and challenges. *Nanomedicine*, **2011**, 6, (2), 317-324.
- [8] Tian, B.; Wang, C.; Zhang, S.; Feng, L.; Liu, Z., Photothermally Enhanced Photodynamic Therapy Delivered by Nano-Graphene Oxide. *ACS Nano*, **2011**, 5, (9), 7000-7009.
- [9] Shen, J.; Zhu, Y.; Yang, X.; Li, C., Graphene quantum dots: emergent nanolights for bioimaging, sensors, catalysis and photovoltaic devices. *Chemical Communications*, **2012**, 48, (31), 3686-3699.
- [10] Lim, S.Y.; Shen, W.; Gao, Z., Carbon quantum dots and their applications. *Chemical Society Reviews*, **2015**, 44, (1), 362-381.
- [11] Hong, G.; Diao, S.; Antaris, A.L.; Dai, H., Carbon Nanomaterials for Biological Imaging and Nanomedicinal Therapy. *Chem. Rev.*, **2015**, 115, (19), 10816-10906.
- [12] Bartelmeß, J.; De Luca, E.; Signorelli, A.; Baldrighi, M.; Becce, M.; Brescia, R.; Nardone, V.; Parisini, E.; Echegoyen, L.; Pompa, P.P.; Giordani, S., Boron dipyrromethene (BODIPY) functionalized carbon nano-onions for high resolution cellular imaging. *Nanoscale*, **2014**, 6, (22), 13761-13769.
- [13] Giordani, S.; Bartelmeß, J.; Frascioni, M.; Biondi, I.; Cheung, S.; Grossi, M.; Wu, D.; Echegoyen, L.; O'Shea, D.F., NIR fluorescence labelled carbon nano-onions: synthesis, analysis and cellular imaging. *J. Mater. Chem. B*, **2014**, 2, (42), 7459-7463.
- [14] Marchesano, V.; Ambrosone, A.; Bartelmeß, J.; Strisciante, F.; Tino, A.; Echegoyen, L.; Tortiglione, C.; Giordani, S., Impact of Carbon Nano-Onions on *Hydra vulgaris* as a Model Organism for Nanoecotoxicology. *Nanomaterials*, **2015**, 5, (3), 1331-1350.
- [15] d'Amora, M.; Rodio, M.; Bartelmeß, J.; Sancataldo, G.; Brescia, R.; Cella Zanacchi, F.; Diaspro, A.; Giordani, S., Biocompatibility and biodistribution of functionalized carbon nano-onions (f-CNOs) in a vertebrate model. *Sci. Rep.*, **2016**, 6, 33923.
- [16] Camisasca, A.; Giordani, S., Carbon nano-onions in biomedical applications: Promising theranostic agents. *Inorg. Chim. Acta*, **2017**, 468, 67-76.
- [17] Frascioni, M.; Maffei, V.; Bartelmeß, J.; Echegoyen, L.; Giordani, S., Highly surface functionalized carbon nano-onions for bright light bioimaging. *Methods Appl. Fluoresc.*, **2015**, 3, (4), 044005.
- [18] Ugarte, D., Onion-Like graphitic particles. *Carbon*, **1995**, 33, 989-993.
- [19] d'Amora, M.; Camisasca, A.; Lettieri, S.; Giordani, S., Toxicity Assessment of Carbon Nanomaterials in Zebrafish during Development. *Nanomaterials*, **2017**, 7, (12), 414.
- [20] Li, M.; Boggs, M.; Beebe, T.P.; Huang, C.P., Oxidation of single-walled carbon nanotubes in dilute aqueous solutions by ozone as affected by ultrasound. *Carbon*, **2008**, 46, (3), 466-475.
- [21] Datsyuk, V.; Kalyva, M.; Papagelis, K.; Parthenios, J.; Tasis, D.; Siokou, A.; Kallitsis, I.; Galiotis, C., Chemical oxidation of multiwalled carbon nanotubes. *Carbon*, **2008**, 46, (6), 833-840.

- [22] Mowbray, D.J.; Paz, A.P.; Ruiz-Soria, G.; Sauer, M.; Lacovig, P.; Dalmiglio, M.; Lizzit, S.; Yanagi, K.; Goldoni, A.; Pichler, T.; Ayala, P.; Rubio, A., Disentangling Vacancy Oxidation on Metallicity-Sorted Carbon Nanotubes. *The Journal of Physical Chemistry C*, **2016**, *120*, (32), 18316-18322.
- [23] Martí, x.; nez, M.T.; Callejas, M.A.; Benito, A.M.; Cochet, M.; Seeger, T.; Ansón, A.; Schreiber, J.; Gordon, C.; Marhic, C.; Chauvet, O.; Fierro, J.L.G.; Maser, W.K., Sensitivity of single wall carbon nanotubes to oxidative processing: structural modification, intercalation and functionalisation. *Carbon*, **2003**, *41*, (12), 2247-2256.
- [24] Ferrari, A.C.; Robertson, J., Interpretation of Raman spectra of disordered and amorphous carbon. *Phys. Rev. B*, **2000**, *61*, 14095.
- [25] Pimenta, M.A.; Dresselhaus, G.; Dresselhaus, M.S.; Cancado, L.G.; Jorio, A.; Saito, R., Studying disorder in graphite-based systems by Raman spectroscopy. *Phys. Chem. Chem. Phys.*, **2007**, *9*, (11), 1276-1291.
- [26] Ferrari, A.C., Raman spectroscopy of graphene and graphite: Disorder, electron-phonon coupling, doping and nonadiabatic effects. *Solid State Commun.*, **2007**, *143*, (1-2), 47-57.
- [27] Molina-Ontoria, A.; Chaur, M.N.; Plonska-Brzezinska, M.E.; Echegoyen, L., Preparation and characterization of soluble carbon nano-onions by covalent functionalization, employing a Na-K alloy. *Chem. Commun.*, **2013**, *49*, (24), 2406-2408.
- [28] Chiu, C.F.; Dementev, N.; Borguet, E., Fluorescence quenching of dyes covalently attached to single-walled carbon nanotubes. *J. Phys. Chem. A*, **2011**, *115*, (34), 9579-9584.
- [29] Lettieri, S.; Camisasca, A.; d'Amora, M.; Diaspro, A.; Uchida, T.; Nakajima, Y.; Yanagisawa, K.; Maekawa, T.; Giordani, S., Far-red fluorescent carbon nano-onions as a biocompatible platform for cellular imaging. *RSC Adv.*, **2017**, *7*, (72), 45676-45681.

# *Chapter 4 - Boron/nitrogen co-doped carbon nano-onions as efficient and durable electrocatalysts for the oxygen reduction reaction*



ACS Appl. Nano Mater. 2018, 1, 10, 5763-5773

## **4.1 Introduction**

In the last decade, the development of new sustainable and eco-friendly energy sources has been the object of intense scientific research due to the high demand in our community and the current environmental concerns [1, 2]. Fuel cell is nowadays the most promising green energy conversion technology but is limited by the kinetically slow oxygen reduction reaction (ORR) at the cathode site, thus it requires the use of a catalysts [3, 4]. To date, carbon-supported platinum (Pt/C) is the most performing catalyst due to the high current density and low overpotential [5, 6].

However, the high cost of Pt and its operational issues such as poor operation durability, fuel crossover and CO poisoning effect have hindered the possible commercialization of fuel cells [7, 8], making essential the development of new low cost catalytic materials with high efficiency.

Carbon nanomaterials (CNMs) have been proposed as potential candidates to replace Pt-based catalysts due to the cost effectiveness and remarkable electromechanical properties [9, 10].

Doping strategies to introduce heteroatoms such as nitrogen (N) and boron (B) in the graphitic skeleton have shown to be an effective way to enhance the negligible catalytic activity of pristine CNMs, resulting in outstanding ORR performance with higher long-term stability to that of standard Pt/C catalysts [11-13]. The presence of dopants in the graphitic structure induces a charge redistribution, breaking the electro-neutrality of the network; as a results of the modification of the native electronic properties, new active site are formed inside the material, thus facilitating the adsorption of oxygen [14, 15]. Furthermore, the presence of more than one dopant (i.e. dual- or multiple-atom doping) has demonstrated to induce higher activity to the CNMs due to the synergistic coupling effects between different heteroatoms [16, 17].

In contrast to other CNMs such as carbon nanotubes and graphene, carbon nano-onions (CNOs) have been only recently investigated as cathode material for ORR. Single-atom doping of CNOs with nitrogen and boron has shown to efficiently enhance the ORR catalytic performance of the pristine material [18-20], thus proving the potentialities of this nanomaterial in electrocatalysis. We recently investigated the effects of a co-doping approach on the CNO electrocatalytic performance [21].

In this chapter, I will discuss about the firstly reported co-doping strategy of CNOs with the aim to develop a novel CNO-based ORR electrocatalyst. The introduction of nitrogen and boron as dopant atoms was accomplished directly during the material synthesis through thermal annealing process to yield boron/nitrogen co-doped CNOs (BN-CNOs). This method is suitable for the low cost and high yield production of carbon-based electrocatalysts. The effects of the heteroatom doping on the ORR activity have been investigated in alkaline medium and the performance compared to those of pristine CNOs (p-CNOs) and the benchmark Pt/C (20 wt%) electrocatalyst. The results showed comparable catalytic activity to that of Pt/C with higher long-term stability and excellent immunity toward methanol crossover, thus confirming that the proposed approach is an efficient way to enhance the ORR performance of CNOs.

## 4.2 Experimental

### 4.2.1 Synthesis of pristine and boron/nitrogen co-doped carbon nano-onions

The synthesis of p-CNOs has been achieved by thermal annealing process of detonation nanodiamonds (DNDs) as discussed in the Chapter 2 (paragraph 2.2.1). For the production of BN-CNOs, the additional presence of boric acid ( $\text{H}_3\text{BO}_3$ ) was employed as B source, while the nitrogen impurities present in DNDs as a result of the production process [22] was exploited as N source.

In particular, prior to the annealing process, a precise amount of DNDs was mixed with boric acid powder (30 wt%) and then transferred in a graphitic crucible. The schematic representation of the synthetic procedure of both CNO materials is reported in Figure 4.1.

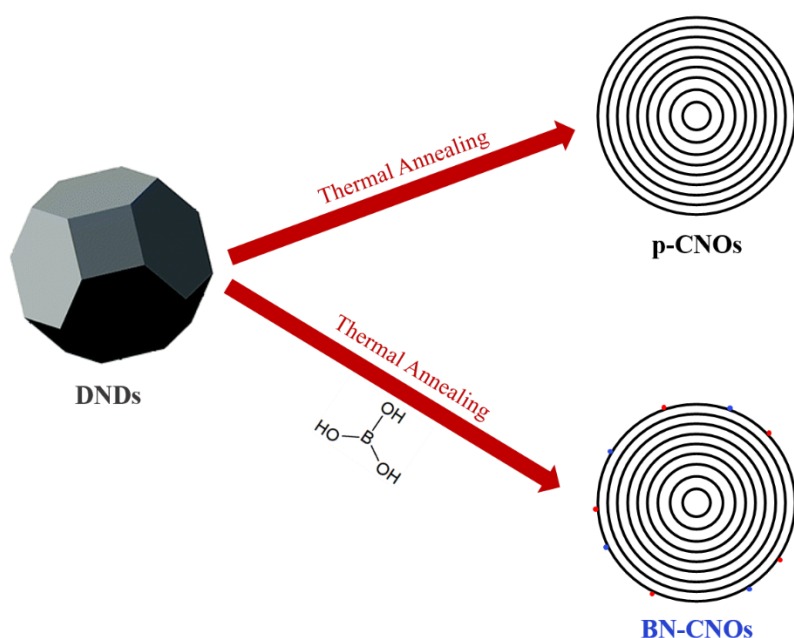


Figure 4.1: Schematic representation of the synthesis of p- and BN-CNOs.

## 4.3 Results and discussion

### 4.3.1 Transmission electron microscopy

The morphology of CNO materials was investigated by high-resolution transmission electron microscopy (HRTEM). At 1650 °C, CNOs with a quasi-spherical shape are typically formed [23], as depicted by the HRTEM image of p-CNOs reported in Figure 2.3. On the contrary, as shown in Figure 4.2A, BN-CNOs consist of polyhedral-shaped nanoparticles.

The formation of this type of CNOs is typically expected by annealing DNDs at higher temperatures (i.e. 1900 °C) [24, 25]. The existence of polyhedral CNOs at lower temperatures is assigned to the



enhanced degree of graphitization achieved during the annealing process induced by the presence of B [26, 27].

In addition, a small fraction of nearly spherical-shaped CNOs is observed in the sample (Figure 4.2B) and this is tentatively assigned to the existence of temperature gradients during the annealing process.

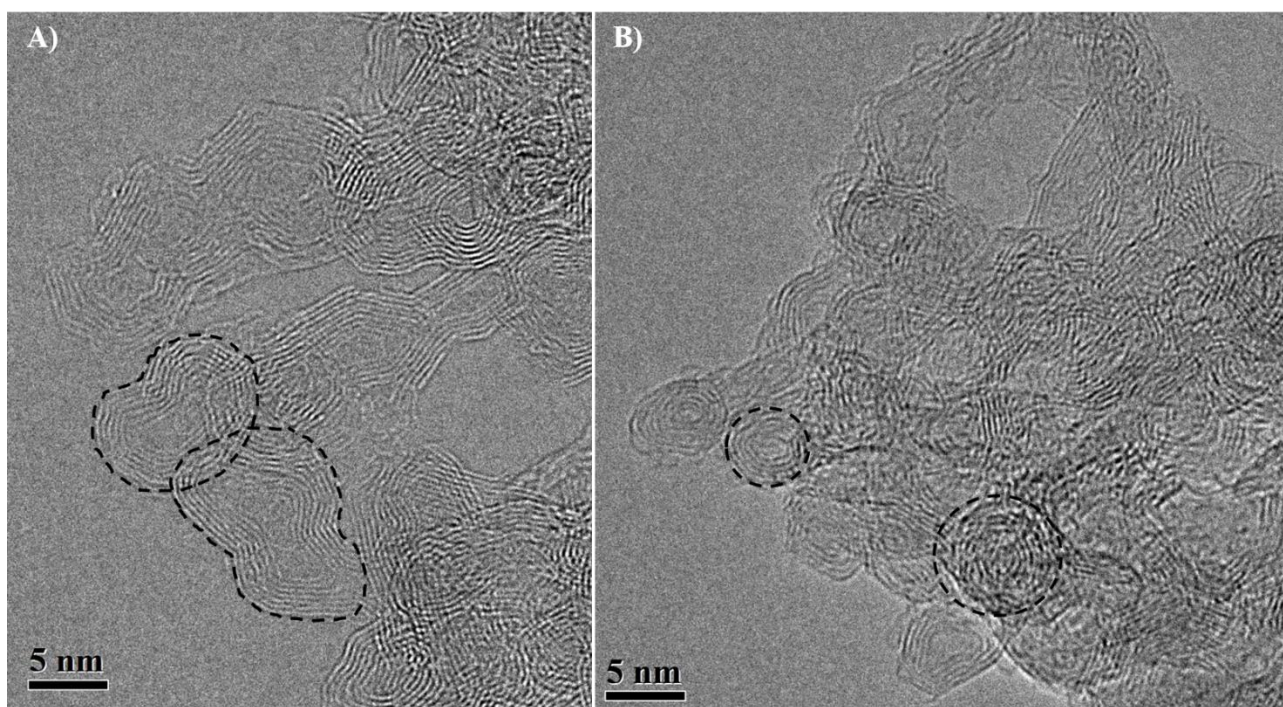


Figure 4.2: Representative HRTEM images of BN-CNOs, showing A) mainly polyhedral shape and B) a small fraction of spherical CNOs. The characteristic morphology is highlighted with black dotted lines.

The composition of BN-CNOs was investigated by energy-filtered TEM (EFTEM) elemental mapping. As shown in Figure 4.3, boron (in green) and nitrogen (in cyan) are distributed in a uniform way in the CNO structure composed of graphitic carbon atoms (in red). This confirms the introduction of both dopants and the homogeneous nature of the co-doped CNOs, in agreement with what observed in similar BN-doped CNMs [28, 29].

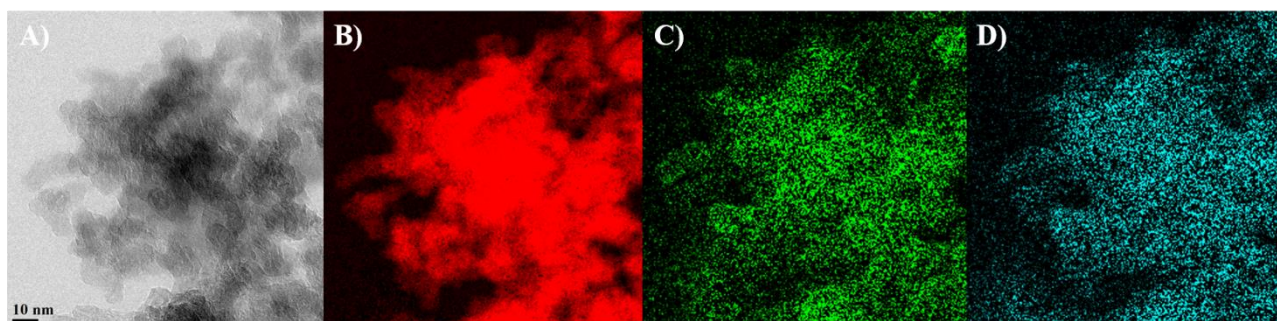


Figure 4.3: Zero-loss bright-field TEM image (A) and corresponding EFTEM elemental mapping of BN-CNOs showing C, B, and N maps in red, green, and cyan, respectively (B-D).

### 4.3.2 Electron energy loss spectroscopy

To further confirm the successful introduction of B and N into the CNO framework, BN-CNOs were characterized by electron energy loss spectroscopy (EELS). From the analysis of the EELS spectrum in the 150-480 eV energy-loss region (Figure 4.4), the three K-ionization edges of B, C and N are observed, with onset centered at 188, 284 and 401 eV, respectively. Similarly to p-CNOs (Figure 2.6B), the C K-edge structure reveals components consistent with what reported for CNOs [30]. The presence of the B and N K-edges peaks, which show typical features of a  $sp^2$  hybridization state [31, 32], confirms the efficacy of the co-doped approach to incorporate dopants into the carbon structure.

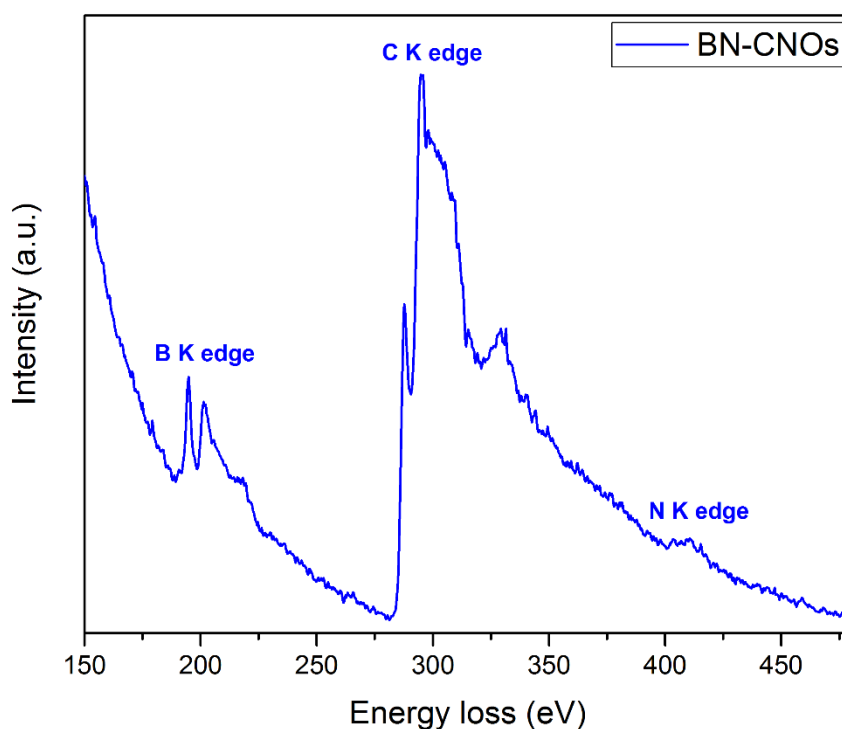


Figure 4.4: EELS spectrum of BN-CNOs showing distinct B, C, and N K-edges.

### 4.3.3 X-ray photoelectron spectroscopy

X-ray photoelectron spectroscopy (XPS) was employed to gain information on the chemical composition of the CNO catalysts (Table 4.1). The XPS survey spectra of p- and BN-CNOs are reported in Figure 4.5. Both samples exhibit peaks assigned to the presence of carbon and oxygen; in addition, from the analysis of the spectrum of BN-CNOs, two further peaks assigned to B and N (at atomic % of 8.0 and 7.4, respectively) are observed, confirming what observed from EELS.

The existence of N in the BN-CNOs, which is not detected in p-CNOs, arise from the diamond precursor (as discussed in Figure 2.8A). DNDs are commonly produced through detonation processes of nitrogen-containing explosives and for this reason, N is incorporated into the structure as impurity during the synthesis [22, 33]. Interestingly, the higher content of N in the co-doped material to that



of DNDs suggests that N is incorporated in the CNO network in combination with B, as observed in other co-doped CNMs [34, 35]. The presence of B plays a central role in the whole process, as suggested by the fact that, during the formation of p-CNOs, N is not introduced in the carbon structure. Therefore, B helps to stabilize N in the CNO lattice as a consequence of the high affinity between the two dopants.

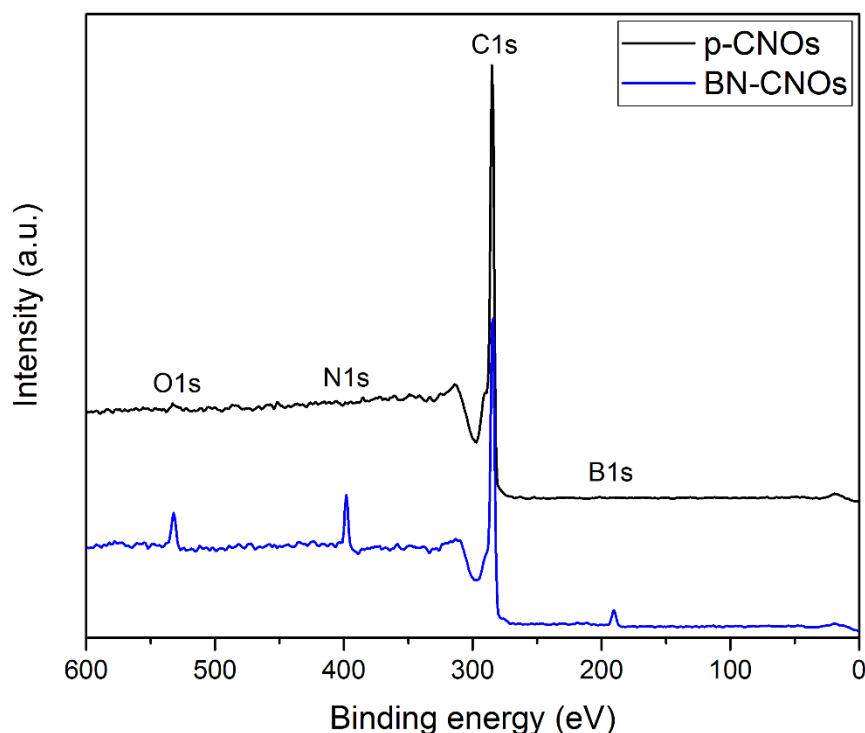


Figure 4.5: XPS survey spectra of p-(black) and BN-CNOs (blue), showing the additional presence of B and N in the doped catalyst..

Table 4.1: Elemental composition of p- and BN-CNOs from XPS analyses.

Sample	C content (%)	O content (%)	N content (%)	B content (%)
p-CNOs	99.4	0.6	-	-
BN-CNOs	80.4	4.2	7.4	8.0

The chemical bonding states of C, B and N were evaluated by acquiring the corresponding high-resolution XPS 1s core levels spectra. The C1s peak of p- and BN-CNOs are shown in Figure 4.6.

The deconvolution of the peak of p-CNOs reveals the existence of six different contributes. In line with what discussed in Chapter 2 (paragraph 2.3.4), these peaks are assigned to carbon atoms in  $sp^2$  and  $sp^3$  hybridization, oxygen-bonded carbon atoms (C-O, C=O and COOH) and the  $\pi-\pi^*$  transition peak (Table 4.2).

The spectrum of BN-CNOs shows substantial differences from that of p-CNOs. First, the C1s peak is slightly broadened, which is indicative of increased structural disorder induced by the introduction of heteroatoms in the hexagonal lattice. Second, the appearance of a new peak, attributed to B atoms

in the CNO lattice (B-C bonds), is observed at 283.5 eV [19]. Finally, the additional presence of  $sp^2$  and  $sp^3$  C-N bonding states is observed overlapping with the oxygen-bonded carbon contributes [36].

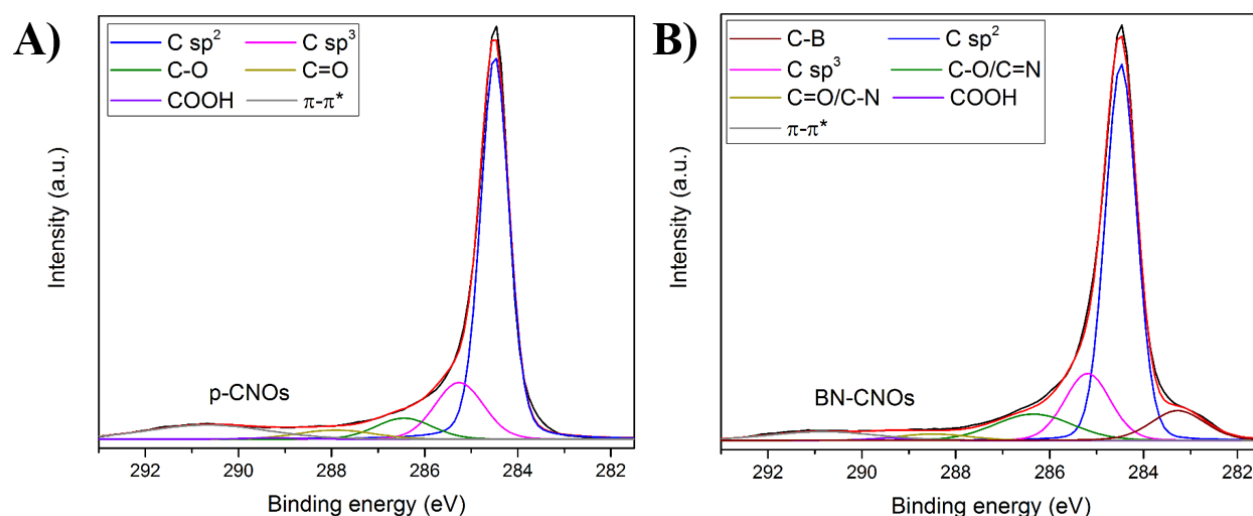


Figure 4.6: High-resolution XPS C1s spectra of A) p- and B) BN-CNOs, including peak deconvolution. Experimental and fitting curves are reported in black and red lines, respectively.

Table 4.2: Chemical state, positions, relative area percentages and FWHM of the deconvoluted C1s peaks of p- and BN-CNOs obtained from XPS analyses.

Sample	C-B (eV)	C-C $sp^2$ (eV)	C-C $sp^3$ (eV)	C-O/C=N (eV)	C=O/C-N (eV)	COOH (eV)	$\pi-\pi^*$ (eV)
p-CNOs	-	284.5 (64.5 %, 0.7)	285.3 (15.3 %, 1.2)	286.4 (6.6 %, 1.4)	287.9 (3.7 %, 1.9)	289.3 (0.4 %, 1.5)	290.7 (9.5 %, 3.0)
BN-CNOs	283.3 (8.3%, 1.3)	284.5 (58.6%, 0.8)	285.2 (15.2%, 1.1)	286.3 (10.1%, 1.9)	288.5 (2.3%, 1.8)	289.4 (0.5%, 1.0)	290.8 (5.0%, 2.7)

The contributions after deconvolution of the N1s and B1s peak of BN-CNOs are reported in Table 4.3. The high-resolution N1s spectrum (Figure 4.7A) exhibits five different peaks assigned to pyridinic (398.4 eV), pyrrolic (400.1 eV), graphitic (401.7 eV) and oxidized N atoms (403 eV) [37, 38]. The sharp peak at 397.9 eV is attributed to B-bonded N atoms (N-B) in the B-N-C bonding state [29, 35, 38]. The high concentration of pyridinic N atoms (55%), reported as the most active ORR sites among the different N states [39, 40], may be essential for the catalytic activity of BN-CNOs. On the other side, the remarkable presence of N-B species (40.5%) may affect to some extent the performance, as typically show low ORR activity [41].

The other N species (pyrrolic, graphitic and oxide) are expected to not be directly involved in the catalytic behavior of BN-CNOs due to their negligible content.

The B1s spectrum of BN-CNOs is reported in Figure 65B and appear at higher binding energy (190 eV) to that of pure B (188 eV), suggesting the incorporation of B atoms in the carbon lattice [42]. The peak can be deconvoluted in three different contributes centered at 189.8, 190.5, and 191.8 eV. The first peak is assigned to B atoms at trigonal sites incorporated in the graphitic lattice by substitution (B-C bonds as  $BC_3$ ), while the third peak arises from B-O bonding states ( $BC_2O$ ,  $BCO_2$  or  $B_2O_3$ ) [19, 32]. Consistently with the N1s peak, the second peak at 190.5 eV is related to the presence of B-N bonds [29, 38, 43], which constitutes the most prominent portion. Among the different B species,  $BC_3$  sites are reported as the most ORR active sites [28, 44].

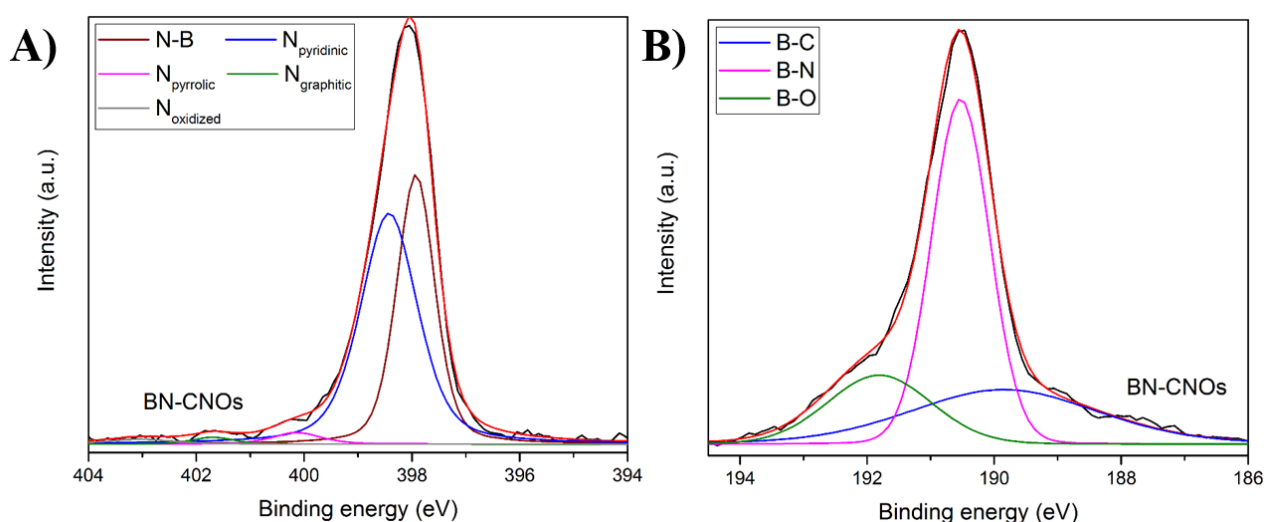


Figure 4.7: High-resolution XPS A) N1s and B) B1s spectra of BN-CNOs, including peak deconvolution. Experimental and fitting curves are reported in black and red lines, respectively.

Table 4.3: Chemical state, positions, relative area percentages and FWHM of the deconvoluted N1s and B1s peaks of BN-CNOs obtained from XPS analysis.

Sample	N 1s					B 1s		
	N-B	N <sub>pyridinic</sub>	N <sub>pyrrolic</sub>	N <sub>graphitic</sub>	N <sub>oxide</sub>	B-C	B-N	B-O
	(eV)	(eV)	(eV)	(eV)	(eV)	(eV)	(eV)	(eV)
BN-CNOs	397.9 (40.5%, 0.8)	398.4 (54.4%, 1.2)	400.1 (2.4%, 1.0)	401.7 (1.2%, 0.9)	403.0 (1.5%, 1.4)	189.8 (28.7%, 3.5)	190.5 (52.3%, 1.0)	191.8 (19.0%, 1.9)

### 4.3.4 X-ray diffraction

X-ray diffraction has been carried out to investigate the influence of the doping process on the crystalline structure of CNOs. XRD spectra of p- and BN-CNOs are reported in Figure 4.8 and exhibit the same graphitic peaks, which are attributed to the (002), (100 + 101), (004), and (110) planes [25, 45]. In particular, the introduction of dopants into the CNO structure produces a sharpening of the (101) diffraction peak in the BN-CNOs pattern, in agreement with what reported for B-doped CNMs [34]. In addition, it leads to a slight decrease in the (002) inter-planar distance (from 3.486 to 3.446 Å) due to the limited diffusion of carbon atoms during the graphitization, which gives rise to a more packed structure [46, 47]. Hagio and co-workers claimed that the decrease in the interlayer spacing in B-doped carbon systems can be ascribed to the electron deficiency of B atoms, which induces a decrease of repulsion in the  $\pi$ - $\pi$  interactions in the graphitic structure [48].

The absence of peaks attributed to  $B_2O_3$  species suggest the complete decomposition of the boron precursor during the annealing process. The very small intensity peaks observed in both XRD spectra may be ascribed to metal impurities present in the DND precursors as a consequence of the detonation synthesis [22]. However, their potential content is extremely low, as depicted by the negligible residue showed by TGA in Figure 4.10, and are supposed not to be exposed at the CNO surface, thus being embedded inside the graphitic shells [49], as suggested by the lack of the corresponding signal in the XPS spectra (Figure 4.5).

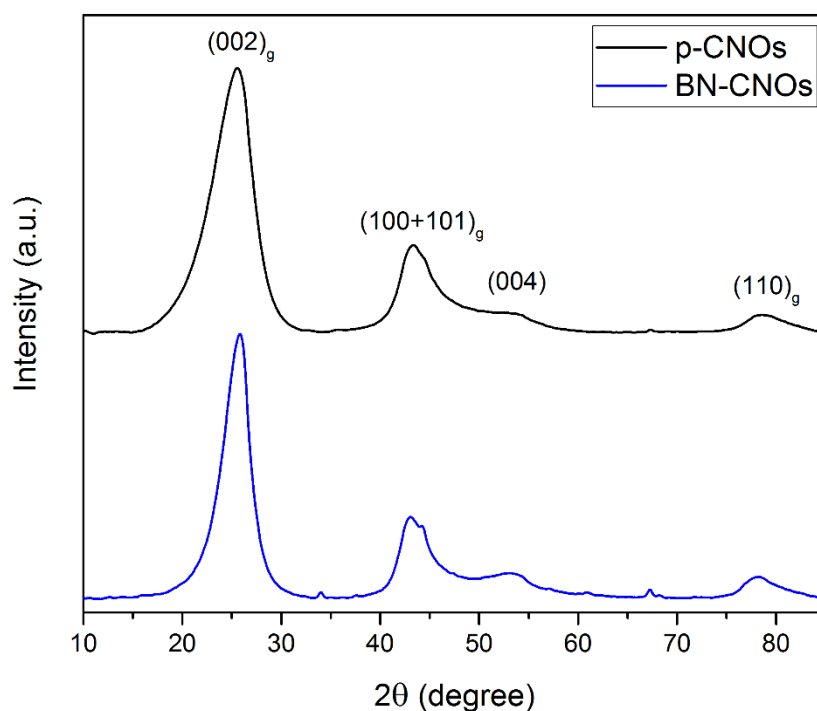


Figure 4.8: XRD patterns of p- (black line) and BN-CNOs (blue line).

### 4.3.5 Raman spectroscopy

The effect of the doping on the graphitic structure has been evaluated by Raman spectroscopy. Figure 4.9 shows the Raman spectra of p- and BN-CNOs, which exhibit in both cases the D-band, which is associated to the structural defects in graphitic materials, and the G-band, arising from the  $E_{2g}$  mode of  $sp^2$  carbon atoms [50, 51]. A very intense D-band is observed for p-CNOs, in agreement with the defective structure of CNOs synthesized by thermal annealing [23]. The Raman spectrum of BN-CNOs exhibits both bands blue-shifted by  $8\text{ cm}^{-1}$  (as depicted from Table 4.4) and a very broad and weak 2D region, suggesting that the introduction of the heteroatoms added disorder to the CNO structure [19]. Further evidence of the enhanced disorder in the graphitic domains can be evaluated from the relative intensity ratio between the D- and G-band ( $I_D/I_G$ ) [52]. As a consequence of the different lengths of the C–C/C–N/C–B bonds, the value increase from 1.53 for p-CNOs to 1.72 for the co-doped CNOs.

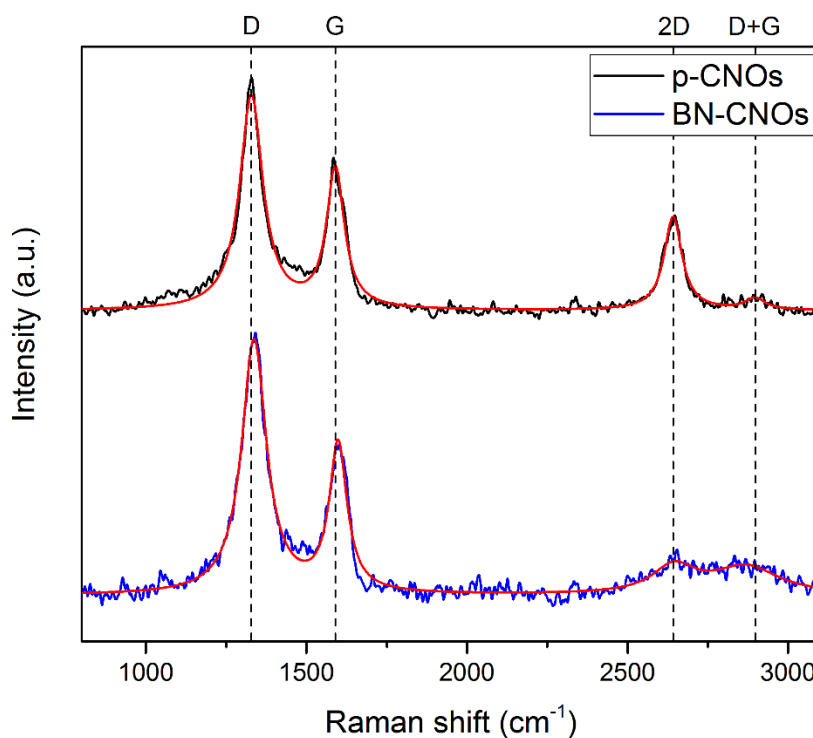


Figure 4.9: Raman spectra of p- (black line) and BN-CNOs (blue line). Fitting curves are reported in red lines.

Table 4.4: D- and G-band positions and  $I_D/I_G$  values of p- and BN-CNOs from Raman analyses.

Sample	D-band ( $\text{cm}^{-1}$ )	G-band ( $\text{cm}^{-1}$ )	$I_D/I_G$ ratio
p-CNOs	1328	1590	1.53
BN-CNOs	1336	1598	1.72

### 4.3.6 Thermogravimetric analysis

The thermal stability of the CNO catalysts was investigated by thermogravimetric analysis (TGA). The TGA weight loss and the corresponding derivatives are reported in Figure 4.10. Similar behavior is observed for both p- and BN-CNOs in air. The CNO derivatives exhibit high thermal stability up to 600 °C without appreciable weigh loss in this range. In particular, the absence of mass loss in the 100-200 °C and 400-500 °C temperature ranges of the TGA plot of BN-CNOs confirms that unreacted boron species in the form of boric acid and B<sub>2</sub>O<sub>3</sub> are not present in the samples (melting points of 170 and 450 °C, respectively), which is in perfect agreement with XRD investigations. Both samples exhibit a single mass loss between 600 and 800 °C due to the decomposition of the carbon skeleton. In particular, BN-CNOs show a lower decomposition temperature compared to p-CNOs (726 and 756 °C as reported in Table 4.5) due to the higher defectiveness induced by the co-doping process. In addition, while p-CNOs exhibit a negligible residual mass at 900 °C of 0.5% (tentatively ascribed to metal traces as previously described), BN-CNOs display a mass residue of about 17%, which can be attributed to the formation of boron oxide at high temperature [53].

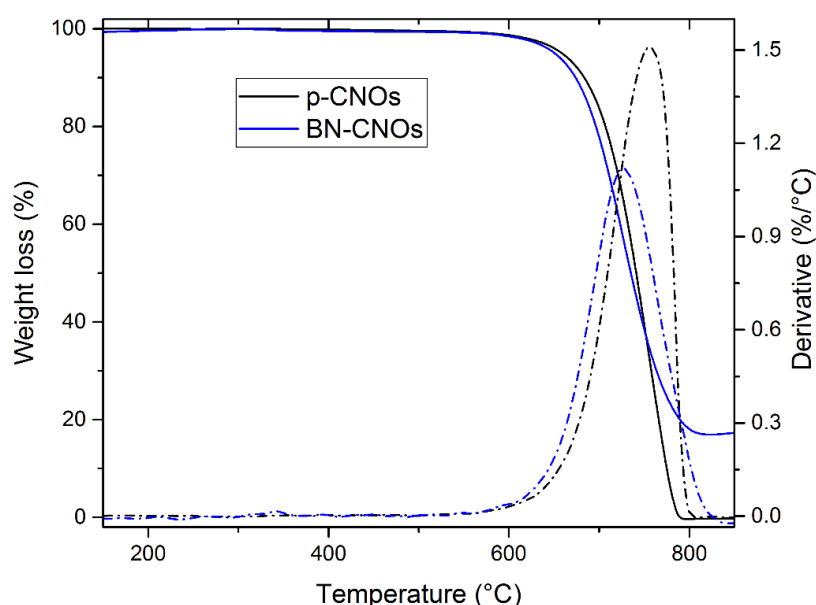


Figure 4.10: TGA (solid lines) and the corresponding weight loss derivatives (dotted lines) of p-(black line) and BN-CNOs (blue line).

Table 4.5: Decomposition temperatures and residues of p- and BN-CNOs from TGA analyses.

Sample	TGA	
	T <sub>D</sub> (°C)	Residue (%)
<b>p-CNOs</b>	756	0.05
<b>BN-CNOs</b>	726	17.0

### 4.3.7 Fourier-transform infrared spectroscopy

Attenuated total reflectance Fourier-transform infrared (FTIR) spectroscopy was employed to evaluate the effect of the doping on the chemical structure. FTIR spectra of p-CNOs is shown in Figure 4.11 (black line), showing no distinctive IR features [30]. After the co-doping process, new vibrational modes are visible in the spectrum of BN-CNOs. The in-plane stretching and out-of-plane bending modes of the atoms belonging to the BCN rings are observed in the 800-1600  $\text{cm}^{-1}$  range [54]. The broad band located at around 1550  $\text{cm}^{-1}$  is attributed to the stretching vibration of  $\text{C}=\text{C}/\text{C}=\text{N}$  bonds. The peaks corresponding to the B-N stretching and bending vibrations are located at about 1367 and 849  $\text{cm}^{-1}$ . The small shoulder at 1400  $\text{cm}^{-1}$  can be ascribed to the asymmetric B-O stretching modes, while the broad band between 1000 and 1300  $\text{cm}^{-1}$  to the superposition of the B-C and C-N stretching modes [55].

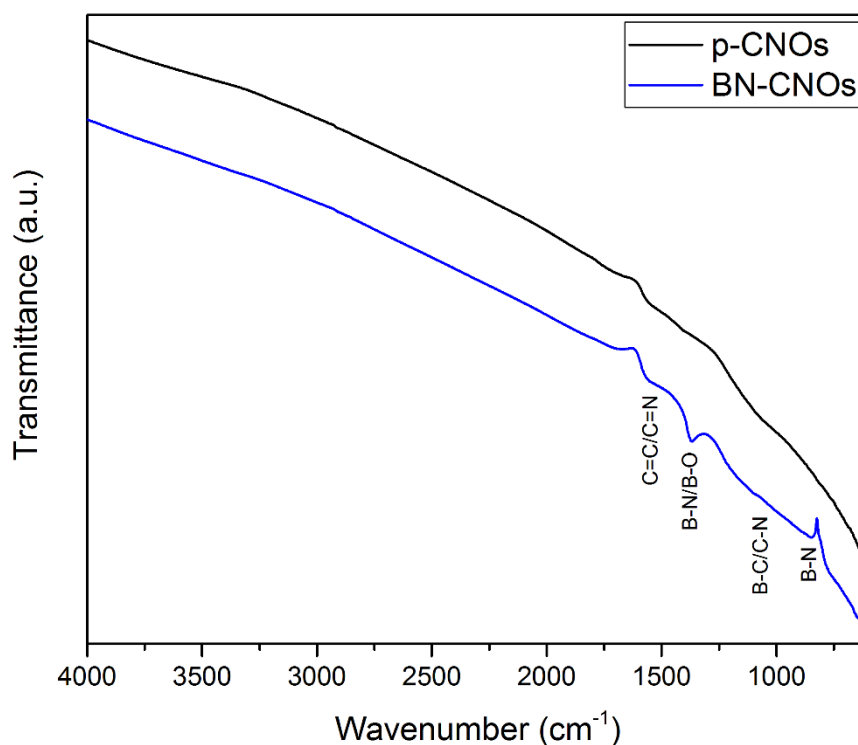


Figure 4.11: FTIR spectra of p-(black line) and BN-CNOs (blue line).

### 4.3.8 BET nitrogen adsorption analysis

BET nitrogen adsorption analyses were performed to investigate the textural characteristic of the CNO materials. The adsorption/desorption isotherms, reported in Figure 4.12, show for both materials a distinctive IV-type isotherm with the presence of a hysteresis loop at high relative pressures, typical of mesoporous materials. In addition, the residual amount of adsorbed gas at low  $P/P_0$  values suggests the presence of micropores in the tested materials. The doping treatment originates a material with a specific surface area (SSA) remarkably lowered to that of p-CNOs, as depicted from Table 4.6. The

pore size distribution has been evaluated by using the Barrett–Joyner–Halenda (BJH) method (insets in Figure 4.12) and both samples exhibit pore with diameter ranging from 2 to 30 nm and a small fraction of micropores (below 2 nm). The results showed that the doping alters the mesoporous structure of CNOs, lowering both SSA and pore volumes.

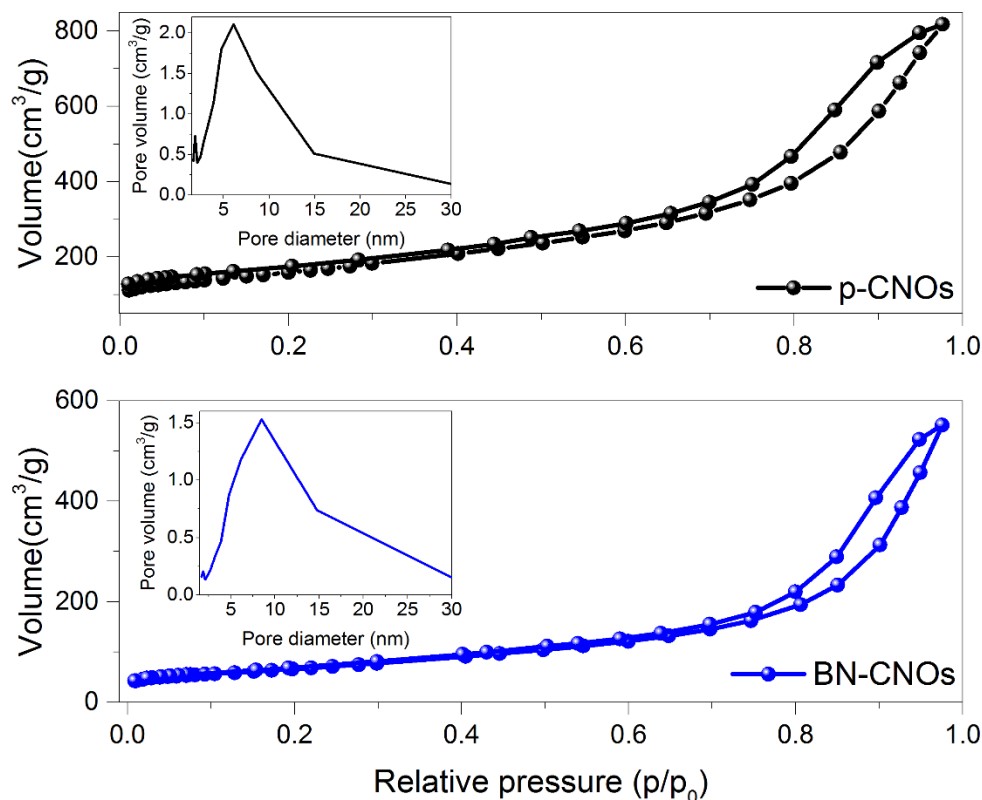


Figure 4.12: Adsorption/desorption isotherms and BJH pore size distributions (inset) of p- (upper panel) and BN-CNOs (bottom panel).

Table 4.6: BET surface areas, BJH pore volumes and pore sizes of p- and BN-CNOs from BET analyses.

Sample	$S_{\text{BET}}$ ( $\text{m}^2/\text{g}$ )	BJH Pore volume ( $\text{cm}^3/\text{g}$ )	BJH Pore size (nm)
p-CNOs	565	1.1	4.7
BN-CNOs	243	0.8	6.1

### 4.3.9 Electrocatalytic investigation towards oxygen reduction reaction

All the characterization techniques have shown that both heteroatoms have been successfully introduced into the graphitic structure of CNOs in different bonding states. Figure 4.13 shows a schematic representation of the CNO surface as suggested by the results obtained from the XPS analyses. The type of species is crucial for the oxygen reduction process. The presence of pyrrolic N



and substitutional B sites (N1 and B1 in Figure 4.13) is expected to give remarkable activity to BN-CNOs, as they are the most performing ORR sites. On the other side, the notable portion of B-N species (N5 and B2 in Figure 4.13) may affect to some extent the overall performance as they are reported to have negative effect on the oxygen adsorption.

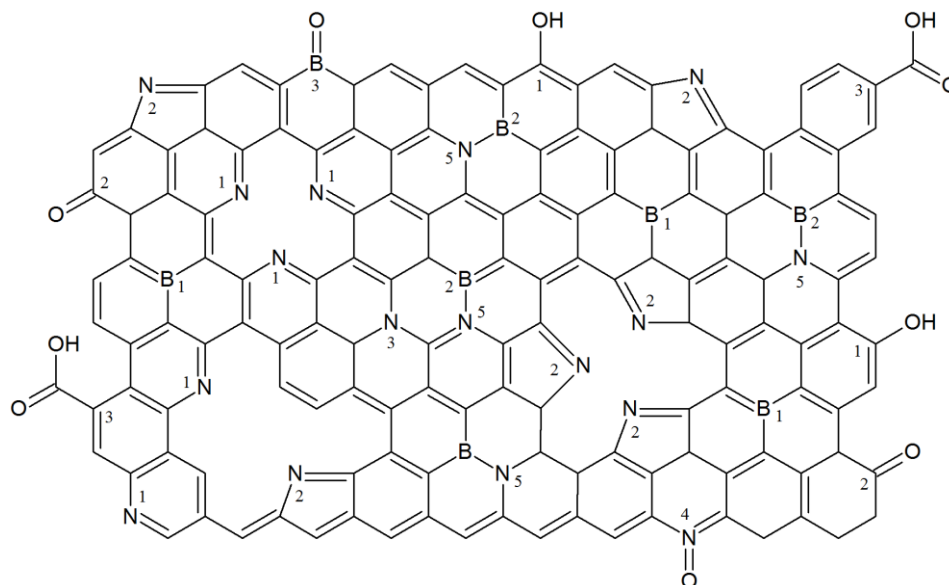


Figure 4.13: Schematic representation of functional groups incorporated on the CNO surface. N1–N5 correspond to different N types (i.e., pyridinic, pyrrolic, graphitic, and oxide, respectively) and B-bonded N atoms; B1–B3 correspond to B-bonded C and N atoms and B oxide, respectively; C1–C3 correspond to hydroxyl, carbonyl, and carboxylic functional groups, respectively.

Dr. Adriano Sacco (IIT) investigated the electrocatalytic activity of p- and BN-CNOs towards ORR in alkaline medium (0.1 M KOH) through different electrochemical techniques. Cyclic voltammetry (CV) was employed to evaluate the reactivity to oxygen molecules of both samples and the corresponding CV curves in O<sub>2</sub>- and N<sub>2</sub>-saturated aqueous solutions are reported in Figure 4.14.

From the analysis of the spectra, two peaks in the range 0.58–0.78 V (*vs* reversible hydrogen electrode, RHE) can be observed for both CNO catalysts in the O<sub>2</sub>-saturated electrolyte. This is a typical characteristic of an ORR active electrocatalyst [56], as confirmed by the vanishing of the peaks when the electrolyte is fluxed with N. A small reduction peak can be still noted in the spectrum of BN-CNOs, attributed to the residual presence of dissolved oxygen molecules [57]. In addition, BN-CNOs exhibit a quite larger reduction current density to that of p-CNOs and this peculiarity is ascribed to the higher catalytic activity of the co-doped samples. In line with what reported for other carbon-based materials [35, 58], the introduction of heteroatoms is an effective way to enhance the ORR electrocatalytic performance of CNOs due to the high content of active sites (i.e. pyridinic N and substitutional B atoms) and the synergic effect of dopant atoms.

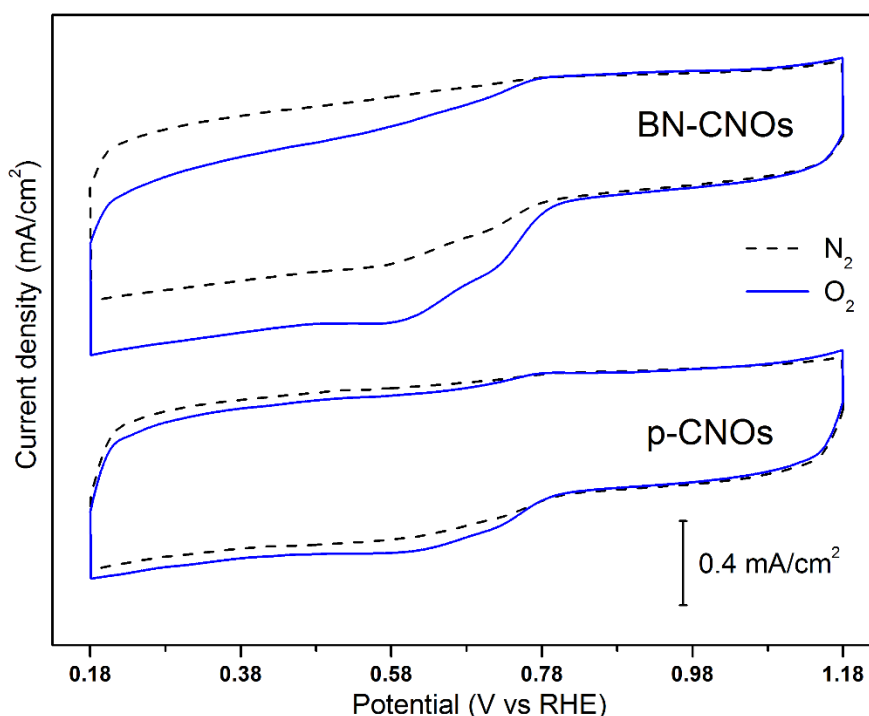


Figure 4.14: CV curves of p- and BN-CNOs in  $O_2$ - and  $N_2$ -saturated aqueous solutions (0.1 M KOH) at 10 mV/s as scan rate.

Rotating disk electrode (RDE) and Rotating ring disk electrode (RRDE) analyses were performed to evaluate the ORR catalytic activity of the proposed materials. The RDE polarization curves of p- and BN-CNOs at different rotation speeds are reported in Figure 4.15A-B. From the analysis of the curves, it is noticeable that the cathodic current increases for potential values lower than the onset and reaches a quasi-plateau behavior when the diffusion limiting occurs [59]. Furthermore, by increasing the rotation speed ( $\omega$ ), the increase of the diffusion-limiting current density  $J$  is observed as a consequence of reduced diffusion distance [59].

From the RDE polarization curves of the CNO derivatives, the onset and half-wave potential have been extracted and reported in Figure 4.15C along with the values of Pt/C [60]. BN-CNOs exhibit slightly lower onset and half-wave potential values to that of p-CNOs, confirming the enhanced ORR activity in line with the CV results and thus the efficacy of the doping approach (

Table 4.7). Further investigation on why the doped CNOs exhibit better ORR performance to that of p-CNOs even if no significant changes are observed in the potential values should be performed.

Compared to Pt/C, BN-CNOs show quite large values and this may be attributed to the high content of connected B-N species in the sample, which lower to some extent the catalytic performance of the CNO catalyst [41]. To have information about the number of electron involved in the oxygen reduction ( $n$ ), the Koutecky–Levich plots have been obtained from the analysis of the RDE polarization curves and are reported in Figure 4.15D for all the tested catalysts. A linear dependency on the square root of  $1/\omega$  is observed for the inverse of the diffusion-limiting current, suggesting a

first-order reaction kinetics with respect to the dissolved oxygen concentration [61]. The Koutecky–Levich equation (equation 1 in Chapter 5, paragraph 2.11) was exploited to fit the experimental data to calculate the  $n$  value for each catalyst.

From the analysis of Figure 4.15B, p-CNOs exhibit a  $n$  value of 3.51, suggesting a predominant four-electron reduction pathway [62]. As a consequence of the co-doping process, BN-CNOs exhibit a larger  $n$  value (i.e. 3.94), confirming their enhanced activity towards ORR. This value is among the largest reported for CNM-based catalysts [11, 19, 28, 35, 36, 43, 58] and other low cost materials [60, 63] and quite close to that of the standard Pt/C (3.97) and the theoretical one (i.e. 4). This feature proves once again the efficacy of the proposed approach in enhancing the ORR performance of p-CNOs.

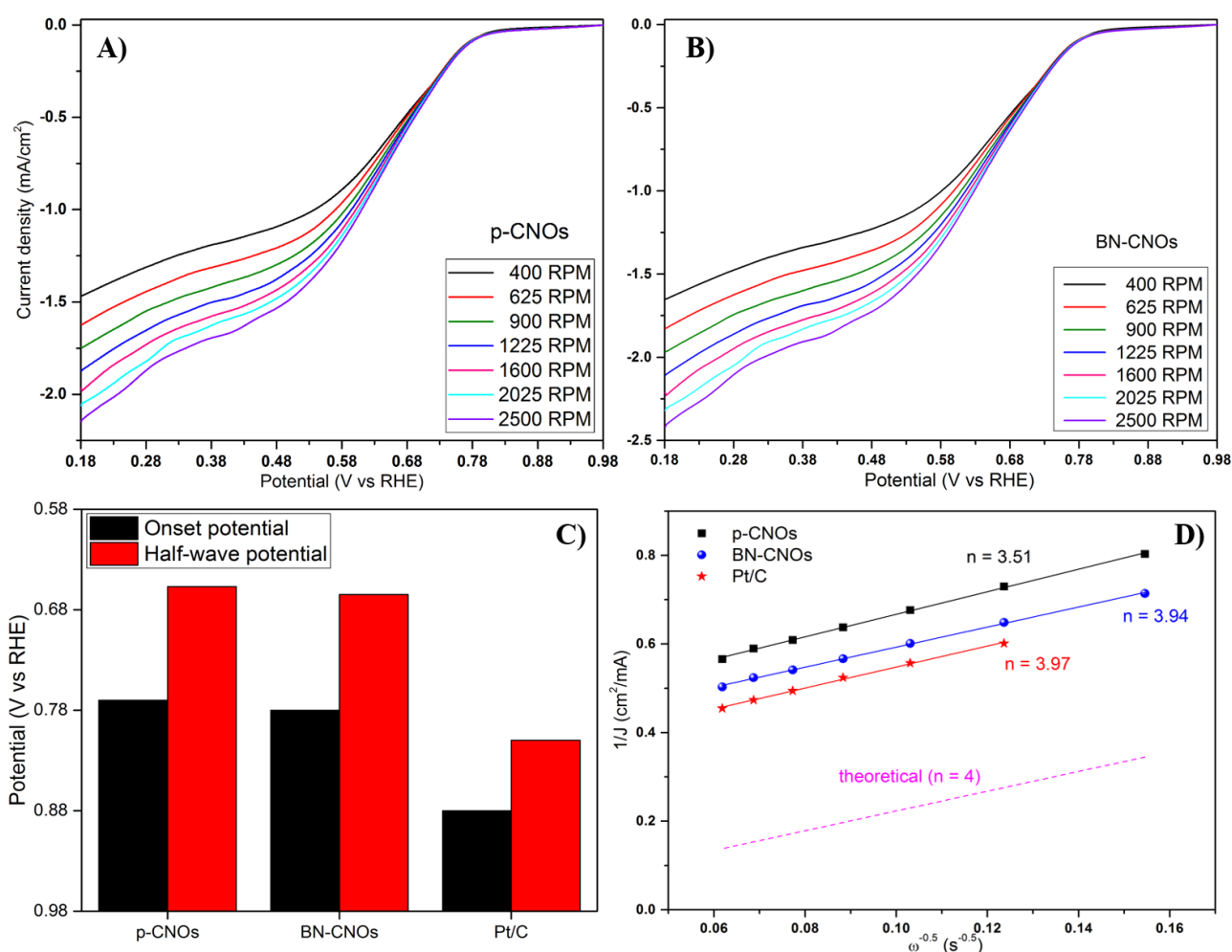


Figure 4.15: RDE polarization curves of A) p- and B) BN-CNOs at different rotation speeds. C) Onset and half-wave potentials of p-CNOs, BN-CNOs, and reference Pt/C catalysts at 1600 rpm. D) Koutecky–Levich plots of p-CNOs, BN-CNOs, and reference Pt/C catalysts at +0.38 V ( $n$  represents the electron-transfer numbers).

Table 4.7: Onset and half-wave of p- and BN-CNOs from RDE analyses.

Sample	Onset potential (V)	Half-wave potential (V)
p-CNOs	0.77	0.657
BN-CNOs	0.78	0.665
Pt/C	0.88	0.81

To further confirm the ORR mechanism, all the catalysts were tested by RRDE analyses, where the disk current  $I_D$  is associate with the four-electron current, while the ring current  $I_R$  with the two-electron peroxide species [64]. The analysis of Figure 4.16A-B shows that both CNO derivatives exhibit a ring current density one or two orders of magnitude less than that showed on the disk, confirming that the oxygen reduction occurs through a four-electron pathway, in accordance with the RDE investigations. Furthermore, BN-CNOs show  $I_R$  values lower than  $10 \mu\text{A}/\text{cm}^2$ , implying a very low formation of peroxide species [56]. The electron-transfer number ( $n$ ) and the peroxide percentage ( $\text{HO}_2^- \%$ ) were calculated from the RRDE polarization curves by using equation 2 and 3, reported in Chapter 6, and their dependence on the applied potential is reported in Figure 4.16C.

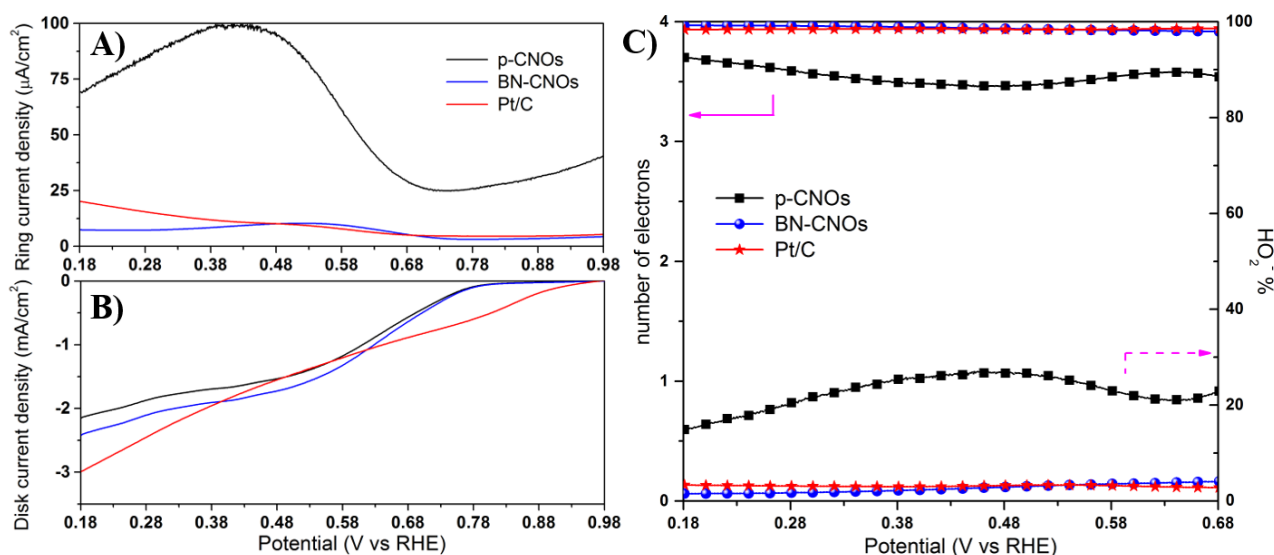


Figure 4.16: A) Ring and B) disk current densities obtained from RRDE analyses of CNO samples and reference Pt/C catalysts at 2500 rpm and a potential of the ring electrode of 1.18 V. C) Comparison of the electron-transfer number (left axis) and the peroxide percentage (right axis) estimated from RRDE analyses at 2500 rpm and different potentials for all of the catalysts.

p-CNOs exhibit  $n$  values in the range 3.46-3.70 and  $\text{HO}_2^- \%$  values lesser than 27% depending on the applied potential in accordance with the RDE results. On the contrary, BN-CNOs exhibit a quasi-constant value ( $3.95 \pm 0.02$ ) close to that of Pt/C ( $3.94 \pm 0.01$ ) in the whole potential range. Furthermore, the negligible production of peroxide species ( $<4\%$ ) further confirms the outstanding

ORR performance of the doped catalysts through a quasi-ideal four-electron reduction pathway. Compared to N-doped CNOs [18, 36, 65], the co-doping strategy is effective in improving the catalytic activity of CNOs.

Electrochemical impedance spectroscopy (EIS) was employed to further investigate the effects of the co-doping on the performance of CNOs. The Nyquist plots of CNO materials are reported in Figure 4.17 and both samples exhibit two frequency-dependent arcs. The small high-frequency arc is associated to the charge-transport properties inside the material, while the high low-frequency arc to the charge-transfer at the catalyst/electrolyte interface [56]. In particular, BN-CNOs show lower impedance values to that of p-CNOs, which is in line with the data obtained from the previous characterization. An equivalent circuit consisting of a series resistance and two resistance/constant phase element parallels (accounting for the high- and low-frequency arcs) were used to fit the experimental data [66]. BN-CNOs exhibit lower values of both charge-transport and charge-transfer resistances to that of p-CNOs (Table 4.8), suggesting that the improved performance of BN-CNOs are due to the better capability of reducing molecular oxygen and to the faster charge transport inside the catalyst.

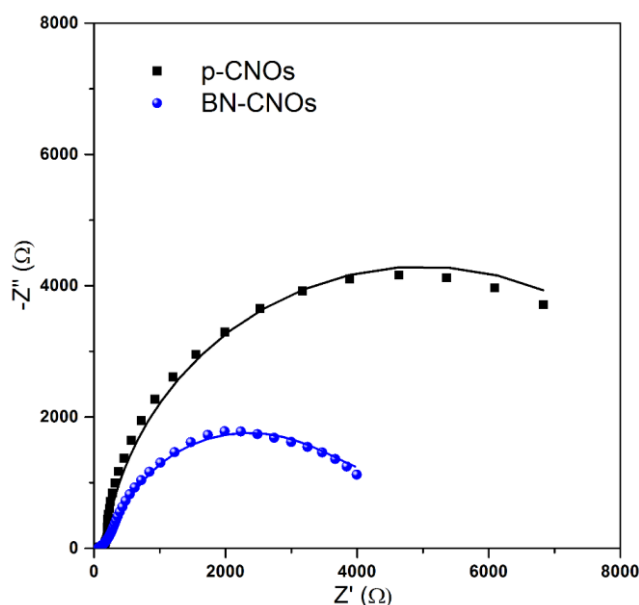


Figure 4.17: Nyquist plots of p- (black line) and BN-CNOs (blue line) measured at +0.68 V and 2500 rpm. Points correspond to the experimental data and continuous lines to the calculated curves.

Table 4.8: Charge-transport and charge-transfer resistances of p- and BN-CNOs from EIS analyses.

Sample	Charge-transport resistance ( $\Omega$ )	Charge-transfer resistance ( $\Omega$ )
p-CNOs	97.6	4888
BN-CNOs	51.4	9663

Chronoamperometry (CA) analyses were performed to evaluate the durability of BN-CNOs; the CA spectra of the co-doped material and the Pt/C catalyst are reported in Figure 4.18. One of the main drawback of Pt/C catalyst is the limited durability due to the detachment of Pt nanoparticles from the carbon support or their aggregation [67], leading to a reduced ORR activity. As confirmed by the experimental results, after 3 h of continuous testing, a decrease of 29% on the initial current can be observed. On the contrary, under the same condition, BN-CNOs is able to retain the 98.7% of the current, showing a remarkable long-term stability. This peculiarity is attributed to the low amount of peroxide species produced during the reduction reaction [68]. Furthermore, the resistance towards methanol crossover was investigated by CA. As shown in the inset of Figure 4.18, the current response of BN-CNOs is not affected by the addition of a 3 M solution of  $\text{CH}_3\text{OH}$ , confirming a complete tolerance to methanol crossover effect [13].

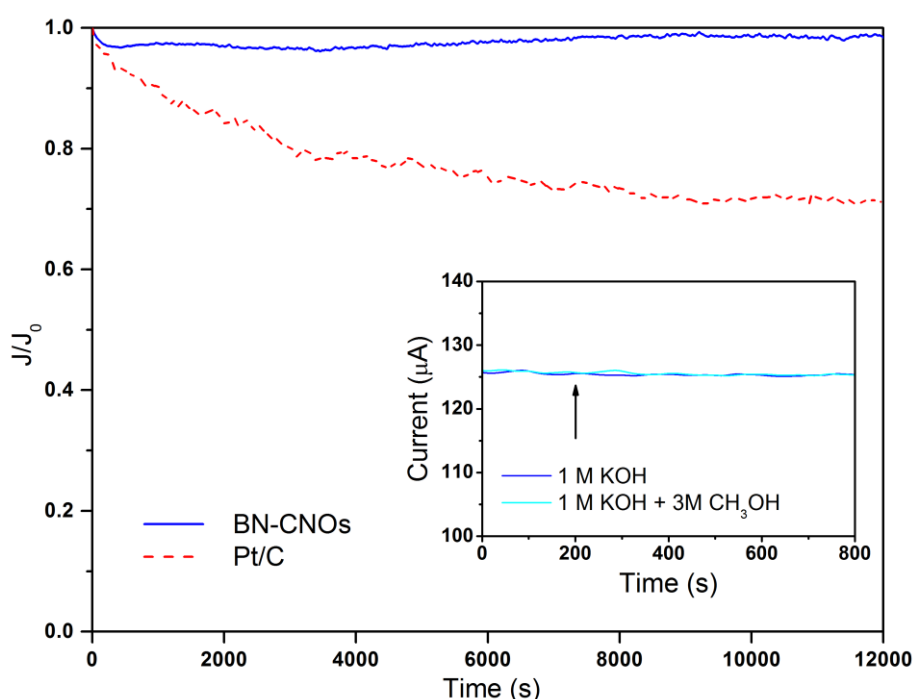


Figure 4.18: Chronoamperometric curves of BN-CNOs and Pt/C catalysts measured at +0.68 V and 2500 rpm in a 0.1 M KOH solution. Both curves have been normalized to the initial current values. The inset shows the CA curves of BN-CNOs acquired with and without the addition of 3 M  $\text{CH}_3\text{OH}$  (the arrow indicates the moment of methanol addition).

The higher ORR activity showed by BN-CNOs compared to p-CNOs are attributed to the formation of beneficial active sites into the CNO structure, which favor the chemisorption of oxygen molecules. Pyridinic N and substitutional B atoms play a central role in the reduction process as they induce a charge redistribution inside the material due to the different electronegativity to that of carbon atoms. The mechanism through which the reduction process occurs is dependent on the dopants. In the case of N, the carbon atoms neighboring N sites are positively charged due to the high electron affinity of nitrogen. In the other case, B atoms themselves are positively charged and they act as a bridge,

transferring electrons to the oxygen molecules. As a consequence of the modified charge density inside the structure, BN-CNOs can efficiently weaken the O-O bond and thus reduce oxygen. It has to be mentioned, however, that the presence of B-N species may affect the overall catalytic activity of BN-CNOs. For this reason, further studies are required to optimize the dopant's configuration in the CNO catalyst.

The results showed also that p-CNOs exhibited a quite good ORR activity, which is unusual for pristine CNMs. This is tentatively ascribed to high defectiveness of the CNO surface (as confirmed by Raman investigation). The ORR catalytic activity in doped CNMs is enhanced as results of the modification of the integrity of  $\pi$  conjugation in the graphitic network. For this reason, the presence of defects can act in a similar way, as reported in literature [69, 70]. The high number of defects along with the high surface area of p-CNOs can offer a high quantity of active sites (even if with lower activity), thus breaking the inactivity of pristine CNMs.

## 4.4 Conclusion

An efficient and low approach has been developed to introduce boron and nitrogen into the CNO network. Thermal annealing of DNDs in the presence of boric acid allowed for the production of the first reported co-doped strategy of CNOs, which was confirmed by several characterization techniques. HRTEM investigations showed that BN-CNOs exhibit mainly a polyhedral shape, while XPS analyses confirmed the presence of the dopant atoms into CNO network. The as-produced material was tested as a possible electrocatalyst for the oxygen reduction reaction and the electrochemical activity was compared to that of p-CNOs and the standard Pt/C catalysts. The results showed that the co-doping process is effective to enhance the ORR performance of CNOs due to the charge redistribution induced by the synergistic effects of the dopants in the form of pyridinic N and substitutional B active sites. Compared to the pristine sample, BN-CNOs showed higher catalytic activity attributed to the higher conductivity and to the quasi-ideal four-electron reduction pathway with a very small production of peroxide species. Furthermore, higher long-term stability and excellent tolerance to methanol crossover was observed in comparison to that of Pt/C.

These results confirm that the proposed co-doping approach is an efficient route to produce ORR electrocatalyst able to rival with the highly expensive platinum-based materials in fuel cells.

## 4.5 References

- [1] Whitesides, G.M.; Crabtree, G.W., Don't Forget Long-Term Fundamental Research in Energy. *Science*, **2007**, *315*, (5813), 796-798.
- [2] Lewis, N.S.; Nocera, D.G., Powering the planet: chemical challenges in solar energy utilization. *Proc. Natl. Acad. Sci. USA*, **2006**, *103*, (43), 15729-15735.
- [3] Steele, B.C.H.; Heinzl, A., Materials for fuel-cell technologies *Nature*, **2001**, *414*, 345-352.
- [4] Arico, A.S.; Bruce, P.; Scrosati, B.; Tarascon, J.-M.; Schalkwijk, W.V., Nanostructured materials for advanced energy conversion and storage devices. *Nat. Mater.*, **2005**, *4*, 366-377.
- [5] Gewirth, A.A.; Thorum, M.S., Electroreduction of dioxygen for fuel-cell applications: materials and challenges. *Inorg. Chem.*, **2010**, *49*, (8), 3557-3566.
- [6] Xia, W.; Mahmood, A.; Liang, Z.; Zou, R.; Guo, S., Earth-Abundant Nanomaterials for Oxygen Reduction. *Angew. Chem. Int. Ed.*, **2016**, *55*, (8), 2650-2676.
- [7] Nie, Y.; Li, L.; Wei, Z., Recent advancements in Pt and Pt-free catalysts for oxygen reduction reaction. *Chem. Soc. Rev.*, **2015**, *44*, (8), 2168-2201.
- [8] Berger, D.J., Fuel Cells and Precious-Metal Catalysts. *Science*, **1999**, *286*, (5437), 49-49.
- [9] Zhang, J.; Xia, Z.; Dai, L., Carbon-based electrocatalysts for advanced energy conversion and storage. *Science Advances*, **2015**, *1*, (7).
- [10] Sawant, S.Y.; Han, T.H.; Cho, M.H., Metal-Free Carbon-Based Materials: Promising Electrocatalysts for Oxygen Reduction Reaction in Microbial Fuel Cells. *Int. J. Mol. Sci.*, **2016**, *18*, (1), 25.
- [11] Gong, K.; Du, F.; Xia, Z.; Durstock, M.; Dai, L., Nitrogen-Doped Carbon Nanotube Arrays with High Electrocatalytic Activity for Oxygen Reduction. *Science*, **2009**, *323*, (5915), 760-764.
- [12] Qu, L.; Liu, Y.; Baek, J.-B.; Dai, L., Nitrogen-Doped Graphene as Efficient Metal-Free Electrocatalyst for Oxygen Reduction in Fuel Cells. *ACS Nano*, **2010**, *4*, (3), 1321-1326.
- [13] Yang, L.; Jiang, S.; Zhao, Y.; Zhu, L.; Chen, S.; Wang, X.; Wu, Q.; Ma, J.; Ma, Y.; Hu, Z., Boron-doped carbon nanotubes as metal-free electrocatalysts for the oxygen reduction reaction. *Angew. Chem. Int. Ed.*, **2011**, *50*, (31), 7132-7135.
- [14] Dai, L.; Xue, Y.; Qu, L.; Choi, H.J.; Baek, J.B., Metal-free catalysts for oxygen reduction reaction. *Chem. Rev.*, **2015**, *115*, (11), 4823-4892.
- [15] Liu, X.; Dai, L., Carbon-based metal-free catalysts. *Nature Reviews Materials*, **2016**, *1*, 16064.
- [16] Daems, N.; Sheng, X.; Vankelecom, I.F.J.; Pescarmona, P.P., Metal-free doped carbon materials as electrocatalysts for the oxygen reduction reaction. *J. Mater. Chem. A*, **2014**, *2*, 4085-4110.
- [17] Yang, Z.; Nie, H.; Chen, X.a.; Chen, X.; Huang, S., Recent progress in doped carbon nanomaterials as effective cathode catalysts for fuel cell oxygen reduction reaction. *J. Power Sources*, **2013**, *236*, 238-249.
- [18] Zhang, Y.; Reed, A.; Kim, D.Y., Nitrogen doped carbon nano-onions as efficient and robust electrocatalysts for oxygen reduction reactions. *Curr. Appl. Phys.*, **2018**, *18*, 417-423.
- [19] Lin, Y.; Zhu, Y.; Zhang, B.; Kim, Y.A.; Endo, M.; Su, D.S., Boron-doped onion-like carbon with enriched substitutional boron: the relationship between electronic properties and catalytic performance. *J. Mater. Chem. A*, **2015**, *3*, 21805-21841.
- [20] Sun, X.; Xu, J.; Ding, Y.; Zhang, B.; Feng, Z.; Su, D.S., The Effect of Different Phosphorus Chemical States on an Onion-like Carbon Surface for the Oxygen Reduction Reaction. *ChemSusChem*, **2015**, *8*, (17), 2872-2876.
- [21] Camisasca, A.; Sacco, A.; Brescia, R.; Giordani, S., Boron/Nitrogen-Codoped Carbon Nano-Onion Electrocatalysts for the Oxygen Reduction Reaction. *ACS Applied Nano Materials*, **2018**, *1*, (10), 5763-5773.
- [22] Mochalin, V.N.; Shenderova, O.; Ho, D.; Gogotsi, Y., The properties and applications of nanodiamonds. *Nat. Nanotechnol.*, **2011**, *7*, (1), 11-23.



- [23] Palkar, A.; Melin, F.; Cardona, C.M.; Elliott, B.; Naskar, A.K.; Edie, D.D.; Kumbhar, A.; Echegoyen, L., Reactivity differences between carbon nano onions (CNOs) prepared by different methods. *Chem. Asian J.*, **2007**, 2, (5), 625-633.
- [24] Tomita, S.; Fujii, M.; Hayashi, S.; Yamamoto, K., Electron energy-loss spectroscopy of carbon onions. *Chem. Phys. Lett.*, **1999**, 305, 225-229.
- [25] Tomita, S.; Burian, A.; Dore, J.C.; LeBolloch, D.; Fujii, M.; Shinji, H., Diamond nanoparticles to carbon onions transformation: X-ray diffraction studies. *Carbon*, **2002**, 40, 1469-1474.
- [26] Sogabe, T.; Nakajima, K.; Inagaki, M., Effect of boron-doping on structure and some properties of carbon-carbon composite. *J. Mater. Sci.*, **1996**, 31, 6469-6476.
- [27] Way, B.M.; Dahn, J.R.; Tiedje, T.; Myrtle, K.; Kasrai, M., Preparation and characterization of BxC<sub>1-x</sub> thin films with the graphite structure. *Phys. Rev. B*, **1992**, 46, (3), 1697-1702.
- [28] Zheng, Y.; Jiao, Y.; Ge, L.; Jaroniec, M.; Qiao, S.Z., Two-step boron and nitrogen doping in graphene for enhanced synergistic catalysis. *Angew. Chem. Int. Ed.*, **2013**, 52, (11), 3110-3116.
- [29] Kim, S.Y.; Park, J.; Choi, H.C.; Ahn, J.P.; Hou, J.Q.; Kang, H.S., X-ray Photoelectron Spectroscopy and First Principles Calculation of BCN Nanotubes. *J. Am. Chem. Soc.*, **2007**, 129, 1705-1716.
- [30] Bartelmeß, J.; De Luca, E.; Signorelli, A.; Baldrighi, M.; Becce, M.; Brescia, R.; Nardone, V.; Parisini, E.; Echegoyen, L.; Pompa, P.P.; Giordani, S., Boron dipyrromethene (BODIPY) functionalized carbon nano-onions for high resolution cellular imaging. *Nanoscale*, **2014**, 6, (22), 13761-13769.
- [31] Redlich, P.; Loeffler, J.; Ajayan, P.M.; Bill, J.; Aldinger, F.; Ruhle, M., B-C-N nanotubes and boron doping of carbon nanotubes. *Chem. Phys. Lett.*, **1996**, 260, 465-470.
- [32] Raidongia, K.; Nag, A.; Hembram, K.P.; Waghmare, U.V.; Datta, R.; Rao, C.N., BCN: a graphene analogue with remarkable adsorptive properties. *Chem. Eur. J.*, **2010**, 16, (1), 149-157.
- [33] Pichot, V.; Stephan, O.; Comet, M.; Fousson, E.; Mory, J.; March, K.; Spitzer, D., High Nitrogen Doping of Detonation Nanodiamonds. *J. Phys. Chem. C* **2010**, 114, 10082-10087.
- [34] Konno, H.; Nakahashi, T.; Inagaki, M.; Sogabe, T., Nitrogen incorporation into boron-doped graphite and formation of B-N bonding. *Carbon*, **1999**, 37, 471-475.
- [35] Baik, S.; Lee, J.W., Effect of boron-nitrogen bonding on oxygen reduction reaction activity of BN Co-doped activated porous carbons. *RSC Adv.*, **2015**, 5, (31), 24661-24669.
- [36] Choi, E.Y.; Kim, C.K., Fabrication of nitrogen-doped nano-onions and their electrocatalytic activity toward the oxygen reduction reaction. *Sci. Rep.*, **2017**, 7, (1), 4178.
- [37] Ratso, S.; Kruusenberg, I.; Vikkisk, M.; Joost, U.; Shulga, E.; Kink, I.; Kallio, T.; Tammeveski, K., Highly active nitrogen-doped few-layer graphene/carbon nanotube composite electrocatalyst for oxygen reduction reaction in alkaline media. *Carbon*, **2014**, 73, 361 - 370.
- [38] Jin, J.; Pan, F.; Jiang, L.; Fu, X.; Liang, A.; Wei, Z.; Zhang, J.; Sun, G., Catalyst-Free Synthesis of Crumpled Boron and Nitrogen Co-Doped Graphite Layers with Tunable Bond Structure for Oxygen Reduction Reaction. *ACS Nano* **2014**, 8, (4), 3313-3321.
- [39] Guo, D.; Shibuya, R.; Akiba, C.; Saji, S.; Kondo, T.; Nakamura, J., Active sites of nitrogen-doped carbon materials for oxygen reduction reaction clarified using model catalysts. *Science*, **2016**, 351, (6271), 361-365.
- [40] Xing, T.; Zheng, Y.; Li, L.H.; Cowie, B.C.C.; Gunzelmann, D.; Qiao, S.Z.; Huang, S.; Chen, Y., Observation of Active Sites for Oxygen Reduction Reaction on Nitrogen-Doped Multilayer Graphene. *ACS Nano*, **2014**, 8, (7), 6856-6862.
- [41] Zhao, Y.; Yang, L.; Chen, S.; Wang, X.; Ma, Y.; Wu, Q.; Jiang, Y.; Qian, W.; Hu, Z., Can boron and nitrogen co-doping improve oxygen reduction reaction activity of carbon nanotubes? *J. Am. Chem. Soc.*, **2013**, 135, (4), 1201-1204.
- [42] Panchakarla, L.S.; Govindaraj, A.; Rao, C.N.R., Nitrogen- and Boron-Doped Double-Walled Carbon Nanotubes. *ACS Nano*, **2007**, 1, (5), 494-500.
- [43] Kim, D.W.; Li, O.L.; Saito, N., Enhancement of ORR catalytic activity by multiple heteroatom-doped carbon materials. *Phys. Chem. Chem. Phys.*, **2015**, 17, (1), 407-413.

- [44] Wang, S.; Zhang, L.; Xia, Z.; Roy, A.; Chang, D.W.; Baek, J.B.; Dai, L., BCN graphene as efficient metal-free electrocatalyst for the oxygen reduction reaction. *Angew. Chem. Int. Ed.*, **2012**, *51*, (17), 4209-4212.
- [45] Mykhaylyk, O.O.; Solonin, Y.M.; Batchelder, D.N.; Brydson, R., Transformation of nanodiamond into carbon onions: A comparative study by high-resolution transmission electron microscopy, electron energy-loss spectroscopy, x-ray diffraction, small-angle x-ray scattering, and ultraviolet Raman spectroscopy. *J. Appl. Phys.*, **2005**, *97*, (7), 074302.
- [46] Kim, S.-M.; Heo, Y.-K.; Bae, K.-T.; Oh, Y.-T.; Lee, M.-H.; Lee, S.-Y., In situ formation of nitrogen-doped onion-like carbon as catalyst support for enhanced oxygen reduction activity and durability. *Carbon* **2016**, *101*, 420-430.
- [47] Wu, G.; Nelson, M.; Ma, S.; Meng, H.; Cui, G.; Shen, P.K., Synthesis of nitrogen-doped onion-like carbon and its use in carbon-based CoFe binary non-precious-metal catalysts for oxygen-reduction. *Carbon*, **2011**, *49*, 3972 - 3982.
- [48] Hagio, T.; Nakamizo, M.; Kobayashi, K., Studies on X-ray diffraction and Raman spectra of B-doped natural graphite. *Carbon*, **1989**, *27*, (2), 259-263.
- [49] Choi, C.H.; Park, S.H.; Woo, S.I., Binary and Ternary Doping of Nitrogen, Boron, and Phosphorus into Carbon for Enhancing Electrochemical Oxygen Reduction Activity. *ACS Nano*, **2012**, *6*, (8), 7084-7091.
- [50] Pimenta, M.A.; Dresselhaus, G.; Dresselhaus, M.S.; Cancado, L.G.; Jorio, A.; Saito, R., Studying disorder in graphite-based systems by Raman spectroscopy. *Phys. Chem. Chem. Phys.*, **2007**, *9*, (11), 1276-1291.
- [51] Ferrari, A.C.; Robertson, J., Interpretation of Raman spectra of disordered and amorphous carbon. *Phys. Rev. B*, **2000**, *61*, 14095.
- [52] Ferrari, A.C., Raman spectroscopy of graphene and graphite: Disorder, electron-phonon coupling, doping and nonadiabatic effects. *Solid State Commun.*, **2007**, *143*, (1-2), 47-57.
- [53] Yuge, R.; Bandow, S.; Yudasaka, M.; Toyama, K.; Iijima, S.; Manako, T., Boron- and nitrogen-doped single-walled carbon nanohorns with graphite-like thin sheets prepared by CO<sub>2</sub> laser ablation method. *Carbon*, **2017**, *111* 675-680.
- [54] Yang, X.; Liu, L.; Wu, M.; Wang, W.; Bai, X.; Wang, E., Wet-chemistry-assisted nanotube-substitution reaction for high-efficiency and bulk-quantity synthesis of boron- and nitrogen-codoped single-walled carbon nanotubes. *J. Am. Chem. Soc.*, **2011**, *133*, (34), 13216-13219.
- [55] Chen, Y.; Yang, S.; Zhang, J., The chemical composition and bonding structure of B-C-N-H thin films deposited by reactive magnetron sputtering. *Surf. Interface Anal.*, **2009**, *41*, (11), 865-871.
- [56] Garino, N.; Sacco, A.; Castellino, M.; Munoz-Tabares, J.A.; Chiodoni, A.; Agostino, V.; Margaria, V.; Gerosa, M.; Massaglia, G.; Quaglio, M., Microwave-Assisted Synthesis of Reduced Graphene Oxide/SnO<sub>2</sub> Nanocomposite for Oxygen Reduction Reaction in Microbial Fuel Cells. *ACS Appl. Mater. Interfaces*, **2016**, *8*, (7), 4633-4643.
- [57] Sacco, A.; Garino, N.; Lamberti, A.; Pirri, C.F.; Quaglio, M., Anodically-grown TiO<sub>2</sub> nanotubes: Effect of the crystallization on the catalytic activity toward the oxygen reduction reaction. *Appl. Surf. Sci.*, **2017**, *412*, 447-454.
- [58] Fei, H.; Ye, R.; Ye, G.; Gong, Y.; Peng, Z.; Fan, X.; Samuel, E.L.G.; Ajayan, P.M.; Tour, J.M., Boron- and Nitrogen-Doped Graphene Quantum Dots/Graphene Hybrid Nanoplatelets as Efficient Electrocatalysts for Oxygen Reduction. *ACS Nano*, **2014**, *8*, (10), 10837-10843.
- [59] Tan, Y.; Xu, C.; Chen, G.; Fang, X.; Zheng, N.; Xie, Q., Facile Synthesis of Manganese-Oxide-containing Mesoporous Nitrogen-Doped Carbon for Efficient Oxygen Reduction. *Adv. Funct. Mater.*, **2012**, *22*, 4584-4591.
- [60] Delmondo, L.; Munoz-Tabares, J.A.; Sacco, A.; Garino, N.; Massaglia, G.; Castellino, M.; Salvador, G.P.; Pirri, C.F.; Quaglio, M.; Chiodoni, A., Thermal evolution of Mn<sub>x</sub>O<sub>y</sub> nanofibres as catalysts for the oxygen reduction reaction. *Phys. Chem. Chem. Phys.*, **2017**, *19*, (42), 28781-28787.

- [61] Liang, Y.; Li, Y.; Wang, H.; Zhou, J.; Wang, J.; Regier, T.; Dai, H., Co(3)O(4) nanocrystals on graphene as a synergistic catalyst for oxygen reduction reaction. *Nat. Mater.*, **2011**, *10*, (10), 780-786.
- [62] Garino, N.; Sacco, A.; Castellino, M.; Munoz-Tabares, J.A.; Armandi, M.; Chiodoni, A.; Pirri, C.F., One-Pot Microwave-Assisted Synthesis of Reduced Graphene Oxide/Iron Oxide Nanocomposite Catalyst for the Oxygen Reduction Reaction. *ChemistrySelect*, **2016**, *1*, 3640 - 3646.
- [63] Xue, Y.; Jin, W.; Du, H.; Wang, S.; Zheng, S.; Zhang, Y., Tuning  $\alpha$ -Fe<sub>2</sub>O<sub>3</sub> nanotube arrays for the oxygen reduction reaction in alkaline media. *RSC Adv.*, **2016**, *6*, (48), 41878-41884.
- [64] Orazem, M.E.; Tribollet, B. *Electrochemical Impedance Spectroscopy*. John Wiley & Sons, Hoboken, NJ, **2008**.
- [65] Chatterjee, K.; Ashokkumar, M.; Gullapalli, H.; Gong, Y.; Vajtai, R.; Thanikaivelan, P.; Ajayan, P.M., Nitrogen-rich carbon nano-onions for oxygen reduction reaction. *Carbon* **2018**, *130*, 645-651.
- [66] Sacco, A., Electrochemical impedance spectroscopy: Fundamentals and application in dye-sensitized solar cells. *Renew. Sustain. Energy Rev.*, **2017**, *79*, 814-829.
- [67] Wu, G.; Santandreu, A.; Kellogg, W.; Gupta, S.; Ogoke, O.; Zhang, H.; Wang, H.-L.; Dai, L., Carbon nanocomposite catalysts for oxygen reduction and evolution reactions: From nitrogen doping to transition-metal addition. *Nano Energy*, **2016**, *29*, 83-110.
- [68] Jaouen, F.; Proietti, E.; Lefèvre, M.; Chenitz, R.; Dodelet, J.-P.; Wu, G.; Chung, H.T.; Johnston, C.M.; Zelenay, P., Recent advances in non-precious metal catalysis for oxygen-reduction reaction in polymer electrolyte fuel cells. *Energy & Environmental Science*, **2011**, *4*, (1), 114-130.
- [69] Jiang, Y.; Yang, L.; Sun, T.; Zhao, J.; Lyu, Z.; Zhuo, O.; Wang, X.; Wu, Q.; Ma, J.; Hu, Z., Significant Contribution of Intrinsic Carbon Defects to Oxygen Reduction Activity. *ACS Catal.*, **2015**, *5*, 6707-6712.
- [70] Jin, H.; Huang, H.; He, Y.; Feng, X.; Wang, S.; Dai, L.; Wang, J., Graphene Quantum Dots Supported by Graphene Nanoribbons with Ultrahigh Electrocatalytic Performance for Oxygen Reduction. *J. Am. Chem. Soc.*, **2015**, *137*, (24), 7588-7591.

# ***Chapter 5 - Materials and methods***

## **5.1 Materials**

Detonation nanodiamonds with a particle size of 4-6 nm (type: uDiamond®Molto) were purchased from Carboneon Ltd and used as received.

All the chemicals (reagents and solvents) were purchased from Sigma Aldrich and Merck in high purity grade and used as received.

For spectroscopic analyses, the solvents were used in a spectrophotometric grade.

The far-red BODIPY dye used in Chapter 3 was synthesized and characterized by Dr. Stefania Lettieri following the procedure reported in reference [1].

## **5.2 Methods**

### **5.2.1 Transmission electron microscopy**

For high-resolution transmission electron microscopy (HRTEM) analyses, the samples were dispersed in ethanol and drop-casted onto copper grids covered with a holey carbon film.

For the samples in Chapters 2 and 3, HRTEM and electron energy loss spectroscopy (EELS) analyses were carried out on a JEOL JEM equipped with a charge coupled device camera (ORius SC1000, Gatan, Inc.) operating at 80 kV.

For the samples in Chapter 4, HRTEM, energy-filtered TEM (EFTEM) imaging and EELS analyses were carried out on a JEOL JEM 2200FS equipped with a Schottky emitter, a CEOS image aberration corrector and an in-column energy filter ( $\Omega$ -type) operating at 200 kV. EFTEM elemental maps were computed using the three-windows method at the K edges of B (10 eV energy slit width), C (16 eV energy slit width) and N (20 eV energy slit width). The EELS spectra were acquired in diffraction mode, with a collection semi-angle of 5.5 mrad, an energy resolution of 1.1 eV and a dispersion of 0.3 eV/pixel. The presented spectra were obtained by background subtraction and plural scattering deconvolution from the raw spectra.

### 5.2.2 X-ray photoelectron spectroscopy

X-ray Photoelectron Spectroscopy (XPS) analyses were carried out using a PHI 5000 VersaProbe XPS spectrometer with a monochromatic Al K $\alpha$  (1486.6 eV) radiation source and a take-off angle of 45°. A spot size of 100  $\mu$ m was used to collect the photoelectron signal for survey and high-resolution spectra with pass energy values equal to 187.85 eV and to 23.5 eV, respectively. Fitting procedure and deconvolution analyses were performed by using Multipak 9.6 dedicated software; RSF values from MultiPak software were utilized for quantitative elemental analysis. The core level peak energies were calibrated to the C1s peak at 284.5 eV (C–C/C–H sp<sup>2</sup> bonds) and the corresponding curve fitting was made with a Gaussian-Lorentzian peak shape after performing a Shirley background correction.

### 5.2.3 X-ray diffraction

X-Ray Diffraction (XRD) measurements were performed using a PANalytical Empyrean X-Ray diffractometer equipped with a 1.8 kW Cu K $\alpha$  ceramic X-ray tube, PIXcel3D 2x2 area detector and operating at 45 kV and 40 mA. The diffraction patterns were collected in air at room temperature in Parallel-Beam (PB) geometry and symmetric reflection mode using a zero-diffraction silicon substrate with continuous scan mode in a range of 10° to 85° and 0.02° as step size. XRD data analysis was carried out using HighScore 4.5 software from PANalytical.

### 5.2.4 Raman spectroscopy

Raman spectra were acquired on a Horiba Jobin Yvon HR 800 UV LabRam Raman microscope. For the Raman measurements, the samples were deposited directly on silicon wafers and excited with a built-in 633 nm or 325 nm laser.

### 5.2.5 Thermogravimetric analysis

Thermogravimetric analysis (TGA) was conducted on a TA Q500 analyser, using a Pt pan as sample holder for the samples described in Chapters 2 and 3. A Netzsch TG 209 F1 Libra instrument and an Al<sub>2</sub>O<sub>3</sub> pan as sample holder were used for samples in Chapter 4.

The procedure was the same for all the samples. After equilibrating the sample at 30 °C for 5 min and then at 100 °C for additional 20 min, the measurement was performed in air using a heating rate of 10 °C/min. The sample weight was monitored until 900 °C.

### 5.2.6 Fourier-transform infrared spectroscopy

Attenuated total reflectance Fourier-transform infrared (ATR-FTIR) spectra were recorded with an ATR accessory (MIRacle ATR, PIKE Technologies) coupled to an FTIR spectrometer (Equinox 70 FT-IR, Bruker). All spectra were recorded on solid sample under vacuum in the range from 4000 to 600  $\text{cm}^{-1}$  with a resolution of 4  $\text{cm}^{-1}$ .

### 5.2.7 Absorption and emission spectroscopy

Absorption spectra were recorded on an Agilent Cary 8454 UV–vis diode array spectrophotometer. Fluorescence spectra were taken on a Horiba Jobin Yvon Fluoromax-4 spectrofluorometer. Quartz glass cells (1.00 cm  $\times$  1.00 cm) were used for the measurements. For the analyses, the samples were dispersed in the appropriate solvent to a final concentration of 1 mg/mL. After sonicating for 15 min at 37 kHz, the solution was diluted in the used solvent to achieve final concentrations of 5, 10 and 20  $\mu\text{g/mL}$ . Before the measurements, the samples were sonicated for additional 20 min at 37 kHz. The fluorescence quantum yield of the far-red BODIPY dye and fluo-CNOs were calculated by Dr. Stefania Lettieri following the procedure described in reference [2].

### 5.2.8 BET nitrogen adsorption analysis

BET nitrogen adsorption/desorption measurements were performed at 77K using Quadrasorb evo analyzer from Quantachrome Instruments. Before the analysis, the samples were degassed at 100  $^{\circ}\text{C}$  under vacuum overnight to remove any adsorbed species. Specific surface area (SSA) was determined using the Brunauer-Emmet-Teller (BET) method in the relative pressure range from 0.1 to 0.3. The pore volumes and the pore-size distributions were determined by applying the Barrett, Joyner, and Halenda (BJH) method to the desorption branch of the isotherms and the non-linear density functional theory (NLDFT) method. Data analysis was carried out using QuadraWin dedicated software from Quantachrome.

### 5.2.9 Dynamic light scattering and zeta-potential

Dynamic light scattering (DLD) analyses were performed on a Malvern Nano-ZS instrument operating in backscattering ( $173^{\circ}$ ) mode and analyzed with the software Zetasizer, with automatic selection of the optimal detector position and number of independent measurements. For carbon nanomaterials, a refractive index value of 2.05 was used, while 1.33 for water. Quartz glass cells (1.00 cm  $\times$  1.00 cm) were used for the measurements. Zeta-potential analyses were performed on the same apparatus using the disposable zeta-potential cuvettes.

For the analyses, the samples were dispersed in the appropriate solvent to a final concentration of 1 mg/mL. After sonicating for 10 min at 37 kHz, the solution was diluted to achieve final concentrations of 5, 10 and 20 µg/mL. Before the measurements, the samples were sonicated for additional 20 min at 37 kHz.

### 5.2.10 Biological methods

The *in vitro* investigation of the CNO derivatives were performed by Dr. Marta d'Amora. The biological methods including sample preparation, cell cultures, cellular viability and confocal imaging are described in reference [1].

### 5.2.11 Electrochemical characterization

The electrocatalytic investigations were performed by Dr. Adriano Sacco. The electrochemical characterizations were conducted by employing an electrochemical workstation (760D, CH Instrument) and a rotating ring disk electrode apparatus (RRDE-3A, ALS). Catalyst samples were deposited on the working electrode (glassy carbon disk/Pt ring, BioLogic, with an active area of 0.13 cm<sup>2</sup>), following an optimized procedure reported elsewhere [3]. Before the catalyst deposition, the working electrode was properly polished with ethanol. The catalyst (2 mg) was dispersed in a solution containing 25 µL of water, 175 µL of 5% Nafion solution, and 100 µL of isopropyl alcohol. The mixture was ultrasonicated for 2 min to form a uniform black dispersion. 10 µL of this formulation was cast-coated onto the disk surface to form a uniform film. The resulting deposition was dried at room temperature for 1 day. Commercial Pt/C (purchased from Sigma-Aldrich) was employed as a reference catalyst. For both CNO- and Pt-based catalysts, the amount of active material was fixed at 0.5 mg/cm [4]. The experiments were carried out at room temperature, employing a 0.1 M KOH (purity 99.995 % metal basis) electrolyte saturated with O<sub>2</sub> (unless otherwise specified) and Pt and Ag/AgCl as the counter and reference electrodes, respectively. The potentials were then referred to a reversible hydrogen electrode (RHE). Onset potential was taken at a current density of 0.1 mA/cm<sup>2</sup>. CV curves were acquired at a 10 mV/s as scan rate in the potential range 0.18–1.18 V in O<sub>2</sub>- and N<sub>2</sub>-saturated electrolytes and until a stable curve was obtained. For RDE characterization, the potential range was 0.18–1.18 V, the scan rate was 5 mV/s, and the rotation speed  $\omega$  was changed between 400 and 2500 rpm. The LSV curves of all catalysts were collected after a stable CV curve was obtained. The electron-transfer number  $n$  was calculated by exploiting Koutecky–Levich plots and the equation [5]:

$$\frac{1}{J} = \frac{1}{0.62nFC_{O_2}D_{O_2}^{2/3}v^{-1/6}\omega^{1/2}} + \frac{1}{J_K} \quad (1)$$

In equation 1,  $J$  and  $J_K$  represent the measured and kinetic current densities, respectively,  $F$  is the Faraday constant,  $C_{O_2}$  and  $D_{O_2}$  are the  $O_2$  bulk concentration and diffusion coefficient, respectively, and  $\nu$  represents the electrolyte kinematic viscosity. RRDE characterization was carried out by employing the same parameters as those of RDE characterization, with the exception of the rotation speed (fixed at 2500 rpm) and ring electrode potential (fixed at 1.18 V). The ring ( $I_R$ ) and disk ( $I_D$ ) currents were acquired and, through the following equations [6], used to calculate the percentage of  $HO_2^-$  and electron-transfer number ( $N$  in equations 2 and 3 represents the Pt ring current collection efficiency).

$$HO_2^- \% = 200 \times \frac{I_R/N}{I_D + I_R/N} \quad (2)$$

$$n = 4 \times \frac{I_D}{I_D + I_R/N} \quad (3)$$

The  $N$  value was calibrated in 0.1 M KOH with a 10 mM  $K_3Fe(CN)_6$  electrolyte and was estimated to be approximately 0.38.

EIS characterization was conducted at 2500 rpm, with a small voltage of 10 mV superimposed to a fixed 0.68 V potential, between  $10^{-2}$  and  $10^4$  Hz. Finally, CA measurements were carried out at 0.68 V and 2500 rpm. The methanol crossover effect was analyzed by performing a CA test at the same potential and rotation speed in the 0.1 M KOH electrolyte upon the addition of 3 M  $CH_3OH$  [7].



## 5.3 References

- [1] Lettieri, S.; Camisasca, A.; d'Amora, M.; Diaspro, A.; Uchida, T.; Nakajima, Y.; Yanagisawa, K.; Maekawa, T.; Giordani, S., Far-red fluorescent carbon nano-onions as a biocompatible platform for cellular imaging. *RSC Adv.*, **2017**, 7, (72), 45676-45681.
- [2] Williams, A.T.R.; Winfield, S.A.; Miller, J.N., Relative fluorescence quantum yields using a computer-controlled luminescence spectrometer. *Analyst*, **1983**, 108, (1290), 1067-1071.
- [3] Yang, X.; Liu, L.; Wu, M.; Wang, W.; Bai, X.; Wang, E., Wet-chemistry-assisted nanotube-substitution reaction for high-efficiency and bulk-quantity synthesis of boron- and nitrogen-codoped single-walled carbon nanotubes. *J. Am. Chem. Soc.*, **2011**, 133, (34), 13216-13219.
- [4] Cheng, S.; Liu, H.; Logan, B.E., Power Densities Using Different Cathode Catalysts (Pt and CoTMPP) and Polymer Binders (Nafion and PTFE) in Single Chamber Microbial Fuel Cells. *Environ. Sci. Technol.*, **2006**, 40, (1), 364-369.
- [5] Tan, Y.; Xu, C.; Chen, G.; Fang, X.; Zheng, N.; Xie, Q., Facile Synthesis of Manganese-Oxide-containing Mesoporous Nitrogen-Doped Carbon for Efficient Oxygen Reduction. *Adv. Funct. Mater.*, **2012**, 22, 4584-4591.
- [6] Wu, J.; Ma, L.; Yadav, R.M.; Yang, Y.; Zhang, X.; Vajtai, R.; Lou, J.; Ajayan, P.M., Nitrogen-Doped Graphene with Pyridinic Dominance as a Highly Active and Stable Electrocatalyst for Oxygen Reduction. *ACS Appl. Mater. Interfaces*, **2015**, 7, (27), 14763-14769.
- [7] Gong, K.; Du, F.; Xia, Z.; Durstock, M.; Dai, L., Nitrogen-Doped Carbon Nanotube Arrays with High Electrocatalytic Activity for Oxygen Reduction. *Science*, **2009**, 323, (5915), 760-764.

## *Chapter 6 - Conclusions and future perspectives*

With the tremendous expansion of nanotechnologies, nanomaterials have attracted growing interest in the past decades and played a significant role in increasing the knowledge in multidisciplinary fields related to physics, chemistry and biology.

Carbon nanomaterials (CNMs) are a class of low-dimensional materials that have aroused a great deal of interest in the past 30 years since the discovery of fullerene in 1985. CNMs have become one of the hottest topics in scientific research and emerged as attractive candidates for a large number of applications. The nanometric size, below 100 nm, is comparable to that of relevant biological entities, making carbon-based nanomaterials an ideal platform for biomedical applications. In addition, due to large specific surface area, cost effectiveness and outstanding electrical and mechanical properties, CNMs have emerged as efficient cathode materials for electrocatalytic processes.

Carbon nano-onions (CNOs) are an interesting member of the carbon family, owning a peculiar multi-layered graphitic structure and physico-chemical properties defined by the production method.

Even if discovered at the same time as carbon nanotubes, CNOs stayed in the shadow of its famous counterpart for a long time. The development of large-scale production methods and surface functionalization strategies allowed CNOs to draw attention among the scientific community, showing promising potential in applicative areas spanning from electronics to biology.

In this Thesis dissertation, the synthesis and characterization of novel CNO derivatives has been presented with the aim to explore new applicative uses of these CNMs in biomedicine and electrocatalysis.

Thermal annealing of detonation nanodiamonds (DNDs) has been selected as CNO synthetic method due to the gram-scale production yield and narrow size distribution and purity of the products.

Several characterization techniques were used to confirm the successful conversion of the DND  $sp^3$ -hybridized carbon structure into the typical CNO  $sp^2$ -graphitic architecture. HRTEM investigations showed the formation of 6 nm-sized quasi-spherical nanoparticles consisting of 7-10 concentric shells. The graphitic nature of CNOs have been proved by XRD and spectroscopy techniques such as

XPS, Raman and EELS, which showed typical features of  $sp^2$  carbon structures. In particular, the high curvature due to the small size and the defectiveness of the CNO surface (as suggested by the prominent D-band in the Raman spectrum) makes them highly reactive and thus a perfect platform for functionalization strategies. Furthermore, CNOs display high thermal stability and large surface area, as depicted from TGA and BET analyses.

Pristine CNOs are intrinsically water-insoluble due to their hydrophobic nature. For biomedical applications, the nanoparticles need to be dispersed uniformly in the physiological environment. For this reason, the CNO surface have been functionalized with carboxylic acid groups through an oxidation reaction in 3 M nitric acid to enhance their dispersing abilities. The successful decoration of CNOs has been confirmed by XPS, as depicted by increase of the oxygen content and the presence of a new peak, assigned to COOH functionalities, in the spectrum of oxi-CNOs. DLS and zeta potential analyses corroborated the enhanced water-solubility of CNOs along with a remarkable stability in solution. The introduction of carboxylic acid groups paved the way for the further functionalization of the CNO surface with a newly synthesized far-red emitting BODIPY dye to develop a novel CNO-based bio-imaging platform. All the characterizations confirmed the presence of the dye onto the CNOs. In addition, the remarkable fluorescent emission properties and high quantum yield of fluo-CNOs allowed for their *in vitro* bio-evaluation in Hela and MCF-7 cells. The fluorescent CNO derivatives showed negligible toxic effects in both the tested cell lines, confirming the biocompatibility of the materials. In addition, the widespread red emission, as depicted by confocal imaging, corroborated the remarkable abilities of fluo-CNOs to be uptaken into the cells and to locate in the lysosomal vesicles. The results discussed confirmed that CNOs are ideal platforms for high-resolution biological imaging and open the way to the development of CNO-based drug delivery systems. In this context, the efficient internalization and bright photoluminescence may be crucial factors for the development of multifunctional CNO derivatives able to act simultaneously as bio-imaging agent and therapeutic drug delivery carrier.

Fuel cells are novel promising green energy devices that allow for the production of electricity through the electrochemical oxidation of a fuel (i.e. hydrogen) and the reduction of oxygen to produce water. The oxygen reduction reaction (ORR) is an important electrocatalytic reaction occurring at the cathode side of these devices. However, the high cost of the standard carbon-based platinum (Pt/C) materials used to catalyze the ORR is the major limitation of their commercialization, thus it is crucial to develop novel catalysts with high efficiency and low cost.

With this in mind, a new co-doping procedure was carried out to prepare a novel CNO-based catalyst for the oxygen reduction reaction (ORR). Thermal annealing of DNDs has been employed to introduce nitrogen and boron atoms into the CNO structure by using boric acid as B source and taking

advantage of the residual nitrogen impurities present in DNDs as N source. This procedure enables for the low cost mass-production of CNO-based catalysts. HRTEM investigations showed the formation of polyhedral-shaped CNOs, while XPS suggested the formation of preferential pyridinic N and substitutional B species, which are reported to be the most active ORR active sites. In addition, the sample contains large amount of connected B-N bonds, which may be detrimental to the ORR performance of the materials. The electrocatalytic activity of BN-CNOs towards ORR was investigated and compared to that of p-CNOs and Pt/C. The findings confirmed that the proposed co-doping process is an efficient way to enhance the performance of the CNOs due to the large amount of beneficial ORR active sites. BN-CNOs show remarkable electroactivity due to the higher conductivity and a very small production of peroxide species, confirming a quasi-ideal four-electron pathway for the oxygen reduction. Furthermore, compared to Pt/C, higher long-term durability was observed as well as excellent tolerance to methanol crossover effects, suggesting the great potentialities of the co-doped catalysts to rival with the standard platinum-based electrodes. It can be noted that the preferential formation of connected B-N species may limit to some extent the catalytic behavior of the catalyst. For this reason, systematic investigations on how to regulate and optimize the dopant's configuration in the CNO catalysts (i.e., to reduce the connected B-N species) is essential to fully exploit the real potential of the material.

Carbon nano-onions, as discussed in this Thesis dissertation, have shown to be a promising material for biological and electrochemical applications. Nevertheless, further investigations are required in order to fully understand the potentialities of these fascinating carbon nano-materials.

Regarding bio-related applications, the development of new CNO-based drug delivery systems is the natural step to be explored in the future. The biocompatibility and the ability to easily cross the cell membrane exhibited by the CNO derivatives make them a promising material for carrying and transporting therapeutic moieties for cancer therapy purposes. Also, the ease of functionalization of CNOs allows for the attachment of ligands onto the surface that can be selectively recognized by receptors over-expressed by cancer cells. This not only may increase the specificity of the delivery systems, but also reduce the exposition of toxic drugs to healthy cells.

For this purpose, CNOs may be functionalized with biologically relevant drug molecules such as doxorubicin, allowing for being used as cargos to deliver these bio-entities to cells.

Furthermore, CNOs should be multi-functionalized with imaging and therapeutic units to develop efficient and specialized drug delivery systems able of both diagnostic and therapeutic purposes.

Finally, *in vivo* investigations should be performed in order to further confirm the biocompatibility of the CNO derivatives.

Regarding the electrochemical applications, new doping approaches should be developed in order to introduce in the CNO network different dopants. Heteroatoms such as sulfur, phosphorus as well as halogens and their combination may be studied for this purpose and their influence towards the oxygen reduction reaction investigated.

Hence, CNO-based materials have the right features to be used for a wide range of applications.